REVISTA Ingeniería

Four-monthly scientific journal

2023

Focus and Scope

The *Ingeniería* journal is a scientific publication that deals with the fields of Engineering and Technology, according to the OCDE's classification of scientific areas. It is published every four months by Universidad Distrital Francisco José de Caldas, and its main goal is to disseminate and discuss advances in research and development in the different areas of Engineering and Technology via original and previously unpublished works with local and international scope. The Journal's intended audience is the academic community, researchers, graduates, productive sectors, and the general public interested in all the disciplines of Engineering.

Editors

Editor-in-chief
Oscar Danilo Montoya Giraldo, PhD.
Universidad Distrital Francisco José de Caldas, Colombia

Associate Editor
Nelson Leonardo Díaz, PhD.
Universidad Distrital Francisco José de Caldas, Colombia

Scientific and editorial committee

PhD. Alonso Salvador Sanchez
Universidad de Alcalá
Spain

PhD. Arul Rajagopalan
Vellore Institute of Technology
Chennai, India.

PhD. Carlos Andrés Peña
Institute for Information and
Communication Technologies -
HEIG-VD, Switzerland.

PhD. Federico Martin Serra
Universidad Nacional de San Luis
Argentina

PhD. Iván Santelices Malfanti
Universidad del Bío-Bío
Chile

PhD. Jesús de la Casa Hdez
Universidad de Jaén
Spain

PhD. José Marcio Luna
Perelman School of Medicine
University of Pennsylvania
United States

PhD. Josep M. Guerrero
Aalborg University
Dinamarca

PhD. Nelson L. Diaz
Universidad Distrital Francisco
José de Caldas
Colombia

PhD. Sarah Greenfield
Centre for Computational
Intelligence De Montfort Interdisciplinary
England

Directives

Giovanny Tarazona Bermúdez, PhD.
Rector

Ángela Parrado Rosselli, PhD.
Director CIDC-Centro de Investigación y Desarrollo Científico

Luz Esperanza Bohórquez, PhD.
Dean Faculty of Engineering

Technical Committee

Ingri Gisela Camacho, BSc.
Editorial Manager

Julian Arcila-Forero, MSc.
Layout Artist (LATEX)

José Daniel Gutiérrez Mendoza
Spanish/English Proofreader

Open Access Policy

The *Ingeniería* journal provides free access to its content. This free access is granted under the principle of making research freely available to the public, which encourages a greater exchange of global knowledge.

Attribution-NonCommercial-ShareAlike 4.0 International (CC BY-NC-SA 4.0)

You are free to:

- **Share** — copy and redistribute the material in any medium or format

- **Adapt** — remix, transform, and build upon the material

- The licensor cannot revoke these freedoms as long as you follow the license terms

Article Processing Charge

No publication fees are charged to the authors or their institutions, nor are any payments made to expert peer reviewers or associate or adjunct editors. The *Ingeniería* journal is funded by Universidad Distrital Francisco José de Caldas, its Faculty of Engineering, and its Central Research Office.

Indexed

Peer-reviewers in this issue

Table of contents

Three-Phase Power Flow Tool for Electric Distribution Grids: A Julia Implementation for Electrical Engineering Students

Oscar Danilo Montoya[1] [ID][✉]*, Alejandro Garces[2] [ID], and Walter Gil-González[2] [ID]

[1]Universidad Distrital Francisco José de Caldas. Bogotá, Colombia.
[2]Universidad Tecnológica de Pereira. Pereira, Colombia.

Most of the concepts involved in Electrical Engineering have been developed from the 20th century to the present day. One of the most popular studies in this field is the power flow problem for electrical systems composed of multiple nonlinear loads (*i.e.*, loads with constant power consumption) (1). This problem is formulated by applying Kirchhoff's voltage law to each node in the system, which results in a set of nonlinear algebraic equations that consider steady-state conditions (2). In this vein, this editorial note presents a tutorial for Electrical Engineering students regarding the general implementation of the three-phase power flow problem in distribution networks via the successive approximations method (3).

General three-phase power flow formulation

The general formula for the power flow solution in three-phase networks is obtained after applying Kirchhoff's voltage law to each network node, which produces the set of constraints defined by

$$-\mathbb{I}_{d3\varphi} = \mathbb{Y}_{ds3\varphi}\mathbb{V}_{s3\varphi} + \mathbb{Y}_{dd3\varphi}\mathbb{V}_{d3\varphi}, \tag{1}$$

where $\mathbb{Y}_{ds3\varphi} \in \mathcal{C}^{3(n-1)\times 3}$ and $\mathbb{Y}_{dd3\varphi} \in \mathcal{C}^{3(n-1)\times 3(n-1)}$ are complex sub-matrices obtained for the nodal three-phase admittance matrix $\mathbb{Y}_{\text{bus}3\varphi}$ (note that this matrix can be obtained using the node-to-branch incidence and the admittance primitive matrices (3)); $\mathbb{I}_{d3\varphi} \in \mathcal{C}^{3(n-1)\times 1}$ is the complex vector of demanded currents, which is a nonlinear function of the demanded voltages $\mathbb{V}_{d3\varphi} \in \mathcal{C}^{3(n-1)\times 1}$ and the constant complex power loads; and $\mathbb{V}_{s3\varphi} \in \mathcal{C}^{3\times 1}$ is the complex power voltage output at the terminals of the substation. Note that $\mathcal{C}$ denotes the set of complex numbers.

---

*[✉] **Correspondence:** odmontoyag@udistrital.edu.co

Remark 1. *The calculation of the demanded current vector $\mathbb{I}_{d3\varphi}$ depends on the load connection type, i.e., Wye (Y) or Delta (Δ).*

To illustrate the general calculation of the three-phase demanded currents, consider the schematic load connections presented in Figs. **1**a and **1**b.
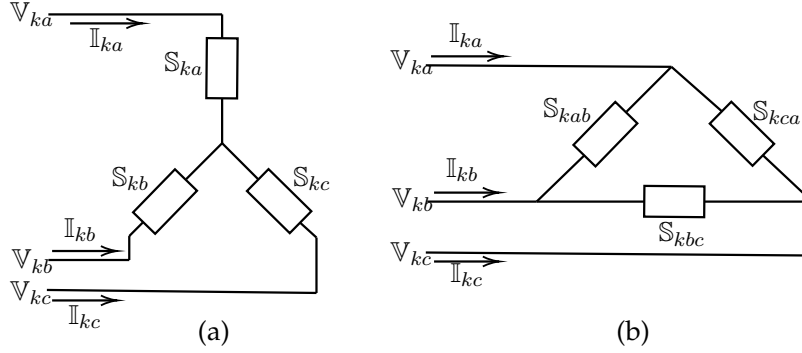
Figure 1. Constant power load: a) Y connection and b) Δ connection

For these load connections, when Tellegen's second theorem is applied (*i.e.*, the relation between voltages, currents, and powers), the following compacted three-phase current formulas are obtained:

$$\mathbb{I}_{k3\varphi}^{Y} = \mathbf{diag}^{-1}\left(\mathbb{V}_{k3\varphi}^{\star}\right)\mathbb{S}_{k3\varphi}^{\star}, \tag{2}$$

$$\mathbb{I}_{k3\varphi}^{\Delta} = \mathbf{diag}^{-1}\left(\mathbf{M}\mathbb{V}_{k3\varphi}^{\star}\right)\mathbb{S}_{k3\varphi}^{\star} + \mathbf{diag}^{-1}\left(\mathbf{M}^{\top}\mathbb{V}_{k3\varphi}^{\star}\right)\mathbf{H}\mathbb{S}_{k3\varphi}^{\star}, \tag{3}$$

$$\mathbb{I}_{d3\varphi}^{\star} = \mathbb{I}_{k3\varphi}^{Y} + \mathbb{I}_{k3\varphi}^{\Delta}, \tag{4}$$

where the matrices $\mathbf{M}$ and $\mathbf{H}$ take the following form

$$\mathbf{M} = \begin{bmatrix} 1 & -1 & 0 \\ 0 & 1 & -1 \\ -1 & 0 & 1 \end{bmatrix}, \ \mathbf{H} = \begin{bmatrix} 0 & 0 & 1 \\ 1 & 0 & 0 \\ 0 & 1 & 0 \end{bmatrix},$$

and $(\cdot)$ is the complex conjugate operation applied to the argument.

Iterative power flow solution

Considering the general power flow formula in (1) and the definition of the demanded current in (4), an iterative power flow formula can be obtained (4).

$$\mathbb{V}_{d3\varphi}^{t+1} = -\mathbb{Y}_{dd3\varphi}^{-1}\left(\mathbb{Y}_{ds3\varphi}\mathbb{V}_{s3\varphi} - \mathbb{I}_{d3\varphi}^{t}\right), \tag{5}$$

where

$$\mathbb{I}_{k3\varphi}^{t} = \mathbf{diag}^{-1}\left(\mathbb{V}_{k3\varphi}^{t,\star}\right)\mathbb{S}_{k3\varphi}^{\star} + \mathbf{diag}^{-1}\left(\mathbf{M}\mathbb{V}_{k3\varphi}^{t,\star}\right)\mathbb{S}_{k3\varphi}^{\star} - \mathbf{diag}^{-1}\left(\mathbf{M}^{\top}\mathbb{V}_{k3\varphi}^{t,\star}\right)\mathbf{H}\mathbb{S}_{k3\varphi}^{\star} \tag{6}$$

for all k in the set of the demanded buses.

Remark 2. *Eqs. (5) and (6) are iteratively solved until the desired error of convergence is reached, i.e.,*

$$\text{máx}\left|\left|\mathbb{V}_{d3\varphi^{t+1}}\right| - \left|\mathbb{V}_{d3\varphi}^{t}\right|\right| \leq \varepsilon, \tag{7}$$

with ε being the convergence's tolerance.

Julia implementation

Julia is an efficient programming environment that combines the advantages of Python, Matlab, and R with the efficiency of well-known programming languages such as C++ or Fortran (5). To illustrate the general implementation of the three-phase power flow problem in Julia, consider a small distribution grid composed of seven buses and six lines, which is unbalanced and operates with a line-to-ground voltage of 23 kV at the terminals of the substation. All the information on this system is directly presented in the Julia scripts. Fig. 2 illustrates the first part of the three-phase power flow problem's implementation in distribution networks.

```julia
# Successive approximation power flow three-phase grids
using DataFrames, LinearAlgebra
# System bases
Vb = 23000; # V
Sb = 1000; # kVA
Zb = (Vb^2)/(Sb*1000);
# System information Data in Ohm
branch_data = DataFrames.DataFrame([
(1, 2, 0.5025, 0.3025),(2, 3, 0.4020, 0.2510),
(3, 4, 0.3660, 0.1864),(2, 5, 0.3840, 0.1965),
(5, 6, 0.8190, 0.7050),(2, 7, 0.2872, 0.4088),]);
DataFrames.rename!(branch_data, [:k, :m, :Rkm, :Xkm])
# System information Data in kVA
node_data = DataFrames.DataFrame([
(1, 1, 0,    0,    0,    0,    0,    0,    0),
(2, 1, 1000, 600,  750,  450,  1250, 750,  1),
(3, 1, 1800, 1000, 0,    0,    900,  500,  0),
(4, 1, 3000, 1800, 0,    0,    4500, 1800, 0),
(5, 1, 0,    0,    2400, 1900, 1200, 950,  1),
(6, 1, 0,    1560, 2100, 0,    1050, 780,  1),
(7, 1, 500,  0,    3000, 1150, 2500, 2300, 0)
]);
DataFrames.rename!(node_data, [:k,:Vk0,:Pka,:Qka,:Pkb,:Qkb,:Pkc,:Qkc,:Type])
```

Figure 2. Parametric information associated with the three-phase 7-bus network

Fig. 2 presents the parametric information of the network, *i.e.*, the distribution line impedance (in this example, the three-phase impedance matrix is assumed to be balanced with values only in its diagonal) and the constant power loads. Note that, if `node_data.Type[k,1] == 1`, the load associated with the k-node is Y-connected; otherwise, it is $\Delta-$connected.

The next step is calculating the nodal admittance matrix. This process is shown in Fig. 3.

Once the nodal admittance matrix has been constructed, the iterative power flow formula defined in (5), the current calculation in (6), and the stopping criterion in (7) are implemented in Julia using a function called `Successive3f(node_data,Ybus3f,error,tmax,Sb)` (Fig. 4). This implementation is intuitive, and the student/researcher can easily follow all the procedures for solving

```
# Nodal admittance matrix construction
N = size(node_data,1); L = size(branch_data, 1); A = zeros(N,L)
for l = 1:L
    k = branch_data.k[l]; m = branch_data.m[l];  A[k,l] = 1;  A[m,l] = -1;
end
A3f = zeros(3*N,3*L); Z3f = complex(zeros(3*L,3*L))
z = (branch_data.Rkm + im*branch_data.Xkm)/Zb
Ybus = A*inv(diagm(z))*transpose(A)
MatrixI = diagm([1.0;1.0;1.0]);
for k = 1:L
    for j = 1:N
        if A[j,k] != 0
            A3f[3*j-2:3*j,3*k-2:3*k] = A[j,k]*MatrixI;
        end
    end
    Z3f[3*k-2:3*k,3*k-2:3*k] = z[k,1]*MatrixI;
end
Ybus3f = A3f*inv(Z3f)*transpose(A3f)
```

Figure 3. General construction of the three-phase nodal admittance matrix

the three-phase power flow problem via the successive approximations method.

Finally, to obtain the general power flow solution for the 7-bus grid used in this example, the power flow function calculates all the phase voltages, which allows obtaining the total grid apparent power losses and reporting the voltage magnitudes and angles per phase. This process is depicted in Fig. **5**. It is worth mentioning that, this figure, the apparent power losses are calculated using Eq. (8).

$$\mathbb{S}_{\text{loss}3\varphi} = \mathbb{V}^{\top} \left(\mathbb{Y}_{\text{bus}3\varphi}\mathbb{V} \right)^{\star}, \tag{8}$$

where $\mathbb{V}$ corresponds to the voltage output obtained by calling the power flow function implemented in Fig. **4** as `V3f = Successive3f(node_data,Ybus3f,error,tmax,Sb)`.

The power flow solution for this numerical example is plotted in Fig. **6**.

The student/researcher interested in the Julia-based three-phase power flow solution presented in this editorial note should thoroughly examine all the codifications and follow each one of the presented plots (see Figs. **2** to **6**) to reach the same numerical solution presented in Fig. **6**.

Conclusion

This editorial note presented an intuitive algorithm based on the successive approximations power flow method with the aim of solving the three-phase power flow problem in electric distribution networks via the Julia programming environment (version 1.9.2). The main idea of this tutorial is to provide a new power flow tool for Electrical Engineering students and researchers, an easily implementable open-source algorithm for conducting studies in unbalanced distribution networks.

```
error = 1e-10; tmax = 1000;
function Successive3f(node_data,Ybus3f,error,tmax,Sb)
    Ydd3f = Ybus3f[4:end,4:end]; Zdd3f = inv(Ydd3f);
    Yds3f = Ybus3f[4:end,1:3];
    Vs3f = node_data.Vk0[1,1]*[exp(1.0*im*0);
    exp(1.0*im*-2*pi/3);
    exp(1.0*im*2*pi/3)];
    global Vd3f = complex(zeros(3*N-3,1))
    Sd3f = complex(zeros(3*N-3,1))
    for j = 1:N-1
        Vd3f[3*j-2:3*j,1]=node_data.Vk0[j,1]*Vs3f;
        Sd3f[3*j-2:3*j,1]=[(node_data.Pka[j+1,1]+im*node_data.Qka[j+1,1])/Sb;
        (node_data.Pkb[j+1,1]+im*node_data.Qkb[j+1,1])/Sb;
        (node_data.Pkc[j+1,1]+im*node_data.Qkc[j+1,1])/Sb];
    end
    global V3f = [Vs3f;Vd3f];
    M = [1 -1 0;0 1 -1;-1 0 1]; H = [0 0 1;1 0 0;0 1 0];
    for t = 1:tmax
        Id3fY = complex(zeros(3*N-3,1)); Id3fD = complex(zeros(3*N-3,1));
        Id3f = complex(zeros(3*N-3,1));
        for k = 1:N-1
            if node_data.Type[k,1] == 1 # Wye load connection
                Id3fY[3*k-2:3*k] = inv(diagm(conj(Vd3f[3*k-2:3*k,1])))*
                conj(Sd3f[3*k-2:3*k,1])
            elseif  node_data.Type[k,1] == 0 # Delta load connection
                Id3fD[3*k-2:3*k] = inv(diagm(M*conj(Vd3f[3*k-2:3*k,1])))*
                conj(Sd3f[3*k-2:3*k,1])+
                inv(diagm(transpose(M)*conj(Vd3f[3*k-2:3*k,1])))*
                H*conj(Sd3f[3*k-2:3*k,1])
            end
        end
        Id3f = Id3fY + Id3fD
        Vdt3f = -Zdd3f*(Id3f + Yds3f*Vs3f)
        if maximum(abs.(abs.(Vd3f) - abs.(Vdt3f))) < error
            global V3f = [Vs3f;Vdt3f]
            println("Iterations: ",t)
            break
        else
            global Vd3f = Vdt3f;
        end
    end
return V3f
end
```

Figure 4. Iterative three-phase power flow solution

```
V3f = Successive3f(node_data,Ybus3f,error,tmax,Sb)
Sloss3f = transpose(V3f)*conj!(Ybus3f*V3f)*Sb
Pos = zeros(N,3);
for k = 1:N
    Pos[k,:] = [3*k-2 3*k-1 3*k];
end
Report = DataFrames.DataFrame(;k = 1:N,
MagVa = abs.(V3f[Int.(Pos[:,1])]),AngVa = angle.(V3f[Int.(Pos[:,1])])*180/pi,
MagVb = abs.(V3f[Int.(Pos[:,2])]),AngVb = angle.(V3f[Int.(Pos[:,2])])*180/pi,
MagVc = abs.(V3f[Int.(Pos[:,3])]),AngVc = angle.(V3f[Int.(Pos[:,3])])*180/pi,)
println("Complex power losses = ",Sloss3f)
println("Voltage report ",Report)
```

Figure 5. Calling the three-phase power flow function and reporting the results

```
Iterations: 6
Complex power losses = ComplexF64[425.3462475757646 + 266.4415246363203im;;]
Voltage report 7x7 DataFrame
 Row   k       MagVa       AngVa        MagVb       AngVb       MagVc       AngVc
       Int64   Float64     Float64      Float64     Float64     Float64     Float64
    1     1    1.0         0.0          1.0         -120.0      1.0         120.0
    2     2    0.989097    0.104014     0.989451    -120.079    0.987362    119.972
    3     3    0.983244    0.094141     0.987838    -120.028    0.984471    119.873
    4     4    0.979802    0.107915     0.986513    -119.977    0.98266     119.798
    5     5    0.987956    0.198423     0.986511    -120.152    0.9845      120.024
    6     6    0.985844    0.340503     0.983201    -120.318    0.981786    120.013
    7     7    0.988823    0.0813783    0.986898    -120.179    0.984177    119.931
```

Figure 6. Three-phase power flow solution in the studied 7-bus grid

Acknowledgements

Referencias

[1] C. Yang *et al.*, "Optimal power flow in distribution network: A review on problem formulation and optimization methods," *Energies*, vol. 16, no. 16, p. 5974, Aug. 2023. ↑ 1

[2] A. Garces, "A linear three-phase load flow for power distribution systems," *IEEE Trans. Power Syst.*, vol. 31, no. 1, pp. 827–828, Jan. 2016. ↑ 1

[3] B. Cortés-Caicedo, L. S. Avellaneda-Gómez, O. D. Montoya, L. Alvarado-Barrios, and H. R. Chamorro, "Application of the vortex search algorithm to the phase-balancing problem in distribution systems," *Energies*, vol. 14, no. 5, p. 1282, Feb. 2021. ↑ 1

[4] O. D. Montoya, J. S. Giraldo, L. F. Grisales-Noreña, H. R. Chamorro, and L. Alvarado-Barrios, "Accurate and efficient derivative-free three-phase power flow method for unbalanced distribution networks," *Computation*, vol. 9, no. 6, p. 61, May 2021. ↑ 2

[5] J. M. Perkel, "Julia: Come for the syntax, stay for the speed," *Nature*, vol. 572, no. 7767, pp. 141–142, Jul. 2019. ↑ 3

Oscar Danilo Montoya

Compatibility and Electromagnetic Interference group, Department of Engineering, Universidad Distrital Francisco José de Caldas; Electrical Engineer, Master in Electrical Engineering, and PhD in Engineering. **Email:** odmontoyag@udistrital.edu.co

Alejandro Garces

Electromagnetic Fields and Energy Phenomena group, Department of Engineering, Universidad Tecnológica de Pereira; Electrical Engineer, Master in Electrical Engineering, and PhD in Engineering. **Email:** alejandro.garces@utp.edu.co

Walter Gil-González

Electromagnetic Fields and Energy Phenomena group, Department of Engineering, Universidad Tecnológica de Pereira; Electrical Engineer, Master in Electrical Engineering, and PhD in Engineering. **Email:** wjgil@utp.edu.co

Research

Study on the Use of Coal Bottom Ash as a Raw Material Replacement for the Production of Clay Bricks

Estudio sobre el aprovechamiento de cenizas de fondo de carbón como reemplazante de materia prima para la elaboración de ladrillos de arcilla

José Fernando Benítez-Vivas[1], Juan Pablo Gutiérrez-López[1], Janneth Torres-Agredo[1] (iD)(✉)*,
Luisa Fernanda Mosquera-Idrobo[1] (iD), and Miguel Fernando Díaz-Huertas[2]

[1]Universidad Nacional de Colombia (Palmira campus), Materiales y Medio Ambiente research group (GIMMA). Palmira, Valle del Cauca, Colombia
[2]C.I. LAGO VERDE S.A.S company, Valle del Cauca, Colombia

Abstract

Context: Masonry bricks are one of the most widely used building materials in the world, which leads to the overexploitation of its raw materials. Its production consumes a large amount of energy and has a large environmental footprint. The clay brick industry can add residues to its raw materials; among those reported are tea processing waste, brick waste, paper industry residues, waste from coffee mills, and coal ashes.

Method: Bottom coal ashes were characterized by X-ray fluorescence, X-ray diffraction, thermogravimetric analysis, electronic microscopy, and particle size analysis. In addition, their density and loss on ignition were determined. The incorporation of ashes in the elaboration of clay bricks was evaluated, with sand replacement percentages of 0, 3, 5, and 7 %. Finally, the physical and mechanical properties of the bricks were evaluated.

Results: The water absorption and apparent porosity increased, while the compressive strength and bulk density decreased with the incorporation of ash in the brick samples, except for those with a 3 % replacement, which showed a better performance in the evaluated properties.

Conclusions: Coal bottom ashes have great potential in the manufacturing of clay bricks. The findings of this study indicate that, by incorporating up to 3 % ashes, bricks can be obtained which comply with the Colombian regulations.

Keywords: Bottom ash, building materials, industrial waste, sustainability

*✉ **Correspondence:** jtorresa@unal.edu.co

Resumen

Contexto: El ladrillo de mampostería es uno de los materiales de construcción más utilizados en todo el mundo, lo que conlleva a una sobreexplotación de sus materias primas. Su producción consume gran cantidad de energía y tiene una gran huella ambiental. La industria de ladrillos de arcilla tiene la capacidad de adicionar residuos a su materia prima; entre los reportados se encuentran residuos del procesamiento del té, residuos de ladrillo, residuos de la industria del papel, residuos del beneficio de café y cenizas de carbón.

Método: Se caracterizaron cenizas de carbón de fondo por fluorescencia de rayos X, difracción de rayos X, análisis termogravimétrico, microscopía electrónica y análisis de tamaño de partícula. Además, se determinó su densidad y pérdida al fuego. Se evaluó la incorporación de cenizas en la elaboración de ladrillos de arcilla, con porcentajes de reemplazo de arena de 0, 3, 5 y 7 %. Finalmente, se evaluaron las propiedades físicas y mecánicas de los ladrillos.

Resultados: La absorción de agua y la porosidad aparente aumentaron, mientras que la resistencia a la compresión y la densidad aparente disminuyeron con la incorporación de cenizas en las muestras de ladrillos, a excepción de aquellas con un reemplazo del 3 %, las cuales presentaron un mejor desempeño en las propiedades evaluadas.

Conclusiones: Las cenizas de fondo de carbón tienen un gran potencial en la fabricación de ladrillos de arcilla. Los hallazgos de este estudio indican que, al incorporar hasta un 3 % de cenizas, se pueden obtener ladrillos que cumplen la normatividad colombiana.

Palabras clave: cenizas, materiales de construcción, residuos industriales, sostenibilidad

Table of contents

1. Introduction

Coal ash is a by-product of coal combustion in thermal plants. It is considered one of the most complex and abundant anthropogenic materials in the world (1). When this residue is not properly disposed of, it can cause contamination in soil and water (1–3). These ashes represent between 5 and 20 % of the coal fed into the process and are divided into bottom ashes (BA) and fly ashes (FA), which represent 5-15 and 85-95 % by total weight of ashes generated, respectively (1). BA refers to the thicker

ashes that fall to the ground through air flows and are collected mechanically, while FA are finer particles captured through electrostatic or mechanical precipitators (4–6).

At a global level, during the last decades, studies on the disposal and use of these ashes have been carried out. For example, due to their chemical and mineralogical composition, they have been used for the production of concrete (7) and the coating of cenospheres (8), among others. It is worth mentioning that BA is less often recycled than FA (9). Currently, the coal ashes generated are not fully used and are stored in ash ponds, lagoons, or landfills (1, 10).

On the other hand, masonry brick is one of the most widely used building materials in the world, with a global annual production of 1.391 billion units. The great demand for this material in the construction sector has generated an overexploitation of its raw materials (11); its production consumes a lot of energy (12–14) and leaves a significant environmental footprint (13, 14).

The clay brick industry can add great amounts of waste to its raw material (15). Therefore, various studies out on the use of waste in the manufacturing of bricks have been carried. However, commercial production is limited due to the absence of standards and a slow acceptance by the industry (14).

The literature has reported the use of tea processing residues (16), brick residues (17), sewage sludge (18), and residual glass powder (12) for manufacturing bricks. Likewise, the use of coal ashes in the production of clay bricks has been studied.

(11) evaluated the use of FA and BA as substitutes for clay in brick manufacturing at two burning temperatures: 950 and 1.050 °C. It was found that the bricks with BA exhibited higher compressive strengths than those that incorporated FA. Compressive strength did not have a significant influence on temperature. On the other hand, it was found that the heavy metals present in the ashes were immobilized in the structure of bricks. Finally, it was concluded that the addition of coal ash in brick manufacturing can reduce the environmental impact of using natural resources and generating waste.

(19) replaced up to 80 % of clay with FA, employing burning temperatures between 800 and 1.000°C. The results showed that the compressive strength and water absorption improved with increasing firing temperature. On the other hand, the compressive strength decreased with the increase in CV content, except for the burning temperature of 1.000 °C. The authors state that FA can be useful for the production of clay bricks.

In the work by (20), at an industrial level, FA were added to bricks (0-25 %) as a replacement for clay at a temperature of 800 °C. The authors found that the addition of up to 20 % FA satisfies the minimum performance requirements of bricks according to the Pakistan building code.

Based on the above, it can be stated that ashes from the combustion of coal can be used as an addition to the ceramic industry. Therefore, the objective of this work was to study the use of coal bottom ash as a replacement for raw materials in clay brick manufacturing.

2. Methodology

For this work, coal bottom ashes (CBAs) were obtained from a Colombian company dedicated to clay brick manufacturing. CBAs are generated during the burning process of ceramic bricks, which is carried out at a temperature of 850 °C in a tunnel-type furnace. In this specific case, the company uses bituminous carbon. This company generates approximately 10 tons of CBAs per month. The samples were collected for five days in a stable furnace regime. Two samples, CBA1 and CBA2, were selected for this study.

The ashes were characterized via X-ray fluorescence (XRF) in a Philips MagixPro PW- 2440 equipped with a Rhodium tube, with a maximum power of 4 KW. Via X-ray diffraction (XRD) using a PANalytical EMPYREAN, the sample was measured in a Bragg-Brentano optical configuration with a high-speed solid-state detector for data acquisition called *PIXCEL*. They were also analyzed by scanning electron microscopy (SEM) using a JEOL frame equipment (JSM 5910 LV) operated at an acceleration voltage of 20 Kv. A chemical composition analysis was performed using an X-ray energy dispersion spectrometer (EDS). A thermogravimetric analysis (TGA) was also performed under oxidizing conditions at an air atmosphere and a heating rate of 10°C/min, with temperature range of 25-1.000°C, in a Q600 TA Instrument. In addition, the particle size distribution was determined by sieving, density, and loss on fire.

Likewise, the particle size was determined by sieving the sand used for brick manufacturing.

The bricks were made at a laboratory with clay, chamotte (ground brick), sand, and bottom ash. For this study, sand was partially replaced with coal bottom ash (CBA1 and CBA2). Table I shows the proportions used to make the bricks. For manufacturing, the raw materials were mixed mechanically, and the amount of water added was adjusted until a malleable consistency was obtained. The bricks were dried at room temperature for one day, in order not to cause fractures during drying. Then, they were placed in an electric oven at 190 °C for 24 hours. Finally, the bricks were placed in a tunnel furnace for 24 h at 850 °C. It is worth mentioning that this last step was carried out in the company's furnace, *i.e.*, under real conditions regarding the burning process.

Table I. Composition of experimental bricks

Type of brick	Clay (%)	CBA (%)	Chamotte (%)	Sand (%)
F0 (control)	75	0	12,5	12,5
F3	75	3	12,5	9,5
F5	75	5	12,5	7,5
F7	75	7	12,5	5,5

Once the bricks were made, tests such as apparent porosity, apparent density, and specific gravity were carried out according to the ASTM C20 standard (21). Additionally, the compressive strength and water absorption were determined according to the NTC 4017:2015 standard (22). Five samples were used for each test.

3. Results and discussion

3.0.1. CBA characterization

The ashes evaluated have similar chemical and physical characteristics, as shown in Table II. Regarding their chemical composition, they are mainly composed of SiO_2, Al_2O_3, and Fe_2O_3, which add up to 89,68 and 92,03 % in weight for CBA1 and CBA2, respectively. To a lesser extent, the ashes have sulfur oxides and calcium, among others. For brick manufacturing, the literature suggests a SiO_2 content (present in clays) of 50-60 % (23). According to Table **II**, the amount of silica present in CBA2 is slightly higher than recommended. It should also be noted that silica can generate an increase in porosity (23). This indicates that, in terms of the silica content, coal ash can be used as a substitute for clay. On the other hand, the presence of Fe_2O_3, a compound related to the formation of hematite, can give the bricks a reddish color (24). Additionally, a loss on ignition of 22,81 and 16,65· % were observed for BA1 and BA2, respectively, which is due to unburned organic matter content.

Table **II** shows that CBAs have heavy metals in their composition, which could leach and cause negative impacts on the environment. Therefore, in a test carried out before employing the CBAs, they were found to be non-hazardous, since the leaching levels of metals of environmental interest (such as Pb, Se, Cr, Hg, and Cd) were below the maximum limit established by Colombian regulations for hazardous waste. In addition, the ecotoxicity test for Daphnia Pulex was applied, which reported a non-ecotoxic residue (25).

Fig. **1** shows the X-ray diffractogram for CBA1, which shows crystalline phases such as quartz (SiO_2), hematite (Fe_2O_3), and anatase ($Ti_{0,784}O_2$), in addition to an amorphous structure. These results agree with the chemical composition of the ashes (Table **II**). Table III shows the semi-quantification of the crystalline and amorphous phases of the ashes, where quartz is the main component (51,7 %) followed by the amorphous phase (34,6 %). The quartz content can be used as a degreasing material (26) which corresponds to sand and chamotte in this specific case.
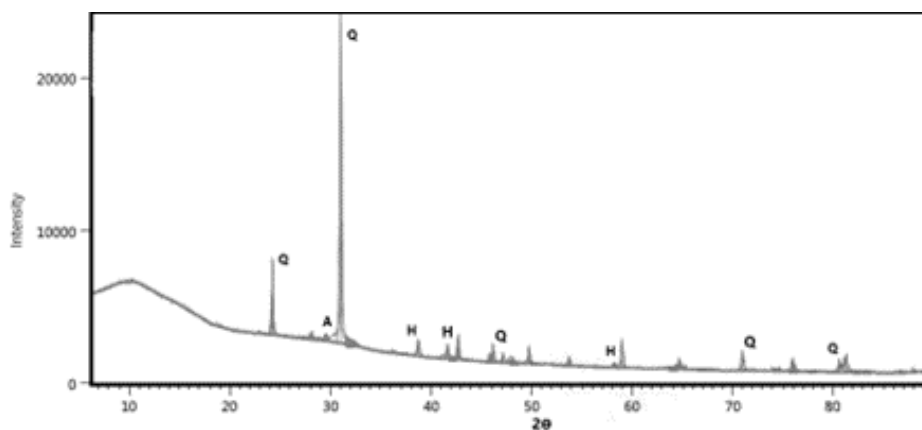
Figure 1. Diffractogram of CBA1. Q: quartz; H: hematite; A: anatase

Table II. Chemical composition and physical properties of CBAs

Characteristics	CBA1	CBA2
SiO_2	59,04	63,12
Al_2O_3	22,00	24,15
Fe_2O_3	8,64	4,76
SO_3	3,80	1,58
CaO	1,77	1,85
TiO_2	1,32	1,30
P_2O_5	1,12	1,05
K_2O	0,92	0,82
Na_2O	0,41	0,47
MgO	0,35	0,39
Cr	0,18	0,02
Ba	0,13	0,15
MnO	0,03	0,02
V	0,02	0,03
Cu	0,01	0,02
Pb	0,01	97 ppm
Zn	76 ppm	51 ppm
Se	-	28 ppm
Sr	0,11	0,10
Ce	0,06	0,09
Y	81 ppm	57 ppm
Density (g/m^3)	2,32	2,34
Loss on ignition (%)	22,81	16,65

Considering the above, that is, due to its chemical and mineralogical composition, coal bottom ash can be used as a substitute for raw material in the manufacturing of clay products (25).

The morphology and chemical composition of CBA1 are shown in Fig. **2**. The ashes exhibit irregular angular particles of different sizes, and some porous particles are contemplated. On the other hand, according to the EDS analysis, the ashes have SiO_2 as the main component, as well as Al_2O_3 to a lesser extent. These results confirm those obtained in the XRF analysis.

Fig. **3** shows the size distribution of the ashes. The particle size was approximately 700 and 500 μm for CBA1 and CBA2, respectively. This difference may be related to the efficiency of the combustion process (25). Likewise, the sand used reported an average particle size of less than 200 μm (Fig. **3**).

The thermogravimetric analysis of CBA2 is presented in Fig. **4**. Note that the ash had a weight loss of approximately 7,7 % at 1.000 °C. The main weight losses, in the range from 450 to 650 °C, are related to the loss of unburned carbon present in the ashes (27).

Table III. Semi-quantification of the crystalline phases and the amorphous phase of CBA1

Phase	Chemical formula	CBA1 (%)
Quartz	SiO_2	51,7
Hematite	Fe_2O_3	11,3
Anatase	$Ti_{0,784}O_2$	2,4
Amorphous	-	34,6

(a)   (b)
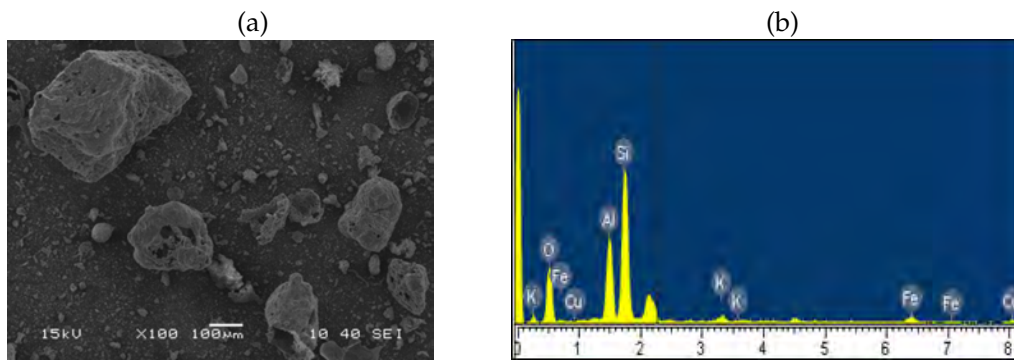
Figure 2. (a) SEM image and (b) EDS pattern of CBA1

(a)   (b)
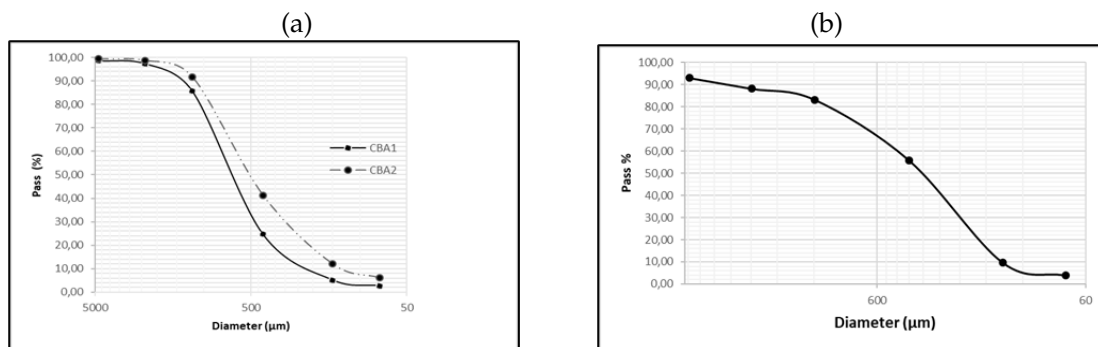
Figure 3. Granulometric curve: (a) bottom ash and (b) sand
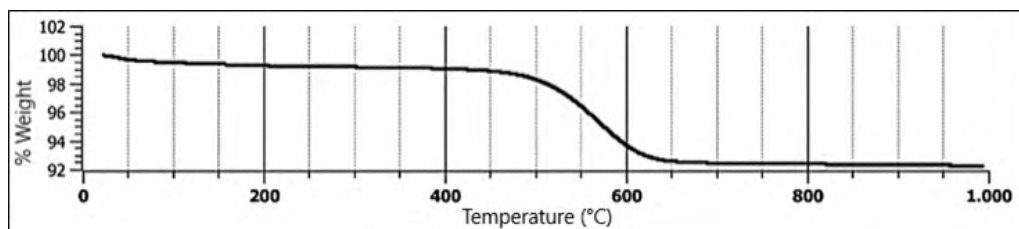
Figure 4. Thermogravimetric analysis of CBA2

3.1. Brick performance evaluation

3.1.1. Water absorption

Water absorption is one of the most important parameters in evaluating the durability of clay bricks (28). Fig. **5** shows the results for the bricks made with sand replacements of 3, 5, and 7 % with CBA1 and CBA2. It is observed that, with the increase in the proportion of ashes, the water absorption becomes slightly higher, except for the bricks with 3 % CBA1. On the other hand, the bricks that incorporated CBA1 at 5 % and CBA2 at 7 % reported the highest absorption with values of 18,27 and 19,56 %, respectively, when compared to the control bricks (16,23 %). This represents increments of 13 and 21 % for the each of the samples, respectively. The NTC 4205-2:2019 for non-structural masonry (solid bricks) establishes that the average maximum water absorption of five pieces must be 17 %. The bricks that incorporated CBA1 at 3 % and CBA2 at 5 % meet this requirement.
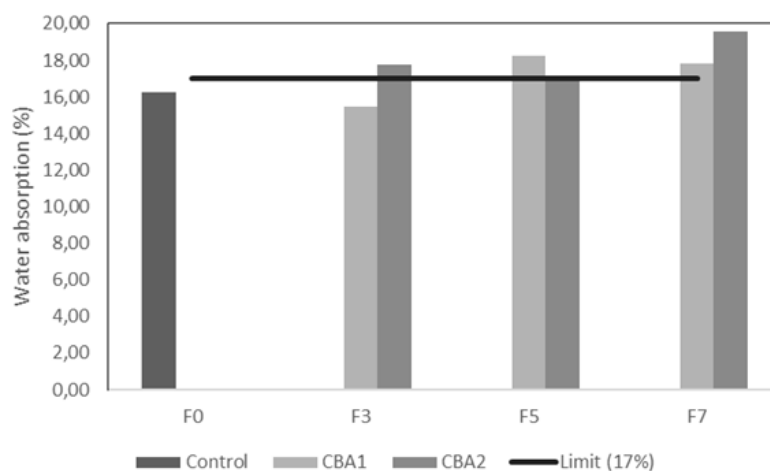
Figure 5. Water absorption of the brick samples

3.1.2. Apparent porosity

Fig. **6** shows the apparent porosity of the bricks, which increased with the incorporation of ashes. This agrees with previous studies where bottom ash was used for manufacturing clay bricks (11). The change in the porosity of the bricks may be related to the different particle sizes of the raw materials used (11). The highest porosities were observed in the bricks that incorporated CBA1 at 5 % and CBA2 at 7 %, with values of 35,53 and 37,17 %, respectively, with respect to the control bricks (31,96 %). On the other hand, the bricks that incorporated CBA1 at 3 % presented a porosity of 31,66 %, similar to that of the control sample.

The increased porosity of the bricks can be attributed to the high percentage of loss on ignition and the low content of fluxing agents present in the ashes (29). On the other hand, bricks with high porosities are lighter and have good insulation properties (29). It is important to mention that water absorption

and apparent porosity are directly related.
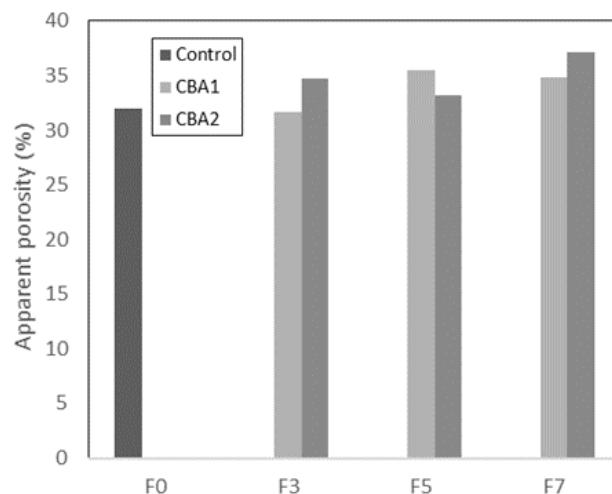
Figure 6. Apparent porosity of the bricks

3.1.3. Apparent density

The apparent density of clay bricks is influenced by the specific gravity of the raw material, the manufacturing methods used, and the degree of combustion (28). This parameter indicates the weight of the bricks (11). Fig. 7 shows the apparent density of bricks with different proportions of CBA. Note that the samples with ashes generated a reduction in the bulk density, *i.e.*, 1,80 g/cm^3 for the control brick and up to 1,62 g/cm^3 for the brick that incorporates CBA2 at 7%. The decreased density in bricks that incorporate ashes has been reported in other studies (11, 30). It can be said that there is an inverse correlation between water absorption/bulk porosity and bulk density.

3.1.4. Compressive strength

Fig. 8 presents the compressive strength of the brick samples. The results show a decrease with the increased incorporation of CBA1 and CBA2. This reduction may be related to the increase in the porosity of the bricks (11). Similar trends were reported in studies incorporating residues in clay brick manufacturing (11, 29, 30). On the other hand, the compressive strength of the sample with CBA1 at 3% (15,72 MPa) showed a slight increase compared to the control sample (14,61 MPa). The NTC 4205-2:2019 establishes that, for non-structural masonry (solid bricks) the average compressive strength of five pieces must be a minimum of 14 MPa. Therefore, the bricks that incorporated CBA1 at 3% meet this requirement. Moreover, the lowest compressive strength was reported by the CBA2 sample at 5% (10,9 MPa), which represents a reduction of approximately 25% with respect to the control sample.

The results of the tests presented in this research indicate that coal bottom ashes have great potential as a raw material in the production of clay bricks. In addition, it is important to highlight that the ashes used in this study, which come from a brick factory, do not require prior treatment to be used in this
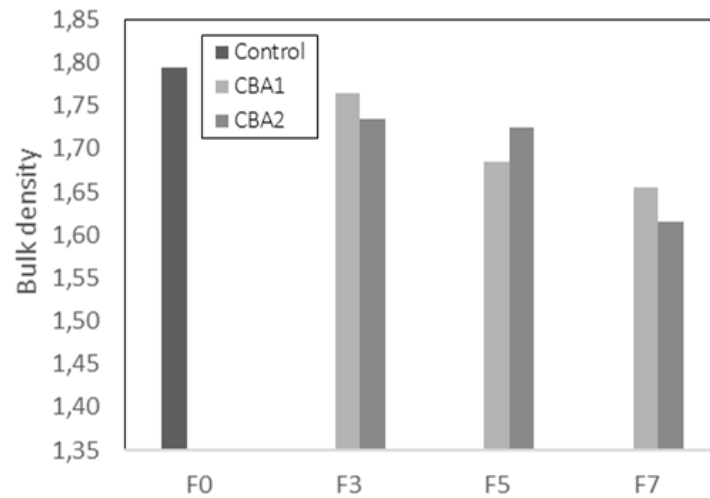
Figure 7. Apparent density of the bricks (g/cm^3)
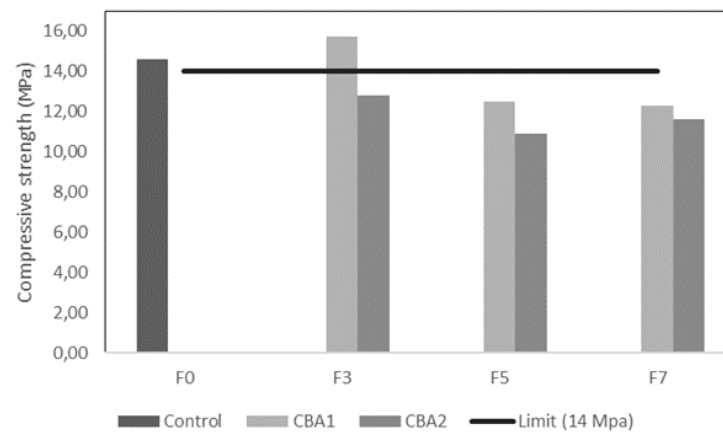
Figure 8. Compressive strength of the bricks

type of process, which constitutes an economic advantage. On the other hand, the use of this waste allows reducing the demand for sand, as well as mitigating or preventing the disposal of this waste in landfills or near the manufacturing sites, which translates into environmental advantages. Finally, we recommend continuing with future studies that allow scaling the production of bricks with CBA to an industrial level.

4. Conclusions

This study evaluated the incorporation of coal bottom ashes in the manufacturing of clay bricks. The ashes used were mainly composed of silica and aluminum oxides, with mineral phases such as quartz and hematite, in addition to a high amorphousness. According to these characteristics, the ashes can be used as degreasing material in the production of clay bricks.

Regarding the properties of the bricks, the absorption of water increased with the incorporation of ashes, which is why the bricks with CBA1 at 3 % and CBA2 at 5 % can be used for non-structural masonry according to the Colombian technical standards. The apparent porosity increased, while the apparent density decreased with the incorporation of coal bottom ashes into the brick samples. Hence, lighter bricks can be obtained.

The compressive strength decreased with the increasing coal ash content. However, the bricks that incorporated CBA1 at 3 % showed a resistance of 15,72 MPa, which satisfies the requirement for non-structural masonry as established by the Colombian regulations.

This study shows that, for the evaluated waste, an up to 3 % replacement of bottom ashes with sand can be used to obtain bricks that meet quality standards of Colombian regulations. The use of coal bottom ashes can reduce the consumption of natural resources for manufacturing clay-based bricks, in addition to reducing the volume of waste for final disposal, which constitutes environmental and economic benefits.

5. Acknowledgments

6. CRediT author statement

All authors: conceptualization, methodology, software, validation, formal analysis, investigation,writing (original draft, writing, review, and editing), data curation.

References

[1] Z. T Yao *et al.*, "A comprehensive review on the applications of coal fly ash," *Earth-Sci. Rev.,* vol. 141, pp. 105-121, 2015. https://doi.org/10.1016/j.earscirev.2014.11.016 ↑2, 3

[2] M. Temimi, J. P. Camps, and M. Laquerbe, "Valorization of fly ash in the cold stabilization of clay materials," *Resourc. Cons. Recyc.*, vol. 15, no. 3-4, pp. 219-234, 1995. https://doi.org/10.1016/0921-3449(95)00038-0 ↑2

[3] M. Ilic, C. Cheeseman, C. Sollars, and J. Knight, J., "Mineralogy and microstructure of sintered lignite coal fly ash," *Fuel*, vol. 82, no. 3, pp. 331-336, 2003. https://doi.org/10.1016/S0016-2361(02)00272-7 ↑2

[4] S. Jala and D. Goyal, "Fly ash as a soil ameliorant for improving crop production – A review," *Bioresource Tech.*, vol. 97, no. 9, pp. 1136-1147, 2006. https://doi.org/10.1016/j.biortech.2004.09.004 ↑3

[5] Z. T. Yao, "Generation, characterization and extracting of silicon and aluminium from coal fly ash," in *Fly Ash: Sources, Applications, and Potential Environmental Impacts*, P. K. Sarker, Ed., New York, NY, USA: Nova Science Publishers, 2013, p. 3-58. ↑3

[6] E. Fidanchevski *et al.*, "Technical and radiological characterization of fly ash and bottom ash from thermal power plant", *J. Radioanalytical Nuc. Chem.*, pp. 1-10, 2021. https://doi.org/10.1007/s10967-021-07980-w ↑3

[7] S. A. Mangi, M. H. W. Ibrahim, N. Jamaluddin, M. F. Arshad, S. H. Khahro, and R. P Jaya, "Influence of coal ash on the concrete properties and its performance under sulphate and chloride conditions", *Environ. Sci. Poll. Res.*, vol. 28, no. 43, pp. 60787- 60797, 2021. https://doi.org/10.1007/s11356-021-15006-x ↑3

[8] P. K. Kolay and S. Bhusal, "Recovery of hollow spherical particles with two different densities from coal fly ash and their characterization", *Fuel*, vol. 117, p. 118-124, 2014. https://doi.org/10.1016/j.fuel.2013.09.014 ↑3

[9] W. J. Lee, J. S. Lee, D. Atarashi, Y. H. Kim, and S. H. Lee, "Pore structure and possibility of fine dust removal for bottom ash sand", *J. Korean Ceramic Soc.*, vol. 57, p. 378-384, 2020. https://doi.org/10.1007/s43207-020-00046-9 ↑3

[10] E. Esmeray and M. Atıs, "Utilization of sewage sludge, oven slag and fly ash in clay brick production", *Const. Build. Mat.*, vol. 194, pp. 110-121, 2019. https://doi.org/10.1016/j.conbuildmat.2018.10.231 ↑3

[11] M. Sutcu, E. Erdogmus, O. Gencel, A. Gholampour, E. Atan, and T. Ozbakkaloglu, "Recycling of bottom ash and fly ash wastes in eco-friendly clay brick production", *J. Clean. Prod.*, vol. 233, pp. 753-764, 2019. https://doi.org/10.1016/j.jclepro.2019.06.017 ↑3, 8, 9

[12] M. Tripathi and V. B. Chauhan, "Evaluation of waste glass powder to replace the clay in fired brick manufacturing as a construction material", *Innov. Infras. Sol.*, vol. 6, no. 3, pp. 1-16, 2021. https://doi.org/10.1007/s41062-021-00492-2 ↑3

[13] M. N. S. Zaimi, N. F. Ariffin, S. M. S. Mohsin, A. M. Hasim, and N. N. Nasrudin, "Behavior on the mechanical performance and scanning electron microscopy of coal waste brick", *Mat. Today: Proc.*, vol. 48, pp. 1816-1820, 2022. https://doi.org/10.1016/j.matpr.2021.09.136 ↑3

[14] Zhang, L., "Production of bricks from waste materials – A review", *Const. Build. Mat.*, vol. 47, pp. 643-655, 2013. https://doi.org/10.1016/j.conbuildmat.2013.05.043 ↑3

[15] A. L. Murmu and A. Patel, A., "Towards sustainable bricks production: An overview", *Const. Build. Mat.*, vol. 165, pp. 112-125, 2018. https://doi.org/10.1016/j.conbuildmat.2018.01.038 ↑3

[16] I. Demir, "An investigation on the production of construction brick with processed waste tea", *Build. Environ.*, vol. 41, no. 9, p. 1274-1278, 2006. https://doi.org/10.1016/j.buildenv.2005.05.004 ↑3

[17] I. Demir, and M. Orhan, "Reuse of waste bricks in the production line", *Build. Environ.*, vol. 38, no. 12, p. 1451-1455, 2003. https://doi.org/10.1016/S0360-1323(03)00140-9 ↑3

[18] C. A. García-Ubaque, A. González-Hässig, and M. L. Vaca-Bohórquez, "Ceramic bricks made from municipal solid waste incineration-derived clay and ashes: A quality study", *Ing. Investig.,* vol. 33, no. 2, p. 36-41, 2013. https://doi.org/10.15446/ing.investig.v33n2.39515 ↑3

[19] C. Leiva *et al*., "Characteristics of fired bricks with co-combustion fly ashes", *J. Build. Eng.,* vol. 5, pp. 114-118, 2016. https://doi.org/10.1016/j.jobe.2015.12.001 ↑3

[20] S. Abbas, M. A. Saleem, S. M. Kazmi, and M. J. Munir, "Production of sustainable clay bricks using waste fly ash: Mechanical and durability properties", *J. Build. Eng.,* vol. 14, pp. 7-14, 2017. https://doi.org/10.1016/j.jobe.2017.09.008 ↑3

[21] *ASTM C20-00, standard test methods for apparent porosity, water absorption, apparent specific gravity, and bulk density of burned refractory brick and shape for boiling water*, ASTM International, West Conshohocken, USA, 2000. ↑4

[22] *NTC 4017, métodos para muestreo y ensayos de unidades de mampostería y otros productos de arcilla*, Instituto Colombiano de Normas Técnicas y Certificación (ICONTEC), Colombia, 2018. ↑4

[23] P. M. Velasco, M. M. Ortíz, M. M. Giró, and L. M. Velasco, "Fired clay bricks manufactured by adding wastes as sustainable construction material – A review", *Const. Build. Mat.,* vol. 63, pp. 97-107, 2014. https://doi.org/10.1016/j.conbuildmat.2014.03.045 ↑5

[24] D. Zuluaga, E. López, M. Pérez, and M. Correa, "Estudio de prototipos de ladrillos cerámicos elaborados con residuos de la minería del oro", *Rev. Col. Mat.,* vol. 15, pp. 51-63, 2020. https://doi.org/10.17533/udea.rcm.342056 ↑5

[25] J. Torres, L. F. Mosquera, P. Paz, and M. F. Díaz, "Evaluation of coal bottom ash for clay brick manufacturing: A preliminary study", *Rev. UIS Ing.,* vol. 20, no. 4, pp. 161-170, 2021. https://doi.org/10.18273/revuin.v20n4-2021013 ↑5, 6

[26] N. Afanador García, A. C. Ibarra Jaime, and C. A. López Durán, "Caracterización de arcillas empleadas en pasta cerámica para la elaboración de ladrillos en la zona de Ocaña, Norte de Santander". *Epsilon,* vol. 1, no. 20, pp. 101-119, 2013. https://ciencia.lasalle.edu.co/cgi/viewcontent.cgi?article=1178&context=ep ↑5

[27] R. Rodríguez-Álvaro, B. González-Fonteboa, S. Seara-Paz, and E. J. Rey-Bouzón, "Masonry mortars, precast concrete and masonry units using coal bottom ash as a partial replacement for conventional aggregates", *Const. Build. Mat.,* vol. 283, art. 122737, 2021. https://doi.org/10.1016/j.conbuildmat.2021.122737 ↑6

[28] N. Phonphuak, S. Kanyakam, and P. Chindaprasirt, "Utilization of waste glass to enhance physical-mechanical properties of fired clay brick", *J. Clean. Prod.,* vol. 112, pp. 3057-3062, 2016. https://doi.org/10.1016/j.jclepro.2015.10.084 ↑8, 9

[29] S. M. Kazmi, S. Abbas, M. A. Saleem, M. J. Munir, and A. Khitab, "Manufacturing of sustainable clay bricks: Utilization of waste sugarcane bagasse and rice husk ashes", *Const. Build. Mat.,* vol. 120, pp. 29-41, 2016. https://doi.org/10.1016/j.conbuildmat.2016.05.084 ↑8, 9

[30] A. R. Djamaluddin, M. A. Caronge, M. W. Tjaronge, and R. Irmawaty, "Fired clay bricks incorporating palm oil fuel ash as a sustainable building material: An industrial-scale experiment", *Int. J. Sust. Eng.,* pp. 1-13, 2020. https://doi.org/10.1080/19397038.2020.1821403 ↑9

José Fernando Benítez Vivas

Born in Palmira (Valle del Cauca), he is a chemical engineer and a Master's student in Environmental Engineering at Universidad Nacional de Colombia (Palmira campus), as well as an active member of the Materiales y Medio Ambiente research group (GIMMA).
Email: jbenitezv@unal.edu.co

Juan Pablo Gutiérrez López

Born in Buga (Valle del Cauca), he is an environmental engineering student at Universidad Nacional de Colombia (Palmira campus), as well as a member of the Materiales y Medio Ambiente research group (GIMMA).
Email: jpgutierrezl@unal.edu.co

Janneth Torres Agredo

Born in Buga (Valle del Cauca), she is a chemical technologist and a materials engineer, as well as a PhD in Engineering with an emphasis on Materials Engineering. She is a full Professor at Universidad Nacional de Colombia, Palmira campus, and coordinator of the Materiales y Medio Ambiente research group (GIMMA). She has participated in various research projects related to the use of pozzolans and the manufacture of new materials with Universidad del Valle and Universidad Nacional de Colombia, some of which have been funded by MinCiencias and the industry. She has authored articles in several journals and presented at specialized national and international events.
Email: jtorresa@unal.edu.co

Luisa Fernanda Mosquera Idrobo

Born in Palmira (Valle del Cauca), she is an environmental engineer from Universidad Nacional de Colombia (Palmira campus), as well as an active member of the Materiales y Medio Ambiente research group (GIMMA).
Email: lufmosqueraid@unal.edu.co

Miguel Fernando Díaz Huertas

Born in Palmira (Valle del Cauca), he is an environmental engineer, as well as a former administrative coordinator of the C.I. LAGO VERDE S.A.S company.
Email: coordinadoradministrativo@cilagoverde.com.co

Research

Characterization of Microbubbles Generated in a Venturi Tube via Image Processing: Effect of Operating Parameters

Caracterización de microburbujas generadas en un tubo Venturi mediante procesamiento de imágenes: efecto de los parámetros operativos

Jhonatan Stiven Mera-Campo[1] ⓘ, Jeimmy Adriana Muñoz-Alegría[2] ⓘ, Juan Fernando Flórez-Marulanda[2] ⓘ ✉ *, and Elena Muñoz-España[2] ⓘ

[1]Department of Physics, Universidad del Cauca, (Popayán, Colombia)
[2]Department of Electronics, Instrumentation, and Control, Universidad del Cauca, (Popayán, Colombia).

Abstract

Context: This research developed a dissolved air flotation system using a Venturi tube to produce microbubbles. The Venturi tube replaces the saturation tank and the pressure-reducing valve of conventional systems.
Method: The system has both suction and injection air inlets, regulates the recirculation flow of the liquid to the tank, and provides a high hydraulic load in a reduced size. Counting and measuring the microbubbles produced via digital image processing helps to characterize the system's performance.
Results: The system with air suction produces smaller bubbles than that with air injection. A higher liquid recirculation pressure produces more bubbles and reduces their size in the case of air suction.
Conclusions: In air injection, the change in flow rate influences the size of the microbubbles. Air injection and recirculation pressure do not influence the number of bubbles generated.

Keywords: dissolved air flotation, microbubble, Venturi tube, wastewater treatment

---

*✉ **Correspondence:** jflorez@unicauca.edu.co

Resumen

Contexto: Esta investigación desarrolló un sistema de flotación por aire disuelto utilizando un tubo Venturi para producir microburbujas. El tubo Venturi sustituye el tanque de saturación y la válvula reductora de presión de los sistemas convencionales.

Método: El sistema tiene entradas de aire tanto por aspiración como por inyección, regula el flujo de recirculación del líquido al tanque y proporciona una alta carga hidráulica en un tamaño reducido. El conteo y la medición por procesamiento digital de imágenes de las microburbujas producidas ayuda a caracterizar el desempeño del sistema.

Resultados: El sistema de succión de aire produce burbujas más pequeñas que el de inyección de aire. Una mayor presión de recirculación del líquido produce más burbujas y reduce su tamaño en el caso de la succión de aire.

Conclusiones: En la inyección de aire, el cambio de caudal influye en el tamaño de las microburbujas. La inyección de aire y la presión de recirculación no influyen en el número de burbujas generadas.

Palabras clave: flotación por aire disuelto, microburbujas, tubo Venturi, tratamiento de aguas residuales

Table of contents

1. Introduction

Environmental regulations stimulate research on wastewater purification and treatment [1]. Conventional treatment methods involve microbial metabolism [2]; the coagulation of colloid particles and solids in the water, selecting the coagulant according to the wastewater; membrane separation, trapping contaminant particles; and flotation or addition of gas bubbles, where the particles suspended in the water rise to the surface attached to the bubbles [3]. Treatment methods have a contaminant removal efficiency that depends on the design, the size of the equipment, and the materials used.

In flotation methods, the particle-bubble collision probability influences the removal efficiency. The bubble must be smaller than the contaminant's particle size [4]. Several flotation techniques include

a cyclonic static microbubble flotation column (5, 6). The combination of flotation columns, cyclone separation, and microbubble generators yields bubbles of less than 10 μm in diameter and has a removal efficiency of 92,19 %. Electro-flotation (7) separates solid particles with bubbles between 15 and 80 μm in diameter which are produced by electrodes. Its separation efficiency is 64,5 %. In dissolved air flotation (DAF) (8), water saturated with pressurized air is passed through a pressure-reducing valve to generate microbubbles of 20-100 μm. This method has a removal efficiency of 90 %. At the industrial level, one of the main contaminants is grease. Industrial grease removal uses the DAF and induced air flotation (IAF) methods (9). The IAF method requires a more extensive setup than DAF. For an effective removal of contaminants and an adequate size reduction, the DAF method offers high efficiency by removing suspended grease particles while having a less complex setup in comparison with other flotation techniques (10).

The DAF method produces bubbles with characteristics such as larger gas-liquid surface area, higher gas retention, and slower rising velocity in order to achieve a high contaminant removal (11). The bubble size distribution influences these properties (12). Macro-bubbles have a high rising velocity and low collision with contaminant particles. Microbubbles decrease in size as they rise until they burst due to stagnation. Nanobubbles remain suspended in the water for longer periods of time without bursting (11). The DAF method uses microbubbles to increase the contaminant removal efficiency and flow velocity (13). The characteristics of microbubbles for flotation treatment are diameters ranging from 1 to 200 μm and an increased bubble inertial pressure with decreasing diameter without collapsing. The area-volume ratio is inversely proportional to the diameter. Cavitation pertains to the formation, growth, and collapse of bubbles (14). Hydrodynamic cavitation produces bubbles by pressure variation with increasing liquid velocities, and it is a low-cost, energy-efficient method (15). Other types of cavitation are acoustic fields, laser light photons, and elementary particles (16). The type of cavitation influences the bubble production efficiency, the equipment footprint, and the associated costs.

Some hydrodynamic cavitation methods involve a spherical body in a tube through which a liquid flows, generating bubbles by the decay of the internal pressure at the constriction of the channel (17). Others utilize the spiral injection of a fluid with a pump in a specific flow zone, reducing the pressure in its central axial part, generating bubbles by gas suction (18). In others, the fluid passes through a Venturi tube, which increases its velocity and reduces its pressure. The gas is self-primed from the low-pressure point and remains mixed with the liquid (19). Furthermore, pressurized solution injection involves injecting an air-water mixture at a pressure of 3-4 atm into a tank at atmospheric pressure. The pressure change causes the supersaturated air to form microbubbles in the water (4). Pressurized dilution is commonly used within the framework of the DAF method. Studies on microbubble generation via Venturi tubes range from laboratory to industrial scales, with bubbles suitable for grease removal in water (12, 19).

The shape, size, motion, forces, and surrounding physicochemical environment make microbubble characterization difficult (20). There are several techniques to determine microbubble parameters, ranging from intrusive to non-intrusive methods (21). In recent years, high-speed camera photography has been used for microbubble characterization. This non-intrusive method is easy to use in industrial

environments and is less expensive than electronic equipment (22, 23) Calibration for image acquisition affects the accuracy of image processing. Camera calibration methods analyze real objects with known measurements. The intrinsic and extrinsic parameters of a camera are extracted from a set of correspondences between real three-dimensional points and two-dimensional image points (24). The calibration of electronic devices is more complex than that of cameras (25, 26). In fact, the potential use of smartphone cameras for microbubble measurement has not yet been investigated.

This research implemented a DAF system with a Venturi tube microbubble generation method, analyzing the influence of the liquid recirculation pressure, the inlet type, and the airflow rate on microbubble production. The characterization of the diameter and the count of microbubbles generated was performed via a measurement system based on digital image processing installed in the contact zone of the DAF tank. This low-cost microbubble measurement system uses a smartphone camera to measure the diameter and count the microbubbles generated in a lab-scale DAF system at room temperature with clean water. The microbubble measurement algorithm developed in MATLAB (under a campus-wide license) allows for a fast and detailed characterization of dense bubble populations with different diameters.

2. Materials and methods

2.1. Venturi tube design and construction

According to Bernoulli's equation, when a liquid flows through a pipe, its velocity increases and its pressure decreases as the cross-sectional area of the pipe narrows. The air suction created in the narrowed or low-pressure area of a Venturi tube aids in the formation of bubbles. Air can be introduced into the tube by drawing it from the atmosphere or by injection using a pneumatic compressor. To produce microbubbles in the desired area, the geometric parameters of the tube must be considered, *i.e.*, the throat diameter, inlet angle, cone diameter, suction diameter, cone length, and outlet angle (Fig. 1). The parameters with the greatest influence on microbubble size are the inlet and outlet angles of the Venturi tube (27).
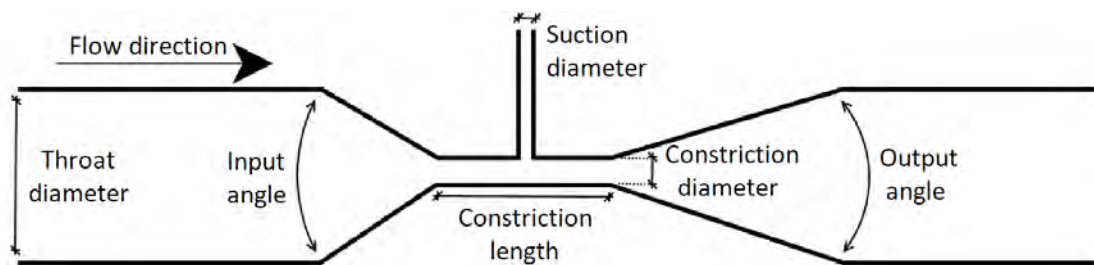
Figure 1. Geometric parameters of a Venturi tube

As the liquid flow increases at the inlet of a Venturi tube, the bubble size decreases if the inlet angle is large relative to the outlet angle. The progressive increase in the orifice diameter to a value smaller than the throat diameter causes a gradual increase in pressure and a decrease in liquid velocity, thus increasing the cavitation intensity. To optimize the size of the generated microbubble, it is necessary for the inlet angle and throat diameter to be at least twice as large as the outlet angle and the narrowing diameter, respectively (27). According to the influence of the geometrical parameters (Fig. **1**), the authors of (28) provide some considerations regarding their optimal values. These parameters (Table **I**) allowed elaborating a CAD design (Fig. **2**a) for 3D-printing in PLA (Fig. **2**b).
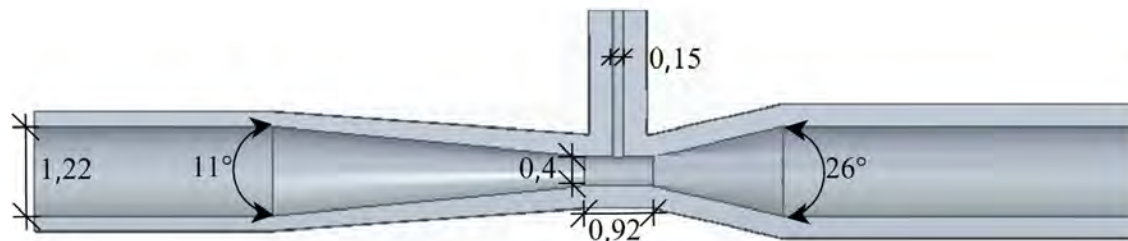
a. CAD design of the tube (dimensions in cm)

b. Printed tube

Figure 2. Developed Venturi tube

Table I. Venturi tube design parameters

Parameter	Measure	Parameter	Measure
Liquid inlet angle	26°	Narrowing length	0,92 cm
Liquid outlet angle	11°	Suction diameter	0,15 cm
Throat diameter	1,22 cm	Tube thickness	0,3 cm
Narrowing diameter	0,4 cm		

2.2. DAF tank design and construction

In the developed DAF system, the recirculation of the liquid through the Venturi tube produces pressurization and mixing with air (29). According to the operation and resistance of the developed Venturi tube (Fig. 2), the maximum recirculation flow rate is 16 L/min. In order to achieve a high rate of rising suspended particles, the design of the proposed flotation tank follows previous models (30), with internal structures for higher efficiency, lower cost, and smaller size (Fig. 3).
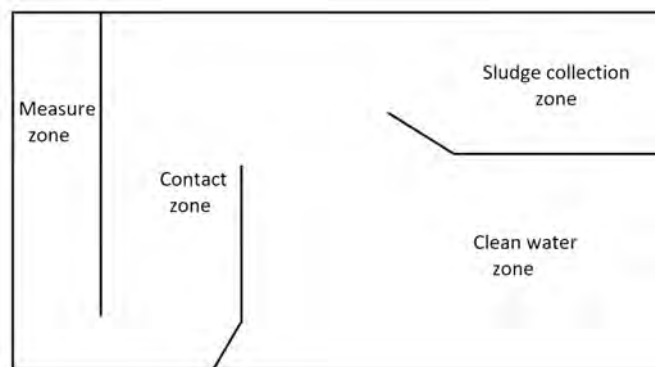
a. Zone distribution
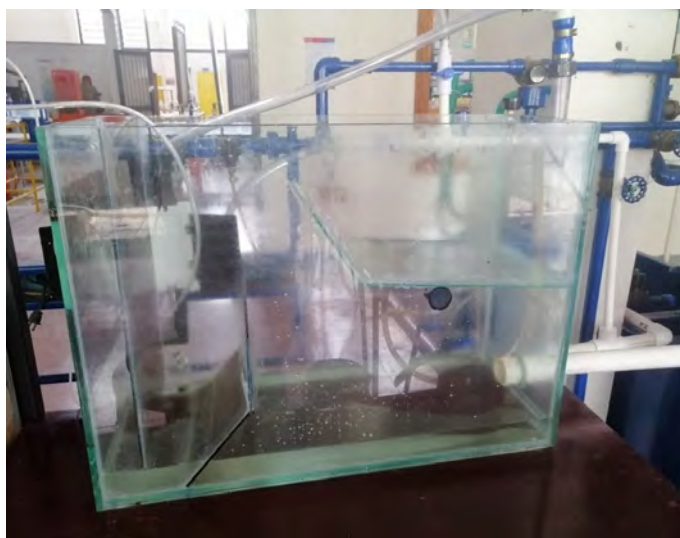
b. Constructed assembly

Figure 3. Developed flotation tank

The four internal zones of the flotation tank are:

- The *measurement zone*, a space in which a portion of the bubbles is periodically lifted, facilitates the acquisition of microbubble images for measurement.

- The *contact zone* is an area of higher concentration of microbubbles and contact with grease

particles in the liquid to be treated.

- In the *clean liquid zone*, the treated liquid flows to another tank and recirculates.

- The *sludge collection area* is a tank for collecting the removed grease particles.

Prior to construction, the CAD design of the flotation tank provides external and internal measurements (Fig. 4). The 53° deflector angle (Fig. 4b) produces a high hydraulic load on the flotation tank, together with a size reduction, without causing turbulence in the contaminants, thus avoiding the re-mixing of contaminants with the treated liquid.
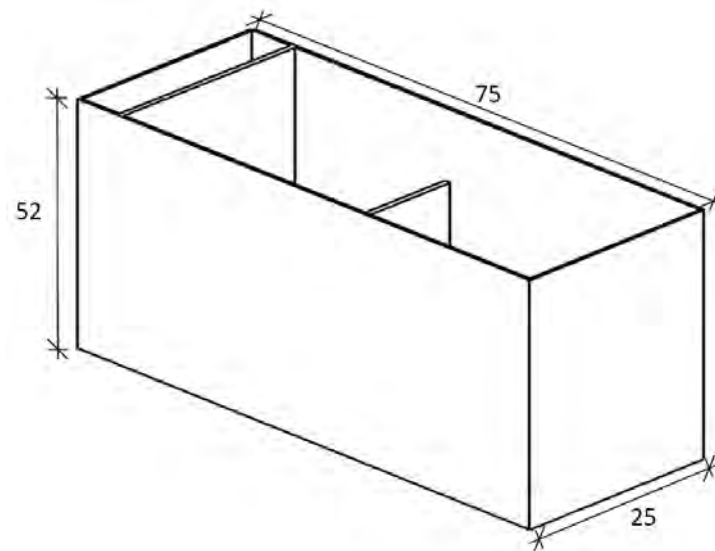
a. External dimensions
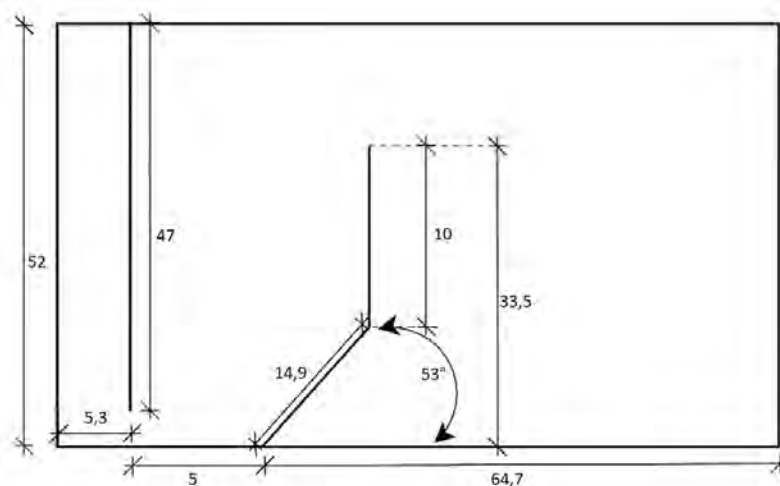
b. Internal dimensions

Figure 4. CAD design of the flotation tank (measurements in cm)

The design parameters of DAF systems are as follows.

- The ratio of kilograms of air used to kilograms of solids separated for high concentrations of solids in the effluent is expressed by Eq. (1) (31):

$$\frac{A_a}{S} = \frac{1,3S_a(fP-1)}{S_s} \tag{1}$$

Where:

A_a/S: air-solids ratio, ml/mg

A_a: Air requirement kg/h

S_a: solubility in air ml/l

F: Fraction of dissolved air at a pressure P

P: Pressure atm

S_s: Influent suspended solids, g/m^3 (mg/L)

- The hydraulic loading (HL) is the total flow rate per unit area (Q/A) (32). The total flow is shown in Eq. (2):

$$Q = Q_{AR} + Q_R \tag{2}$$

where Q_{AR} is the treatment flow rate and Q_R is the recirculation flow rate, expressed as Eq. (3):

$$Q_R = \frac{A_a}{\alpha X_S^P} \tag{3}$$

Here, X_S^P is the solubility of air in pure water at the working temperature and pressure (for temperatures between 20 and 30 °C, it varies between 18 and 15 ppm), and α is the impurity coefficient of the wastewater (nominal values are between 0,60 and 0,80) (33).

- The recirculation rate (%R) is the ratio of the recirculation flow and the total flow.

- The hydraulic retention time (HRT), which indicates the residence time of the water to be treated in the flotation tank, is the ratio between the volume of water to be treated (V) and the total flow rate.

The design of the flotation tank and the Venturi tube determine the parameter values of the developed DAF system (Table II). The efficiency varies according to the ratio between the kilograms of air used and the kilograms of separated solids (A/S), with values between 0,005 and 0,09 (30).

2.3. DAF system instrumentation

The developed system includes a flotation tank for removing contaminant particles; a tank for water treatment, with liquid temperature control and a mechanical stirrer for mixing and temperature homogenization; an auxiliary tank to receive the treated water; two 2 HP motor pumps with a flow rate of 20 L/min, the first of which is responsible for the water flowing through the hydraulic circuit and the second for the removal of the separated sludge from the collection area of the flotation tank; three 1 inch light gate valves and four 1/2 inch unthreaded PVC ball valves; and a portable pneumatic compressor for injecting air into the Venturi tube.

Table II. Flotation tank design parameters

Parameter	units	Calculated value
HL	m/h	5,12
HRT	min	3,25
%R	%	0,53
Q_R	m³/min	0,016
QAR	m³/min	0,014
Q	m³/min	0,03
A_a	kg/h	0,008568

The DAF system's flotation tank uses 1 cm thick glass, and the partitions inside it use 4 mm thick glass. The holding and auxiliary tanks are made of plastic and have a capacity of 160 L. The system uses a water rotameter (0-1.000 L/h) and a pressure gauge (0-60 psi) to measure the flow rate and the recirculation pressure from motor pump 1 to the Venturi tube. To measure the airflow into the Venturi tube, an air rotameter is used (0,3-0,5 L/min) (Fig. 5).

Figure 5. Developed DAF system

The Venturi tube is located at 3 cm from the bottom of the flotation tank. The coupling of the Venturi tube and the hydraulic circuit uses a 3/4 inch, 2 mm thick transparent hose. The air inlet uses a 1/8 inch, 1 mm thick hose for the duct leading to the narrowing zone (Fig. 6).

2.4. Microbubble measurement system

The main components of the microbubble measurement system are a 20-megapixel Huawei Mate 20 Lite smartphone camera with a 3X digital zoom, F/1,8 aperture, a 5.120 x 3.840 pixel resolution per
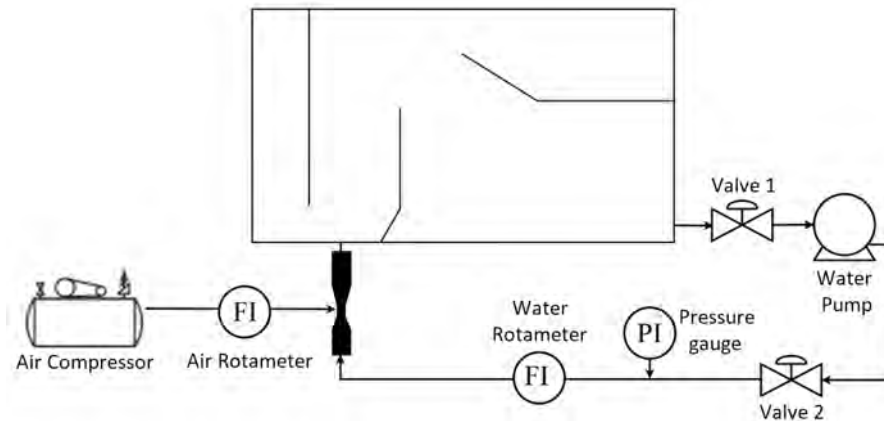
Figure 6. Flow diagram of the microbubble generation process

frame, and slow-motion recording features. The smartphone camera has a 15X macro lens, and images are captured in an area of 1,8 x 2,2 cm with an 18 W LED lamp lighting system at 110 Vac located backlit to the camera. The experimental setup components and adjustment accessories cost approximately 300 USD (Fig. 7).

 A code developed offline in MATLAB measures the diameters and microbubble counts of the captured
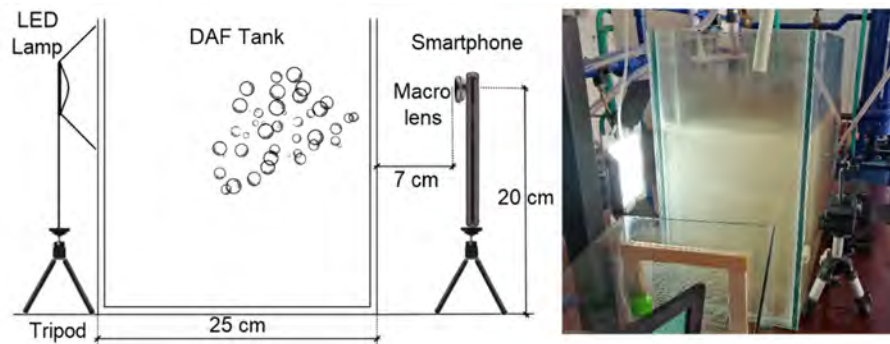
Figure 7. Microbubble measurement system developed

images, all of which are taken while the DAF system runs on clean water. The microbubble images are extracted from a 1.280 x 720-pixel slow-motion video featuring 20 seconds of operation as recorded by the measurement system. There is a two-second interval between each frame analyzed, resulting in a total of 10 images. Image processing is performed in three steps:

1. *Thresholding by V-plane*: In this case, a value of 0,95 is determined by trial and error, obtaining more detail than automatic thresholding segmentation methods.

2. *Application of MATLAB correction filters (imdilate, imfill, imclearborder):* In each thresholded image, two white fringes are generated by the surfaces bounding the measurement area. The filters remove these fringes and fill the gaps inside the microbubble borders.

3. *Microbubble measurement using the imfindcircles MATLAB function:* For each 1. 280 x 720-pixel image, this function calculates the number and pixel radii of the microbubbles. With the radius of each bubble, the average and the standard deviation are calculated. Finally, the pixel size ratio converts these pixel values to μm. In this case, each pixel is 5,79 μm.

The microbubble measurement algorithm was developed in MATLAB 2019a and executed on a desktop computer with an Intel i3 processor, 8 GB RAM, an MSI Gt 730 4 GB Oc graphics card, and a Windows 10 operating system with a 64-bit architecture. The measurement algorithm takes 3 to 4 min to process the images (Fig. 8).
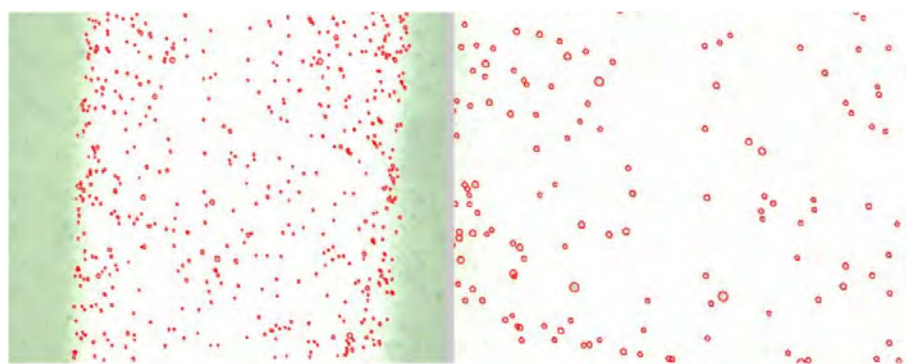
Figure 8. Circle detection: standard image on the left, zoomed region of the image on the right

3.   Results and discussion

The microbubble production of the proposed system helps to analyze the influence of recirculation pressure and the inlet air flow rate to the Venturi tube on the size of microbubbles created by air suction and injection.

3.1.   Hydrodynamic cavitation with air suction

The DAF system works with an air suction of less than 0,3 L/min, as higher values produce macrobubbles. In this case, there is a variation in pressure and recirculation flow (Fig. 9), which determines the number and diameter of the microbubbles produced. At an initial recirculation flow rate of 16 L/min, the pressure is 36 psi. Reducing the flow rate through the recirculation line produces a pressure of 34 psi.

The increase in recirculation pressure from 34 to 36 psi reduces the diameter of the bubbles. The average diameter for the two pressures differs by 4 μm. At 36 psi, a bubble diameter of 134,90 μm corresponds to 52 % of the bubbles generated. At 34 psi, this percentage drops to 32 % for the same diameter. 34 % of the bubbles generated at 34 psi have a diameter of 161,00 μm. At both pressures, bubble diameter values between 134,90 and 161,00 μm are generated: 82 % of the population at 36 psi and 66 % at 34 psi. The average number of bubbles detected per area is 1.143 at 36 psi and 531 at 34 psi.
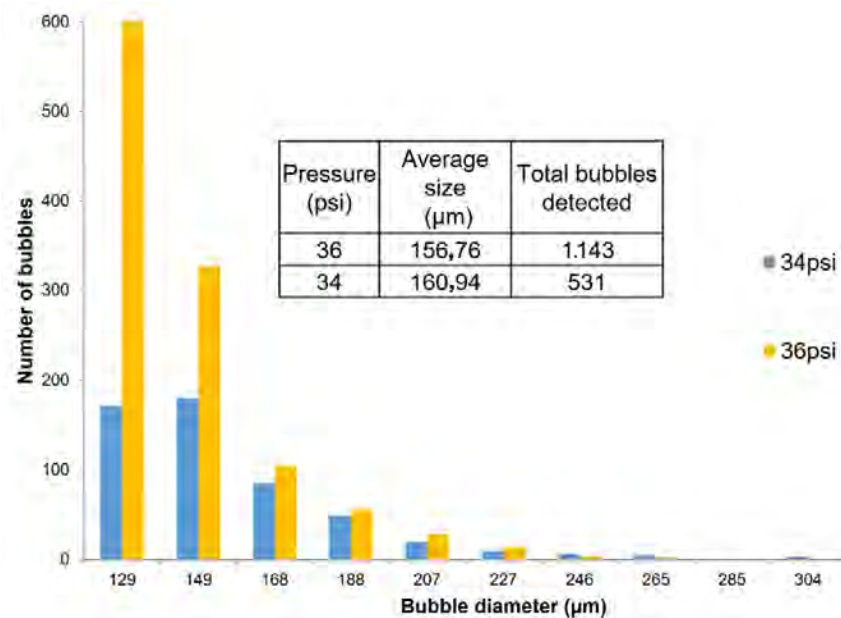
Figure 9. Microbubble population at recirculation pressures of 36 and 34 psi

3.2. Hydrodynamic cavitation with air injection

A 2^2 factorial design (Table **III**) was used to analyze the average diameter and number of bubbles produced by air injection. Its evaluation factors are the air injection flow rate (0,3 and 0,5 L/min) and the recirculation pressure (36 and 34 psi). There are four measurements for each combination.

Table III. Evaluation combinations regarding air injection

Air injection	Repetition	34 psi				36 psi			
		D (μm)	σD	N	σN	D (μm)	σD	N	σN
0,3 L/min	1	160,5588	18,4615	251	24,03	160,7424	18,4761	258	13,63
	2	160,6102	18,5416	218	28,69	160,7314	18,4779	243	15,73
	3	160,4565	18,4620	254	26,72	160,7364	18,4147	271	15,31
	4	160,3694	18,4615	252	24,03	160,7421	18,4759	260	13,45
0,5 L/min	1	161,3271	18,7146	242	13,4	161,0551	19,3956	260	16,15
	2	161,8995	18,7151	223	16,72	161,7751	19,3495	237	18,31
	3	161,3271	18,7136	242	13,4	161,0552	19,7285	236	18,41
	4	161,2013	18,7146	244	13,65	161,0551	19,3945	264	16,32

The results of the factorial design (α-value of 0,05, Table **IV**), indicate, with a p-value of 0,886, that the average bubble diameter does not vary significantly for different recirculation pressures. The p-value of $7,49 \times 10^{-5}$ indicates that the variation in the air injection flow rate affects the size of the microbubbles. On the other hand, the air flow rate, with a p-value of 0,3014, and the recirculation pressure (0,0838)

have no influence on the number of bubbles generated. In no case does the variation of the parameters in combination influence the size and number of microbubbles.

Table IV. Results of the factorial design for air injection

	Sum Sq.	Mean Sq.	F-value	P-value	Confidence intervals, percentile 95 %
Microbubble size					
Microbubble size					
Pressures	0,0013	0,0013	0,021	0,886	[-0,248; 0,284]
Flow rates	2,0652	2,0652	34,564	7,49e-05	[0,452; 0,984]
Pressure-Flow	0,1962	0,1962	3,284	0,095	[-0,717; 1,453]
Microbubble density					
Pressures	663,1	663,2	3,555	0,0838	[-2,003; 27,753]
Flow rates	217,6	217,7	1,166	0,3014	[-22,253; 7,503]
Pressure-flow	7,6	7,6	0,041	0,8438	[-48,921; 42,921]

3.3.   Oil and grease removal

The cleaning tests consist of treating the synthetic domestic wastewater with the DAF prototype for 16 min. During the first minute, the system stabilizes at the set recirculation pressure and air injection. In the next seven minutes, the system forms a small region of foam or suspended solids. Within the next eight minutes, the system has a visible layer of solids, particularly the presence of oils and grease, which, in this case, were analyzed at Corporación Autónoma Regional del Cauca's laboratory using the SM5520D Soxhlet method.

For each pair of parameters (34 psi at a 0,1 L/min air injection and 36 psi at a 0,1 L/min air injection), five cleaning tests were performed, with a new Venturi tube for each one, measuring the oil and grease concentration (Table V). The average grease and oil removal at 34 psi was 89,22 %, as well as 83,64 % at 36 psi. An ANOVA test, with an α-value of 0,05 and a p-value of 0,038, indicates a difference between the two evaluated parameter levels.

3.4.   Discussion

By comparing both models for microbubble generation according to the smaller diameters obtained, it can be stated that air injection produces bubbles of a larger average size (160 μm) than air suction (156 μm). A higher air flow rate increases the amount of dissolved air in the water, which requires an increased recirculation pressure to break up the air cloud. Likewise, the increased air reduces the number of bubbles generated by the low air breakup. The bubbles are larger because of the larger amount of air, preventing the generation of new bubbles.

Table V. Oil and grease removal efficiencies

| Concentration of untreated oils and grease | Recirculation pressure: 34 psi; air injection: 0,1 L/min | | Recirculation pressure: 36 psi; air injection: 0,1 L/min | |
| | Oil and grease concentration DAF treatment | | Oil and grease concentration DAF treatment | |
(mg/L)	(mg/L)	Efficiency (%)	(mg/L)	Efficiency (%)
589	95,3	83,82	103	82,51
589	75,6	87,16	99,5	83,11
589	23,8	95,96	107	81,83
589	67,1	88,61	73,6	87,50
589	55,8	90,53	98,6	83,26

For most of the characteristics evaluated, there is no significant difference in the variation of the recirculation pressure. However, at a practical level, according to the results obtained, it is advisable to work with 34 psi, as it generates a lower cavitation effect in the Venturi tube and a lower power consumption of the system and the tests performed with synthetic domestic wastewater. This pressure reported a higher percentage of grease and oil removal.

The results show that the Venturi tube produces bubbles suitable for DAF systems. The Venturi tube replaces the saturation tank and the pressure-reducing valve in the proposed system. These components account for 10 to 30 % of the total costs in conventional DAF systems (27). Implementing our proposal on an industrial scale would result in a minimum 10 % reduction in the cost of conventional DAF systems, as well as a reduction in the space required for installation.

The advent of modern cameras and computer processing power allows for the automatic online and offline monitoring of bubbles (21), as shown in Table **VI**. Nevertheless, it is necessary to calibrate the camera with a high accuracy, as this affects the performance and estimation of extrinsic and intrinsic parameters (24, 34, 35). The use of digital image processing equipment with offline or online algorithms costs more than 1.000 USD. The developed system generates an offline MB measurement with low computational cost and fast response times, which allows to take different samples in the field and make control decisions directly.

Regarding the location of the camera to measure microbubbles in DAF systems, measurement is typically performed at the top of the tank (40, 41). At this point, the bubbles have reached their maximum size, and their removal capacity is reduced. Another way is to take a sample of the generated bubbles (38, 43). In this case, the bubbles are measured before they reach their maximum size. However, changes in the uncontrolled environment of the bubbles may cause the analyzed sample to be unrepresentative. The developed microbubble measurement system performs a direct measurement of the bubbles generated by placing the chamber in the contact zone of the DAF tank, providing an adequate characterization of the generated microbubbles in order to determine their possible use in the removal of contaminants. Regardless of the location of the camera, any microbubble measurement

Table VI. Offline and online methods for microbubble measurement

Techniques	Offline Online	Bubble parameter	Processing time (s)	Ref.
First version algorithm	Offline	BSD-velocity-trajectory	-	(36)
Concave point extraction algorithm	Offline	BSD-diameter	-	(37)
CHT-Single bubble Algorithm	Online	BSD-diameter	60-300	(38)
CHT-CNN-CCA-WaldBoost+LBP-Trees CNN	Online	BSD-diameter	-	(39)
WaldBoost+Trees	Online	Bubble detection	120-180	(40)
Watershed algorithm	Offline	Bubble detection	-	(41)
Watershed algorithm-CHT	Online	BSD-diameter	-	(42)
DFT-Otsu algorithm	Online	BSD-diameter	0,03-0,18	(43)
GSC	Online	Bubble detection	120	(44)
CCA	Online	Bubble detection	40	(45)

system with digital image processing must have adequate lighting and adjust the chamber exposure parameters according to the characteristics of the environment in which the DAF system is located.

4.   Conclusions

This research developed a DAF system using a Venturi tube microbubble generation method. The system replaces the saturation tank and the pressure-reducing valve of conventional systems, which leads to a reduction in the size of the proposed DAF system without affecting the hydraulic load. A microbubble measurement system counts and measures the microbubbles.

The proposed DAF system allows varying the recirculation pressure of the treated water and an air inlet by air injection or suction. The analysis of the variations in recirculation pressure and the inlet air flow rate evidenced the influence of these parameters on the quantity and size of the microbubbles generated. Regarding the combinations of parameters analyzed, the DAF system with a suction inlet air flow rate of less than 0,3 L/min and a treated water recirculation pressure of 36 psi generates a high number of microbubbles with the smallest possible size. In the case of air injection, increasing the inlet air flow rate generates an increase in microbubble size. There is no influence on the number of bubbles generated for any given air flow rate and recirculation pressure.

Digital image processing is convenient for the estimation of microbubble parameters. The developed microbubble measurement system costs about 300 USD, a value below the equipment that is often used in research. For adequate detection and measurement, it is necessary to obtain images with a distinction between the background and the air bubbles, generating a good definition of the perimeter. The images in this study were taken with an ISO value of 320 and a shutter speed of 1/1.000 in an area of 1,8 x 2,2 cm.

5. CRediT author statement

Jhonnatan Stiven Mera Campo: Methodology, investigation, software, writing – original draft.
Jeimmy Adriana Muñoz Alegria: Methodology, investigation, software, writing – original draft.
Juan Fernando Flórez Marulanda: Conceptualization, formal analysis, validation, and writing – original draft.
Elena Muñoz España: Data visualization, investigation, supervision, and writing – review.

References

[1] C. Li, J. Li, N. Wang, Q. Zhao, and P. Wang, "Status of the treatment of produced water containing polymer in oilfields: A review," *J. Environ. Chem. Eng.*, vol. 9, no. 4, art. 105303, 2021. https://doi.org/10.1016/j.jece.2021.105303 ↑2

[2] L. Yu, M. Han, and F. He, "A review of treating oily wastewater," *Arabian J. Chem.*, vol. 10, pp. S1913-S1922, 2017. https://doi.org/10.1016/j.arabjc.2013.07.020 ↑2

[3] G. L. Muniz, A. C. Borges, and T. C. F. da Silva, "Performance of natural coagulants obtained from agro-industrial wastes in dairy wastewater treatment using dissolved air flotation," *J. Water Process Eng.*, vol. 37, art. 101453, 2020. https://doi.org/10.1016/j.jwpe.2020.101453 ↑2

[4] R. Prakash, S. K. Majumder, and A. Singh, "Flotation technique: Its mechanisms and design parameters," *Chem. Eng. Processing-Process Intens.*, vol. 127, pp. 249-270, 2018. https://doi.org/10.1016/j.cep.2018.03.029 ↑2, 3

[5] G. Pooja, P. S. Kumar, and S. Indraganti, "Recent advancements in the removal/recovery of toxic metals from aquatic system using flotation techniques," *Chemosphere*, vol. 287, art. 132231, 2022. https://doi.org/10.1016/j.chemosphere.2021.132231 ↑3

[6] X. Yan, S. Meng, A. Wang, L. Wang, and Y. Cao, "Hydrodynamics and separation regimes in a cyclonic-static microbubble flotation column," *Asia-Pacific J. Chem. Eng.*, vol. 13, no. 3, art. e2185, 2018. https://doi.org/10.1002/apj.2185 ↑3

[7] R. Mohtashami and J. Q. Shang, "Electroflotation for treatment of industrial wastewaters: a focused review," *Env. Proc.*, vol. 6, no. 2, pp. 325-353, 2019. https://doi.org/10.1007/s40710-019-00348-z ↑3

[8] F. C. P. e Silva, N. M. P. e Silva, J. M. Luna, R. D. Rufino, V. A. Santos, and L. A. Sarubbo, "Dissolved air flotation combined to biosurfactants: a clean and efficient alternative to treat industrial oily water," *Rev. Environ. Sci. Biotechnol.*, vol. 17, no. 4, pp. 591-602, 2018. https://doi.org/10.1007/s11157-018-9477-y ↑3

[9] Z. Khan *et al.*, "Current developments in esterification reaction: A review on process and parameters," *J. Ind. Eng. Chem.*, vol. 103, pp. 80-101, 2021. https://doi.org/10.1016/j.jiec.2021.07.018 ↑3

[10] D. Mesa and P. R. Brito-Parada, "Scale-up in froth flotation: A state-of-the-art review," Sep. *Purif. Technol.*, vol. 210, pp. 950-962, 2019. https://doi.org/10.1016/j.seppur.2018.08.076 ↑3

[11] M. Alheshibri, J. Qian, M. Jehannin, and V. S. J. Craig, "A history of nanobubbles," *Langmuir*, vol. 32, no. 43, pp. 11086-11100, 2016. https://doi.org/10.1021/acs.langmuir.6b02489 ↑3

[12] A. Gordiychuk, M. Svanera, S. Benini, and P. Poesio, "Size distribution and Sauter mean diameter of micro bubbles for a Venturi type bubble generator," *Exp. Therm. Fluid. Sci.*, vol. 70, pp. 51-60, 2016. https://doi.org/10.1016/j.expthermflusci.2015.08.014 ↑3

[13] K. H. A. L. Mahmood, S. J. Wilkinson, and W. B. Zimmerman, "Airlift bioreactor for biological applications with microbubble mediated transport processes," *Chem. Eng. Sci.*, vol. 137, pp. 243-253, 2015. https://doi.org/10.1016/j.ces.2015.06.032 ↑3

[14] T. Temesgen, T. T. Bui, M. Han, T. Kim, and H. Park, "Micro and nanobubble technologies as a new horizon for water-treatment techniques: A review," *Adv. Colloid Interface Sci.*, vol. 246, pp. 40-51, 2017. https://doi.org/10.1016/j.cis.2017.06.011 ↑3

[15] N. Asaithambi, P. Singha, M. Dwivedi, and S. K. Singh, "Hydrodynamic cavitation and its application in food and beverage industry: A review," *J. Food Process Eng.*, vol. 42, no. 5, art. e13144, 2019. https://doi.org/10.1111/jfpe.13144 ↑3

[16] N. Nirmalkar, A. W. Pacek, and M. Barigou, "On the existence and stability of bulk nanobubbles," *Langmuir*, vol. 34, no. 37, pp. 10964-10973, 2018. https://doi.org/10.1021/acs.langmuir.8b01163 ↑3

[17] Y. Yoo *et al.*, "Method for Determining Optimum Operational Conditions of Microbubble Scrubber Using Image Processing.," *J. Environ. Informatics*, vol. 38, no. 2, pp. 83-92, 2021. https://doi.org/10.3808/jei.202100457 ↑3

[18] I. v Naumov, B. R. Sharifullin, and V. N. Shtern, "Vortex breakdown in the lower fluid of two-fluid swirling flow," *Phys. Fluids*, vol. 32, no. 1, art. 14101, 2020. https://doi.org/10.1063/1.5132584 ↑3

[19] C. H. Lee, H. Choi, D.-W. Jerng, D. E. Kim, S. Wongwises, and H. S. Ahn, "Experimental investigation of microbubble generation in the venturi nozzle," *Int. J. Heat Mass Transf.*, vol. 136, pp. 1127-1138, 2019. https://doi.org/10.1016/j.ijheatmasstransfer.2019.03.040 ↑3

[20] B. Swart *et al.*, "In situ characterisation of size distribution and rise velocity of microbubbles by high-speed photography," *Chem. Eng. Sci.*, vol. 225, art. 115836, 2020. https://doi.org/10.1016/j.ces.2020.115836 ↑3

[21] F. Noelle, M. R. Molteno, and R. W. M. Pott, "Calibrated bubble depth determination using a single camera," *Chem. Eng. Res. Design*, vol. 164, pp. 11-22, 2020. https://doi.org/10.1016/j.cherd.2020.09.023 ↑3, 14

[22] M. Lichti and H.-J. Bart, "Bubble size distributions with a shadowgraphic optical probe," *Flow Meas. Inst.*, vol. 60, pp. 164-170, 2018. https://doi.org/10.1016/j.flowmeasinst.2018.02.020 ↑4

[23] R. Prakash, S. Kumar Majumder, and A. Singh, "Bubble size distribution and specific bubble interfacial area in two-phase microstructured dense bubbling bed," *Chem. Eng. Res. Design*, vol. 156, pp. 108-130, 2020. https://doi.org/10.1016/j.cherd.2020.01.032 ↑4

[24] X. Chen *et al.*, "Fourier-transform-based two-stage camera calibration method with simple periodical pattern," *Opt. Lasers Eng.*, vol. 133, art. 106121, 2020. https://doi.org/10.1016/j.optlaseng.2020.106121 ↑4, 14

[25] P. F. Fazzini, P. G. Merli, and G. Pozzi, "Electron microscope calibration for the Lorentz mode," *Ultramicroscopy*, vol. 99, no. 2, pp. 201-209, 2004. https://doi.org/10.1016/j.ultramic.2004.01.002 ↑4

[26] Q. Zhang, H. Xie, W. Shi, and B. Fan, "A novel sampling moiré method and its application for distortion calibration in scanning electron microscope," *Opt. Lasers Eng.*, vol. 127, art. 105990, 2020. https://doi.org/10.1016/j.optlaseng.2019.105990 ↑4

[27] M. Li, A. Bussonnière, M. Bronson, Z. Xu, and Q. Liu, "Study of Venturi tube geometry on the hydrodynamic cavitation for the generation of microbubbles," *Miner. Eng.*, vol. 132, pp. 268-274, 2019. https://doi.org/10.1016/j.mineng.2018.11.001 ↑4, 5, 14

[28] Y. Xiong and F. Peng, "Optimization of cavitation venturi tube design for pico and nano bubbles generation," *Int. J. Min. Sci. Technol.*, vol. 25, no. 4, pp. 523-529, 2015. https://doi.org/10.1016/j.ijmst.2015.05.002 ↑5

[29] P. Mavros and K. A. Matis, *Innovations in Flotation Technology*, Dodrecht, Netherlands: Springer Science & Business Media, 2013. ↑6

[30] P. Palaniandy, M. N. Adlan, H. A. Aziz, M. F. Murshed, and Y.-T. Hung, "Dissolved air flotation (DAF) for wastewater treatment," *Waste Treat. Serv. Utility Ind.*, pp. 145-182, 2017. https://doi.org/10.1201/b22213-5 ↑6, 8

[31] M. Salgot and M. Folch, "Wastewater treatment and water reuse," *Curr. Opin. Environ. Sci. Health*, vol. 2, pp. 64-74, 2018. https://doi.org/10.1016/j.coesh.2018.03.005 ↑8

[32] P. Pazouki, R. A. Stewart, E. Bertone, F. Helfer, and N. Ghaffour, "Life cycle cost of dilution desalination in off-grid locations: A study of water reuse integrated with seawater desalination technology," *Desalination*, vol. 491, art. 114584, 2020. https://doi.org/10.1016/j.desal.2020.114584 ↑8

[33] M. A. Santos, F. Capponi, C. H. Ataíde, and M. A. S. Barrozo, "Wastewater treatment using DAF for process water reuse in apatite flotation," *J. Clean. Prod.*, vol. 308, art. 127285, 2021. https://doi.org/10.1016/j.jclepro.2021.127285 ↑8

[34] X. Lin, J. Song, X. Chen, and H. Yang, "Ultrasound-activated sensitizers and applications," *Angewandte Chemie Int. Ed.*, vol. 59, no. 34, pp. 14212-14233, 2020. https://doi.org/10.1002/anie.201906823 ↑14

[35] H. He, H. Li, Y. Huang, J. Huang, and P. Li, "A novel efficient camera calibration approach based on K-SVD sparse dictionary learning," *Measurement*, vol. 159, art. 107798, 2020. https://doi.org/10.1016/j.measurement.2020.107798 ↑14

[36] M. Qadafi, S. Notodarmojo, and Y. Zevi, "Effects of microbubble pre-ozonation time and pH on trihalomethanes and haloacetic acids formation in pilot-scale tropical peat water treatments for drinking water purposes," *Sci. Total Env.*, vol. 747, art. 141540, 2020. https://doi.org/10.1016/j.scitotenv.2020.141540 ↑15

[37] S. Zhong, X. Zou, Z. Zhang, and H. Tian, "A flexible image analysis method for measuring bubble parameters," *Chem. Eng. Sci.*, vol. 141, pp. 143-153, 2016. `https://doi.org/10.1016/j.ces.2015.10.033` ↑15

[38] S. J. Gulden, C. Riedele, S. Rollié, M.-H. Kopf, and H. Nirschl, "Online bubble size analysis in micro flotation," *Chem. Eng. Sci.*, vol. 185, pp. 168-181, 2018. `https://doi.org/10.1016/j.ces.2018.04.009` ↑14, 15

[39] J. Ilonen *et al.*, "Comparison of bubble detectors and size distribution estimators," *Pat. Recognit. Lett.*, vol. 101, pp. 60-66, 2018. `https://doi.org/10.1016/j.patrec.2017.11.014` ↑15

[40] X. Wang, C. Song, C. Yang, and Y. Xie, "Process working condition recognition based on the fusion of morphological and pixel set features of froth for froth flotation," *Miner. Eng.*, vol. 128, pp. 17-26, 2018. `https://doi.org/10.1016/j.mineng.2018.08.017` ↑14, 15

[41] H. Zhang, Z. Tang, Y. Xie, X. Gao, and Q. Chen, "A watershed segmentation algorithm based on an optimal marker for bubble size measurement," *Measurement*, vol. 138, pp. 182-193, 2019. `https://doi.org/10.1016/j.measurement.2019.02.005` ↑14, 15

[42] N. N. Misra, R. Phalak, and A. Martynenko, "A microscopic computer vision algorithm for autonomous bubble detection in aerated complex liquids," *J. Food Eng.*, vol. 238, pp. 54-60, 2018. `https://doi.org/10.1016/j.jfoodeng.2018.06.007` ↑15

[43] L. Vinnett, J. Sovechles, C. O. Gomez, and K. E. Waters, "An image analysis approach to determine average bubble sizes using one-dimensional Fourier analysis," *Miner. Eng.*, vol. 126, pp. 160-166, 2018. `https://doi.org/10.1016/j.mineng.2018.06.030` ↑14, 15

[44] M. de Langlard, H. Al-Saddik, S. Charton, J. Debayle, and F. Lamadie, "An efficiency improved recognition algorithm for highly overlapping ellipses: Application to dense bubbly flows," *Pat. Recognit. Lett.*, vol. 101, pp. 88-95, 2018. `https://doi.org/10.1016/j.patrec.2017.11.024` ↑15

[45] N. Strokina, J. Matas, T. Eerola, L. Lensu, and H. Kälviäinen, "Detection of bubbles as concentric circular arrangements," *Machine Vision App.*, vol. 27, pp. 387-396, 2016. `https://doi.org/10.1007/s00138-016-0749-7` ↑15

Jhonnatan Stiven Mera Campo

Received a degree in Physical Engineering from Universidad del Cauca in December 2021. He has a strong interest and orientation towards vision and artificial intelligence, in addition to instrumentation and control in industrial processes. He is currently working as an engineering analyst for one of the leaders in the field of vision and artificial intelligence, the Colombian company INTECOL SAS, located in the city of Medellín, developing artificial vision algorithms and industrial software for the quality inspection of products in different industries (among other use cases).
Email: jhonnatans@unicauca.edu.co

Jeimmy Adriana Muñoz Alegría

Received a degree in Physical Engineering in 2017 and a Master's degree in Industrial Automation in 2022, both from Universidad del Cauca. She is currently a PhD student in Energy, Water, and

Environment at Universidad de La Serena, Chile, with research interests in renewable energy, wastewater treatment technology, and the application of artificial intelligence in the environment.
Email: jeimymunoz@unicauca.edu.co

Juan Fernando Flórez Marulanda

Received a degree in Electronics and Telecommunications Engineering, specializing in Telematics Networks and Services and Industrial Computing, as well as a Master's degree in Electronics Engineering from Universidad del Cauca. He teaches at Universidad del Cauca since 1998, guiding subjects involving instrumentation, control, computer vision, and automation while advising degree works related to ISA, ISO, and IEEE standards and industrial process automation methodologies.
Email: jflorez@unicauca.edu.co

Elena Muñoz España

Received a degree in Electronics and Telecommunications Engineering and a Master's degree in Electronics Engineering from Universidad del Cauca. She is currently working as a full professor at Universidad del Cauca, Colombia. Her research interests include control systems, computer vision, and medical image processing.
Email: elenam@unicauca.edu.co

Construction of Formability Limit Curves for Low-Carbon Steels Used in the Manufacture of Pressure Cylinders

Construcción de curvas límite de formabilidad para aceros de bajo carbono utilizados en la manufactura de cilindros a presión

Jhon Erickson Barbosa-Jaimes[1] ![iD] ✉ *, Ismael Humberto García-Páez[2] ![iD], and Claudia Liliana Casadiego[3] ![iD]

[1]Grupo de investigación Gestindustriales EOCA, Universidad Nacional Abierta y a Distancia UNAD, Cúcuta, Colombia
[2]Grupo de investigación en Diseño Mecánico, Materiales y Procesos, Universidad Francisco de Paula Santander, Cúcuta, Colombia
[3]Grupo de Investigación en Competitividad y Sostenibilidad para el Desarrollo, Universidad Libre, Cúcuta, Colombia.

Abstract

Context: The aim of this study is to determine the formability of SG295 (2,2 mm thick) and SG325 (2,3 mm thick) steel sheets, as well as their relationship with the sheets' behavior in deep drawing and stretching operations. To this effect, chemical, metallographic, and mechanical analyses of the sheets were carried out.

Method: The chemical analysis was carried out via optical emission spectrometry, and the metallographic structure was analyzed using the ASTM E3 standard. The intrinsic properties related to the formability of materials such as the elongation to fracture for a 50 mm gauge length, the conventional yield limit at 0,2 % elongation, the ultimate strength, the strain hardening exponent, and the anisotropy coefficient at 15 % elongation were determined through tensile tests according to ASTM E8M, ASTM E646, and ASTM 517. Forming limit curves were determined under ASTM E2218, for which a device was designed, built, and attached to a universal testing machine.

Results: The results for the SG295 and SG325 steel sheets were as follows: tensile strength; 450 and 520 MPa; elongation at fracture: 24,9 and 17,2 %; strain hardening exponent: 0,24 and 0,19; normal anisotropy: 1,64 and 1,29; planar anisotropy: 0,23 and -0,02. The FLD0 determined from the formality limit curves (FLCs) for the two steel sheets showed ε_1 values of 0,281 and 0,336, respectively.

Conclusions: Although the intrinsic properties (such as A_{50}, n, and r_m) of the SG295 steel sheet show values related to a greater formability, the FLCs show that SG325 steel performs slightly better due to its greater thickness.

Keywords: anisotropy, deep drawing, metallic sheet, mechanical properties, stretching

* ✉ **Correspondence:** jhon.barbosa@unad.edu.co

Resumen

Contexto: El objetivo de este trabajo fue determinar la formabilidad de láminas de acero SG295 (2,2 mm de grosor) y SG325 (2,3 mm de grosor), así como su relación con el comportamiento de éstas frente a operaciones de estirado y embutido profundo. Para tal fin, se realizaron análisis químicos, metalográficos y mecánicos en las láminas.

Método: El análisis químico se realizó mediante espectrometría de emisión óptica, y la estructura metalográfica se analizó utilizando el estándar ASTM E3. Las propiedades intrínsecas relacionadas con la formabilidad de los materiales, tales como el alargamiento a la fractura para una longitud de referencia de 50 mm, el límite de rendimiento convencional al 0,2 % de elongación, la resistencia última, el exponente de endurecimiento por deformación y el coeficiente de anisotropía al 15 % de elongación se determinaron mediante pruebas de tracción de acuerdo con ASTM E8M, ASTM E646 y ASTM 517. Las curvas límite de formabilidad se determinaron bajo la norma ASTM E2218, para lo cual se diseñó, construyó y acopló un dispositivo a una máquina universal de ensayos.

Resultados: Los resultados para las láminas de acero SG295 y SG325 fueron los siguientes: resistencia a la tracción: 450 y 520 MPa; elongación hasta fractura: de 24,9 y 17,2 %; exponente de endurecimiento por deformación: 0,24 y 0,19; anisotropía normal: 1,64 y 1,29; anisotropía planar: 0,23 y -0,02. Los FLD0 determinados a partir de las curvas límite de formalidad (CLF) para las dos láminas de acero mostraron valores para ε_1 de 0,281 y 0,336 respectivamente.

Conclusiones: Aunque las propiedades intrínsecas (como A_{50}, n y r_m) de la lámina de acero SG295 presentan valores relacionados con una mayor formabilidad, las CLF muestran que el acero SG325 se desempeña ligeramente mejor debido a su mayor espesor.

Palabras clave: anisotropía, embutido profundo, lámina metálica, propiedades mecánicas, estirado

Table of contents

1. Introduction

The mechanical formability of metal sheets is very important in the manufacture of structural elements for the automotive industry, electrical appliances, and the overall metalworking industry (1). Formability is the measure of the amount of deformation of a metal sheet before it fails, either by fracture or by localized necking, and it cannot be defined based on a single parameter, but depends, among others, on the particular forming process (for example, deep drawing and stretching operations), on the thickness of the sheet, and, to a large extent, on the intrinsic properties of the material (2,3).

The formability and quality of a product are directly or indirectly influenced by intrinsic properties such as ultimate strength (σ_u), the elastic limit (σ_y, 0,2 %), elongation to fracture, the strain hardening exponent (n), normal anisotropy (r_m), and planar anisotropy (δr) (4,5).

Elongation to fracture is a measure of the ductility of a material and is therefore related to the formability of a metal sheet (2). The strain hardening exponent n, is a measure of how rapidly a metal becomes stronger and harder due to plastic deformation (6). In a material with a high value of n, the thickness is reduced more uniformly in drawing operations, and the elongation is greater before localized necking appears, which is why it is an indicator of good formability (7). The normal anisotropy r_m defines the behavior of a metal sheet in terms of thinning during deep drawing and stretching operations. This occurs in the formation process and is defined by the preferential orientation of the grains and by the alignment of impurities and inclusions through the thickness (mechanical fibration) (8). Additionally, it indicates the ability of the metal sheet to resist thinning or thickening when subjected to drawing operations (6, 9). Finally, sheets with a high value of r_m, are preferred, given that, in sheets with a low normal anisotropy, localized cracks or necks may appear during the manufacturing process. On the other hand, the planar anisotropy Δr value should be as close to zero as possible; if its value is high, the sheet will deform more in some directions, forming the so-called *ears* in the drawing process (10).

One of the tests that allow predicting the ease of forming metal sheets and has had an important development is the forming limit diagram (FLD) (1). In this test, a series of metallic strips of different widths, which are marked with a network of circles, are tested according to ASTM E 2218 (11). The deformations of the circles are measured along the major and minor axes (ε_1 and ε_2), classifying the points as good (no localized necking), marginal (localized necking), and fractured. The forming limit curve (FLC) is plotted on the boundary between the good and the marginal points (11). In the sheet forming process, the deformation is uniform up to the maximum stress (*i.e.*, maximum load capacity of the material). Then, diffuse necking occurs, and the deformation is localized only in this area until fracture takes place (12,13).

Over the years, theoretical and empirical models have been developed to predict the formability of sheet metal. Some intrinsic properties of the sheet material have been used by some authors to develop empirical approximations of the FLD, with different levels of adjustment to the experimental results, such as the one proposed by (12) and those described by (14).

The main purpose of this work was to experimentally measure the formability of SG295 and SG325 steel sheets (2,2 and 2,3 mm thick) used by the metalworking industry. To this effect, various specimens were subjected to standardized traction tests: ASTM E 8M (15), ASTM E 646 (16), and ASTM E 517 (17). This, in addition to the simulative test for determining the FLC as per the ASTM E 2218 standard (11). To support the analysis of the results, the chemical composition of the sheets was determined, and a metallographic analysis was conducted.

This article is structured as follows. Section 2 describes the materials and methods used in the chemical, metallographic, and mechanical characterization of steel sheets. In Section 3, the results are presented, and a discussion is proposed. Finally, Section 4 presents the main conclusions of this research.

2.　Materials and methods

2.1.　Chemical composition and metallographic analysis

The material's chemical composition was determined using an optical emission spectrometer (OES). The microstructure was observed and micrographs were taken in a reflected light optical microscope (ZEISS, Axio Scope A1).

2.2.　Tensile test

The specimens were prepared according to (15), in order to determine the conventional yield limit at a 0,2 % elongation (σ_y, 0,2 %), the ultimate strength (σ_u), and the elongation to fracture for a 50 mm gauge length (A_{50}) (Fig. 1).
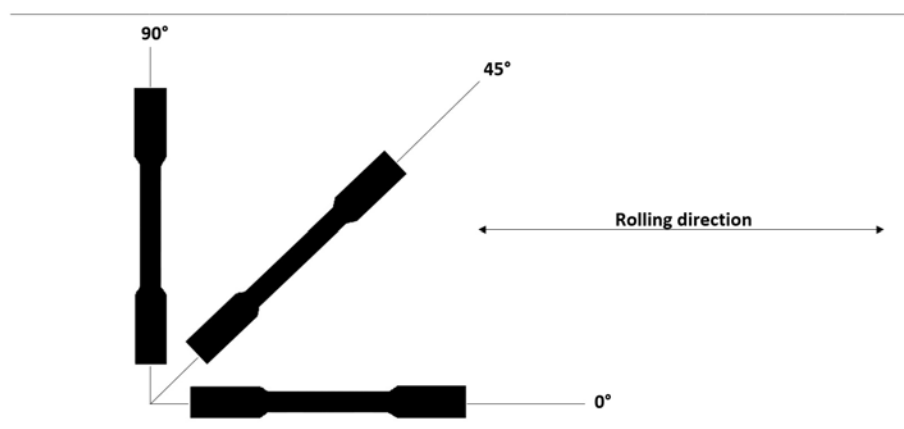
Figure 1. Assembly for cutting the specimens. Orientations of 0, 45, and 90° with respect to the last lamination

The tensile properties were calculated from the data obtained via a universal testing machine (SHIMADZU, AG 250) (Fig. 2).
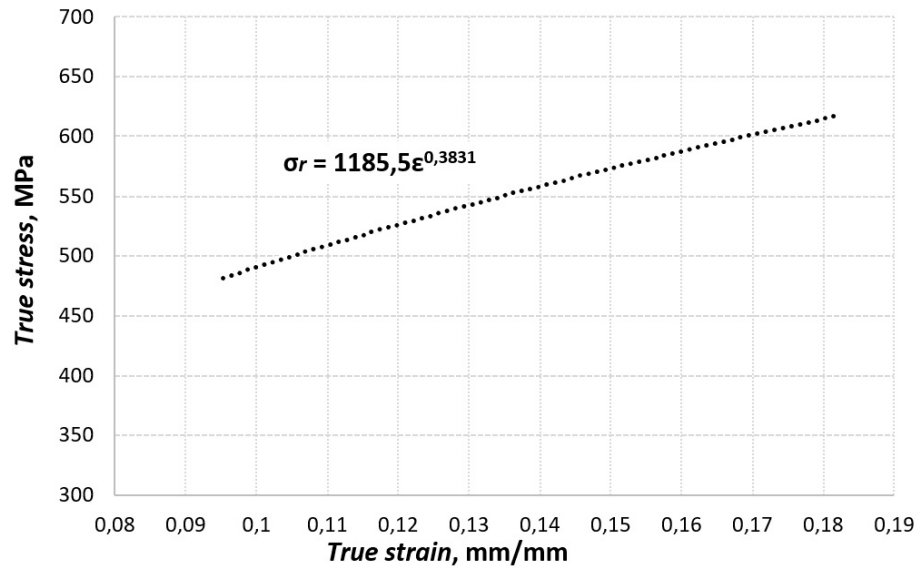
Figure 2. True stress-true strain diagram from the elastic limit to maximum stress

2.3. Strain hardening exponent, n

To determine this parameter, the specifications given by the ASTM E 646 standard (16) were followed. As suggested in said document, method B was used because the elastic deformations are much lower than 10 % of the total deformation. The value of n was obtained from the slope of the curve σ_r vs ε in Fig. **2**, calculated from Eqs. (1), (2), and (3).

$$\sigma_r = k \cdot \varepsilon^n \tag{1}$$

$$\sigma_r = \sigma \cdot (1 + \epsilon) \tag{2}$$

$$\varepsilon = \ln(1 + \epsilon) \tag{3}$$

σ_r= true stress
ε = true strain
k= strength coefficient
n = strain-hardening exponent
σ_r= engineering stress
ϵ= engineering strain

2.4. Normal anisotropy coefficient, r

This parameter was determined according to ASTM E 517 (17). Four specimens were tested for each orientation with respect to the rolling direction (0, 45, and 90°), up to a deformation of 15 % of the original length (l_o) and at a test speed of 4 mm/min. r_m and Δr were calculated using Eqs. (4), (5), and (6), taking the dimensions shown in Fig. **3** as reference.

$$r = \frac{\varepsilon_w}{\varepsilon_t} = \frac{\ln\left(\frac{w_o}{w_f}\right)}{\ln\left(\frac{l_f \cdot w_f}{l_o \cdot w_o}\right)} \tag{4}$$

$$r_m = \frac{r_0 + 2r_{45} + r_{90}}{4} \tag{5}$$

$$\Delta r = \frac{r_0 - 2r_{45} + r_{90}}{2} \tag{6}$$

w = width strain

ε_t = thickness strain

l_o = original gauge length

l_f = final gauge length

w_o = original width

w_f = final width
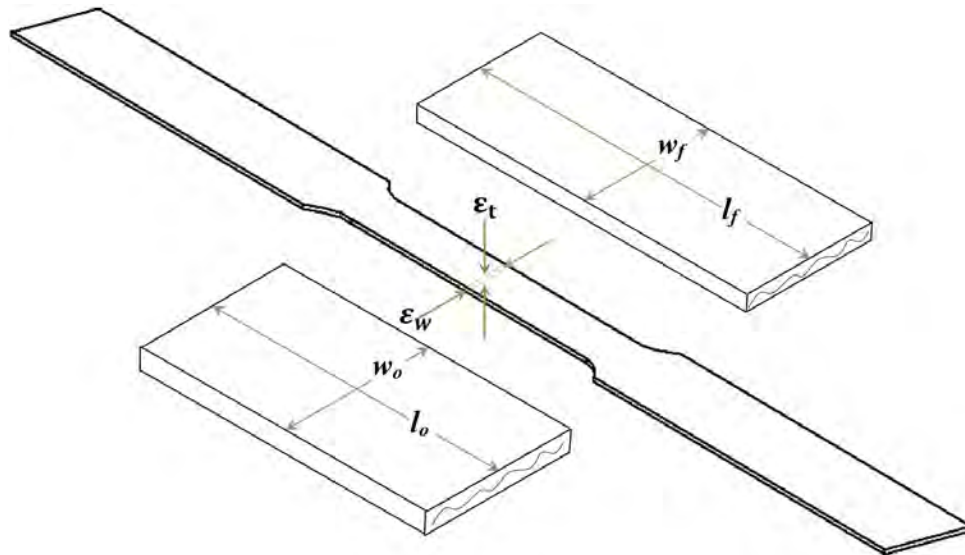
Figure 3. Dimensions for determining the r-values

2.5.   Forming limit curves

The FLCs were determined according to ASTM E 2218 (11). Seven specimens (rectangular strips) with lengths of 175 mm and widths from 25 to 175 mm with 25 mm increments were manufactured and engraved with a grid of circles 2,5 mm in diameter. The sheets were deformed with a lubricated hemispherical punch which was designed exclusively for the test and attached to a universal machine (IBERTEST) (Fig. 4). The deformation percentage of the circles along the length and width of the sheets was determined, and the curve of each sheet was drawn.
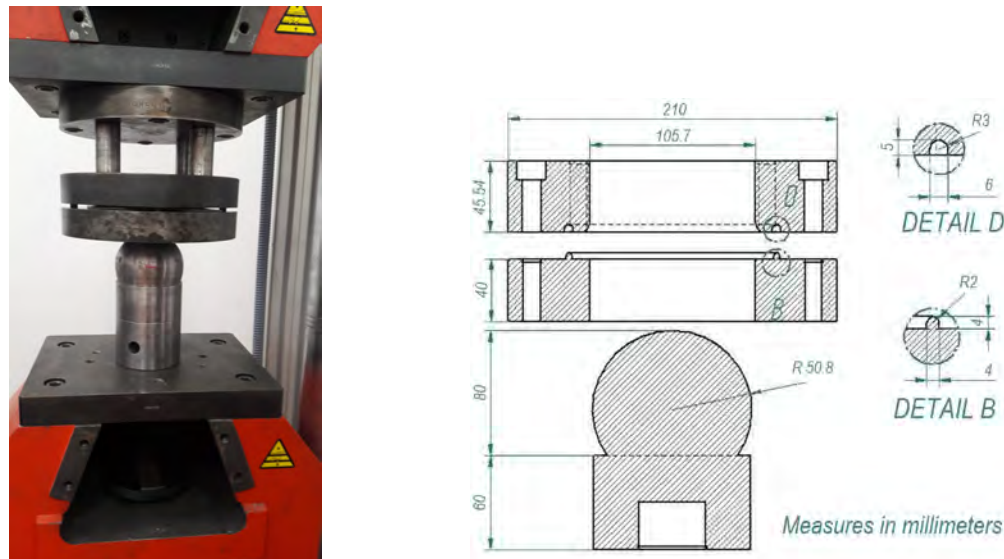
Figure 4. a) Device to determine the FLCs attached to the IBERTEST universal machine; b) measurements of the device according to (11)

3.   Analysis and discussion of results

3.1.   Chemical composition

The results of the chemical analysis for the SG295 and SG325 steel sheets are presented in Table I. The values for the main components (carbon, manganese, silicon, phosphorus, and sulfur) are within the limits established for SG295 and SG325 steel sheets as per the JIS G3116 standard (18). Given their chemical composition, the two steels can be classified as *carbon steels*, and more specifically as *mild steels* (2).

Table I. Chemical analysis of SG295 and SG325 steels

Element	SG295 %w/w	SG325 % w/w	Element	SG295 %w/w	SG325 % w/w	Element	SG295 % w/w	SG325 % w/w
C	0,168	0,178	Ni	0,021	0,015	Pb	0,003	0,003
Si	0,003	0,075	Cu	0,012	0,010	Sb	0,001	0,002
Mn	0,694	0,974	Al	0,033	0,022	Sn	0,001	0,001
P	0,017	0,014	As	0,002	0,003	V	0,003	0,003
S	0,005	0,003	B	-	0,000	W	-	-
Cr	0,021	0,021	Co	0,003	0,002	Zn	-	0,001
Mo	0,007	0,006	Nb	0,001	0,001			

3.2. Microstructure

The metallographic structure of the steels is shown in Fig. 5. As can be seen, the microstructure of SG295 steel is ferrite (90 %) and pearlite (10 %) with very fine equiaxed grains (10 ASTM). No grain elongation is observed in the rolling direction due to the recrystallization process inherent to hot rolling.

The microstructure of SG325 steel is ferrite (80 %) and pearlite (20 %), with the presence of small globules of retained carbide. The grains are equiaxed due to the recrystallization process inherent to hot rolling. The grain size is very fine (10-11 ASTM), which indicates higher strength but lower ductility. In the case of sheet metal, this fine grain size causes the appearance of orange peel. It should be noted that, in sheet metal forming operations, an ASTM grain size of 7 is preferred (8).
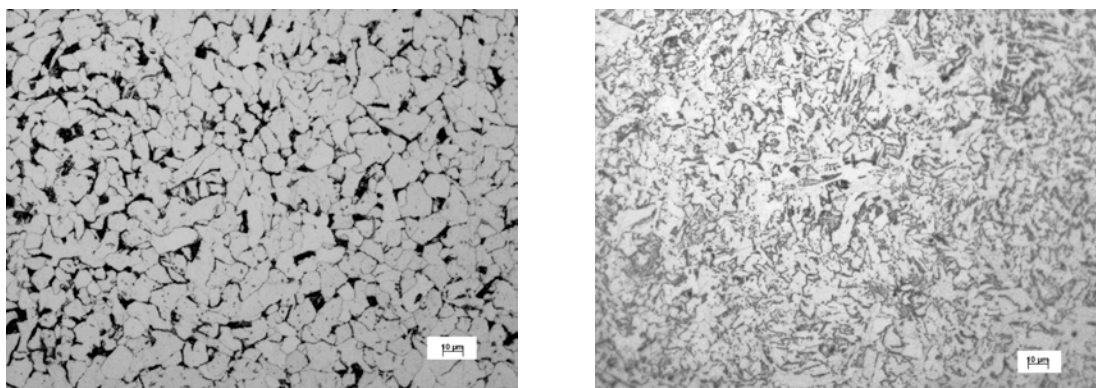
Figure 5. Micrograph of the steel samples: (a) SG295 and (b) SG325. Magnification: 500X; scale bar: 10 μm.

3.3. Conventional yield limit at 0,2 % elongation, σ_y (0,2 %), and ultimate strength, σ_u

The values of these properties are different depending on the orientation in which they were measured (Table II). The average tensile strength for both cases is slightly above the expected limits, *i.e.*, 440 and 490 MP for SG295 and SG325 steel sheets according to JIS G3116 (18).

Regarding σ_y (0,2 %), the values are much higher than expected (295 and 325 MPa) for SG295 and SG325 steel sheets according to (18).

3.4. Elongation to fracture for a 50mm gauge length, A_{50}

The tested sheets have a value slightly below the established limits (26 and 22 %) for SG295 and SG325 steel sheets according to (18).

3.5. Strain hardening exponent, *n*

In both cases, the sheets with an orientation of 45° with respect to the last rolling show the lowest value, especially in SG325 steel. These values are slightly below those reported by (8) for annealed low carbon steel (0,26), but they coincide with those presented by (6) for hot-rolled 0,2 % carbon steel (0,22).

Table II. Results of the tensile tests for the two steel sheets

Sheet	Orientation	Yield strength (σ_y) Mpa	Tensile strength (σ_u) Mpa	Percent elongation in 50 mm (A50) %	Strain-Hardening Exponents, n	Plastic strain ratio r(15)	Normal anisotropy rm	Planar anisotropy Δr
SG295	0°	357,5 ± 0,7	431,5 ± 79,9	24,56 ± 0,51	0,23 ± 0,01	0,64 ± 0,17	1,64	0,23
2,2	45°	343,0 ± 0,0	456,0 ± 1,4	28,84 ± 0,79	0,23 ± 0,01	1,41 ± 0,19	1,64	0,23
mm	90°	346,1 ± 0,7	462,3 ± 0,4	21,26 ± 2,55	0,25 ± 0,05	3,12 ± 0,68		
SG325	0°	391,2 ± 0,6	514,3 ± 0,4	23,07 ± 0,95	0,22 ± 0,01	0,94 ± 0,09		
2,3	45°	410,0 ± 1,4	518,5 ± 3,5	17,94 ± 0,57	0,16 ± 0,06	1,31 ± 0,19	1,29	-0,02
mm	90°	405,5 ± 13,4	527,5 ± 0,7	10,72 ± 0,57	0,21 ± 0,00	1,61 ± 0,13		

3.6. Anisotropy coefficient, r

The r_m values are slightly above the ranges published by (8) for hot-rolled steel (0,8-1,0). However, they are similar to the range mentioned by (9) for hot-rolled 0,2 % carbon steel (1,0-1,6). In both cases, there is a high dispersion of the data, and an increase in anisotropy with the orientation angle is observed, especially in the case of the SG295 sheet. These differences can be associated with the crystallographic texture of the material, as suggested by some authors (19, 20).

3.7. Forming limit diagrams, FLD

The morphology of the rectangular samples after deformation is shown in Figs. 6 and 7. To measure the deformation of the initial network of circles, the resulting ellipses were classified according to their appearance as good (no localized necking), marginal (localized necking), or fractured. The real deformations in the major (ε_1) and the minor axes (ε_2) were determined according to Eqs. (7) and (8).

$$e_{1,2} = \frac{L_f - d_o}{d_o} \tag{7}$$

$$\varepsilon_{1,2} = \ln(1 + e_{1,2}) \tag{8}$$

In Figs. 8 and 9, the deformation data of the initial network of circles are represented for SG295 and SG325, respectively. The various points correspond to the deformations of the circles in and around the fault region. Triangles represent ellipses where fractures or fissures occurred, squares represent ellipse marginals, and circles represent good ellipses. Thus, the forming limit curve is the line that separates the good points at the limit or border of the region that contains them.

Figure 6. The seven SG325 steel specimens deformed to failure
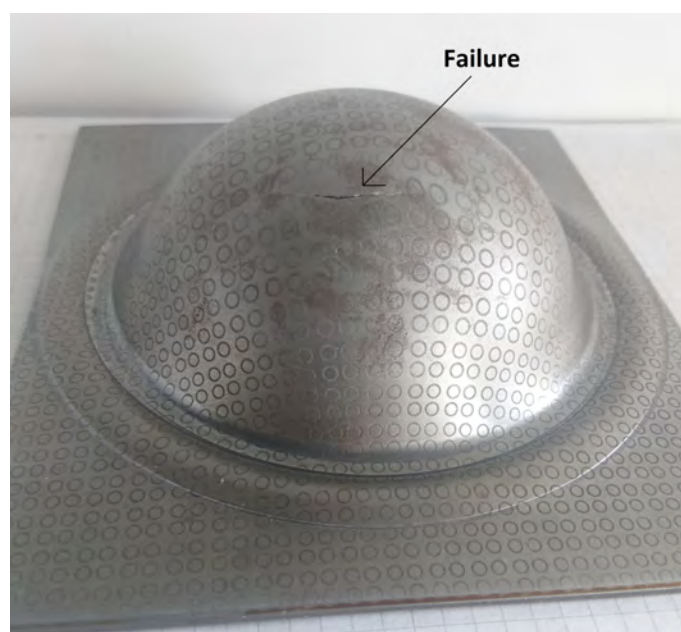
Figure 7. 150 mm wide specimen, where the failure after the test is shown in detail

The formability limit curves in Figs. **8** and **9** exhibit a similar behavior in both steel sheets. However, the values of the largest true strain ε_1, in the flat strain condition FLD_0 (the lowest point of the curve) were different: 0,281 and 0,336 for SG295 and SG325, respectively. These values are lower than the 0,385 found by (**8**) for low-carbon steel and the 0,460 and 0,457 determined by (**21**) and (**22**) in low-carbon steels for deep drawing with 2 and 1,4 mm thickness, respectively.

The only difference between the two curves is on the left: the SG325 slider has a steeper slope, and therefore a greater area in the safe zone. This behavior may be the effect of its greater thickness since previous studies have found that the curve rises with the thickness of the sheet (**4**, **12**).

In addition to the experimental curve, Figs. **8** and **9** show two curves with empirical predictions made with the equations of the Keeler and Brazier (**23**) and Paul S. K. (**12**) models and the data in Table **II**. The Keeler and Brazier approximation model depends on the thickness of the shell and the strain
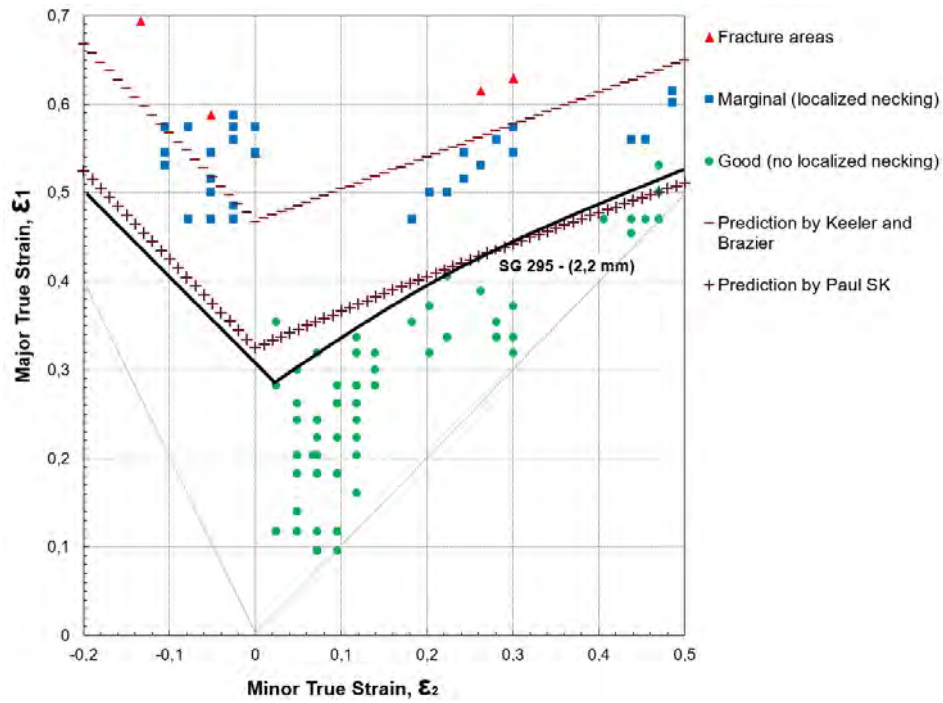
Figure 8. FLD for metallic sheets of SG295 steel
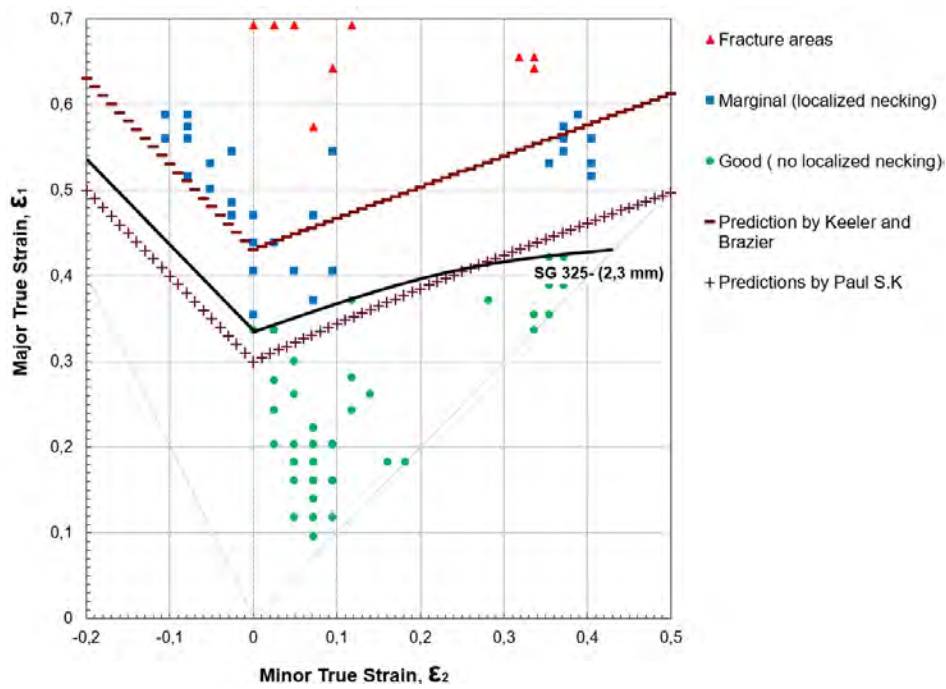
Figure 9. FFLDs for metallic sheets of SG325 steel

hardening exponent n in order to determine the FLD_0, while the Paul S. K. model also includes the ultimate strength σ_u, the elongation to fracture A_{50}, and the anisotropy coefficient r. In both models, the left side of the curve is a straight line with a slope (-1), while the slope on the right side of the curve is 20° in (23) and is determined depending on the value of FLD0 in (12).

In the two steel sheets, it can be seen that the Paul S. K. prediction, the one that contemplates the greatest number of variables in the model, is the one with the best fit and is below the experimental curve, whereas that of Keeler and Brazier (23) is above it.

4.   Conclusions

The results of the chemical and metallographic analysis of the materials classifies them as carbon steels, more specifically mild steels, with ferrite as the main microconstituent and the presence of pearlite and retained carbon globules.

SG325 steel reported better values in the characteristics of tensile strength σ_u, and the elastic limit σ_y (0,2 %), while SG295 behaved better against the elongation to fracture A_{50}, the strain hardening exponent n, and the normal anisotropy r_m.

In both materials, the values of the anisotropy coefficient increase with the angle of orientation regarding the last lamination.

The forming limit curves are very similar. However, the SG325 sheet achieves a greater area of deformation in the safety condition, which may be due to its greater thickness.

5.   Acknowledgments

References

[1] J. E. Barbosa, I. H. García, and J. Fuentes, "Estimación vía experimental de la formabilidad de láminas de aluminio de pureza comercial," *Rev. Lat. Metalurgia Mat.*, vol. 29, no 2, pp. 128-134, Dec. 2009. [Online]. Available: http://ve.scielo.org/scielo.php?script=sci_arttext&pid= S0255-69522009000200008 ↑3

[2] D. R. Askeland and W. J. Wright, *Ciencia e ingeniería de los materiales*. México, D.F: Cengage Learning, 2017. ↑3, 7

[3] C .L. Casadiego, J. E. Barbosa, and I. H. García, "Determinación experimental de la formabilidad de láminas de acero SG295 mediante sus propiedades tensiles," *Rev. Col. Tec. Av.*, vol. 1, no. 29, pp. 9-15, 2017. [Online]. Available: https://doi.org/10.24054/16927257.v29.n29.2017.2480 ↑3

[4] ASM International, *Metals handbook volume 14. Forming and forging*. USA: ASM International, 1996. ↑ 3, 10

[5] A. E. Tekkaya and T. Altan, *Sheet metal forming: Fundamentals*. USA: ASM International, 2012. [Online]. Available: http://search.ebscohost.com.bibliotecavirtual.unad.edu.co/login.aspx?direct=true&db=nlebk&AN=513307&lang=es&site=eds-live&scope=site ↑ 3

[6] R. Gedney, *Tensile testing for determining the formability of sheet metals*. Norwood, MA, USA: ADMET Inc., 2013. ↑ 3, 9

[7] J.A. Schey, *Introduction to manufacturing processes*. USA: McGraw-Hill, 2000. ↑ 3

[8] S. Kalpakjian and S. R. Schmid, Manufactura, *ingeniería y tecnología*. México, DF: Pearson Educación, 2008. ↑ 3, 8, 9, 10

[9] R. Gedney, *Measuring the plastic strain ratio of sheet metals*. Norwood, MA, USA: ADMET Inc., 2013. ↑ 3, 9

[10] J. E. Barbosa, I. H. García, and V. García, "Análisis de la formabilidad de láminas de acero AISI 304 con diferentes espesores mediante sus propiedades de tracción" *Rev. UIS Ing.*, vol. 21, no 4, pp. 97-106, Dec. 2022. https://doi.org/10.18273/revuin.v21n4-2022009 ↑ 3

[11] *Standard test methods for determining forming limit curves*, ASTM E 2218, ASTM International, West Conshohocken, 2015. ↑ 3, 4, 6, 7

[12] S. K. Paul, "Prediction of complete forming limit diagram from tensile properties of various steel sheets by a nonlinear regression based approach," *J. Manuf. Processes*, vol. 23, pp. 192-200, 2016. https://doi.org/10.1016/j.jmapro.2016.06.005 ↑ 3, 10, 12

[13] S. K. Paul, "Controlling factors of forming limit curve: A review," *Adv. Ind. Manuf. Eng.*, vol. 2, art. 100033, 2021. https://doi.org/10.1016/j.aime.2021.100033 ↑ 3

[14] R. Shang, Z. Shao, and J. Lin, "A review on modeling techniques for formability prediction of sheet metal forming," *Int. J. Lightweight Mat. Manuf.*, vol. 1, no. 3, pp. 115-125, Sep. 2018. https://doi.org/10.1016/j.ijlmm.2018.06.003 ↑ 3

[15] *Standard test methods for tension testing of metallic materials [metric]*, ASTM E 8M, ASTM International, West Conshohocken, 2013. ↑ 4

[16] *Standard test methods for tensile strain-hardening exponents (n − values) of metallic sheet materials*, ASTM E 646, ASTM International, West Conshohocken, 2016. ↑ 4, 5

[17] *Standard test methods for plastic strain ratio r for sheet metal*, ASTM E 517, ASTM International, West Conshohocken, 2018. ↑ 4, 5

[18] *Steel sheet, plates and strip for gas cylinders*, JIS G 3116, Japanese Standards Association (JIS), Tokyo, 2020. ↑ 7, 8

[19] M. J. Serenelli, M. A. Bertinetti, and J. W Signorelli, "Influencia de la textura cristalográfica en la dispersión de coeficientes de lankford en una chapa de acero galvanizada de bajo carbono," *Mec. Comp.*, vol. XXVII, no. 14, pp. 993- 1001, Nov. 2008. [Online]. Available: https://cimec.org.ar/ojs/index.php/mc/article/view/1467 ↑ 9

[20] J. A. Newell, *Ciencia de materiales, aplicaciones en ingeniería*. México, DF: Alfaomega, 2010. ↑9

[21] D. R. Kumar, "Formability analysis of extra-deep drawing steel," *J. Mat. Processing Tec.*, vol. 130-131, pp. 31-41, Dec. 2002. https://doi.org/10.1016/S0924-0136(02)00789-6 ↑10

[22] K. Sipos, J. Martínez, N. Burgos, and H. Pesenti, "Aceros para embutido profundo: fabricación, caracterización, microestructura y texturas," *Rev. Metalurgia*, vol. 41, no. Extra, pp. 58-63, Dec. 2005. http://dx.doi.org/10.3989/revmetalm.2005.v41.iExtra.999 ↑10

[23] S. P. Keeler and W. G. Brazier, "Relationship between laboratory material characterization and press-shop formability," *Microalloying*, vol. 75, pp. 517-530, 1975. ↑10, 12

Jhon Erickson Barbosa Jaimes

Master of Mechanical Engineering, Universidad Nacional Experimental del Táchira UNET. Professor at Universidad Nacional Abierta y a Distancia (UNAD). He works as a researcher in the Gestindustriales EOCA research group.
Email: jhon.barbosa@unad.edu.co

Ismael Humberto García Páez

PhD in Inorganic Chemistry, validated as Doctor of Chemical Sciences by Universidad Autónoma de Madrid. Master of Metallurgic Engineering from Universidad Industrial de Santander. Professor at Universidad Francisco de Paula Santander (UFPS). He belongs to the Diseño Mecánico, Materiales y Procesos research group (GIDIMA), where he serves as a researcher.
Email: ismaelhumbertogp@ufps.edu.co

Claudia Liliana Casadiego

Master of Materials Science and Technology, Universidad Francisco de Paula Santander. Professor at Universidad Libre de Colombia. She belongs to the Competitividad y Sostenibilidad para el Desarrollo research group (GICSD), where she serves as a researcher.
Email: claudial.casadiegop@unilibre.edu.co

Research

Study Of the Effect of Titanium Additions on The Mechanical and Corrosion Properties of AISI 316 Powder Metallurgical Steel

Estudio del efecto de adiciones de titanio en las propiedades mecánicas y de corrosión del acero pulvimetalúrgico AISI 316

Luz Adriana Cañas Mendoza[1] [ID][✉]*, Yaneth Pineda Triana[2] [ID], and Lais Mujica Roncery[2] [ID]

[1]Universidad Tecnológica de Pereira (Pereira, Colombia)-Universidad Pedagógica y Tecnológica de Colombia (Tunja, Colombia)
[2]Universidad Pedagógica y Tecnológica de Colombia (Tunja, Colombia)

Abstract

Context: Powder metallurgy uses metallic and/or non-metallic powders that, through mixing, compacting, and sintering operations, allow obtaining large series of products. In austenitic stainless steels, $Cr_{23}C_6$-type carbides can precipitate at temperatures between 450 and 950 °C. When this occurs, the steel is susceptible to being attacked at its grain boundaries by a phenomenon called *sensitization*. Titanium is added as a 'stabilizer' because it has a greater affinity with carbon for the formation of species at a temperature of approximately 900 ºC, and, during cooling it consumes the carbon forming MC-type carbides, inhibiting the precipitation of $Cr_{23}C_6$.

Method: The composition and morphology of the powders were characterized, leading to the formulation of an alloy matrix consisting of a mixture of AISI 316 steel powders of two different particle-size distributions in a proportion that produced the highest density and the lowest porosity in the sintered material. Titanium was added at two levels (0,4 and 1,0 wt %), and sintering was carried out with nitrogen. The corrosion rate was determined by potentiodynamic polarization. Vickers hardness and pin-on-disk wear tests were performed. The stages were complemented with a microstructural analysis.

Results: The addition of 0,4 wt % of titanium decreased the steel's rate of corrosion, albeit in the absence of passivation. The microstructure consists of austenite, ferrite, and TiC precipitates. The addition of 1,0 wt %Ti showed an increase in the corrosion rate, with a microstructure containing austenite, ferrite, TiC carbides, and the Laves η-Fe_2Ti phase.

Conclusions: The results were compared against thermodynamic simulations in the Thermo-Calc software, which were consistent with the microstructural analysis, showing the phenomena of stabilization as well as the precipitation of intermetallic phases and highlighting the importance of establishing strict controls in the formulation of powder metallurgical alloys due to the transformations that can take place due to the effect of the thermal cycles of the process.

Keywords: powder metallurgy, sensitization, stabilization, sintering, austenitic stainless steels

*✉ **Correspondence:** luzadriana@utp.edu.co

Resumen

Contexto: La pulvimetalurgia utiliza polvos metálicos y/o no metálicos que, mediante operaciones de mezcla, compactación y sinterización, permiten obtener grandes series de productos. En los aceros inoxidables austeníticos, los carburos de tipo $Cr_{23}C_6$ pueden precipitar a temperaturas entre 450 y 950 °C. Cuando esto ocurre, el acero es susceptible de ser atacado en sus límites de grano por el fenómeno denominado *sensitización*. El titanio se agrega como 'estabilizador' porque tiene mayor afinidad con el carbono para la formación de especies a una temperatura de aproximadamente 900 °C y, durante el enfriamiento, consume el carbono formando carburos tipo MC, inhibiendo la precipitación de $Cr_{23}C_6$.

Método: Se caracterizó la composición y morfología de los polvos, lo que condujo a la formulación de una matriz de aleación compuesta por una mezcla de polvos de acero AISI 316 de dos granulometrías diferentes en una proporción que produjo la mayor densidad y la menor porosidad del material sinterizado. Se añadió titanio en dos niveles (0,4 y 1,0 % en peso) y se sinterizó con nitrógeno. La velocidad de corrosión se determinó por polarización potenciodinámica. Se realizaron pruebas de dureza Vickers y de desgaste *pin-on-disk*. Las etapas se complementaron con un análisis microestructural.

Resultados: La adición de 0,4 % en peso de titanio disminuyó la velocidad de corrosión del acero, si bien en ausencia de pasivación. La microestructura consiste en precipitados de austenita, ferrita y TiC. La adición de 1,0 % en peso de Ti mostró un aumento en la velocidad de corrosión, con una microestructura que contenía austenita, ferrita, carburos de TiC y la fase Laves η-Fe_2Ti.

Conclusiones: Los resultados fueron comparados con simulaciones termodinámicas del *software* Thermo-Calc, consistentes con el análisis microestructural, mostrando los fenómenos de estabilización y la precipitación de fases intermetálicas, y destacando la importancia de establecer un control estricto en la formulación de aleaciones pulvimetalúrgicas debido a las transformaciones que pueden generarse por efecto de los ciclos térmicos del proceso.

Palabras clave: pulvimetalurgia, sensitización, estabilización, sinterización, aceros inoxidables austeníticos

Table of contents

1. Introduction

In the worldwide metallic materials manufacturing industry, powder metallurgy has been progressively gaining prominence. This is due to the versatility of the process and the feasibility of manufacturing parts using different types of matrices, allowing for a wide variety of morphologies, in addition to the possibility of using different compaction, sintering, and finishing treatment processes to obtain parts with special properties (1). The industrial applications of powder metallurgical stainless

steels have increased, although they continue to represent a small fraction with respect to their forged counterparts, especially in terms of behavior against corrosion. Most stainless- steel and other high-alloy powders are made by spraying into water or by inert gas and centrifugal spraying. Water-atomized powders have an irregular particle shape and are widely used for cold compaction and sintering. The densities of sintered parts are typically below 95 % of their theoretical values, which is why their mechanical and physical properties are unfavorable compared to those of dense materials. The corrosion behavior of powder metallurgical stainless steels depends on the synergistic effect of factors such as the chemical composition (which determines the quality of the passive layer and the efficiency of the protection against the environment), the surface conditions of the component, the intermetallic phases that are unfavorable for corrosion resistance, interconnected pores (because they increase the exposed surface area), and the amount, morphology, and size of the pores (2).

Compaction and densification are difficult tasks during the sintering of stainless-steel powders due to their strength, hardness, and work hardening. Depending on the particle size distribution, compaction pressure, and sintering temperature, the sintering density is normally between 80 and 90 % of the theoretical value. The low final density and interconnected porosity cause poor mechanical properties and low corrosion resistance (3, 4) observed that the porosity of powder metallurgical products manufactured by the conventional route affects their mechanical properties at room temperature, that the behavior under fatigue conditions improves when the porosities are fine and rounded, and that this behavior worsens when there are coarse and angular porosities. This is because the pores contribute to the initiation and propagation of cracks under fatigue conditions. Other factors affect the behavior of these materials under dynamic stresses. For instance, the fatigue behavior of PM austenitic stainless steels is also affected by precipitates (carbides, nitrides) and the microstructure of the matrix. The study by (5) analyzed the effect of porosity on the microstructure and mechanical properties of 316L powder metallurgical steel for use in implants. It was found that tensile and fatigue strength increased in samples sintered with higher density. Components with low density and larger, irregular, and clustered pores showed higher deformation and premature failure.

Austenitic stainless steels have higher corrosion resistance than ferritic and martensitic stainless steels, but they are susceptible to sensitization. This phenomenon consists of a loss of corrosion resistance when steels are slowly cooled from the dissolution temperature (1.100 °C) or when they are heated to temperatures between 500 and 850 °C. When an austenitic steel containing more than 0,03 % carbon is heated above 500 °C, chromium carbides begin to form at the junctions of the austenite grains. These carbides have a variable composition, their chromium content is between 30 and 90 %, and their carbon content is between 1 and 2 %. The carbides are formed from the carbon and chromium of the nearest austenite crystals. The crystals are poorer in these elements due to the decrease in the percentages of chromium and carbon in said areas. The steel located in the vicinity of the carbides ceases to be stainless (%Cr less than 11 %), and it is attacked by chemical agents (6). This phenomenon is common in processes that are carried out at temperatures around the critical range, as is the case of welding or cooling after sintering in powder metallurgy. A method to counteract the sensitization that generates localized corrosion in grain boundaries or intergranular corrosion (CIG) consists of thermally treating redissolution of carbides. This involves heating the component to temperatures

between 1.050 and 1.150 °C. The goal is for the alloying elements to be in a solid solution, followed by rapid cooling to room temperature to prevent the formation of new carbides (7). Another method used to avoid sensitization is the addition of stabilizing elements such as titanium or niobium, as they have a greater affinity for carbon than chromium. Titanium, however, has the advantage that, once titanium carbide (TiC) forms, it does not dissolve easily in iron. When titanium-added austenitic steel is heated within the forming temperature range (700-900 °C), titanium carbides begin to precipitate instead of chromium carbides. This prevents the reduction of chromium in the austenite crystals close to the TiC. Stainless steels of this type are denoted as *stabilized*. Titanium carbides avoid sensitization since they precipitate in the austenitic matrix and improve the mechanical properties of the final part by increasing its hardness, mechanical strength, and wear resistance. Titanium additions to 316L stainless steel have also been used as biomaterials for the manufacture of implants and medical devices. In (8), it was found that the addition of boron and titanium to steel obtained via conventional powder metallurgy with nitrogen as a sintering atmosphere has a positive effect on the densification, corrosion resistance, and microhardness of the sintered components. Nitrogen diffused into the samples, producing the deposition of nitrides and favoring the formation of a superficial layer of nitrides that controlled the dissolution of the metal, thus improving resistance to corrosion in saline media.

Electrochemical methods are widely used to analyze cast and wrought stainless steels due to the quantitative information they provide about corrosion rates and mechanisms. These criteria can also be applied to sintered materials, although the presence of pores and metallurgical defects can complicate the interpretation of electrochemical data (9, 10) reduced the porosity of a powder metallurgical ferritic stainless steel by adding small gas-atomized spherical powders (AISI 316L and 430L) to larger irregular water-atomized powders (AISI 434L). The alloy obtained had the structure of duplex steel. A reduction in the number of large pores was observed, the corrosion rate decreased, and the corrosion potential increased in tests in neutral media with and without chlorides. This evaluation was carried out using electrochemical polarization tests (10).

The technological versatility of powder metallurgical processes allows varying the composition of alloys from elemental and pre-alloyed metal powders to obtain steels with improved properties. The purpose of this study was to manufacture powder metallurgical stainless steel from powders with different particle sizes and with titanium additions in order to study the changes in its physical and mechanical properties and corrosion resistance. The combination of particles with different average sizes reduced the porosity and increased the density of the preforms and sintered specimens. The addition of 0,4 wt % titanium to an AISI 316 powder metallurgical steel caused the precipitation of titanium carbides with some ferrite regions. This allowed the steel to be stabilized by preventing the precipitation of $Cr_{23}C_6$ chromium carbides. When increasing the amount of titanium to 1 wt %, the presence of the Laves η-Fe_2Ti intermetallic phase was observed nucleating from the ferrite, causing an increase in the corrosion rate of the steel. Adding titanium to the steel produced an increase in hardness and a decrease in the wear coefficient, which is explained by the precipitation of carbides and intermetallic phases. It was concluded that controlling the composition is a fundamental factor in generating microstructural changes and the precipitation of intermetallic phases, as the microstructure determines the final properties of the component.

2.   Materials and methods

The starting raw materials consisted of AISI 316 pre-alloyed stainless-steel powders with average sizes of 45 and 150 μm, elemental titanium powders of 45 μm, and zinc stearate ($Zn(C_{18}H_{35}O_2)_2$) as a lubricant in a proportion of 1 wt%. The metal powders were characterized by determining their chemical composition, size, and morphology. The tests were carried out with atomic absorption (AA) and energy dispersion spectrometry in a scanning electron microscope (SEM-EDS) for semi-quantitative elemental analysis. For the AISI 316 steel powders, the chemical composition provided by the manufacturer (GOODFELLOW) was taken as reference. The purity of the elemental titanium powders (SIGMA-ALDRICH) was confirmed via X-ray diffraction (XRD). The morphology and size of the powders were determined with a Carl Zeiss EVO MA 10 scanning electron microscope using an EHT current of 20 kV. With the secondary electron detector, the length and width of 30 different particles were measured from the acquired images. Based on this measurement, the aspect ratio (AR) was determined according to the ASTM F1877 standard (11), where AR is the ratio between the largest (d_{max}) and the smallest diameter (d_{min}). The apparent density of the metal powders was determined based on the ASTM B703 standard (12) using a cylinder of known internal volume that was filled with the sample (up to its capacity). Subsequently, the sample was weighed, and its density was determined from the ratio of mass and volume.

After characterizing the raw materials, preforms were obtained by mixing and compaction. Once the quantities of each mixture (metal powders and lubricant) were obtained, a planetary mill was used in the absence of grinding bodies for 20 minutes at 150 rpm in order to obtain a homogeneous distribution of the powders. Subsequently, uniaxial compaction was carried out, applying a pressure of 800 MPa in a universal electromechanical machine (Microtest EM/500/FR). By compacting with the established parameters, preforms with a cylindrical geometry, a diameter of 10 mm (+/- 0,15), and a height of 4 mm (+/- 0,1) were obtained.

Both the preforms and the sintered specimens were characterized by determining their density, porosity, morphology, and microstructure. The porosity was determined via image analysis with the Fiji software (ImageJ) from 30 micrographs of each specimen at a 200X magnification, which were obtained using a scanning electron microscope. The density of the preforms and the sintered samples was determined based on the procedure described by the ASTM B962 standard (13): via a gravimetric technique using deionized water and impregnation oil.

Sample sintering was performed in a CARBOLITE STF/TZF tube furnace using grade-four nitrogen as the sintering atmosphere and a dew point of -60 °C, which guarantees a dry and pure atmosphere (with less than 10 ppm of oxygen). The sintering temperature was set to 1.200 ºC, a value used for austenitic stainless steels (14–17). Fig. **1** shows the thermal cycles of the sintered samples.

The pre-sintering treatment carried out at 450 ºC aimed to eliminate the lubricant and was followed by an increase in temperature to 1.200 °C for the sintering process. Afterwards, stabilization was carried out at a temperature of 900 ºC to favor the precipitation of Ti species (carbides, nitrides, and/or
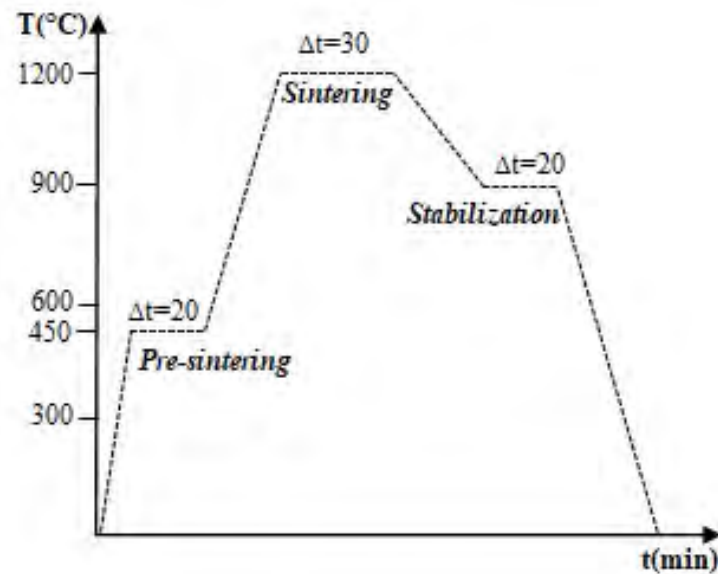
Figure 1. Thermal cycles diagram for the sintering of powder metallurgical alloys

carbonitrides), aiming to avoid chromium carbide precipitation (around 800 ℃) as well as the presence of free carbon. Quenching was performed in the water at room temperature. A characterization of the sintered samples and an evaluation of different properties were conducted to determine the effects of modifying the composition of AISI 316 powder metallurgical steel by adding titanium as an alloying element.

Mechanical properties such as hardness were determined under the guidelines of the ASTM E384 standard for measurement on the Vickers HV scale (18). A QV-1000DM Micro Vickers Hardness Tester was used, applying a load of 100 gf for 20 seconds. A wear resistance evaluation was carried out via the pin-on-disk test, according to the ASTM G99 standard (19), using a MT/60/NI Microtest tribometer.

Corrosion resistance was evaluated through electrochemical tests, obtaining potentiodynamic polarization curves while using a GAMRY 750 Potentiostat Galvanostat at room temperature. The linear polarization resistance (LPR) and the active/passive characteristics of the metal/solution system were determined, and the corrosion rate (in mpy) was calculated. The samples were polished on 2000 sandpaper as surface preparation before testing. Each sample was placed in a cell with a hole of a known area, using a 1N H_2SO_4 solution with 250 ppm NaCl as the electrolyte. An Ag/AgCl (3M KCl) reference electrode and a platinum counter electrode were used. A first test was carried out to determine the open circuit potential. The LPR was determined by employing a potential difference of ±20 mV concerning this value. Potentiodynamic polarization tests were performed with a potential difference of -400 mV for the cathodic polarization and with +1500 mV for the anodic curve. This, in order to determine the passivation and transpassivation zones. The tests were carried out while taking the ASTM G3, ASTM G5, ASTM G59, and ASTM G102 standards as reference (20–23).

3. Results and discussion

The results obtained during the characterization of the metallic powders, the preforms, and the sintered samples are presented below. Fig. 2 shows the micrographs, obtained via scanning electron microscopy (SEM); the chemical composition, determined by energy dispersion spectrometry (EDS) and atomic absorption (AA) in comparison with the values provided by the powder suppliers; and the diffractograms, obtained using X-ray diffraction (XRD) on the metallic powders.

Element (%ow/w)	AISI/SAE 316 (45µm)		
	Supplier	EDS	AA
Cr	16,5 – 20,0	18,11	19,9
Ni	8,0 – 14,0	9,9	9,73
Mo	2,5 – 3,5	2,17	---
Mn	<2	---	0,118
C	<0,08	---	---
Si	---	0,96	0,645
Ti	---	0,03	0,015
Fe	Balance	Balance	66,3

Element (%ow/w)	AISI/SAE 316 (150µm)		
	Supplier	EDS	AA
Cr	16,5 - 20,0	17,06	19,8
Ni	8,0 – 14,0	10,45	9,486
Mo	2,5 – 3,5	2,18	---
Mn	<2	---	0,104
C	<0,08	---	---
Si	---	1,23	0,605
Ti	---	0,022	0,014
Fe	Balance	Balance	66,33

Titanium Powder (45µm)
Supplier
Purity 99,98%
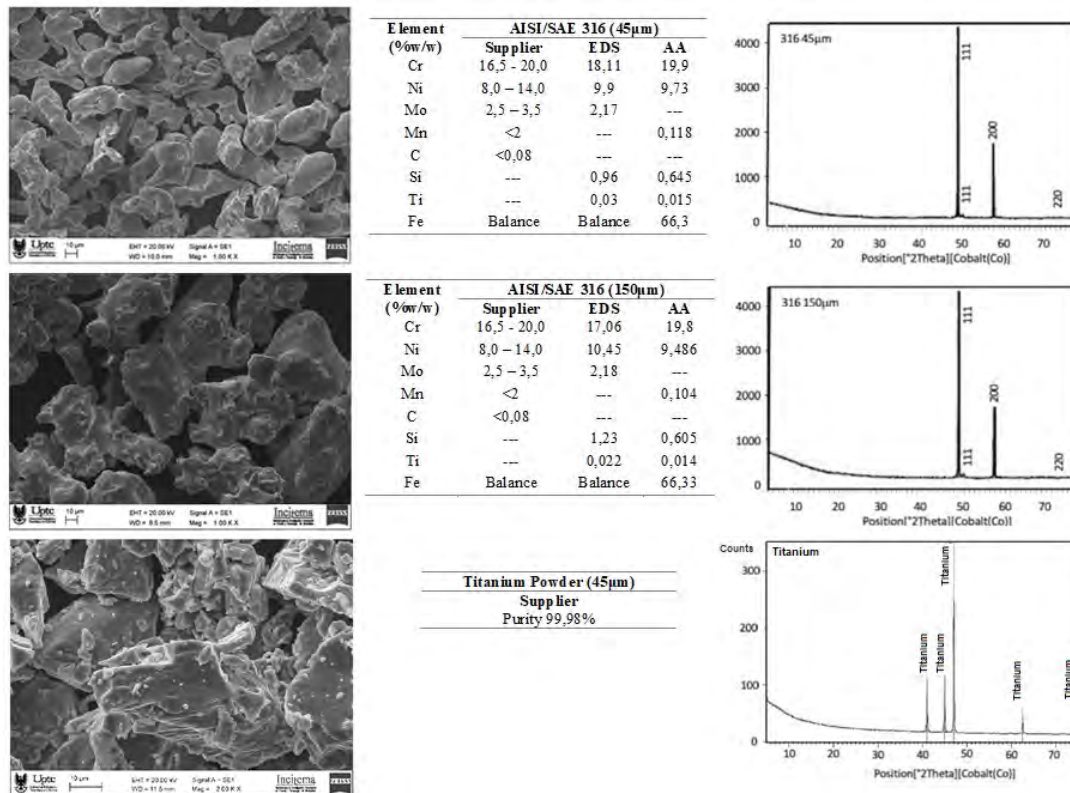
Figure 2. SEM micrographs, chemical composition (EDS, AA), and diffractograms (XRD) of metallic powders

The values obtained through the characterization techniques confirm that the elements are within the range provided by the supplier. For the two types of AISI 316 steel powders, diffraction planes (111), (200), and (220) are observed, corresponding to the face-centered cubic structure of austenite. The diffractograms confirm the purity of the elemental titanium powders. Fig. 2 shows that, for the AISI 316 steel powders, the particles have an irregular shape, typical of the water atomization process; whereas, for the titanium powders, the morphology is sponge-like, as these stem from grinding a sponge made (*i.e.*, the Kroll process), resulting in irregular particles. In both cases, the morphologies are appropriate for alloy compaction and sintering processes. The Aspect Ratio (AR) for the 45 μm AISI 316 powders was 1,4406, and, for the 150 µm powders, it was 1,5692. These AR values confirm the irregular shape of the particles. Table I shows the apparent density values of the metal powders.

Table I. Apparent density of metallic powders

Apparent density of 316 steel powders (45 μm)	Apparent density of 316 steel powders (150 μm)	Apparent density of titanium powders (45 μm)
3,1566 g/cm^3	3,2148 g/cm^3	2,0923 g/cm^3

The low apparent density values are related to unsettled particles and voids. Because a volume greater than the real one is taken, the calculated density is lower than the actual value (hence the term *apparent*).

In preliminary tests, five types of mixtures of 45 and 150 μm AISI 316 steel powders were evaluated in order to define the most appropriate mixture in terms of the highest density, the lowest porosity, and the lowest corrosion rate. Based on these results, the alloy matrix was defined, which consists of a mixture of 65 wt% of 150 μm AISI 316 powders and 35 wt% of 45 μm AISI 316 powders. With this matrix, the alloys with titanium additions were prepared. Based on the composition of stabilized austenitic stainless steels (AISI 321), where the recommended amount of titanium is about five times the percentage of carbon, which exceeds 0,02 wt%, and considering the nitrogen traces, additions of 0,4 and 1,0 wt%Ti were established. With these percentages, we expected to have enough titanium to stabilize the alloy, as well as an additional amount aiming at the formation of other species such as carbides, nitrides, and/or carbonitrides. Table **II** presents the nomenclature of the samples and the properties determined for both the preforms and the sintered samples.

Table II. Sample characterization results

Sample	Porosity (%)		Density (g/cm^3)		Hardness (HV)	Wear coefficient (mm^3/N.mm)	Wear depth (μm)
	Preforms	Sintered	Preforms	Sintered			
1(316)	5,90	4,69	7,12	7,66	231	1,18E-06	48,6
2(316+0,4Ti)	5,82	4,43	7,14	7,67	255	2,51E-07	24,7
3(316+1Ti)	5,56	4,36	7,21	7,70	251	2,59E-07	21,0

Table **II** shows the variations in the porosity and density of the preforms and sintered samples, where the effect of the sintering process is observed in the elimination of part of the interconnected porosities between the powder particles, given that all the porosity values of the sintered samples are below their green counterparts. It is also evident that the addition of titanium generates lower porosity values and higher densities for the evaluated ranges and the two types of samples (preforms and sintered samples).

This behavior is due to the size of the particles, as the matrix combines 150 and 45 μm AISI 316 steel powders and the average size of the titanium powders is 45 μm. Therefore, in Fig. **3**, it is observed that the titanium is arranged in the spaces formed between the largest particles, favoring the reduction of empty spaces and increasing packing.
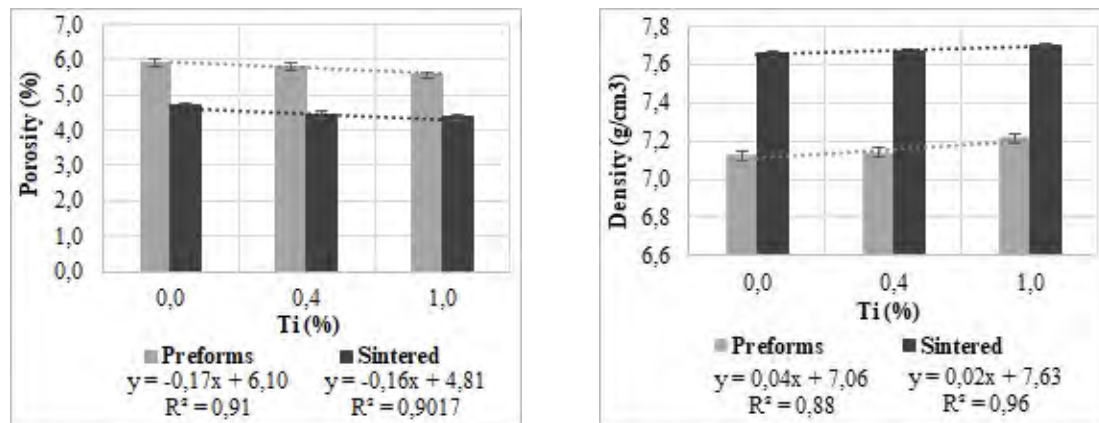
Figure 3. Morphology of preforms determined by SEM (EHT=20,00KV, SIGNAL A=SE1, WD=11 mm, MAG= 70 x 100 μm)

Regarding the results obtained for hardness (Table **2**), the alloys containing titanium have increased hardness when compared to Ti-free steel. In the case of the wear coefficient and the wear depth generated during the pin-on-disk test, the addition of 0,4 wt%Ti causes a drastic decrease in the two properties, with minimal variations when adding 1,0 wt% of the alloy element.

The effect of adding titanium on the mechanical and tribological properties of AISI 316 steel is supported by the microstructural observation presented after the corrosion resistance results. Table **III** shows the results obtained in the potentiodynamic tests aimed at determining the corrosion rate of the alloys.

Table III. Results obtained via potentiodynamic tests for sintered alloys. Electrolyte: 1N H_2SO_4 solution with 250ppm NaCl; reference electrode (Ag/AgCl 3M KCl); platinum counter electrode

Sample	β_a [mV/decade]	β_c [mV/decade]	i_{corr} [mA/cm^2]	E_{corr} [mV]	LPR [Ohms]	Vcorr [mpy]
1(316)	7,07	7,58	0,00238	-518,4	854,9	**1,07**
2(316+0,4Ti)	699,70	449,80	0,00168	-553,6	90.490,0	**0,76**
3(316+1Ti)	3,82	3,41	0,00231	-586,6	434,2	**1,04**

The results show that the addition of 0,4 wt%Ti reduces the corrosion rate of the sintered steel to the minimum value obtained, and it is observed that higher additions have an adverse effect, as the corrosion rate increases from 0,76 mpy in sample 2(316+0,4Ti) to 1,04 mpy in sample 3(316+1Ti), which corresponds to a growth of 1,4 orders of magnitude, with the latter value approaching that reported for steel without titanium. The analysis of the behavior of the materials under study requires observing the graphs obtained in the polarization tests, which represent the variables necessary to determine the rate of corrosion, as well as the active/passive behavior of the samples' surface. Fig. **4** shows the measured polarization curves of the sintered samples.

Figure 4. Tafel curves of potentiodynamic polarization for the sintered steels. Electrolyte: 1N H2SO4, 250 ppm NaCl

According to Fig. **4**, the behavior is similar for samples 1(316) and 3(316+1Ti), in which the formation of the passive film is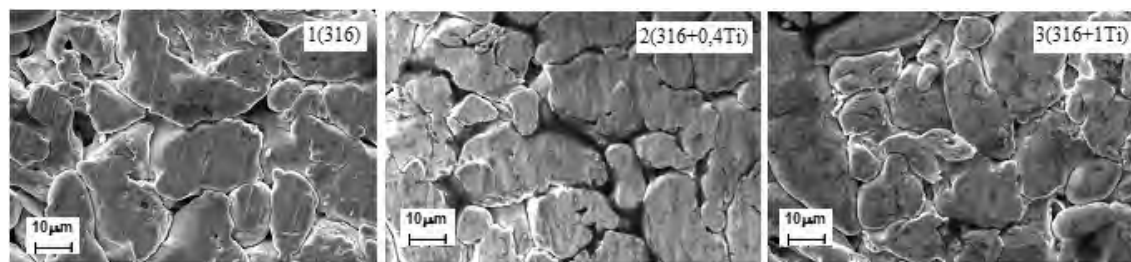 observed in the intermediate range between the passivation and transpassivation potentials. Although the corrosion rates calculated for these samples from the Tafel slopes and the linear polarization resistance LPR are very close, the sample with 1 wt %Ti shows a higher and unstable passivation current ip. Both curves show that the current tends to increase in the passivation range. On the other hand, sample 2(316+0,4Ti) does not show a critical passivation current but a lower and more stable current which could be associated with the formation of a passive layer. The addition of 0,4 wt %Ti shifts the corrosion and passivation currents towards lower values with regard to the other samples, which produces a lower corrosion rate. The potentiodynamic graphs of this composition show that the steel passed directly to the passivation zone without going through the dissolution zone.

Based on the chemical composition of each alloy, the Thermo-Calc software was used to predict the equilibrium phases via computational thermodynamics. Calculations were carried out at the sinterization and stabilization temperatures described in Fig. **1**. The compositions used in the software correspond to those determined during the experimental characterization of metal powders, with the aim of obtaining results consistent with the material. Phase quantification was performed for each alloy during these two stages, highlighting that the final microstructure corresponds to the one formed during the stabilization stage (900 °C). Table **IV** shows the theoretical percentages of the phases present.

Table IV. Quantification (molar fraction) of phases in sintered alloys (sinterization + stabilization) in Thermo-Calc

Sample/Phases	Austenite (γ)	Ferrite (α)	$Cr_{23}C_6$	Ti(C,N)	Laves (η)	TOTAL
1(316)	0,99		0,01			1
2(316+0,4Ti)	0,97	0,02		0,01		1
3(316+1Ti)	0,85	0,13		0,01	0,01	1

Because the interaction of the elements generates the precipitation of different phases, the aforementioned simulation tool allows analyzing the microstructural observation. Thus, according to the theoretical calculations, the presence of chromium carbides ($Cr_{23}C_6$), titanium compounds with

carbon and/or nitrogen Ti(C,N), and probably an intermetallic Laves(η) phase is expected. Fig. **5** shows the observed microstructures.
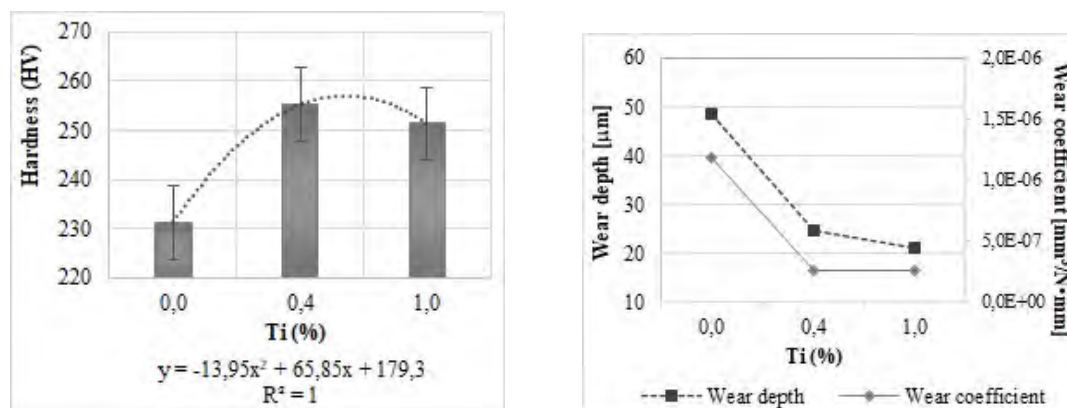

Figure 5. Micrographs of sintered alloys. a) Sample 1(316) obtained via SEM, b) sample 2(316+0.4Ti) obtained via SEM, 3) sample 3(316+1Ti) obtained via OM (left) and SEM (right)

Fig. **5**a shows the micrograph of sample 1(316) obtained via SEM with backscattered electrons. The observation was complemented with elemental mapping, showing the presence of carbon in grain boundaries, which is attributed to the formation of carbides. The remaining porosity in the sintered alloy offers favorable sites for the deposition of oxides, which, in this case, may correspond to those formed from the silicon detected in the characterization. Open and unconnected porosities remain, with a rounded and elongated morphology. Carbides of the $Cr_{23}C_6$ form preferentially precipitate at the grain boundaries on the surface of the pores, although there are small depositions of these carbides inside the grains. There is agreement with the structure projected with the thermodynamic calculations, although, qualitatively, the percentage of carbides seems to exceed the value predicted by the software.

The microstructure observed in Fig. **5**b, obtained via SEM with backscattered electrons for sample 2(316+0,4Ti), is distributed as determined by the software, since it consists of austenite grains with intragranular precipitates of TiC (nitrides, which have an elongated morphology, were not identified in these samples). Ferrite regions (α) were also observed in the areas of high pore density. No intermetallic phase or $Cr_{23}C_6$ chromium carbide precipitates were found. With this composition, titanium meets the objective of stabilization, avoiding the sensitization of stainless steel.

Fig. **5**c shows micrographs (OM and SEM) of sample 3(316+1Ti), in which the theoretically predicted phases can be identified. The high titanium content has two main effects on the microstructure: it inhibits the precipitation of chromium carbides ($Cr_{23}C_6$) and, in turn, induces the presence of the Laves η-Fe_2Ti phase. The precipitation of intermetallic phases is counterproductive to the stabilization of the material. The microstructures show the deposition of intragranular titanium carbides and nitrides. According to the observed distribution, it can be inferred that the Laves η-Fe_2Ti phase nucleates from the interior of the ferrite (α), taking advantage of the titanium from this solid solution. Apparently, there are some regions where this intermetallic phase has grown to consume the ferrite. In addition to the phase distribution, it is observed that, in general, the remaining porosity of the material is located in the

ferrite regions (α). The elemental distribution of titanium observed by SEM suggests that its diffusion begins at the surface of the Fe(α) particles, initially stabilizing the Fe(α) phase, up to a saturation point that produces a concentration gradient high enough for particle nucleation. Furthermore, the laminar topology of the intermetallic compound η-Fe$_2$Ti confirms its precipitation by diffusion inside the ferrite. For these samples, it can be concluded that, although the observed phases coincide with the predicted ones, the observed amounts differ from the theoretical ones, *i.e.*, a higher percentage of the Laves phase η-Fe$_2$Ti and a lower percentage of Fe(α) in comparison with the calculated values (Table **IV**). The Laves phase (η) is the name given to intermetallic compounds with a hexagonal-type unitary cell, whose shape depends on the composition of the alloy, which can vary between Fe$_2$Mo and Fe$_2$Ti.

The contrast of the microstructures observed in the three alloys explains the results regarding their performance. The increase in hardness and the decrease in the wear coefficient due to the presence of titanium when compared to the first sample is attributed to the precipitation of TiC carbides that are deposited inside the grains. These carbides are present as secondary phases, and their formation takes advantage of carbon in a solid solution. As for the corrosion rate, alloy 1(316) shows the presence of chromium carbides (Cr$_{23}$C$_6$), which cause the sensitization of austenitic stainless steels, generating a high rate of corrosion, since, as per its stoichiometry, it is a Chromium-rich compound that precipitates at the grain boundaries of austenite. In case of alloy 2(316+0,4Ti), the stabilization of the steel was achieved, avoiding the phenomenon of sensitization. Therefore, this alloy exhibits the lowest corrosion rates. In the 3(316+1Ti) alloy, the presence of ferrite and the intermetallic compound Laves η-Fe$_2$Ti was observed, with the formation of a passive layer, which is expected for this type of steel. It was observed that, if the titanium content is higher than that required for stabilization, it generates a detriment in the corrosion rate ([24], [25]).

4.   Conclusions

Titanium additions in AISI 316 powder metallurgical stainless steel decrease the porosity and increase the density of the preforms, and therefore of the sintered samples. This proves the importance of combining particles of different sizes to obtain less porous components and higher densification in manufacturing processes through conventional powder metallurgy.

The direct relationship between the wear depth generated with the pin-on-disk test and the wear coefficient was confirmed. By determining the mechanical properties of the alloys studied, it was observed that the hardness of a powder metallurgical steel made from AISI 316 significantly increases when titanium is incorporated due to the precipitation of titanium compounds, *i.e.*, Ti(C,N).

The performance reported in the potentiodynamic polarization tests, complemented with a microstructural analysis, showed that the addition of 0,4 wt %Ti to AISI 316 powder metallurgical steel decreases its corrosion rate by preventing the precipitation of intermetallic compounds and Cr$_{23}$C$_6$ chromium carbides. In this case, titanium performs its function in the stabilization of the steel, avoiding sensitization. With larger additions of the alloying element, an adverse effect was observed, due to the precipitation of the Laves η-Fe$_2$Ti phase.

Changes in the composition of systems as complex as stainless steels, which are made by increasing the proportion of their alloying elements, do not guarantee improved properties in terms of corrosion resistance, since a series of phenomena come into play which involve atomic diffusion processes, thermodynamic energy favorable for the formation of certain compounds, and concentration gradients when the modified elements do not dissolve within the ferrous matrix. Added to the above, the morphology of steels obtained through manufacturing processes using conventional powder metallurgical methods makes it impossible to eliminate porosity in the final product.

The modification of the initial composition of AISI 316 austenitic stainless steel allows concluding that the addition of 0,4 wt % of elemental titanium improves its mechanical properties, reduces the rate of electrochemical corrosion of the alloy, promoting the precipitation of titanium carbides, and achieves stabilization. The potentiodynamic plots of this composition show that the steel changed directly to the passivation zone without going through the dissolution zone.

5.   Acknowledgements

6.   CRediT author statement

Luz Adriana Cañas: Conceptualization, investigation, methodology, formal analysis, visualization, writing: original draft.
Yaneth Pineda Triana: Formal analysis, funding acquisition, project administration, resources, supervision, visualization, writing: review and editing.
Lais Mujica Roncery: Formal analysis, visualization, writing: review and editing.

References

[1] M. Groover, *Fundamentos de manufactura moderna: materiales, procesos y sistemas*, 3rd ed., New York, NY, USA: McGraw-Hill, 2007. ↑2

[2] A. Szewczyk-Nykiel, "The influence of molybdenum on corrosion resistance of sintered austenitic stainless steels," *Tech. Trans.*, vol. 2015, pp. 131-142, 2015. https://doi.org/10.4467/2353737XCT.15.344.4865 ↑3

[3] M. Rosso, "Contribution to study and development of PM stainless steels with improved properties," *J. Achievements Mater. Manuf. Eng.*, vol. 24, no. 1, p. 178, 2017. https:

//www.researchgate.net/publication/40804796_Contribution_to_study_and_
development_of_PM_stainless_steels_with_improved_properties ↑3

[4] S. Schmid and S. Kalpakjian, *Manufactura, ingeniería y tecnología*, 5 ed., México: Pearson-Prentice Hall, 2008. ↑3

[5] N. Kurgan, Effect of porosity and density on the mechanical and microstructural properties of sintered 316L stainless steel implant materials," *Mater. Design*, vol. 55, p. 235-241, 2014. https://doi.org/10.1016/j.matdes.2013.09.058 ↑3

[6] J. J. Ibáñez Montenegro, "Estudio de la soldadura en aceros austeníticos," undergraduate thesis, Fac. Ingeniería, Univ. Piura, Carabobo, Venezuela, 2005. ↑3

[7] J. P. Vázquez, "Estudio de la precipitación de carburos en el acero inoxidable AISI 304 en enfriamiento continuo," Master's thesis, Fac. Ing. Mec. Elec., Univ. Autónoma de Nuevo León, Nuevo León, México, 1996. ↑4

[8] S. Ali *et al.*, "Synthesis, surface nitriding and characterization of Ti-Nb modified 316L stainless steel alloy using powder metallurgy," *Mater.*, vol. 14, no. 12, art. 3270, 2021. https://doi.org/10.3390/ma14123270 ↑4

[9] E. Klar and P. K. Samal, *Powder metallurgy stainless steels: Processing, microstructure, and properties*, Novelty, OH, USA: ASM International, 2007. ↑4

[10] Moral *et al.*, "Aqueous Corrosion Behaviour of Sintered Stainless Steels Manufactured from Mixes of Gas Atomized and Water Atomized Powders,". *Corr. Sci.*, vol. 51, no. 8. p. 1653, 2009. https://doi.org/10.1016/j.corsci.2009.04.017 ↑4

[11] *Standard Practice for Characterization of Particles*, ASTM F1877, ASTM International, 2016. https://doi.org/10.1520/F1877-16 ↑5

[12] *Standard test method for apparent density powders using Arnold meter*, ASTM B703, ASTM International, 1994. https://doi.org/10.1520/b0703-94r99e01 ↑5

[13] *Standard test methods for density of compacted or sintered powder metallurgy (PM) products using Archimedes' principle*, ASTM B962-15, ASTM International, 2015. https://doi.org/10.1520/b0962-15 ↑5

[14] G. S. Upadhyaya, *Powder metallurgy technology*, 1st ed., Cambridge, UK: Cambridge International Science Publishing, 2002. ↑5

[15] S. Ali *et al.*, "Investigation of alloy composition and sintering parameters on the corrosion resistance and microhardness of 316L stainless steel alloy," in *Advances in Manufacturing II: Lecture Notes in Mechanical Engineering*, B. Gapiński, M. Szostak, and V. Ivanov, Eds., Cham, Germany: Springer, 2019, pp. 532-541. https://doi.org/10.1007/978-3-030-16943-5_45 ↑5

[16] A.-M. Bandar, "Powder metallurgy of stainless steel: State of the art, challenges and development," in *Stainless Steel*, A. Pramanik and A. K. Basak, Eds., Jubail, Saudi Arabia: Nova Science Publishers, 2015, pp. 37-80. ↑5

[17] T. DebRoy *et al.*, "Additive manufacturing of metallic components – Process, structure and properties," *Prog. Mater. Sci.*, vol. 92, pp. 112-224, Mar. 2018. https://doi.org/10.1016/j.pmatsci.2017.10.001 ↑5

[18] *Standard test method for Knoop and Vickers hardness of materials*, ASTM E 384-11, ASTM International, 2011. https://doi.org/10.1520/e0384-10e02 ↑6

[19] *Standard test method for wear testing with a pin-on-disk apparatus*, ASTM G99-17, ASTM International, 2017. https://doi.org/10.1520/g0099-05 ↑6

[20] *Standard practice for conventions applicable to electrochemical measurements in corrosion testing*, ASTM G3-89, ASTM International, 2010. https://doi.org/10.1520/g0003 ↑6

[21] *Standard reference test method for making potentiostatic and potentiodynamic anodic polarization measurements*, ASTM G5-94, ASTM International, 2011. https://doi.org/10.1520/g0005-14e01 ↑6

[22] *Standard test method for conducting potentiodynamic polarization resistance measurements*, ASTM G59-97, ASTM International, 2020. https://doi.org/10.1520/g0059-97r14 ↑6

[23] *Standard practice for calculation of corrosion rates and related information from electrochemical measurements*, ASTM G102-89, ASTM International, 2015. https://doi.org/10.1520/g0102-89r15e01 ↑6

[24] A. F. Padilha et al., "Stainless steel heat treatment," in *Encyclopedia of Iron, Steel, and Their Alloys (Online Version)*, Taylor & Francis Group, 1st Edition, 2016, pp. 1–28. ↑12

[25] X. Q. Chen, W. Wolf, R. Podloucky, and P. Rogl, "Ab initio study of ground-state properties of the Laves phase compounds TiCr2, ZrCr2, and HfCr2," *Phys. Rev. B Condens. Matter Mater. Phys.*, vol. 71, art. 174101, 2005. https://doi.org/10.1103/PhysRevB.71.174101 ↑12

Luz Adriana Cañas Mendoza

Metallurgical engineer, Universidad Industrial de Santander (UIS), Bucaramanga, Colombia; Master of Metallurgical Engineering, Universidad Industrial de Santander (UIS), Bucaramanga, Colombia; PhD in Materials Science and Engineering, Universidad Pedagógica y Tecnológica de Colombia (UPTC), Tunja, Colombia. She is a researcher of the following research groups: Materiales Avanzados (Addvanced Materials, GIMAV), Integridad y Evaluación de Materiales (Materials Integrity and Evaluation, GIEM), and Materiales de Ingeniería (Engineering Materials, GIMI). She is a professor at Universidad Tecnológica de Pereira (UTP), Pereira, Colombia, since 2007, as well as a tutor for the Semillero de Investigación en Ingeniería y Manufactura de Materiales (Materials Engineering and Manufacturing Research Seedbed, SIIMA-UTP).
Email: luzadriana@utp.edu.co

Yaneth Pineda Triana

Metallurgical engineer, Universidad Pedagógica y Tecnológica de Colombia (UPTC), Tunja, Colombia; PhD in Mechanical and Materials Engineering, Universidad Politécnica de Valencia – Internacional; senior researcher recognized by MinCiencias (Colombian Ministry of Science, Technology, and Innovation). She is a professor at Universidad Pedagógica y Tecnológica de Colombia (UPTC), Tunja, Colombia, since 1994. Researcher and coordinator of the failure analysis area at Instituto para la Investigación y la Innovación en Ciencia y Tecnología de Materiales (Institute for Research and Innovation in Materials Science and Technology, INCITEMA); coordinator of the Master's Program in

Metallurgy and Materials Science of Universidad Pedagógica y Tecnológica de Colombia (UPTC), Tunja, Colombia; coordinator of the Doctoral Program in Materials Science and Engineering of Universidad Pedagógica y Tecnológica de Colombia (UPTC), Tunja, Colombia.
Email: yaneth.pineda@uptc.edu.co

Lais Mujica Roncery

Chemical engineer, Universidad Nacional de Colombia (UNAL), Bogotá, Colombia; Master of Chemical Engineering, Universidad Industrial de Santander (UIS), Bucaramanga, Colombia; PhD in Engineering, Ruhr- Universität Bochum, Bochum, Germany; senior researcher recognized by MinCiencias (Colombian Ministry of Science, Technology, and Innovation). She is a professor at Universidad Pedagógica y Tecnológica de Colombia (UPTC), Tunja, Colombia, since 2017. Director of Grupo de Investigación en Materiales Siderúrgicos (Siderurgic Materials Research Group) at UPTC, Tunja, Colombia (2017-2022); director of Instituto para la Investigación y la Innovación en Ciencia y Tecnología de Materiales (Institute for Research and Innovation in Materials Science and Technology, INCITEMA), Tunja, Colombia, since 2023.
Email: lais.mujica@uptc.edu.co

Research

Soft Skills Requirements for the Engineering Sector: The Case of the Mechanical Engineering Industry

Requerimientos de habilidades blandas en el sector de ingeniería: el caso de la industria de ingeniería mecánica

Yenny Carolina Jaimes-Acero[1] ID, Gonzalo Moreno-Contreras[2] ID y Rafael Bolívar-León[2] ID ✉ *

[1] Instructora del SENA (San José de Cúcuta, Colombia)
[2] Universidad de Pamplona, (Pamplona, Colombia)

Abstract

Context: There is currently a high demand of professionals with highly developed soft skills, but there is no clarity about which ones. The purpose of this article is to determine which soft skills are required at different organizational levels in the mechanical engineering sector.

Method: A survey was designed and applied to 81 mechanical engineers graduated from Universidad de Pamplona. The instrument evaluated the level of development of 10 soft skills in the undergraduate program, in addition to the level required for an entry-level job as well as for a technical and an executive position. The statistical tools employed were the bilateral Kolmogorov-Smirnov test, the median, the mode, a Kruskal-Wallis ANOVA, and a Games-Howell *post hoc* test.

Results: The training level regarding soft skills was found to be acceptable (Me=3), specifically for creativity, negotiation, and nonverbal communication skills, while those related to presenting before audiences, critical thinking, recognition, responsibility, integrity, and humility show greater development (good, Me=4). On the other hand, report writing, emotional competencies, and critical thinking are the most important skills (Me=5) for an entry-level job. To ascend to technical positions, those related to presenting before different audiences, the recognition of team members, and leadership are required. For managerial positions, nonverbal language, negotiation, supervision, and entrepreneurship skills are also required (Me=5).

Conclusions: Written communication, emotional competencies, and critical thinking should be bolstered in order to provide alumni with higher competitiveness. As for technical and managerial positions, a higher development of the ten analyzed soft skills is needed. Undergraduate and graduate programs should include these new business requirements in their curricula in order to increase the competitiveness of their alumni.

Keywords: soft skills, soft skills requirements in businesses, soft skills in engineering

*✉ **Correspondence:** rbolivarl@unipamplona.edu.co

Resumen

Contexto: Actualmente, existe una gran demanda de profesionales con habilidades blandas altamente desarrolladas, pero no hay claridad sobre cuáles son. El propósito de este artículo es determinar cuáles son las habilidades blandas que se requieren en diferentes niveles organizacionales en el sector de la ingeniería mecánica.

Método: Se diseñó y aplicó una encuesta a 81 ingenieros mecánicos egresados de la Universidad de Pamplona. El instrumento evaluó el nivel de desarrollo de 10 habilidades blandas en el pregrado, así como el nivel requerido para un primer empleo y para un cargo técnico y uno gerencial. Las herramientas estadísticas utilizadas fueron la prueba bilateral de Kolmogórov-Smirnov, la mediana, la moda, el ANOVA de Kruskall-Wallis, y la prueba *post hoc* de Games-Howell.

Resultados: Se encontró que el nivel de formación de habilidades blandas es aceptable (Me=3), específicamente para las habilidades de creatividad, negociación y comunicación no verbal, mientras que las de exponer frente a diferentes audiencias, pensamiento crítico, reconocimiento, responsabilidad, integridad y humildad demuestran un mayor desarrollo (bueno, Me=4). Por otro lado, la escritura de informes, la competencia emocional y el pensamiento crítico son las habilidades más importantes (Me=5) para el primer empleo. Para asenso a posiciones técnicas, se requiere además habilidades relacionadas con exponer ante diferentes audiencias, el reconocimiento de los miembros del equipo de trabajo y liderazgo. Para cargos gerenciales, se requiere también la integridad, el lenguaje no verbal, la negociación, la supervisión y el emprendimiento (Me=5).

Conclusiones: Debe potenciarse la comunicación escrita, la competencia emocional y el pensamiento crítico para dar mayor competitividad al recién egresado. En relación con los cargos técnicos y gerenciales, se necesita un mayor desarrollo de todas las 10 habilidades blandas investigadas. Los programas de pregrado y postgrado deben incluir estos nuevos requerimientos empresariales en sus currículos para incrementar la competitividad de sus egresados.

Palabras clave: habilidades blandas, requerimientos empresariales de habilidades blandas, habilidades blandas en ingeniería

Tabla de contenidos

1. Introducción

Actualmente, las habilidades blandas son destrezas que elevan la competitividad de los profesionales y se constituyen como una necesidad apremiante para el sostenimiento de las empresas y su expansión en el mercado. LinkedIn (1) realizó un estudio con 5.000 profesionales de alto desempeño en 35 países sobre las destrezas más importantes de un profesional, enmarcando tres fundamentales: la flexibilidad en el trabajo (91 %), el anti-acoso (72 %) y la transparencia en el pago (53 %) –se observa que la de mayor impacto fue una habilidad blanda. Por otro lado, el Foro Económico Mundial (2) definió la necesidad de un fuerte desarrollo en las habilidades blandas de comunicación, pensamiento crítico y resiliencia para afrontar los retos del futuro. Así mismo, la CEPAL (3) determinó que América Latina es la región donde existe una mayor brecha entre las habilidades requeridas por el sector empresarial y las ofrecidas por la fuerza laboral, aconsejando una formación de habilidades técnicas y blandas en los jóvenes que permita mayor adaptación al cambio, mejor inserción y mayor movilidad laboral. Adicionalmente, existen investigaciones a nivel internacional (4–6) y Latinoamérica (7, 8) que alertan sobre el requerimiento de estas habilidades en los diferentes sectores industriales, comerciales y de servicios, además de dar cuenta de que la formación universitaria generalmente no incluye estas habilidades. En relación con la ingeniería mecánica a nivel mundial, se observa la misma reflexión (9–11). Por otro lado, la Asociación Colombiana de Facultades de Ingeniería (ACOFI) y la Universidad del Norte (12) establecieron que las habilidades blandas son necesarias para el desarrollo profesional en el sector laboral, y aconsejan su inclusión en los pensum de ingeniería (13), en aras de facilitar el diseño, el mejoramiento y la optimización de los sistemas que el profesional interviene.

Actualmente, estas habilidades tienen gran demanda en las organizaciones para potenciar la eficiencia y productividad, y se requieren para asegurar, mantener y escalar de nivel dentro de una organización (4,11,14–16). Sin embargo, la mayor parte de la formación en ingeniería en las instituciones de educación superior se enfoca en aspectos técnicos y deja de lado dichas habilidades. Algunos estudios han identificado esta necesidad (17) y proponen que se incluya, en el currículo de estos programas, una formación a partir de entrenamientos y que aplique metodologías de aprendizaje no habituales, con la finalidad de alinear la formación de los ingenieros con la demanda actual de las empresas (18,19). A pesar de la gran demanda de ingenieros con competencias en habilidades blandas, existe un desconocimiento sobre cuáles y qué nivel de su desarrollo son necesarios según el cargo desempeñado en diferentes organizaciones, y, más aún, qué significan y cuáles son las acciones concretas que las determinan. Este artículo es un aporte para esclarecer dichas dudas, y le será útil a los gerentes, especialmente de las empresas pequeñas y medianas; a los ingenieros que se desempeñan en cualquier nivel organizacional; a los programas de ingeniería y sus docentes, que empiezan a ser conscientes de dicha necesidad de formación; y a la construcción continua del conocimiento en esta área específica del saber.

2. Estado del arte

En el siglo XXI, las necesidades de formación de un ingeniero se han especializado, y se requieren otras habilidades que antes solo eran necesarias a nivel gerencial. La necesidad de brindar soluciones

integradas en contextos diferentes le exige al ingeniero demostrar competencia en habilidades duras –las habitualmente requeridas por su área técnica, junto con un alto conocimiento en calidad, desarrollo de procesos, diseño y dirección de sistemas complejos de ingeniería, entre otras– pero también en habilidades blandas (18). Estas últimas son necesarias para poder entender la organización y sus contextos; adaptarse a los cambios rápida y eficientemente; liderar o trabajar con equipos multidisciplinarios; negociar o comunicarse efectivamente con clientes internos, externos y proveedores; y tomar decisiones asertivas, entre otras acciones (18). Las empresas de ingeniería consideran el desarrollo de las habilidades blandas como un factor decisivo en la contratación de sus empleados, donde los más competitivos son los que demuestran un alto desarrollo en ellas (17). Esto se debe a factores como cambios emergentes en todo nivel; la globalización (18); las nuevas tendencias de cultura organizacional basadas en personas, innovación y felicidad; las nuevas formas de *marketing* digital; el trabajo remoto o híbrido que se ha impulsado a partir del COVID-19; y la revolución industrial 4.0 (20). Por otro lado, en relación con el análisis de la competitividad de los programas de ingeniería, las habilidades blandas deben analizarse desde diferentes puntos de vista: los estudiantes buscan experiencias educativas gratificantes en un tiempo corto y desarrollar las competencias requeridas a nivel laboral, permitiéndoles asegurar trabajos de buena calidad (18); las empresas buscan contratar egresados que demuestren competencia, *i.e.*, profesionales experimentados y hábiles y que cuenten con destrezas adicionales (17, 18); las universidades están buscando atraer estudiantes, ser financieramente exitosas y sobresalir como producto de su calidad; y la sociedad espera que sus ingenieros diseñen y desarrollen los mejores sistemas, garantizando su seguridad (18) y la sostenibilidad del medio ambiente. Es precisamente allí donde las habilidades blandas toman su importancia como el centro de unión entre los requerimientos de los diferentes actores.

2.1. Habilidades blandas

El término *habilidades blandas* no está completamente definido, tanto así que estas también son referidas como habilidades sociales, emocionales, socioemocionales y no-cognitivas y como competencias genéricas, transversales o de empleabilidad, y se relacionan con actitudes, atributos, rasgos y prácticas de comportamiento personal. Dichas habilidades permiten la creación y el desarrollo de relaciones positivas, la resolución positiva de conflictos y alcanzar las metas comunes de un equipo, e influyen en cómo una persona enfoca su aprendizaje e interactúa con su ambiente de trabajo.

En 2010, la Universidad Goldsmiths de Londres propuso un inventario de 15 habilidades blandas (6) que han sido usadas también como base en diferentes estudios relacionados con la ingeniería (4, 21–23). Fred Kofman (24, 25) propuso que, para que una empresa logre una alta productividad de manera sostenible (26, 27), debe centrarse en la generación de valor en sus empleados. Esto se logra a través del desarrollo de siete actitudes. Con estas dos referencias como eje central, y tomando otras a partir del análisis bibliográfico, se seleccionaron 10 habilidades blandas, que se definen a continuación y se decantan en acciones específicas para su evaluación (Tabla I).

Responsabilidad: La habilidad de responder. La capacidad de dar respuesta efectiva a una situación que afecte la obtención de un resultado especifico, tomando consciencia y asumiendo cómo se ha contribuido a dicha situación y cómo se puede ayudar a solucionarla. Las personas que han

desarrollado esta habilidad se identifican por el alto nivel de cumplimiento de sus compromisos, independientemente de factores externos, y por la capacidad de ser conscientes y asumir las consecuencias de sus actos. Habitualmente se esfuerzan por dar la milla de más, y retrasan la gratificación inmediata a favor de objetivos a largo plazo (8, 26–28).

Integridad: Esta habilidad está asociada con las acciones orientadas por valores esenciales, y se plasma habitualmente en normas y principios socialmente aceptados. Las personas íntegras priman el bien colectivo sobre los intereses personales y son correctos en sus actuaciones según sus referentes, y proponen que no solo el resultado o el éxito es lo importante, sino que además las acciones que lo logran deben estar fundamentadas en valores esenciales (8, 10, 26, 29).

Humildad: Una gran limitante del avance de una organización es que sus trabajadores crean que lo saben todo y se cierren al aprendizaje continuo. Esta habilidad se centra en la disposición de adquirir nuevos conocimientos, habilidades y destrezas para utilizarlos en el trabajo –e incluso en diferentes dominios de la vida. También está relacionada con la aceptación de la crítica y el reconocer públicamente cuando se está equivocado (8, 10, 26–29).

Pensamiento crítico: La capacidad para comprender, evaluar, deducir información y proponer conclusiones. Esta permite resolver problemas, tomar decisiones apropiadas, hacer suposiciones, probar la legitimidad de algo y ver situaciones desde diferentes puntos de vista. Esta habilidad es central para la toma de decisiones acertadas con el foco en un objetivo y basadas en la evidencia. Permite planificar y organizar eficazmente un equipo de trabajo y reducir el reproceso, ahorrando dinero y tiempo (10, 14, 17, 29).

Comunicación: La capacidad de comunicarse con una amplia variedad de personas y de forma verbal, escrita y corporal. Par ello, es necesario exhibir un vocabulario amplio que permita adaptarse a los diferentes niveles de su contraparte, escribir de manera clara y leer corporalmente las emociones y la predisposición a cierto tipo de conversaciones. Esto se puede evidenciar en la escritura de reportes, presentaciones orales, *blogs* y publicaciones en redes sociales, así como en reuniones con compañeros en un entorno técnico o comercial. Esta habilidad ayuda a definir metodologías para afrontar conversaciones difíciles de manera eficiente (10, 14, 15, 17, 29–31).

Negociación: Esta habilidad redefine el concepto de *conflicto* en términos de un proceso de aprendizaje y crecimiento mutuo; determina las bases de un conflicto y lo clasifica como individual, relacional u operacional; y propone metodologías efectivas para la negociación en los diferentes tipos de conflicto que ocurren comúnmente en el trabajo en equipo.

Coordinación de acciones: Muchos de los reprocesos y problemas en los equipos radican en la falta de especificidad para hacer un compromiso, para realizar su seguimiento y, en caso requerido, expresar un reclamo o una disculpa. Esta habilidad es muy importante para mantener la motivación y el empoderamiento, incrementar la valía personal y realizar un reconocimiento de personas o equipos. En resumen, la coordinación de acciones se define en términos de la efectividad para realizar compromisos

y seguimientos y para expresar reclamos, disculpas y reconocimientos. Esta habilidad es clave para desempeñarse de manera competente y adecuada en la interacción con otros, en aras de lograr metas en común. Se puede evidenciar su desarrollo en la ejecución efectiva de proyectos de cualquier índole. Esta habilidad también permite identificar claramente los objetivos de un equipo de trabajo y orientar acciones para conseguirlos (8, 10, 15, 17, 29, 30).

Competencia emocional: La habilidad para identificar y gestionar los sentimientos personales y las reacciones inconscientes ante problemas y desafíos. Este concepto realza la importancia del desarrollo emocional y, a partir de las emociones propias o de otros, permite analizar situaciones. Su desarrollo conlleva el progreso en el desempeño laboral y una mejor predisposición hacia el trabajo. Lograr un estado de maestría emocional es indispensable en el camino del crecimiento empresarial (17).

Liderazgo: Este concepto se refiriere a una persona que tiene seguidores debido a su capacidad de visualizar y concretar resultados. El líder otorga a sus subordinados la autoridad y el apoyo para tomar decisiones, utiliza y personaliza adecuadamente el reconocimiento y los incentivos, da ejemplo, se muestra consistente y mantiene altos estándares de integridad y conducta ética –incluso en situaciones difíciles–, aprende de la experiencia, incrementa su intuición a partir de los errores y analiza tanto los éxitos como los fracasos en busca de oportunidades para mejorar (10, 14, 15, 29, 30).

Emprendimiento: Se define como un sistema individual o colectivo enfocado en el desarrollo de algo nuevo, que puede ir desde la concepción de ideas hasta la creación de empresas. La capacidad emprendedora tiene cuatro componentes: la capacidad de innovar y ser creativo, la capacidad de identificar y explotar nuevas oportunidades de negocio, la capacidad y voluntad de asumir riesgos y la capacidad de crear y desarrollar redes empresariales. Esta habilidad permite generar estrategias ideales para expandir la productividad y el desarrollo general de cualquier organización (10, 29, 32).

La Tabla **I** resume algunos criterios que indican el desarrollo de habilidades blandas en miembros de un equipo de trabajo.

3. Metodología

Las preguntas planteadas en esta investigación fueron las siguientes: ¿Cuáles son las habilidades blandas requeridas por las empresas de ingeniería mecánica en los diferentes niveles organizacionales? ¿Cuál es la brecha entre las habilidades blandas requeridas y las formadas durante el pregrado?

Para ello se realizó un investigación cuantitativa, usando una encuesta para recopilar información de los participantes (38), la cual se diseñó teniendo en cuenta tres dimensiones.

La primera, llamada Demográfica & Empresa, consistió en determinar la demografía de la población encuestada y las características de la empresa en la que trabajaba. Esta dimensión contenía 11 preguntas que hicieron las veces de indicadores.

Tabla I. Criterios para medir habilidades blandas

Categorías	Criterios para medir habilidades blandas (indicadores)	Referencia
Responsabilidad	Asume la responsabilidad de resolver situaciones (por causa propia o de otros) que dificultan el logro de los objetivos	(8, 26, 28)
Integridad	Toma decisiones profesionales basadas en la integridad y la ética	(8, 10, 26, 29)
Humildad	Admite que no sabe o que puede estar equivocado, especialmente en situaciones de incertidumbre o confrontación	(26)
Pensamiento crítico	Toma decisiones basadas en hechos, datos e información confiables	
Comunicación	C1. Maneja con eficacia conversaciones difíciles o conflictivas; C2. Usa e identifica el lenguaje no verbal (postura corporal, brazos, piernas, contacto visual, etc.) durante una conversación; C3. Expone efectivamente un tema a una audiencia de cualquier nivel de conocimiento (i.e., uso de medios de enseñanza y excelente desempeño); C4. Escribe claramente informes de gestión y/o informes técnicos	(10, 15, 17) (26, 29, 30) (33–35)
Negociación	Lleva a cabo negociaciones efectivas en situaciones con diferentes intereses y puntos de vista	(26, 36)
Coordinación de acciones	A1. Adquiere compromisos adecuados con su equipo de trabajo (*i.e.*, el cumplimiento es alto y el reproceso bajo); A2. Supervisa el desarrollo de las tareas sin generar rechazo en los empleados; A3. Reclama efectivamente en caso de incumplimiento de los compromisos adquiridos; A4. Reconoce los logros de las personas dentro de un equipo	(26, 37)
Competencia emocional	Resuelve situaciones con calma y manteniendo el equilibrio emocional	
Liderazgo	Lidera efectivamente equipos pequeños (de máximo 8 personas) en el cumplimiento de metas específicas	
Emprendimiento	B1. Analiza el nivel de riesgo de las posibles soluciones a un problema; B2. Analiza ideas de negocios considerando metodologías de soporte técnico, de marketing, logísticas, legales, de estructura organizacional y de capital humano; B3. Resuelve creativamente problemas de diferentes tipos	(1, 8, 11) (15, 29, 35) (36)

Nota: Las letras al inicio corresponden a la codificación utilizada para establecer los indicadores.

Las preguntas de la segunda y tercera dimensión, que medían la formación en pregrado y los requerimientos de la empresa en habilidades blandas, se diseñaron a partir de los criterios definidos en la Tabla I.

La segunda dimensión, *Formación en Pregrado*, determinó el nivel de desarrollo de estas habilidades en la formación del pregrado mediante 10 indicadores y una escala Likert de 5 puntos, con los siguientes niveles formación: 1) muy deficiente, 2) deficiente, 3) aceptable, 4) bueno y 5) excelente.

La tercera dimensión, llamada *Requerimientos de la Empresa*, determina la importancia de las habilidades definidas para tres niveles organizacionales: el primer empleo del ingeniero, cargos técnico-administrativos y cargos gerenciales. Esta dimensión utilizó 18 indicadores para cada nivel organizacional, para un total de 54 indicadores y una escala de Likert con los siguientes niveles: 1) sin importancia, 2) de poca importancia, 3) moderadamente importante, 4) importante y 5) muy importante.

La validez de la encuesta fue positiva según la evaluación de tres expertos, *i.e.*, una doctora en estadística, una magister en educación certificada en diferentes orientaciones de *coaching* y un magister en administración. La confiabilidad del instrumento se determinó mediante el Coeficiente Alfa de Cronbach, que obtuvo una consistencia interna excelente, con un valor de $\alpha = 0,95$. En el estudio participaron 81 ingenieros egresados de la carrera de Ingeniería Mecánica del total de 210 que existían al momento de la aplicación de la encuesta, para un error calculado de 8 % y una confiabilidad del 95 %.

Mediante una prueba bilateral de Kolmogorov-Smirnov, donde se obtuvo valor $p < 0,05$ para todos los indicadores, se determinó que los datos son no normales y no paramétricos. Esto implica que su análisis debe realizarse desde la mediana y la moda, y los estadísticos utilizados deben aplicar para este tipo de datos (39). Por ello, el análisis estadístico utilizó herramientas no paramétricas como la mediana, la moda, el rango, un análisis de varianza (ANOVA) Kruskall-Wallis, y la prueba *post hoc* de Games-Howell.

4. Resultados

A continuación, muestran los resultados de la dimensión demográfica (Tabla II). En la Fig. 1 se muestra la impresión sobre el nivel de formación de las habilidades blandas en pregrado (rojo) y los requerimientos de dichas habilidades para cada nivel de jerarquía organizacional investigado, *i.e.*, primer empleo (azul), cargo técnico (naranja) y cargo gerencial (verde). Los resultados se muestran en términos de mediana y moda en lugar de media y desviación estándar, debido a que los datos son no normales y no paramétricos según prueba bilateral de Kolmogorov-Smirnov.

Un análisis general de los resultados mostrados a la izquierda de la Fig. 1 evidencia la necesidad inmediata de que los egresados cuenten con un desarrollo importante (Me=4) en prácticamente todas las habilidades blandas investigadas –incluso, este desarrollo debe ser muy importante (Me=5) en algunas de sus habilidades. Además, los resultados que se muestran en las Figs. 1 y 2 describen un aumento en la importancia de dichas habilidades para poder acceder a niveles jerárquicos más altos. Es importante resaltar que, para un nivel gerencial, aunque solo 13 de los 18 indicadores requieren un desarrollo muy importante (Me=5), la tendencia evidenciada en la moda es que prácticamente todos son muy importantes. A continuación, se muestran los resultados obtenidos para cada uno de los niveles jerárquicos investigados.

(a)

(b)
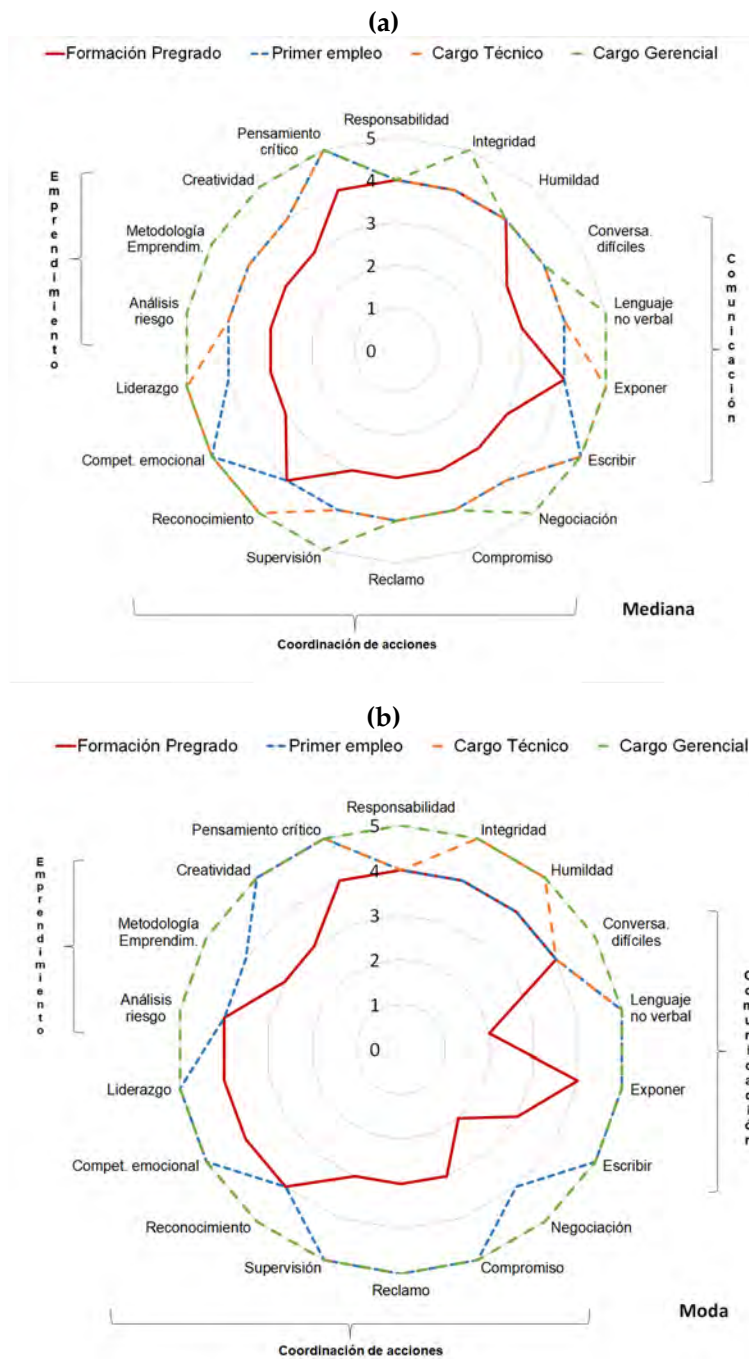
Formación: 2) deficiente, 3) aceptable, 4) buena. Niveles organizacionales: 4) importante, 5) muy importante.

Figura 1. Desarrollo de habilidades blandas en la formación de pregrado y nivel requerido por la empresa (**a.** mediana; **b.** moda o tendencia)

Tabla II. Resultados de la dimensión Demografía & Empresa

Categorías	Grupos				
Edad (años)	Hasta 29	30 a 39		Mayor a 40	
	28,40 %	69,20 %		2,50 %	
Género	Masculino			Femenino	
	92,60 %			7,40 %	
Nivel	No aplica	Junior		Senior	
	23,5 %	43,20 %		33,30 %	
Rango	Gerente	Ingeniero área proceso	Consultor	Docente	Otro
	9,90 %	55,60 %	3,70 %	14,80 %	16,00 %
Función	Gerenciales	Administrativa/operacional		Técnicas	Otras
	9,90 %	43,20 %		30,90 %	16,00 %
Número de personas a cargo	1 a 8	9 a 24	25 a 39	Mas de 40	
	45,70 %	30,90 %	13,60 %	9,90 %	
Tipo empresa	Publica	Privada		Mixta	
	16 %	80,20 %		3,70 %	
Cobertura	Regional	Nacional		Internacional	
	27,20 %	40,70 %		32,10 %	
Tamaño empresa No. trabajadores	Micro ($\leq$10)	Pequeña (11 a 50)	Mediana (51-199)	Grande ($\geq$ 200)	
	3,70 %	16 %	17,30 %	63 %	
Actividad económica	Minería Energía	Industria manufactura	Transporte	Educación	Otros
	34,60 %	17,30 %	17,30 %	14,80 %	16,00 %
Cultura organizacional	Orientada a resultados	Orientada a innovación	Orientada a personas	Orientada a normas	
	40,70 %	8,60 %	13,70 %	37 %	

Nota lateral: Demografía (filas Edad–Función); Características de la empresa (filas Número de personas a cargo–Cultura organizacional).

4.1.   Ingeniero recién graduado

Como se observa en las Figs. **1** y **2**, las tres habilidades que son muy importantes (Me=5) para el primer empleo son comunicación (específicamente escribir informes técnicos), competencia emocional y pensamiento crítico. La moda de 10 indicadores corresponde al valor "muy importante" (Mo=5). De esto se infiere que, además de las tres habilidades mencionadas, las de comunicación (específicamente lenguaje no verbal y exponer frente a diferentes audiencias), la coordinación de acciones (específicamente compromiso, reclamo y supervisión), el liderazgo y el emprendimiento (específicamente la creatividad) son importantes para incrementar la competitividad del recién graduado en su entrada a la vida profesional.

Para determinar si existía variación para este nivel jerárquico en cada uno de los grupos definidos en la dimensión demográfica (Tabla **II**) en relación con las habilidades blandas investigadas, se realizó un análisis no paramétrico de Kruskall-Wallis (ANOVA), donde los valores con un nivel de significancia $p < 0,05$ definían la existencia de dicha variación. Se encontró que, entre los 11 grupos demográficos posibles, solo el tamaño de la empresa mostraba una diferencia estadística en relación con el requerimiento de habilidades blandas, es decir, dependiendo del tamaño de la empresa, se necesitan diferentes niveles de desarrollo. Para comprender con mayor profundidad este comportamiento, se aplicó una prueba bilateral *post hoc* de Games-Howell, cuyo resultado se muestra a la izquierda de la Fig. **3**.
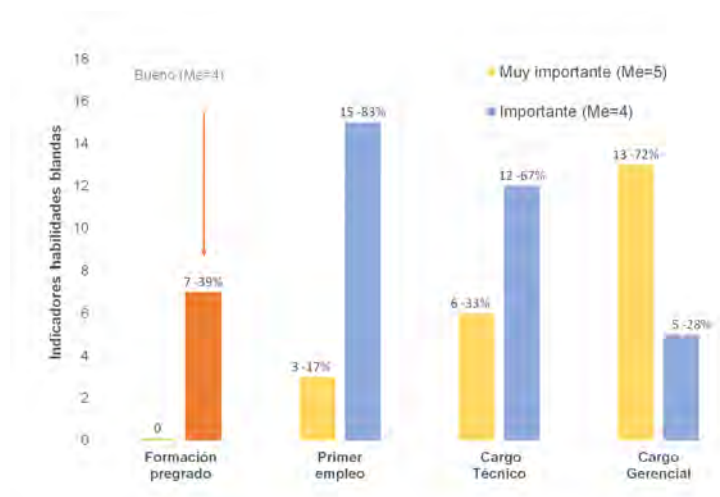
Figura 2. Comparación de habilidades formadas y requeridas para cada nivel jerárquico

Este análisis estadístico demuestra que, para que un recién egresado tenga la posibilidad de trabajar para empresas de ingeniería de tamaños micro ($\leq$ 10 empleados) y pequeño (entre 11 y 50), requiere un desarrollo muy importante (Me>4,5) en las habilidades de comunicación (específicamente en escritura de informes y exponer frente a diferentes audiencias) y coordinación de acciones (específicamente en reclamos), pero no así en la de negociación (Me=3,3). A su vez, si el egresado desea trabajar en empresas medianas (entre 51 y 199 empleados) los niveles de desarrollo de las habilidades descritas anteriormente son inversos, pero, para este tamaño de empresa, la habilidad de negociación aumenta en importancia (Me=3,3 y 3,7). Finalmente, si su opción es trabajar en una empresa grande ($\leq$ 200 empleados), las cuatro habilidades deben tener un nivel de desarrollo importante (3,9<Me<4,3).

4.2.   Cargos técnicos

Para un cargo de ingeniería en una posición técnica (Figs. **1** y **2**), *i.e.*, ingeniero de proyectos, de área o de procesos, se requiere un nivel muy importante (Me=5) en seis habilidades blandas, incluyendo las tres definidas para el primer empleo y adicionando las de comunicación (exponer frente a diferentes audiencias), coordinación de acciones (reconocimiento) y liderazgo. Otras diez habilidades que tienden a requerir un desarrollo muy importante (Mo=5) son la integridad, la humildad, la coordinación de acciones (negociación) y el emprendimiento (análisis de nivel de riesgo y aplicación de metodologías de emprendimiento). Al ocupar un cargo técnico, los requerimientos de habilidades blandas exigen al ingeniero una mayor efectividad en las presentaciones a audiencias de diferentes niveles jerárquicos (superiores, pares y personal técnico a cargo). Además, estos profesionales empiezan a hacerse cargo de equipos de trabajo más grandes y complejos, y deben tener habilidades para liderarlos, reconocer sus resultados públicamente tanto a nivel individual como grupal, coordinar acciones generando compromisos sostenibles, realizar supervisión sin predisponer al personal, y, en caso de incumplimiento, realizar reclamos efectivos que no minen las relaciones interpersonales. Esto se evidencia en el valor "muy importante" de la moda (Mo=5) para dichas habilidades. Además de liderar personal, los ingenieros en este cargo empiezan a involucrarse en el mejoramiento de la producción
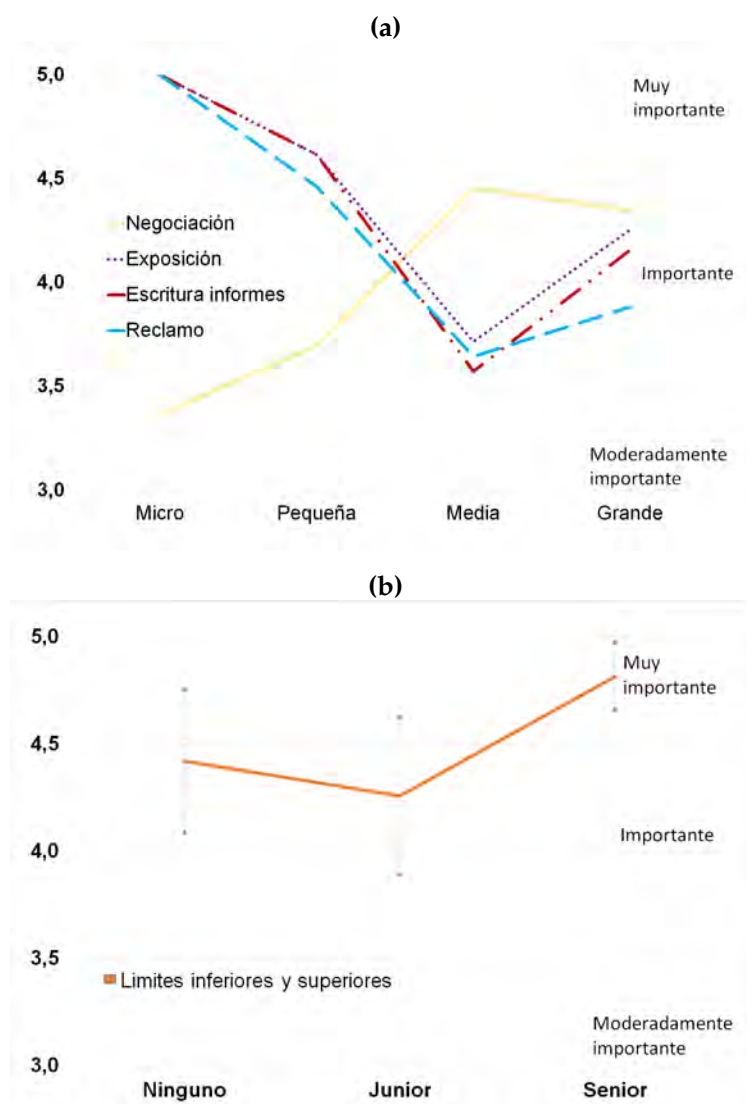
(a)

(b)

Figura 3. *Post hoc* de Games-Howell de algunas habilidades blandas (**a.** en relación con el tamaño de la empresa para el primer empleo; **b.** escribir informes técnicos en relación con cargos técnicos)

de la empresa o el diseño de nuevos productos y servicios, y es allí donde aparece la habilidad de emprendimiento, específicamente en relación con el análisis de riesgo para toma de decisiones y el conocimiento de metodologías asociadas con aspectos técnicos, organizacionales, de *marketing*, logísticos, entre otros que permiten mejorar o crear productos o servicios en una empresa.

Al realizar un análisis de Kruskall-Wallis (ANOVA), entre todos los indicadores demográficos y de habilidades blandas, únicamente el nivel de ingeniero (ninguno, *junior* o *senior*), mostró una diferencia estadística ($p<0,05$) en la habilidad de comunicación, específicamente en la escritura de informes. Se realizó la prueba *post hoc* de Games-Howell, encontrando lo que se muestra a la derecha de la Fig. 3:

no existe diferencia estadística en los requerimientos de escritura de informes para un ingeniero no catalogado o *junior*, pero sí entre estos dos y un ingeniero *senior*, aunque dicha diferencia es pequeña.

4.3. Cargos gerenciales

Como se observa en las Figs. **1** y **2**, las siete habilidades blandas que deben desarrollarse completamente para ascender a cargos gerenciales –además de las seis que requiere el cargo técnico– son la integridad, la comunicación (específicamente el lenguaje no verbal), la coordinación de acciones (específicamente la negociación y la supervisión) y el emprendimiento con todos sus indicadores (40). Las funciones principales de este cargo, *i.e.*, mantener y expandir la compañía, giran en torno a las habilidades de comunicación y se apoyan en la integridad, las cuales, aunque se requieren también en niveles jerárquicos inferiores, para este cargo son indispensables. Con respecto a la comunicación, los dos indicadores que no requerían un alto desarrollo en el cargo previo eran las conversaciones difíciles y el lenguaje no verbal, y, aunque este último tiene una tendencia a ser muy importante desde el primer empleo, solo hasta el cargo gerencial aparece con un alto requerimiento, lo cual es entendible, pues, a este nivel organizacional, el lenguaje corporal permite leer la predisposición emocional de la contraparte para las conversaciones y expresarse de manera asertiva con el cuerpo. Así mismo, la habilidad de negociación incrementa su exigencia, pues se convierte en una herramienta fundamental para que el gerente cierre acuerdos satisfactorios con proveedores, clientes, líderes de trabajadores y, en algunos casos, competidores. La satisfacción de todas las partes una vez se cierra una negociación es un indicativo del futuro de la relación entre ellas. Con respecto a la supervisión, aunque también tiende a ser muy importante desde el primer empleo, para este caso se requiere que su desarrollo esté completo; a este nivel jerárquico, las no conformidades o los resentimientos personales por supervisiones mal dirigidas permean prácticamente toda la organización, incrementando los reprocesos con sus costos asociados y generando un clima organizacional tenso. Finalmente, en relación con la creatividad, este nivel jerárquico es el que direcciona y financia la innovación en la compañía en el ámbito de la mejora o la creación de productos o servicios, por lo cual se exige el máximo desarrollo en esta habilidad.

El análisis de Kruskall-Wallis (ANOVA) mostró que, de todos los indicadores demográficos, únicamente el tipo de cultura organizacional (orientada a resultados, normas, personas o innovación) tenía diferencia estadística ($p < 0.05$) con la habilidad de comunicación, específicamente en la escritura de informes. Según la prueba *post hoc* de Games-Howell (Fig. **4**), en organizaciones con culturas orientadas tanto a normas como a resultados, la exigencia en la escritura de informes es importante (Me=4,2 y 3,9), mientras que, en aquellas con una orientación hacia las personas, esta habilidad es más valiosa (muy importante, Me=4,7). En organizaciones orientadas a la innovación, existe una gran dispersión de los resultados, y no puede definirse una tendencia estadísticamente.

4.4. Formación de habilidades blandas en pregrado

Los encuestados egresados del programa de Ingeniería Mecánica de la Universidad de Pamplona evaluaron el desarrollo de sus habilidades blandas en la formación de pregrado como "aceptable" (Me=3). En la Fig. **1** se puede apreciar la variación entre el nivel de formación en el pregrado y los requerimientos en cada nivel organizacional. Se evidencia que las habilidades como la responsabilidad,
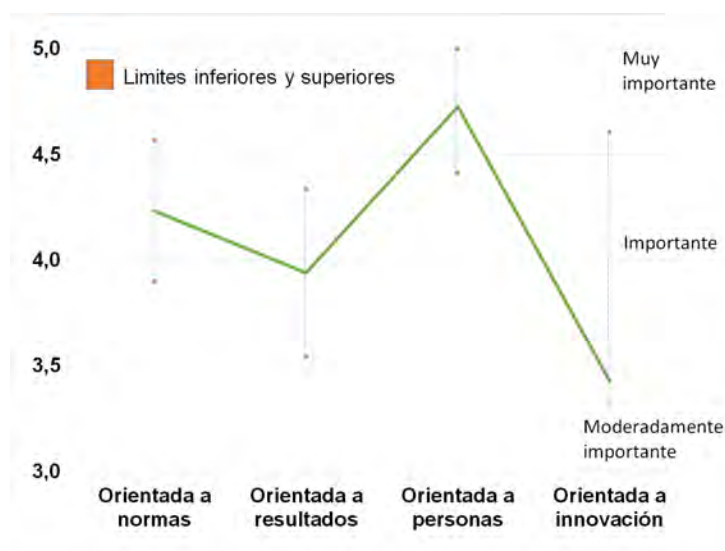
Figura 4. *Post hoc* de Games-Howell para la escritura de informes técnicos en relación con la cultura organizacional en cargos gerenciales

la integridad, la humildad, la comunicación (específicamente exponer frente a diferentes audiencias), la coordinación de acciones (específicamente el reconocimiento y el pensamiento crítico) son las más desarrolladas (con un buen nivel de formación, Me=4), mientras que otras habilidades como la comunicación, la negociación en coordinación de acciones, la competencia emocional, el liderazgo y el emprendimiento muestran un nivel de formación aceptable (Me=3).

Como puede apreciarse (Fig. 1), la habilidad de comunicación comprende cuatro habilidades específicas, pero solo el indicador de exponer frente a diferentes audiencias se valoró con un buen nivel (Me=4), mientras que las otras tres son aceptables (Me=3). Incluso el indicador de lenguaje no verbal y la negociación tienden a estar (moda) a un nivel de formación deficiente (Mo=2). Estos resultados demuestran que, en la formación de pregrado, solo cinco indicadores de los 18 medidos (28 % de lo requerido), están al nivel que requiere un recién egresado. Esta diferencia aumenta al ascender de nivel jerárquico en la empresa, donde, para un cargo técnico, solo se forman tres habilidades (17 % de lo requerido) y para el gerencial solo dos (11 % de lo requerido) al nivel que se exige (Fig. 2). Estos resultados brindan evidencia concreta sobre la brecha entre las habilidades blandas requeridas por las empresas y las formadas durante el pregrado, lo cual ha sido mencionado por diferentes autores.

5. Discusión

El objetivo de este trabajo fue determinar cuáles son las habilidades blandas que requiere un ingeniero mecánico en empresas de ingeniería en diferentes niveles organizacionales, así como cuál es la brecha entre este requerimiento y su formación en el pregrado.

En relación con la primera pregunta de investigación (*¿Cuáles son las habilidades blandas requeridas por las empresas de ingeniería mecánica en los diferentes niveles organizacionales?*), los resultados muestran claramente los requerimientos, las tendencias y la variación para los niveles organizacionales. Al igual que lo encontrado por otros autores, se evidenció empíricamente una preponderancia (Me=5) de tres habilidades: comunicación (10, 17–19, 41–44), pensamiento crítico y competencia emocional (41). Sin embargo, otros investigadores también han encontrado la creatividad (10, 17, 43), el liderazgo (41, 43–45), la productividad, el autoaprendizaje (41) y la interacción multidisciplinaria en equipos de trabajo (10, 18, 41, 44). Los indicadores homólogos de estas habilidades en este trabajo (autoaprendizaje ≅ humildad, interacción multidisciplinaria e interacción con equipos de trabajo ≅ coordinación de acciones) no eran muy importantes para el primer empleo, pero sí constituyen necesidades para el ascenso en la jerarquía organizacional. Esta investigación también encontró que, de 18 indicadores para las diez habilidades blandas analizadas, quince de ellos son importantes (Me=4) para el primer empleo. Para ascender a un cargo técnico, además de las requeridas para el primer empleo, se suman las habilidades de comunicación (exponer frente a diferentes audiencias), las de coordinación de acciones (reconocimiento de equipos de trabajo) y las de liderazgo. Para un cargo gerencial, las diez habilidades blandas y sus 18 indicadores tienden requerir un desarrollo completo (Mo=5). Algunos autores han determinado que las habilidades más importantes en cargos directivos en áreas de ingeniería son aquellas relacionadas con la organización de equipos, la gestión de proyectos, la gestión de compromisos y la resolución de problemas (41, 46), coincidiendo con lo encontrado en esta investigación en relación con las habilidades de coordinación de acciones, liderazgo, comunicación y negociación. Sin embargo, como se evidencia empíricamente este trabajo, para este nivel organizacional es necesario el desarrollo de prácticamente todas las habilidades blandas.

La relevancia de la habilidad comunicativa en los tres niveles jerárquicos, demostrada en este estudio y por otros investigadores (10, 17–19, 41–44), hace necesario priorizar su desarrollo. Esta habilidad es esencial en los profesionales recién graduados y en todos los niveles organizacionales; es necesaria para el desarrollo de la personalidad, en ambientes de cooperación y coordinación necesarios en proyectos de ingeniería, para interactuar efectivamente con equipos de trabajo, personas de diferente nivel jerárquico, clientes y proveedores (18) y para intercambiar diferentes puntos de vista. Un desarrollo inadecuado da la impresión que el profesional no ha sido entrenado apropiadamente y que sus conocimientos son pobres en el área técnica (19), lo cual disminuye su competitividad. Por otro lado, la industria 4.0 requiere de profesionales que tengan esta habilidad fuertemente desarrollada (44, 47), además de otras como la facilidad de comunicación en otros idiomas, el trabajo en equipo y el liderazgo (44).

Respecto a la pregunta *¿Cuál es la brecha entre las habilidades blandas requeridas y las formadas durante el pregrado?*, se encontró que la formación de dichas habilidades, aunque es aceptable según los encuestados, no cumple con el nivel exigido para el primer empleo; solo el 28 % de los indicadores está al nivel exigido, guardando coherencia con la brecha entre la formación universitaria y lo requerido en la industria que se sugiere en prácticamente toda la bibliografía consultada. Incluso algunos autores han señalado de manera puntual las carencias en liderazgo, emprendimiento, habilidades personales (4, 35), comunicación, profesionalismo y responsabilidad (4, 48) de los profesionales recién graduados, lo

cual coincide con lo encontrado en esta investigación. Si se analizan los requerimientos para un nivel superior en la organización, como el de una posición técnica en ingeniería, la brecha se torna más grande, pues aparecen nuevas exigencias en el desarrollo de habilidades (*i.e.*, exponer frente a diferentes audiencias, el reconocimiento, y el liderazgo). Adicionalmente, en posiciones gerenciales, se exigen precisamente aquellas habilidades que muestran un menor desarrollo en el pregrado.

El nivel de desarrollo de habilidades blandas en los programas universitarios puede variar según la institución, el programa específico y el desarrollo económico del país. En general, este nivel de desarrollo depende de las prioridades y los recursos de la institución. En instituciones educativas que no se han desarrollado adecuadamente y apuntan a mejorar la competitividad de sus egresados, es indispensable que se entrene a los docentes en este tipo de habilidades (35, 49), en aras de integrarlas a sus estrategias pedagógicas o desarrollar otras (50). Además, en sus *pensum*, los programas deben incluir materias específicas orientadas al desarrollo de estas habilidades, utilizando diferentes metodologías de enseñanza (51) como la experiencial-vivencial (52). Esto aseguraría una mayor competitividad en los recién egresados, así como una curva de aprendizaje mucho menor para el ascenso dentro de una organización, con la posibilidad de acceder a puestos gerenciales en menor tiempo.

Finalmente, como aportes de esta investigación, puede listarse lo siguiente, primero, estos resultados empíricos sirven de brújula para que los ingenieros de cualquier nivel y los estudiantes de programas de ingeniería puedan determinar las habilidades que deben desarrollar según su proyección profesional y, a partir de ello, realizar entrenamientos que lleven a su crecimiento.

Segundo, para los programas de ingeniería que estén preguntándose qué otros elementos deben contener una formación de profesionales que responda a las nuevas tendencias globales y cuál es el camino para mejorar su competitividad, se abre una posibilidad concreta de crecimiento en el desarrollo de las habilidades blandas definidas en esta investigación, lo cual implica, a su vez, el desarrollo de dichas habilidades en sus docentes. Esta formación puede darse a partir de reformas curriculares, de cambios en los contenidos programáticos o incluso a través de actividades extracurriculares, tales como cursos de formación específicos, participación en proyectos de capítulos de organizaciones internacionales, participación en eventos de semilleros de investigación o actividades interdisciplinarias cuyo enfoque implique el desarrollo de alguna de las habilidades mencionadas. El cómo incluir esta formación en los programas dependerá del nivel que ellos definan desarrollar y los recursos que destinen. Una decisión orientada a incrementar estas habilidades en los niveles descritos en este artículo les brindará a futuros egresados mayores opciones en el mundo laboral, mayor facilidad y menor tiempo de aprendizaje de dichas habilidades y, por ende, la posibilidad de ascensos más rápidos dentro de las organizaciones.

Tercero, una de las principales limitantes para comprender la necesidad de habilidades blandas para la formación en el área de ingeniería es que existe un alto desconocimiento sobre su conceptualización, que debería incluir tanto las acciones con que ellas se definen como las maneras de medir su desarrollo. Este trabajo propone y conceptualiza diez habilidades blandas, algunas de ellas con subdivisiones, y define acciones concretas que pueden ser utilizadas para diseñar diferentes instrumentos de

medición, como la encuesta aplicada en esta investigación, ayudando a llenar el mencionado vacío de conocimiento.

Cuarto, a partir de los análisis realizados, se puede afirmar que, si bien existe una tendencia general en algunas de las habilidades blandas especificadas, se evidencia que algunas situaciones asociadas a la demografía implican variaciones en el nivel de desarrollo requerido. Se definió que el nivel de desarrollo de algunos indicadores de las habilidades de comunicación y coordinación de acciones depende del tamaño de la empresa, la cultura organizacional y el nivel jerárquico.

Quinto, a pesar de que diferentes autores mencionan una brecha entre lo requerido por las industrias y lo impartido por la academia, esta no está claramente definida. Nuestra investigación define específicamente las habilidades blandas que conforman esta brecha, encontrando que, solo comparado con el primer empleo, existe una brecha del 72 % en las habilidades blandas requeridas. A medida que se escala en la jerarquía organizacional, esta brecha incrementa.

6. Conclusiones

Se logró identificar las habilidades blandas necesarias para tres niveles jerárquicos organizacionales en el área de la Ingeniería Mecánica: para un primer empleo, escribir informes técnicos, competencia emocional y pensamiento crítico; para un cargo técnico, las habilidades anteriores más las de integridad, humildad, negociación y emprendimiento; y, para un cargo gerencial, prácticamente todas las habilidades investigadas.

Se encontró que hay una variación en la exigencia del desarrollo de algunas habilidades dependiendo del tamaño y cultura de la organización. Respecto al tamaño, se encontró que, en el caso de los recién graduados, para las micro- y pequeñas empresas se requiere un mayor desarrollo en la escritura de informes, en la habilidad de exponer frente a diferentes audiencias y en la expresión de reclamos. Entretanto, para las empresas medianas, la habilidad de negociación adquiere mayor importancia y, para grandes empresas, estas cuatro habilidades requieren un nivel de desarrollo alto. En relación con la cultura organizacional, se encontró que, para los cargos técnicos, en las empresas orientadas a normas o a resultados, la habilidad de escribir informes técnicos es más demandante que para las organizaciones orientadas a personas.

La brecha entre las habilidades blandas desarrolladas en el pregrado y las requeridas para un primer empleo es bastante grande; solo el 28 % de las habilidades muestran el desarrollo requerido. En este sentido, los programas deben enfocarse en mejorar el nivel de dichas habilidades y, dependiendo de la competitividad que deseen conferirles a sus egresados, pueden desarrollar en primera instancia las habilidades comunicativas, de competencia emocional y de pensamiento crítico. En segunda instancia, pueden incluir la habilidad de exponer frente a diferentes audiencias, el reconocimiento, y el liderazgo. Cabe añadir que, en tercera instancia, deben desarrollarse todas las habilidades analizadas en este estudio.

Los programas de pregrado y postgrado deben formar a sus docentes en estas habilidades para que puedan incorporarlas en sus diferentes estrategias de enseñanza, además de incluir espacios de enseñanza específicos en sus *pensum* que utilicen metodologías de enseñanza-aprendizaje experiencial-vivencial.

Como limitaciones de este estudio, hay que añadir que los ingenieros encuestados son egresados de un mismo programa de formación, así como el hecho de que el programa donde se realizó estudio es relativamente nuevo (no han pasado más 15 años desde su primer egresado), por lo que existen pocos profesionales en cargos gerenciales de alto nivel y de desarrollo a nivel de doctorado. A pesar de estas dos limitaciones, la investigación brinda aportes válidos para el programa en cuestión, los cuales pueden extenderse a otros programas considerando el respaldo de la bibliografía analizada.

Como trabajos futuros, se propone profundizar en los requerimientos específicos de habilidades blandas en los diferentes sectores industriales, empresariales y profesionales, así como comparar su nivel de desarrollo en diferentes niveles de formación universitaria. Adicionalmente, en programas académicos que implementen este tipo de formación, deben diseñarse y aplicarse instrumentos para medir su impacto en los aspectos académicos e integrales de los estudiantes, así como, a largo plazo, valorar el incremento en la competitividad de los egresados.

7. Agradecimientos

8. Contribución de autores

Todos los autores contribuyeron de igual forma en la investigación.

Referencias

[1] Linkedln, "Global talent trends 2019," 2019. [Online]. Available: https://business.linkedin.com/content/dam/me/business/en-us/talent-solutions/resources/pdfs/global_talent_trends_2019_emea.pdf ↑3, 7

[2] H. H. F. Fore and R. E. Moritz, "Reimaginar el futuro de las habilidades: ¿qué piensan los jóvenes?," *Foro Económico Mundial*, 2020. [Online]. Available: https://es.weforum.org/agenda/2020/07/reimaginar-el-futuro-de-las-habilidades-que-piensan-los-jovenes/ ↑3

[3] N. U. CEPAL, "Perspectivas económicas de América Latina 2017: juventud, competencias y emprendimiento," *CEPAL*, 2016, [Online]. Available: http://hdl.handle.net/11362/40721 ↑3

[4] O. I. Akinbobola, "Predicting innovative work behavior from soft skills and emotional demands – Abilities fit in knowledge economy," *Manag. Econ. Res. J.*, vol. 6, no. 3, pp. 1-8, Jul. 2020. https://doi.org/10.18639/MERJ.2020.9900013 ↑3, 4, 15

[5] J. A. Botke, P. G. W. Jansen, S. N. Khapova, and M. Tims, "Work factors influencing the transfer stages of soft skills training: A literature review," *Educ. Res. Rev.*, vol. 24, pp. 130-147, 2018. https://doi.org./10.1016/j.edurev.2018.04.001 ↑3

[6] T. Chamorro-Premuzic, A. Arteche, A. J. Bremner, C. Greven, and A. Furnham, "Soft skills in higher education: Importance and improvement ratings as a function of individual differences and academic performance," *Educ. Psychol.*, vol. 30, no. 2, pp. 221-241, Mar. 2010. https://doi.org/10.1080/01443410903560278 ↑3, 4

[7] C. I. Astudillo Yañez and F. I. Meléndez Seguel, "Análisis de las habilidades blandas de un técnico en mantenimiento aeronáutico," undergraduate thesis, Univ. Técnica Federico St. Maria, Valparaíso, Chile, 2014. [Online]. Available: https://repositorio.usm.cl/handle/11673/49068 ↑3

[8] G. Chigó Bustos and M. Olguín Ramírez, "Competencias y habilidades blandas claves para ingenieros comerciales de la Universidad de Chile," undergraduate thesis, Univ. Chile, Santiago, Chile, 2006, [Online]. Available: http://repositorio.uchile.cl/handle/2250/108389 ↑3, 5, 6, 7

[9] K. Cohen and R. Katz, "Teaching mechanical design practice in academia," *Procedia CIRP*, vol. 36, pp. 177-181, 2015. https://doi.org/10.1016/j.procir.2015.01.043 ↑3

[10] W. O. A. S. W. Ismail, N. Hamzah, I. Y. A. Fatah, and A. Zaharim, "Professional skills requirement of mechanical engineers," *IOP Conf. Series: Mat. Sci. Eng.*, vol. 697, no. 1, art. 12016, 2019. https://doi.org/10.1088/1757-899X/697/1/012016 ↑3, 5, 6, 7, 15

[11] W. O. A. S. W. Ismail, N. Hamzah, I. Y. A. Fatah, and A. K. Muhammad, "The essential of engineering education involving critical thinking and problems solving skills among mechanical engineer employees," *IOP Conf. Series: Mat. Sci. Eng.*, vol. 697, no. 1, art. 12017, 2019. https://doi.org/10.1088/1757-899X/697/1/012017 ↑3, 7

[12] Acofi and U. del Norte, "Buenas prácticas de assessment en programas de ingeniería," 2020. [Online]. Available: https://www.acofi.edu.co/wp-content/uploads/2020/06/BUENAS-PRACTICAS-ACOFI-2020.pdf ↑3

[13] Acofi, "Lineamientos curriculares para Ingeniería Industrial en Colombia," 2020. [Online]. Available: https://www.acofi.edu.co/wp-content/uploads/2020/11/Lineamientos-Curriculares-para-Ingenieria-Industrial-en-Colombia_ed2.pdf ↑3

[14] S. Tem, A. Kuroda, and K. N. Tang, "The importance of soft skills development to enhance entrepreneurial capacity," *Int. Educ. Res.*, vol. 3, no. 3, p. 1, Jul. 2020. https://doi.org/10.30560/ier.v3n3p1 ↑3, 5, 6

[15] M. Itani and I. Srour, "Engineering students' perceptions of soft skills, industry expectations, and career aspirations," *J. Prof. Issues Eng. Educ. Pract.*, vol. 142, no. 1, art. 4015005, 2016. https://doi.org/10.1061/(ASCE)EI.1943-5541.0000247 ↑3, 5, 6, 7

[16] J. C. Neri Torres and C. A. Hernández Herrera, "Los jóvenes universitarios de ingeniería y su percepción sobre las competencias blandas," *RIDE. Rev. Iberoam. para la Investig. y el Desarro. Educ.*, vol. 9, no. 18, pp. 768-791, 2019. https://doi.org/10.23913/ride.v9i18.445 ↑3

[17] K. N. Tang, "Beyond employability: Embedding soft skills in higher education," *Turkish Online J. Educ. Technol. - TOJET*, vol. 18, no. 2, pp. 1-9, 2019. [Online]. Available: https://files.eric.ed.gov/fulltext/EJ1211098.pdf ↑3, 4, 5, 6, 7, 15

[18] F. Munir, "More than technical experts: Engineering professionals' perspectives on the role of soft skills in their practice," *Ind. High. Educ.*, vol. 36, no. 3, pp. 294-305, Jun. 2022. https://doi.org/10.1177/09504222211034725 ↑3, 4, 15

[19] I. Kakepoto, A. Laghari, and G. S. Buriro, "Engineering communication skills for novice engineers: A pilot project," *Glob. Educ. Stud. Rev.*, vol. VII, no. I, pp. 12-19, Mar. 2022. https://doi.org/10.31703/gesr.2022(VII-I).02 ↑3, 15

[20] D. Jelonek, T. Nitkiewicz, and P. Koomsap, "Soft skills of engineers in view of industry 4.0 challenges," in *Conf. Quality Prod. Improv.*, vol. 2, no. 1, pp. 107-116, 2020. https://doi.org/10.2478/cqpi-2020-0013 ↑4

[21] W. Teng, C. Ma, S. Pahlevansharif, and J. J. Turner, "Graduate readiness for the employment market of the 4th industrial revolution: The development of soft employability skills," *Educ. Train.*, vol. 61, no. 5, pp. 590-604, 2019. https://doi.org/10.1108/ET-07-2018-0154 ↑4

[22] B. P. Belsches, W. Farmer, C. Jacobs, P. Krebs, S. Swygard, and E. Wilcox, "Workforce development : Soft skills training initiatives in the city of Charlottesville," *PLAN 5420: Local Economic Development*, 2016. [Online]. Available: http://www.culturecurrent.com/peter/docs/Charlottesvile%20Soft%20Skills%20FINAL.pdf ↑4

[23] G. C. A. Gang, S. I. Hashmi, and C. B. Seok, "Perceiving the importance of job-related skills in the 4th industrial revolution era from the perspectives of graduates and employers," *Int. J. Adv. Sci. Technol.*, vol. 29, no. 11s, pp. 702-713, 2020. [Online]. Available: http://sersc.org/journals/index.php/IJAST/article/view/20039/10183 ↑4

[24] A. Bowring, "Reappraisal and the victim-player framework: A dynamic duo for executive coaches," in *Forbes*, Oct. 2020. [Online]. Available: https://www.forbes.com/sites/forbescoachescouncil/2020/10/28/reappraisal-and-the-victim-player-framework-a-dynamic-duo-for-executive-\coaches/?sh=2207375b635d ↑4

[25] Alisa Cohn, "Leading the leadership revolution at LinkedIn," in *Forbes*, Nov. 2017. [Online]. Available: https://www.forbes.com/sites/alisacohn/2017/11/02/leading-the-leadership-revolution-at-linkedin/?sh=5d68dad51b9c ↑4

[26] F. Kofman, *La empresa consciente: Cómo construir valor a través de valores*. Buenos Aires, Argentina: Penguin Random House Grupo Editorial Argentina, 2018. ↑4, 5, 7

[27] F. Kofman, *Metamanagement 3 Tomos*. La Calera, Chile: GS, 2003. ↑4, 5

[28] O. Marrero Sánchez, R. Mohamed Amar, and J. Xifra Triadú, "Habilidades blandas: necesarias para la formación integral del estudiante universitario," *Rev. Científica Ecociencia*, vol. 5, pp. 1-18, Dec. 2018. https://doi.org/10.21855/ecociencia.50.144 ↑5, 7

[29] I. Zergout, S. Ajana, C. Adam, and S. Bakkali, "Modelling approach of an innovation process in engineering education: The case of mechanical engineering," *Int. J. High. Educ.*, vol. 9, no. 2, p. 25, Dec. 2019. https://doi.org/10.5430/ijhe.v9n2p25 ↑5, 6, 7

[30] S. Shekhawat, "Enhancing employability skills of engineering graduates," in *Enhancing Future Skills and Entrepreneurship. Sustainable Production, Life Cycle Engineering and Management*, K. Sangwan and C. Herrmann, eds., Cham, Germany: Springer, 2020, pp. 263-269. https://doi.org/10.1007/978-3-030-44248-4_26 ↑5, 6, 7

[31] S. Prasad, M. Ehrensberger, M. P. Gibson, H. Kim, and E. A. Monaco, "Biomaterial properties of titanium in dentistry," *J. Oral Biosci.*, vol. 57, no. 4, pp. 192-199, Nov. 2015. https://doi.org/10.1016/j.job.2015.08.001 ↑5

[32] M. J. Sousa and M. do R. Almeida, "Entrepreneurial skills development," in Recent Advances in *Applied Economics*, 2014. [Online]. Available: http://www.wseas.us/e-library/conferences/2014/Lisbon/AEBD/AEBD-18.pdf ↑6

[33] L. J. Pujol and G. E. Dabos, "Artículo de revisión satisfacción laboral: una revisión de la literatura acerca de sus principales determinantes," *Estud. Gerenciales*, vol. 34, pp. 3-18, 2018. https://doi.org/10.18046/j.estger.2018.146.2809 ↑7

[34] R. Selwyn and I. Renaud-Assemat, "Developing technical report writing skills in first and second year engineering students: A case study using self-reflection," *High. Educ. Pedagog.,* vol. 5, no. 1, pp. 19-29, Jan. 2020. https://doi.org/10.1080/23752696.2019.1710550 ↑7

[35] R. Singh Dubey, J. Paul, and V. Tewari, "The soft skills gap: A bottleneck in the talent supply in emerging economies," *Int. J. Hum. Resour. Manag.*, vol. 33, no. 13, pp. 2630-2661, Jan. 2021. https://doi.org/10.1080/09585192.2020.1871399 ↑7, 15, 16

[36] D. Chenoy, S. M. Ghosh, and S. K. Shukla, "Skill development for accelerating the manufacturing sector: the role of 'new-age' skills for 'Make in India,'" *Int. J. Train. Res.*, vol. 17, no. sup1, pp. 112–130, Jul. 2019. https://doi.org/10.1080/14480220.2019.1639294 ↑7

[37] F. Kofman, *Metamanagement-Tomo 3 (Filosofía): La nueva consciencia de los negocios*. Buenos Aires, Argentina: Grito Sagrado, 2008. ↑7

[38] J. Check and R. K. Schutt, "Teacher research and action research," in *Research Methods in Education*, Washington DC, USA: Sage Research Methods, 2012, ch. 12, pp. 255-272. https://doi.org/10.4135/9781544307725.n12 ↑6

[39] A. Diego Gutiérrez, "Test de bondad de ajuste multivariante," undergraduate thesis, Univ. Cantabria, 2018. [Online]. Available: https://repositorio.unican.es/xmlui/bitstream/handle/10902/15639/Diego+Gutierrez+Andrea.pdf;jsessionid=EF80639DED9A116498220C33B46BF958?sequence=1 ↑8

[40] Y. C. Jaimes-Acero, A. Granados-Comba, and R. Bolívar-León, "Soft skills requirements for engineering entrepreneurship," *Rev. Fac. Ing.*, vol. 31, no. 59, art. e14167, 2022. https://doi.org/10.19053/01211129.v31.n59.2022.14167 ↑13

[41] M. Á. Gómez, R. F. Herrera, E. Atencio, and F. C. Munoz-La Rivera, "Key management skills for integral civil engineering education," *Int. J. Eng. Pedagog.*, vol. 11, no. 1, p. 64, Jan. 2021. https://doi.org/10.3991/ijep.v11i1.15259 ↑15

[42] H. Chaibate, A. Hadek, S. Ajana, S. Bakkali, and K. Faraj, "A comparative study of the engineering soft skills required by Moroccan job market," *Int. J. High. Educ.*, vol. 9, no. 1, p. 142, Dec. 2019. `https://doi.org/10.5430/ijhe.v9n1p142` ↑15

[43] S. Ahadi and S. Kasraie, "Contextual factors of entrepreneurship intention in manufacturing SMEs: the case study of Iran," *J. Small Bus. Enterp. Dev.*, vol. 27, no. 4, pp. 633-657, 2020. `https://doi.org/10.1108/JSBED-02-2019-0074` ↑15

[44] M. Bucur and A. Ban, "The importance of the concept of communication among future engineers-a pre-test for a European study," *Procedia Manuf.*, vol. 32, pp. 348-355, 2019. `https://doi.org/10.1016/j.promfg.2019.02.224` ↑15

[45] J. Daley and B. Baruah, "Leadership skills development among engineering students in Higher Education – An analysis of the Russell Group universities in the UK," Eur. *J. Eng. Educ.*, vol. 46, no. 4, 528-556, Oct. 2020. `https://doi.org/10.1080/03043797.2020.1832049` ↑15

[46] S. Fletcher and K. R. V. Thornton, "The top 10 soft skills in business today compared to 2012," *Bus. Prof. Commun. Q.*, vol. 2023, art. 232949062211484, Jan. 2023. `https://doi.org/10.1177/23294906221148453` ↑15

[47] J. Trevelyan, "Transitioning to engineering practice," *Eur. J. Eng. Educ.*, vol. 44, no. 6, pp. 821-837, Nov. 2019. `https://doi.org/10.1080/03043797.2019.1681631` ↑15

[48] K. Tsirkas, A.-P. Chytiri, and N. Bouranta, "The gap in soft skills perceptions: A dyadic analysis," *Educ. + Train.*, vol. 62, no. 4, pp. 357-377, Apr. 2020. `https://doi.org/10.1108/ET-03-2019-0060` ↑15

[49] I. S. Rampasso, O. L. G. Quelhas, R. Anholon, M. B. Pereira, J. D. A. Miranda, and W. S. Alvarenga, "Engineering Education for Sustainable Development: Evaluation Criteria for Brazilian Context," *Sustainability*, vol. 12, no. 10, art. 3947, May 2020. `https://doi.org/10.3390/su12103947` ↑16

[50] H. Valdés, C. Correa, and F. Mellado, "Proposed model of sustainable construction skills for engineers in Chile," *Sustainability*, vol. 10, no. 9, art. 3093, Aug. 2018. `https://doi.org/10.3390/su10093093` ↑16

[51] P. Ponce, L. Ibarra, O. Mata, and A. Molina, "How to develop research skills among undergraduate engineering students to tackle current ongoing topics? A Smart-Grid case study," *Int. J. Electr. Eng. Educ.*, vol. 58, no. 2, pp. 113-141, Apr. 2021. `https://doi.org/10.1177/0020720918816004` ↑16

[52] Y. C. Acero, R. Suárez Castrillón, and A. M. Bolívar León, "Aspects that develop soft skills – A way for inclusion in engineering programmes," *World Trans. Eng. Technol. Educ.*, vol. 20, no. 1, pp. 13-18, 2022. [Online]. Available: `http://www.wiete.com.au/journals/WTE&TE/Pages/Vol.20,No.1(2022)/02-Bolivar-Leon-R.pdf` ↑16

Yenny Carolina Jaimes-Acero

Nació en Pamplona, Norte de Santander, Colombia. Obtuvo sus títulos como administradora comercial y de sistemas, de especialista en Alta Gerencia y de magister en Ciencias Económicas y Empresariales en la Universidad de Pamplona, y su título de especialización tecnológica en Diagnóstico y Consultoría Empresarial en el SENA. Tutora del SENA desde 2006. Sus áreas de interés son: competitividad, habilidades blandas, *marketing*, cultura organizacional.

Email: ycjaimes@misena.edu.co

Gonzalo Moreno-Contreras

Nació en Ragonvalia (Norte de Santander), Colombia. Obtuvo su título como ingeniero mecánico en la Universidad Francisco de Paula Santander, de Magister en Ingeniería Mecánica en la Universidad de los Andes, y de Doctor en Ingeniería Mecánica en la Universidad Federal de Santa Catarina. Profesor de la Universidad de Pamplona desde 2005. Pertenece al grupo de investigación de ingeniería mecánica GIMUP y es docente del programa de maestría en Ingeniería de la Universidad Santo Tomas en Tunja. Sus áreas de interés son: estática y dinámica de sistemas mecánicos con énfasis en diseño de mecanismos.

Email: gmoren@unipamplona.edu.co

Rafael Bolívar-León

Nació en Capitanejo (Santander), Colombia. Obtuvo su título como ingeniero y magister en Ingeniería Metalúrgica en la Universidad Industrial de Santander y el de Doctorado en Ingeniería en la RWTH-Aachen, Alemania. Es *coach* ontológico de Lifetraining América y *coach* de Negocios Conscientes de la CBC. Profesor de la Universidad de Pamplona desde 2003 y director del grupo de investigación Asciende. Sus áreas de interés son: competitividad, habilidades blandas, cultura, satisfacción y felicidad organizacional en el área de desarrollo humano y empresarial.

Email: rbolivarl@unipamplona.edu.co

Performance Analysis of a Backward/Forward Algorithm Adjusted to a Distribution Network with Nonlinear Loads and a Photovoltaic System

Análisis del desempeño de un algoritmo Backward/Forward ajustado a una red de distribución con cargas no lineales y un sistema fotovoltaico

Alejandra Martínez-Peñaloza[1] 🆔✉*, Gabriel Ordóñez-Plata[1] 🆔, and German Alfonso Osma-Pinto[1] 🆔

[1]Universidad Industrial de Santander (Bucaramanga, Colombia).

Abstract

Context: The backward/forward (BF) algorithm is a sweep-type technique that has recently been used as a strategy for the power flow analysis of ill-conditioned networks. The purpose of this study is to evaluate the performance of the BF algorithm compared to that of a computational tool such as Simulink, with both strategies adjusted to the operating conditions of a distribution network with nonlinear components (loads and photovoltaic system), unbalanced loads, and harmonic distortion in the voltage and current signals.

Method: The study case is a low-voltage distribution network with a radial topology, unbalanced loads, and nonlinear components. The BF algorithm is adjusted to consider two approaches of the Norton model: a coupled admittance matrix and a decoupled admittance matrix. The latter is also used in the network model created in Simulink. The performance of the algorithm is evaluated by analyzing 18 operation scenarios defined according to the presence and use intensity of the loads and solar irradiance levels (low and high).

Results: In general, the three strategies could successfully determine the waveform and RMS values of the voltage signals with errors of less than 0,8 and 1,3 %, respectively. However, the performance of the strategies for the estimation of current signals and power parameters shows errors of 5-300 % depending on the level of solar irradiance at which the photovoltaic system operates.

Conclusions: The results show that the BF strategy can be used to analyze unbalanced power grids with increasing penetration of renewable generation and the integration of nonlinear devices, but the performance of this strategy depends on the load model applied to represent the behavior of nonlinear devices and generation systems.

Keywords: backward/forward, Norton model, nonlinear loads, PV system, Simulink

*✉ **Correspondence:** alejandra2198146@correo.uis.edu.co

Resumen

Contexto: El algoritmo *backward/forward* (BF) es una técnica de barrido que se ha utilizado recientemente como estrategia para el análisis de flujo de energía de redes mal acondicionadas. El objetivo de este estudio es evaluar el desempeño del algoritmo BF comparado con el de una herramienta computacional como Simulink, con ambas estrategias ajustadas a las condiciones de operación de una red de distribución con componentes no lineales (cargas y sistema fotovoltaico), desbalance en las cargas y distorsión armónica en tensión y corriente.

Método: El caso de estudio es una red de distribución de baja tensión con topología radial, cargas desequilibradas y componentes no lineales. El algoritmo BF se ajusta para considerar dos enfoques del modelo Norton: matriz de admitancia acoplada y matriz de admitancia desacoplada. Este último también se utiliza en el modelo de red creado en Simulink. El desempeño del algoritmo se evalúa mediante el análisis de 18 escenarios de funcionamiento definidos según la presencia e intensidad de uso de las cargas y los niveles de irradiancia solar (baja y alta).

Resultados: En general, las tres estrategias podrían determinar con éxito los valores de forma de onda y RMS de las señales de tensión con errores menores de 0,8 y 1,3 % respectivamente. Sin embargo, el desempeño de las estrategias para la estimación de señales de corriente y parámetros de potencia presenta errores de 5-300 % dependiendo del nivel de irradiancia solar en el cual el sistema fotovoltaico se encuentre operando.

Conclusiones: Los resultados muestran que la estrategia BF se puede utilizar para analizar redes eléctricas desbalanceadas con creciente penetración de generación renovable e integración de dispositivos no lineales, pero el rendimiento de la misma depende del modelo de carga aplicado para representar el comportamiento de los dispositivos no lineales y de los sistemas de generación.

Palabras clave: *backward/forward*, modelo Norton, cargas no lineales, sistema FV, Simulink

Table of contents

1. Introduction

Power flow analysis is a tool that makes it possible to conduct studies on power generation dispatch, distribution network analysis, load control, network reconfiguration planning, and distributed energy resource (DER) integration (*e.g.*, photovoltaic (PV) generators, electric vehicles, and energy storage units) (1).

However, solving a power flow is a complex task due to the number of variables and their mathematical formulations. Therefore, iterative method have been proposed, such as the Gauss-Seidel approach, impedance matrices, and the backward/forward (BF) technique with admittance summation. These methods are based on a linear system that operates only at the fundamental frequency (2,3).

In recent years, sweep iterative methods such as BF have been used to study radial distribution networks, as they can ensure the convergence of the power flow while considering network characteristics such as load imbalance and the high R/X ratio of conductors (1,4,5).

In addition, sweep methods are a viable option for conducting studies on the behavior of a grid with distributed generation integration and the presence of nonlinear devices (2,6,7).

Moreover, variants of harmonic power flow analysis algorithms have been proposed for application in distribution networks, which consider frequency variations associated with DERs and nonlinear loads. Among these, algorithms in the frequency domain stand out for their effectiveness in reducing computational times (2,8–16).

For example, (10) proposed a method based on harmonic sweeps to improve the accuracy of harmonic analyses in distribution systems. (2) proposed a rapid and effective harmonic sweep method that solves harmonic power flows for radial distribution networks with integrated distributed generation units. (16) presented a new algorithm for fundamental power flow and harmonic power flow, with the aim of evaluating the impacts of integrating renewable generation and nonlinear loads in distribution grids. Kettner *et al.* (13) proposed a method to solve the three-phase harmonic power flow with the integration of CIDERs in the systems.

It is considered to be a generic and modular representation of system elements and the coupling between harmonics.

Some researchers have adjusted the BF algorithm to introduce distributed generators and nonlinear loads. (1) proposed a new BF-based power flow analysis approach that organizes grid information to facilitate programming by reducing the search for connections between nodes.

 (4) presented an alternative approach to the BF sweep, whose advantage is convergence speed in distribution networks with controlled voltage nodes (PV). (5) proposed a method based on the concept of *independent lines* to consecutively order the distribution network lines, which is subsequently applied

to the Kirchhoff law-based BF sweep algorithm.

Although the algorithms for analyzing the power flows of distribution networks propose adaptations to the new conditions, few studies have considered integrating PV generation, load imbalance, and nonlinear loads (single-phase, two-phase, or three-phase) simultaneously.

Additionally, considering nonlinear devices in power flow analysis requires models that represent their harmonic nature and take the harmonic interaction between voltage and current into account (8, 13–16). It is common to use the fundamental frequency-dependent current source model for these loads, which does not consider such harmonic interactions (2, 8, 14–16). In light of this, other load models may be suitable, such as the Norton equivalent coupled admittance matrix model, as well as proposing or studying the performance of harmonic power-flow solution algorithms that consider the actual conditions of distribution networks.

Therefore, studies on distribution networks with these characteristics are necessary; they allow, among other things, characterizing the harmonic distortion pollution caused by the high presence of electronic loads and the increasing penetration of PV systems in low-voltage distribution networks (10), which tend to increase power losses and interference in communications while decreasing the lifetime of the installed equipment (14, 17–20).

In this sense, the contribution of this lies in the fact that it determined the performance of a BF sweep-type algorithm whose mathematical approach was adapted to the conditions of the electricity distribution network in a university building (unbalanced loads, nonlinear loads, the integration of a PV system, and harmonic distortion in the feed signal) in order to solve the harmonic power flow. Moreover, the nonlinear devices and PV system were modeled using the coupled and decoupled admittance matrix methods of the Norton equivalent model.

The performance analysis consisted of an evaluation of the strengths and weaknesses of three power flow solution strategies: BF with the coupled Norton model (BF-NC), BF with the decoupled Norton model (BF-ND), and Simulink with the decoupled Norton model (SIM-ND). This evaluation compared the waveform results and RMS values of the voltage and current signals and power parameters, such as apparent, active, non-active power as well as the power factor.

The SIM-ND and BF-ND strategies allowed inferring the effect of adjusting the traditional BF algorithm, given that they employ the same data and input parameters. The BF-NC strategy was studied to determine the implications of using a more complex load model in the mathematical approach of the BF algorithm.

2. Methodology

Figure 1 illustrates the methodology used in this study, which begins with a description of the case study (Section 2.1) and the modeling of the network components (Section 2.2). Then, it presents the

adaptation of the BF algorithm for a three-phase, unbalanced, and nonlinear case study (Section 2.3), along with the network's modeling in Simulink (Section 2.4), and the definition of simulation scenarios (Section 2.5). Finally, Section 2.6 is dedicated to the resulting data processing and error indicators (Section 2.6).
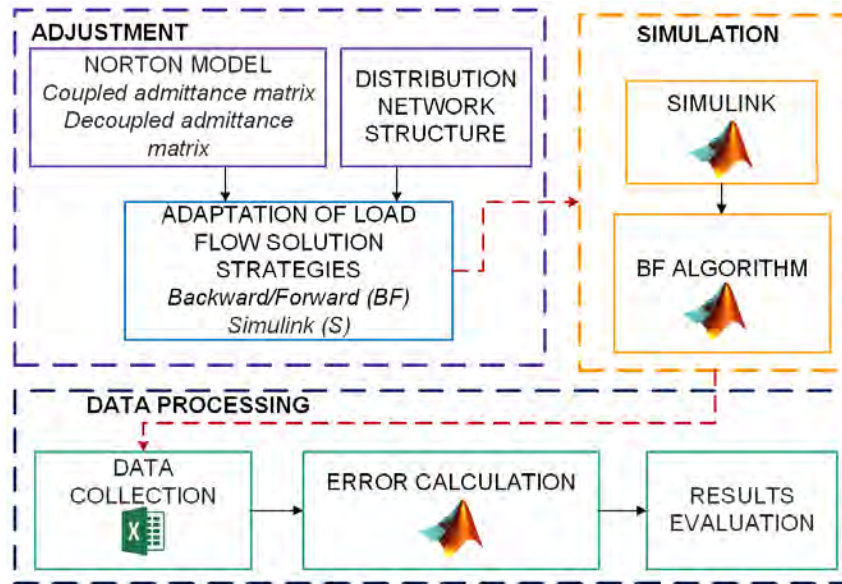

Figure 1. Diagram of the methodology

2.1. Study case

The electrical network in the case study is a section belonging to the network of the Electrical Engineering Building of Universidad Industrial de Santander. This building is located in Bucaramanga, Colombia, at 7°8' North, 73°0' West. During daylight hours (6 a.m. to 6 p.m.), the temperature ranges between 24 and 28 °C, while the solar irradiance varies between 2,0 and 7,6 kWh/m^2 day, with an average of 4,9 kWh/m^2 day (21, 22). Fig. **2** presents the solar irradiance of one week for the month of June, 2018. The solar irradiance for that year was used for our case study.
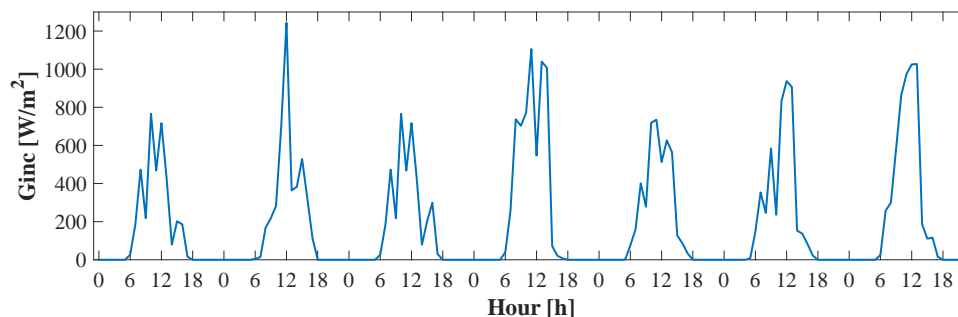

Figure 2. Solar irradiance during a week for the month of June

Fig. **3** shows a five-level building with an area of approximately 2.700 m^2. The first four levels are for classrooms and student areas, and the fifth level is for the administrative area. Different strategies for the rational and efficient use of energy (REUE) have been implemented, such as natural lighting and ventilation, green roofs (580 m^2), automation systems, and PV generation systems.

Figure 3. Electrical Engineering Building

Fig. **4** shows the single-line diagram of the studied network (TP4), with each branch containing lighting loads, air extractors, and THWN 12AWG conductors. There is a TP4 distribution board for the electrical network on the fourth floor of the building. It consists of a lighting sub-board (TALU4) and a common coupling point (PCC) for the PV system installed on the terrace. The TALU4 contains ten single-phase circuits with dimmable luminaires, air extractors (classrooms), and on/off luminaires (bathrooms and corridors). The PV system has the following units: a solar tracker SS-1 (one panel), SFV1 (18 panels), SFV2 (18 panels), and SFV3 (six panels). Table **I** lists the general characteristics of the luminaires, air extractor, and PV systems.
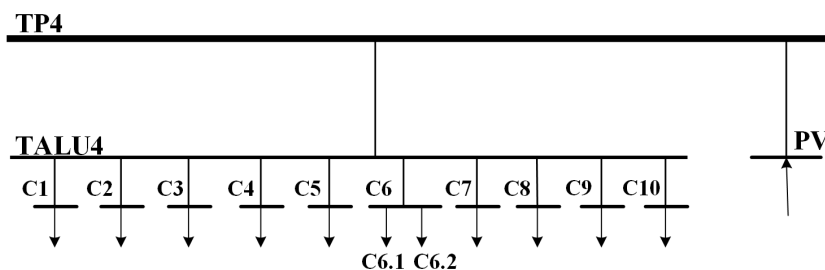

Figure 4. Single-line diagram of the studied low-voltage network

Table I. General characteristics of the loads and PV system

Device type	Rated power	Control type	Circuit	Device number	Total power installed	Features
On-off fluorescent luminaire	68 W single phase	On/Off (Presence sensor)	C5	3 luminaires	204 W	2 tubes T5 (28 W) and electronic ballast
Dimmable fluorescent luminaire	70 W single phase	Dimmable (0 to 10 Vdc) (Sensors and automation system)	C1	10 luminaires	700 W	4 tubes T8 (17 W) and electronic ballast
			C2	12 luminaires	840 W	
			C3	12 luminaires	840 W	
			C4	12 luminaires	840 W	
			C6.1	6 luminaires	420 W	
Air extractor TD 500/150-160 SILENT	66 W single phase	-	C6.2	3 extractors	198 W	Angular speed 2466 RPM
			C7	3 extractors	198 W	
			C8	3 extractors	198 W	
			C9	3 extractors	198 W	
			C10	3 extractors	198 W	
PV system	CI Phase A of 4620 W Phase B of 4080 W Phase C of 3255 W	-	PV	-	-	43 micro-inverters of MPPTtechnology SFV1-18 (M250) SFV2-18 (M250) SFV3-6 (IQ7+) SS-1 (M250)

2.2. Modeling the elements

The studied distribution network is made up of a transformer, conductors, nonlinear loads, and a PV system. For these components (except for the transformer), it is necessary to establish a dependency on frequency changes in the frequency domain.

The transformer of the building has a capacity of 630 kVA and 13,2 kV/220 V, as well as a Δyn5 connection. This element is defined as the simulated network voltage source and, therefore, as an infinite power node or SLACK with a nominal phase voltage of 127 V.

The electrical conductors of the network circuits under study are of the THWN type and of different wire gauges. Their distance corresponds to the separation between the board and load. These elements are represented as frequency-dependent impedance Z_h, as expressed in Eq. (1), where h indicates the harmonic order of the frequency under study, R is the resistance, and X_L is the inductive reactance. Table II describes the characteristic of the electrical wires of each network circuit.

$$Z_h = R + jhX_L \tag{1}$$

Finally, the nonlinear loads and the PV system are represented by Norton equivalent models of coupled and decoupled admittance matrices, as shown in Eqs. (2) and (3), respectively. This coupled

Table II. Characteristics of the electric wires

Electric circuit	Phase	Phase wire gauge	Neutral wire gauge	Distance [m]	Phase impedance	Neutral impedance
Transformer-TP4	ABC-N	#2 THWN	#4 THWN	24,3	0,0159+j0,0035	0,0247+j0,0038
TP4-TALU4	ABC-N	#10 THWN	#12 THWN	2,4	0,0094+j0,0003	0,0157+j0,0004
TP4-PV	ABC-N	#8 THWN	#8 THWN	3,0	0,0076+j0,0005	0,0076+j0,0005
TALU4-C1	AN			43,0	0,2820+j0,0506	0,4373+j0,0081
TALU4-C2	BN			33,0	0,2164+j0,0384	0,3356+j0,0062
TALU4-C3	CN			22,0	0,1443+j0,0245	0,2237+j0,0041
TALU4-C4	AN			24,0	0,1574+j0,0268	0,2440+j0,0045
TALU4-C5	BN	#12 THWN	#12 THWN	10,0	0,0656+j0,0111	0,1017+j0,0019
TALU4-C6	CN			31,0	0,2033+j0,0346	0,3152+j0,0058
TALU4-C7	AN			18,0	0,1180+j0,0201	0,1830+j0,0034
TALU4-C8	BN			13,0	0,0852+j0,0145	0,1322+j0,0024
TALU4-C9	CN			25,0	0,1640+j0,0279	0,2542+j0,0047
TALU4-C10	AN			46,0	0,3017+j0,0513	0,4678+j0,0087

approach allows the study of the harmonic interaction between the voltage and the current signals.

$$
\begin{bmatrix} \bar{I}_1 \\ \bar{I}_3 \\ \vdots \\ \bar{I}_H \end{bmatrix} = \begin{bmatrix} \bar{I}_{\text{ref1}} & \bar{Y}_{1,1} & \bar{Y}_{1,3} & \dots & \bar{Y}_{1,K} \\ \bar{I}_{\text{ref3}} & \bar{Y}_{3,1} & \bar{Y}_{3,3} & \dots & \bar{Y}_{3,K} \\ \vdots & \vdots & \vdots & \ddots & \vdots \\ \bar{I}_{\text{refH}} & \bar{Y}_{H,1} & \bar{Y}_{H,3} & \dots & \bar{Y}_{H,K} \end{bmatrix} \begin{bmatrix} 1 \\ \Delta V_1 \\ \Delta V_3 \\ \vdots \\ \Delta V_K \end{bmatrix} \tag{2}
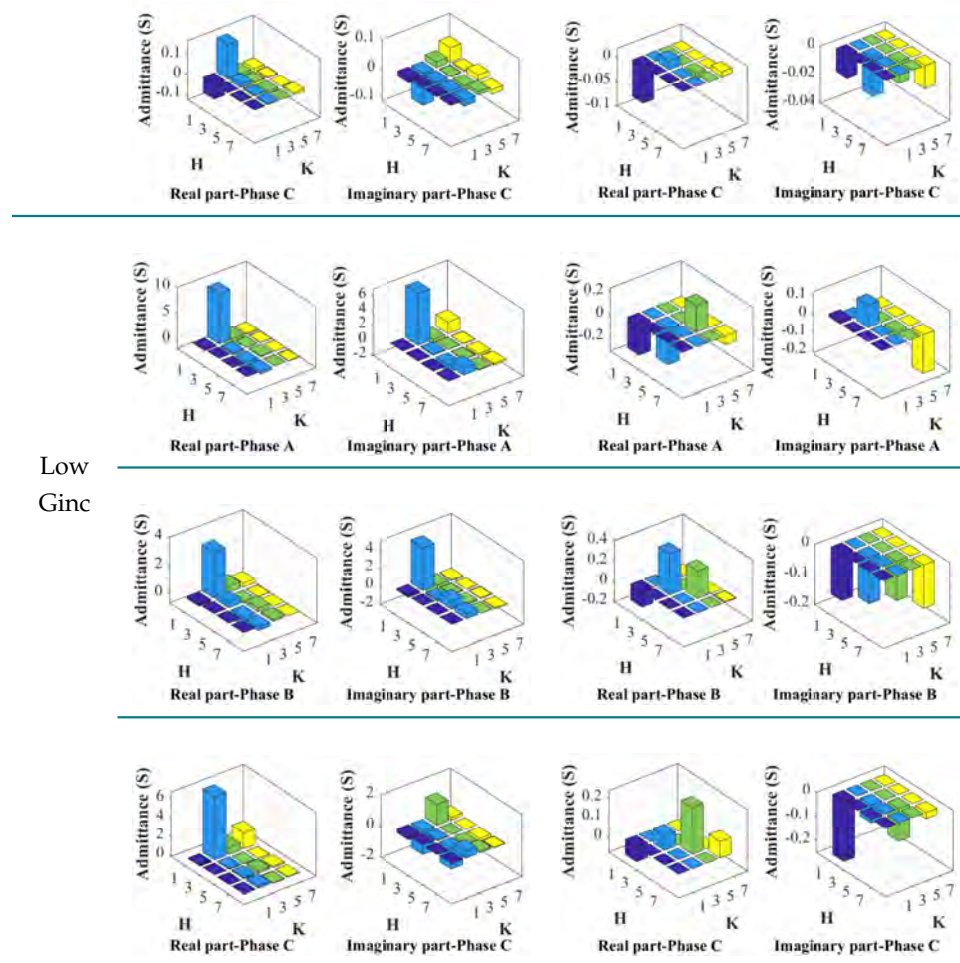$$

$$
\begin{bmatrix} \bar{I}_1 \\ \bar{I}_3 \\ \vdots \\ \bar{I}_H \end{bmatrix} = \begin{bmatrix} \bar{I}_{\text{ref1}} & \bar{Y}_{1,1} & 0 & \dots & 0 \\ \bar{I}_{\text{ref3}} & 0 & \bar{Y}_{3,3} & \dots & 0 \\ \vdots & \vdots & \vdots & \ddots & \vdots \\ \bar{I}_{\text{refH}} & 0 & 0 & \dots & \bar{Y}_{H,K} \end{bmatrix} \begin{bmatrix} 1 \\ \Delta V_1 \\ \Delta V_3 \\ \vdots \\ \Delta V_K \end{bmatrix} \tag{3}
$$

Here, $\bar{I}$ represents the current vector of the device, $\bar{I}_{ref}$ frequency concatenated with the $\bar{Y}$ admittance matrix, $\Delta \bar{V}$ is the vector of the voltage signal variations. The dimensions of the H and K models indicate the highest odd harmonic order used for the current and voltage signals, respectively.

Table III presents the coupled and decoupled Norton models for each nonlinear element (luminaires, extractors, and the PV system). The model for each single-phase load (luminaire or air extractor) was graphically represented by the real and imaginary parts of the admittance matrix for each operating condition. The PV system is a three-phase component, represented by six admittance matrices for each operating condition. The on/off luminaires and extractors have one operating condition, the dimmable luminaires have two operating conditions according to dimmer level (0 and 10 Vdc), and the PV system has three operating conditions according to solar irradiance (high and low) (23–26).

Table III. Norton equivalent models for each element

Device		Coupled Norton model		Decoupled Norton model	
On/off fluorescent luminaire					

Low
Ginc

2.3. Adapted backward/forward (BF) iterative algorithm

Generally, the BF iterative sweep algorithm using Kirchhoff's laws is employed to solve the power flows of distribution networks. It orders the network nodes to systematize the iterative process of calculating the currents that flow through the conductors from the currents injected into the nodes. Similarly, it helps to calculate the voltages in the lower nodes, starting from the voltage of the source node. Fig. 5 illustrates the nodal ordering applied to the scheme.

For this case study, adjusting the algorithm's mathematical approach to the characteristics of the network allows considering unbalanced loads, harmonic distortion in the feeder, and the use of the Norton model to represent nonlinear loads and the PV system, as shown in Fig. 6.

The dotted blocks in Fig. 6 highlight the process added or adjusted according to network characteristics, such as the input of the Norton models of nonlinear loads and the PV system and the initialization of the voltage signal for all k frequencies. Calculations within the iterative process are
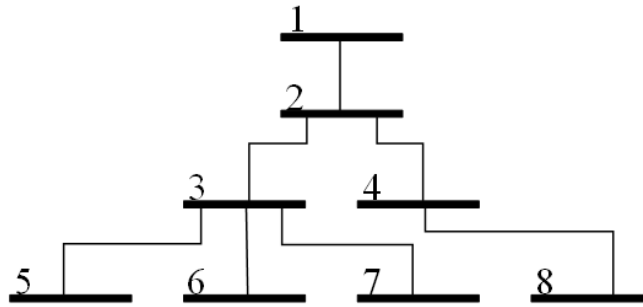
Figure 5. Example of nodal ordering scheme

consecutively performed for each k frequency. The third, fifth, and seventh harmonic orders were the harmonic frequencies adopted for the study, as they were the most representative within the feeder signal. Therefore, the frequency value of k was 4.

There is a general stage involving the initialization of the conditions for the power flow, which includes the input of the data characteristics of the network, the input of the Norton models for each of the nonlinear loads and the PV system, the creation of arrays that represent the connections of the circuits in the network, and the input of the initial conditions of the voltage signal into each of the nodes of the network. Note that the initial voltage conditions were obtained from a prior review of the voltage signals of the studied electrical network at different times of the day. In addition, the initial conditions of each node corresponded to the voltage of the SLACK bus.

The iterative process of this method consists of two sub-processes. First, the backward sweep calculates the injected currents in the load nodes and PV system according to the Norton model (BF-NC and BF-ND). The current I_B flowing through branches is calculated using Eq. (4), where I_L is the load or PV system current connected to the node, and $I_{i,N}$ is the current of the branches i connected to the node N.

$$I_B = I_L + \sum I_{i,N} \tag{4}$$

Next, the forward sweep is initialized and calculates the voltage drops of the branches, considering the I B currents and the specific impedances of each conductor. The node voltages were obtained progressively from the SLACK node to the farthest node. At the beginning of each forward sweep cycle, it is necessary to maintain the tension of the SLACK node in its initial conditions and apply Eq. (5), where V_{N-1} is the voltage of the upper node, V_N is the voltage of the lower node, and $I_B Z_h$ represents the voltage drop in the branches.

$$V_N = V_{N-1} - I_B Z_h \tag{5}$$

The node voltage and branch current data are stored in arrays and exported to an Excel file. After finishing the iterative process, the percentage error in magnitude and the absolute error in phase angles between the current and previous iteration data are calculated to find the desired nodal voltage branch current values.
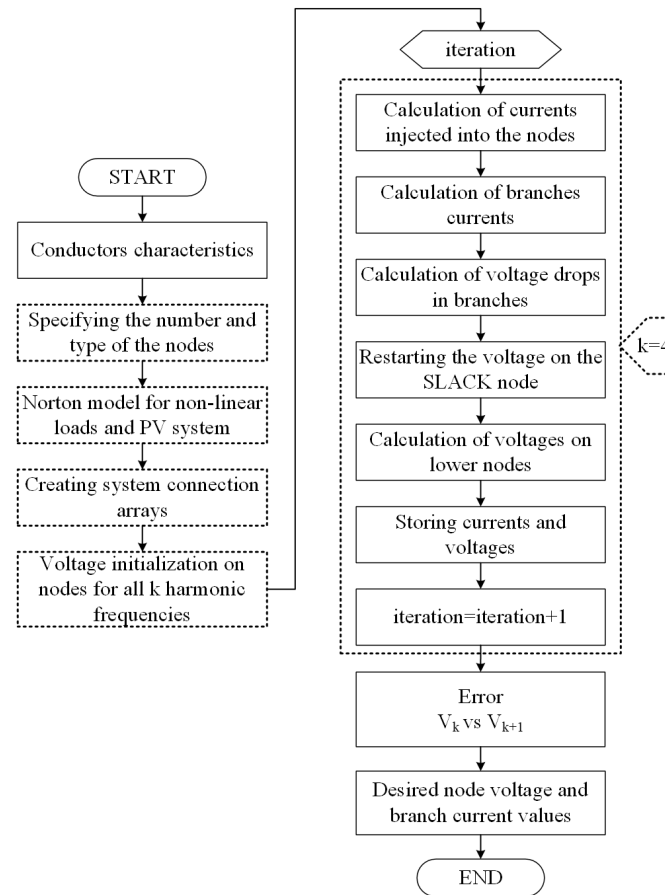
Figure 6. Adapted backward-forward (BF) algorithm flowchart

2.4. Modeling the electric network in Simulink

The main objective of this study was to analyze the performance of the BF algorithm adjusted and programmed in MATLAB. To corroborate the results obtained by the BF-ND strategy, the electrical network was modeled in Simulink, considering the use of the decoupled Norton model to represent the loads and the PV system (SIM-ND strategy).

Simulink is a tool that solves power flows using the approach and solution of the state equations of the model in the frequency domain.

The modeling of the studied network considered its characteristics and the most representative odd harmonic orders (third, fifth, and seventh). The network was represented by four subsystems, one at each frequency (Fig. 7). In addition, there is a subsystem containing result export blocks from Simulink to MATLAB in order to facilitate the treatment of the data and compare them with the values estimated by the BF algorithm. The MATLAB Function and Controlled Current Source blocks allow modeling the loads and the PV system in each subsystem by applying only the Norton decoupled matrix model.
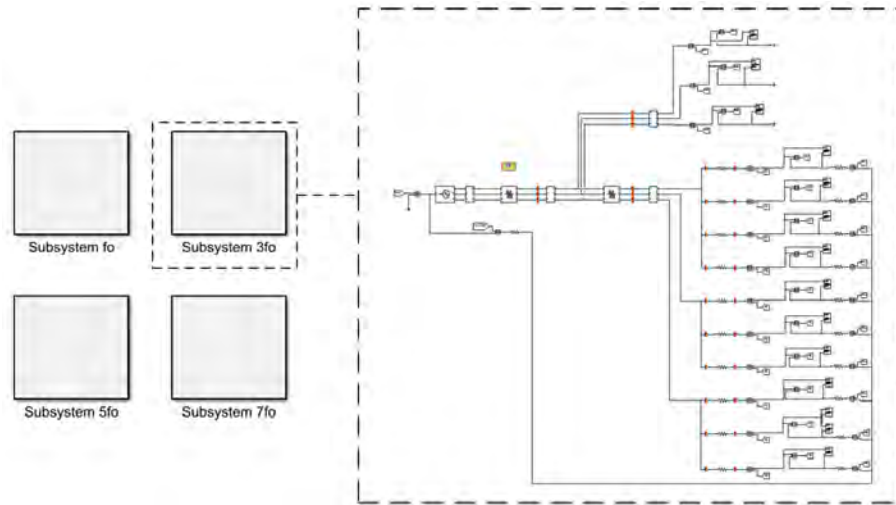
Figure 7. General structure of the Simulink model

2.5.   Operation scenarios

Table **IV** presents 18 scenarios for the operation of the electricity grid under study, which are based on two inputs. The first input corresponds to the operating conditions of the dimmable luminaires (0 and 10 Vdc), the on/off luminaires, the air extractors (on), and the PV system for two levels of solar irradiance (high-H and low-L). The second input is the representativeness of the number of devices in simultaneous operation.

2.6.   Data processing

At the end of each simulation, the magnitude and phase-angle data of the node voltages, branch currents, and neutral currents were stored in an Excel file corresponding to each operation scenario. The magnitude and phase angle data were discriminated by each harmonic order under study (fundamental, third, fifth, and seventh).

After the simulation of the operation scenarios had been completed, the normalized root mean square errors (NRMSEs) were calculated by importing the data stored in Excel to the MATLAB Workspace. These errors were estimated from the waveforms obtained using the three analyzed strategies. Similarly, the RMS values of the voltage node and current in the branches were calculated. Finally, the power parameters were estimated to analyze the performance of the strategies in terms of the apparent, active, and non-active power, as well as the power factor.

Table IV. Operation scenarios for the study case

	On/off luminaires		Dimmable luminaires				Extractors		Photovoltaic system	
	Min	**Max**	**Min**		**Max**		**Min**	**Max**	**H**	**L**
			0 Vdc	**10 Vdc**	**0 Vdc**	**10 Vdc**				
E1	✓		✓						✓	
E2	✓			✓						✓
E3		✓			✓				✓	
E4		✓				✓				✓
E6							✓			✓
E8							✓		✓	
E9								✓		✓
E11								✓	✓	
E12									✓	
E14										✓
E15	✓		✓				✓		✓	
E16	✓			✓			✓			✓
E17		✓			✓		✓		✓	
E18		✓				✓	✓			✓
E19	✓		✓					✓	✓	
E20	✓			✓				✓		✓
E21		✓			✓			✓	✓	
E22		✓				✓		✓		✓

3. Results

This section presents the results obtained while estimating the electrical grid voltage, current signals, and power parameters. First, it shows the evolution of method performance (Section 3.1). Then, it presents the analysis of RMS values (Section 3.2), waveforms and NRMSEs (Section 3.3), influence factors (Section 3.4), and network power parameters (S, P, QF, and fp) (Section 3.5). Finally, it presents a brief analysis of the performance of the studied power flow strategies (Section 3.6).

3.1. Evolution of the performance of strategies

Fig. 8 shows the evolution of RMS errors in voltage for node TP4 (VTP4) and the current for branch SLACK-TP4 (ISLACK-TP4), considering the operation scenarios. These errors were calculated for each scenario by selecting average values for each iteration. The results obtained by the BF-ND and BF-NC strategies are acceptable at the end of the second iteration, with average errors of 2,5e5 % for the voltage and 2,0e-2 % for the current.
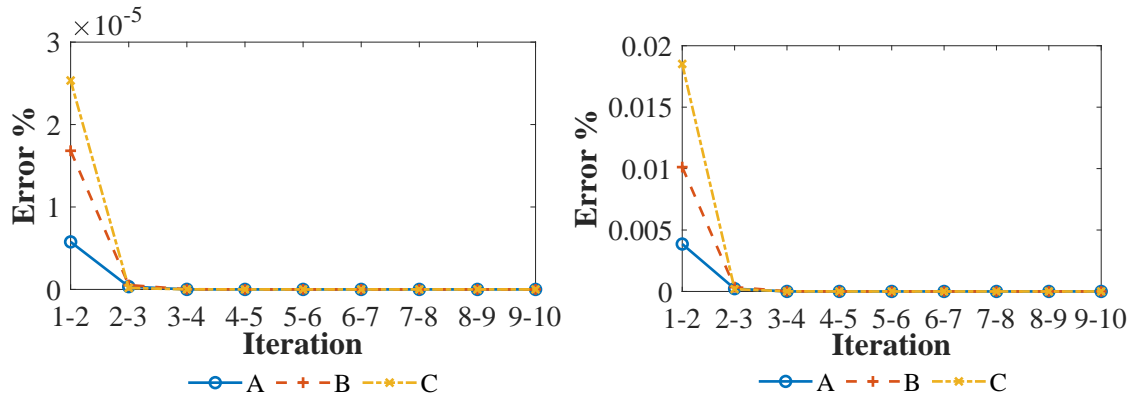
Figure 8. Evolution of the estimation error of the RMS voltage and current values at each iteration

3.2. RMS values

Fig. **9** shows the single-line scheme of the studied electrical network that relates the RMS values of nodal voltage and branch current obtained by applying the BF algorithm with decoupled Norton modeling (Fig. **9**a) and coupled Norton modeling (Fig. **9**b). Specifically, it shows the results for the estimates of Scenario 22, where all the luminaires and air extractors work and the PV system operates under low solar irradiance, which implies high levels of THDi (25).
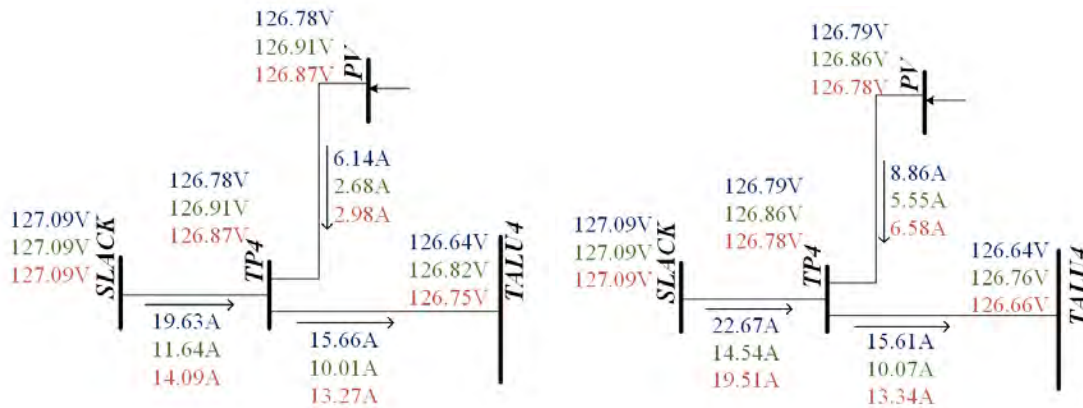

Figure 9. Voltages and currents for operation scenario 22. The blue, green, and red values refer to voltage or current values for phases A, B, and C, respectively

There was a difference in the VRMS voltage drop values between the lower and SLACK nodes. The two strategies exhibit a similarity of VRMS values, with differences of less than 0,1 V in most load circuits and TP4 and TALU4 nodes.

In terms of the IRMS, there is a significant difference between the values of the two strategies because the coupled model correctly estimates the actual waveform of the current consumed by the

load, unlike the decoupled model (23, 24, 26). This difference is more noticeable in the PV system IRMS injected with differences of 2,7-3,6 A due to the low satisfaction in the estimation of currents by the decoupled model for low solar irradiance (25).

Figs. 10 to 13 show the errors of the RMS values calculated for the three strategies. Fig. 10 shows that the VRMS errors in the TP4 node do not exceed 0,08 % in scenarios where the PV system operates at low solar irradiance (*e.g.*, E2, E4, E6, and E9). In comparison, the errors are less than 0,02 % for scenarios in which the PV system operates at a high solar irradiance level (*e.g.*, E1, E3, E4, and E7).
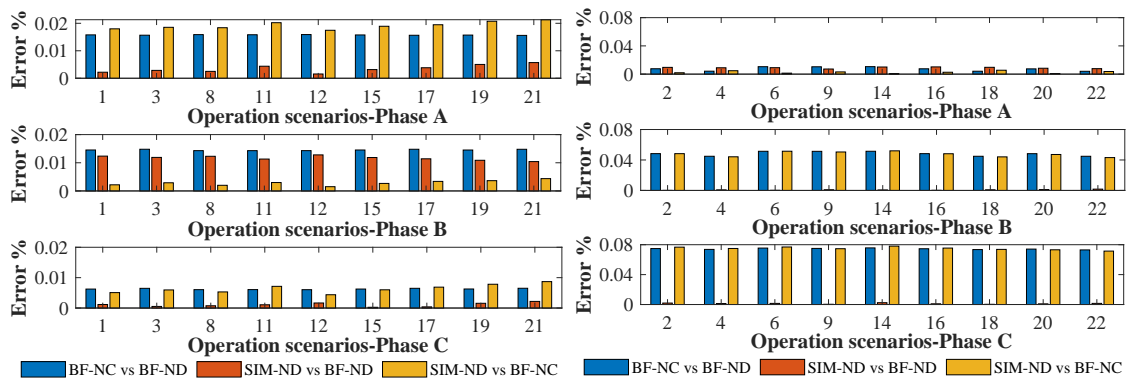

Figure 10. Voltage signal RMS value errors in node TP4 for the operation scenarios

In contrast, Figs. 11 to 13 show the estimation errors regarding the IRMS. Fig. 11 compares the performance of IRMS error strategies for the SLACK-TP4 branch in scenarios where the PV system operates at low solar irradiance levels (E2, E4, E6, E9, E14, E16, E18, E20, and E22). The resulting errors are between 20 and 150 %. These differences between the strategies are caused by the power signal estimation capability of the Norton decoupled model (ND) compared to the Norton coupled model (NC), the latter being the most successful.
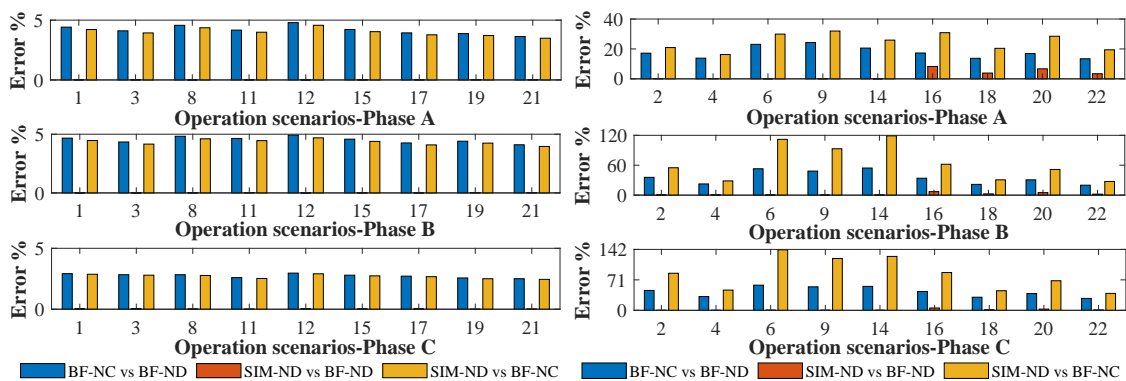

Figure 11. SLACK-TP4 branch current signal RMS values errors for operation scenarios

This may be a consequence of that observed in Fig. **12**, where the errors of the IRMS injected by the PV system in scenarios where it operates at low solar irradiance are greater than 20 %. However, in the specific scenarios E16, E18, E20, and E22, phase B and phase C errors exceed 150 % when comparing SIM-ND strategies against BF-NC.
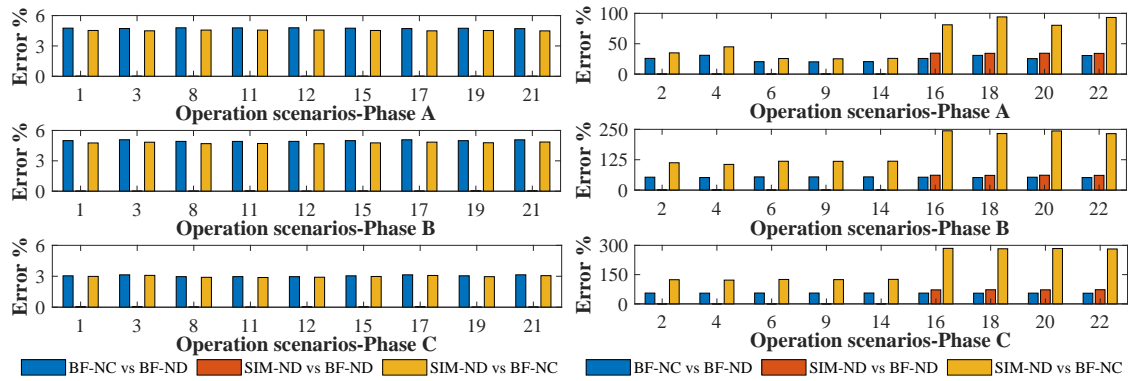

Figure 12. TP4-PV system branch current signal RMS value errors for the operation scenarios

Fig. **13** shows IRMS errors greater than 1,0 % in scenarios E1, E3, E15, E17, and E21, where the dimmable luminaires operate with the lowest dimmer level (0 Vdc), which provides greater harmonic distortion (THDi >18 %) than other levels of control (THDi <15 %) (23, 24).
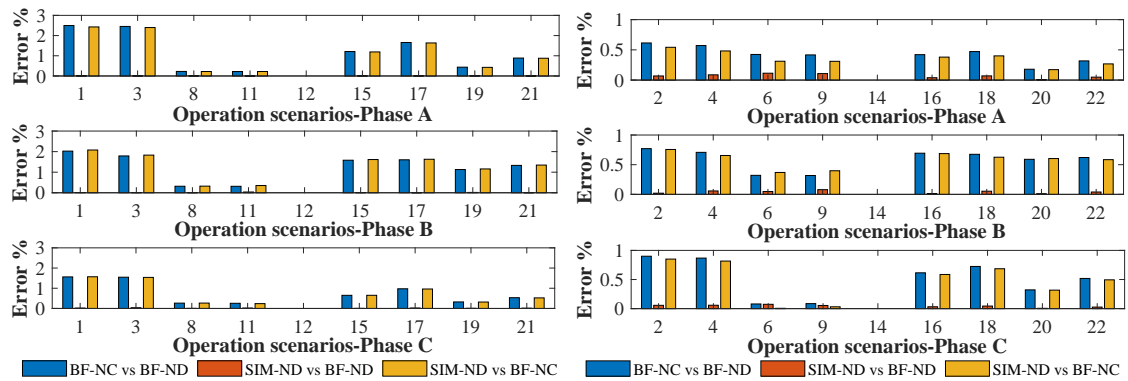

Figure 13. TP4-TALU4 branch current signal RMS value errors for operation scenarios

3.3. Waveforms and normalised root mean square errors (NRMSEs)

Fig. **14** presents the characteristics of the waveform of the SLACK bar and those estimated using the three strategies (SIM-ND, BF-ND, and BF-NC). There is a predominance of the flat-top waveform type in these waveforms, where the fifth harmonic order prevails over the third and seventh orders. Similarly, the voltage waveforms obtained using the three strategies are significantly similar.

Fig. **15** shows a comparison of the NRMSEs of the voltage signals obtained via the three strategies for the TP4 node in each operation scenario. In general, the values were less than 0,05 %. However, in
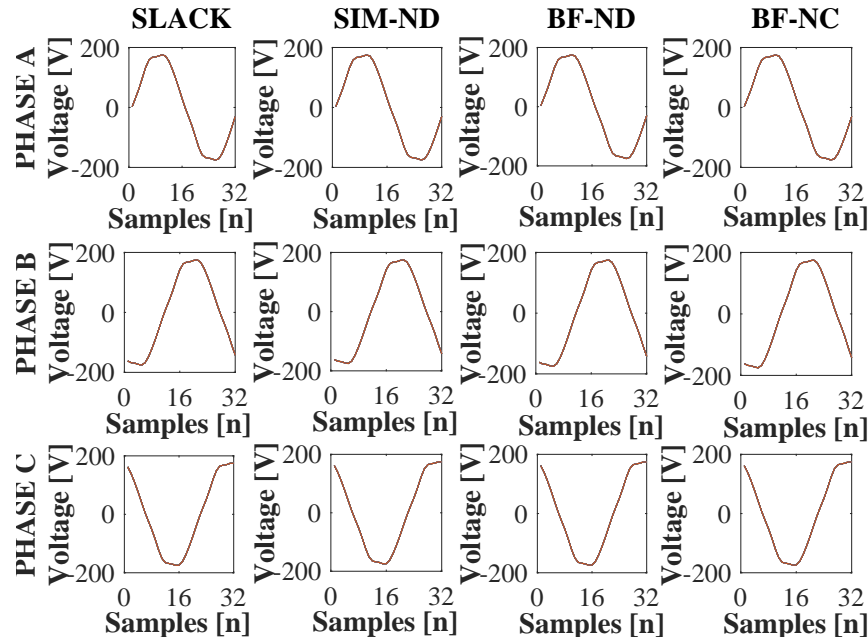
Figure 14. Voltage signal waveforms for all operation scenarios

scenarios where the PV system injects power at a low solar irradiance level and the dimmable luminaires operate at their maximum dimmer level (10 Vdc – E14, E16, E20, and E22), phase A errors are between 0,05 and 0,1 % when comparing SIM waveforms-ND with BF-NC, and BF-NC with BF-ND.
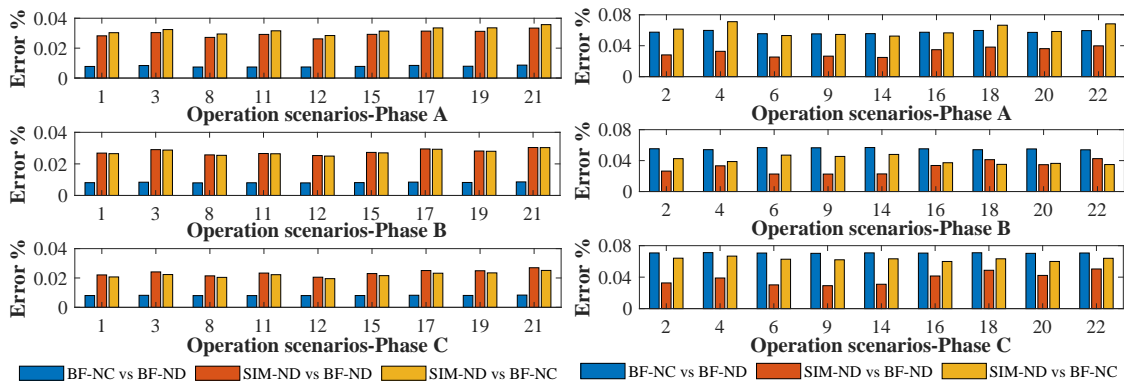
Figure 15. Voltage normalized root mean square errors (NRMSEs) at node TP4 for all operation scenarios

This is the result of an overload in phase A luminaire circuits and the PV system. Similarly, the estimation of the current signal injected by the PV system with the coupled and decoupled Norton models shows differences when analyzing low solar irradiance levels. (25) found that the coupled model estimates the waveform with an NRMSE of less than 2 %, in contrast to the decoupled model, with an error close to 20 %. It should be noted that, although there is prior knowledge of the current

performance of Norton models in the modeling of loads and PV systems, this study aims to review the possible impacts of using these models on the voltage and power parameters.

The waveforms of the current signals (Figs. **16**, **17**, and **18**) reveal the differences between the current signals estimated using each of the three strategies.

Fig. **16** clearly shows the differences between the waveforms of the current signals in the SLACK-TP4 branch, considering scenarios where the PV system operates at high solar irradiance (Fig. **16**a) and scenarios with low solar irradiance levels (Fig. **16**b). The reason for this is the impossibility of the decoupled Norton model to estimate the current signal successfully at this PV system operation level.
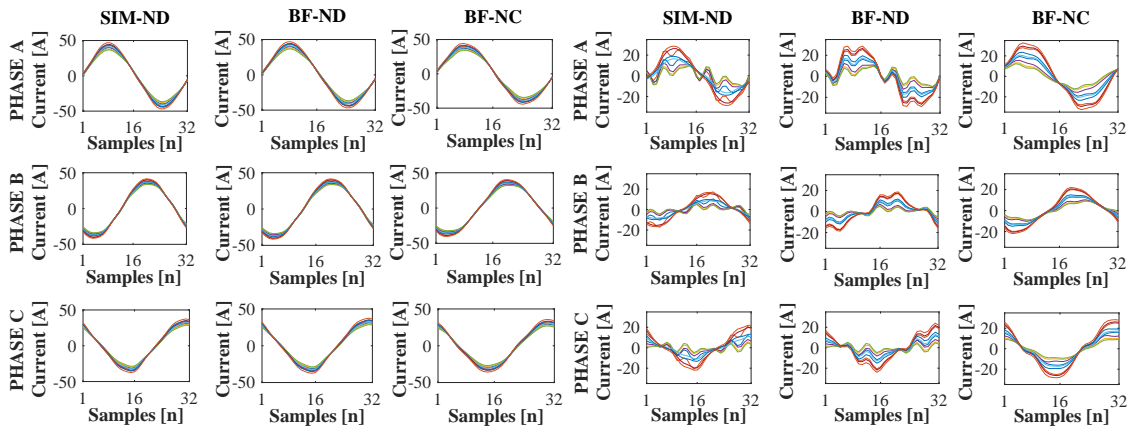

Figure 16. Current signal waveforms on the SLACK-TP4 branch for all operation scenarios

Fig. **17** shows the current waveforms of the TP4-TALU4 branch, where the signals estimated by the three strategies are very similar. However, in the high solar irradiance scenarios (Fig. **17**a), the maximum peak current value is 10 A. In the low-solar-irradiance scenarios (Figure **17**b), the peak value is 20 A. This is because of the close relationship between the dimmer levels of the dimmable luminaires and the operation of the PV system.

Confirming what is shown in Fig. **16**, Fig. **18** reveals the differences between the waveforms of the currents injected by the PV system operating at the two levels of solar irradiance: high (Fig. **18**a) and low (Fig. **18**b), demonstrating the inability of the decoupled Norton model to estimate the injected current signal at low solar irradiance.

In general, the current waveform injected by the PV system at high solar irradiance levels (Fig. **18**a) predominantly affects the current of the SLACK-TP4 branch above the current waveforms from the TALU4 board (Fig. **18**a). In contrast, in scenarios with low solar irradiance, the waveform of the current from the TALU4 board (Fig. **18**b) is predominant in the SLACK-TP4 branch current above the PV system waveform (Fig. **18**b) because the luminaires and air extractors operate at their maximum power, whereas the PV system does not.
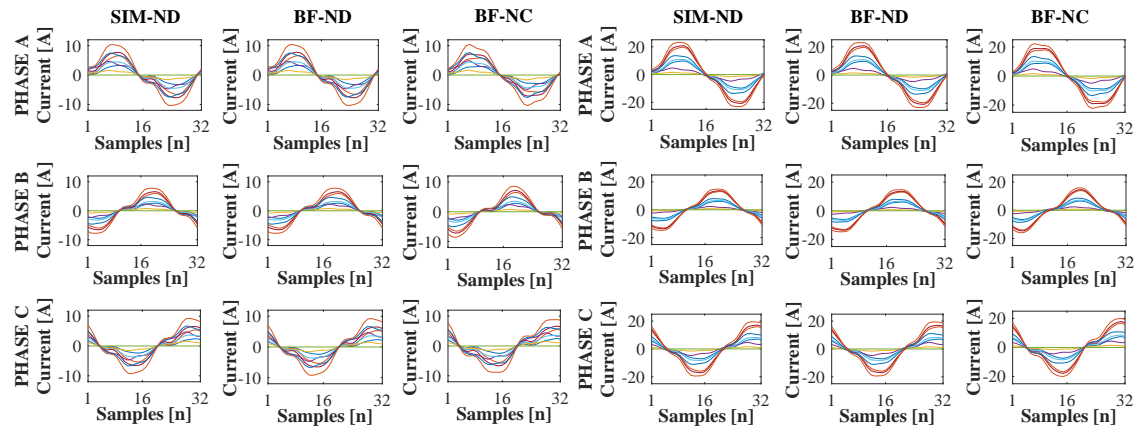
Figure 17. Current signal waveforms on the SLACK-TP4 branch for all operation scenarios
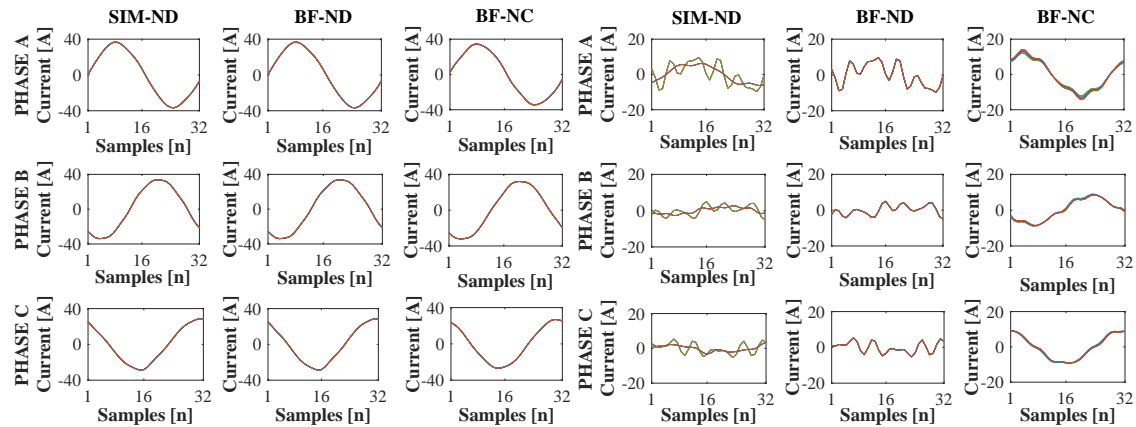

Figure 18. Current signal waveforms on the SLACK-TP4 branch for all operation scenarios

Figs. **19** and **20** present the NRMSEs of the waveforms of the current signals in the TP4-PV and TP4-TALU4 branches. Fig. **19** shows the scenarios where the low solar irradiance levels (E2, E4, E6, E9, E14, E16, E18, E20, and E22) work; there is a difference between the waveforms estimated by BF-NC and those estimated by SIM-ND and BF-ND, obtaining NRMSEs greater than 20 %.

In contrast, in scenarios E1, E3, E7, E8, E15, and E17, the NRMSEs for the estimated current signals were less than 1,0 % since the PV system operated at a high irradiance level.

Fig. **20** shows the NRMSEs of the current waveforms of the TP4-TALU4 branch. The NRMSEs obtained are greater than 3,9 % for the scenarios where the dimmable luminaire operates at a low dimmer level (0 Vdc - E1, E3, E15, E17, E19, and E21), contrary to the scenarios in which the luminaire operates at a high dimmer level (10 Vdc – E2, E4, E16, E18, E20, and E22), with NRMSEs of less than 3,3 %.
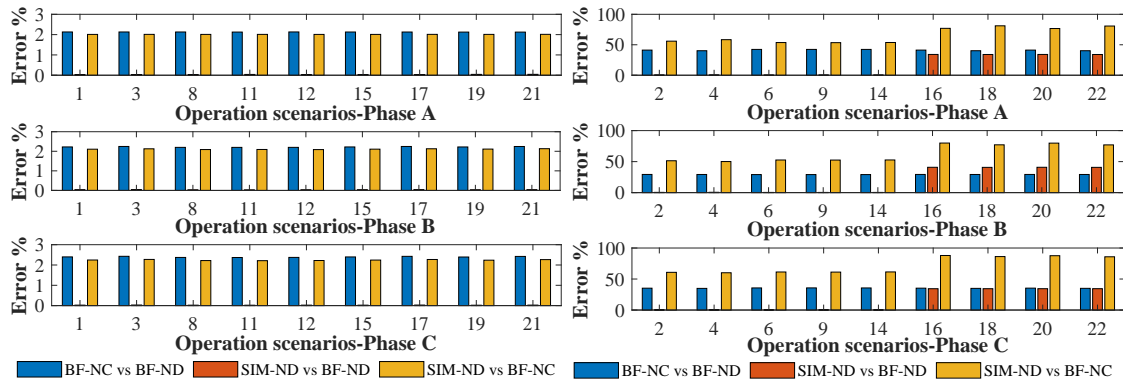
Figure 19. Current NRMSEs in the TP4-PV branch for all operation scenarios

The reason for these errors is that the dimmable luminaires, at the low dimmer level (0 Vdc), have a THDi index higher than 19 %, and, at a high dimmer level (10 Vdc), the THDi index is less than 13 % (24).
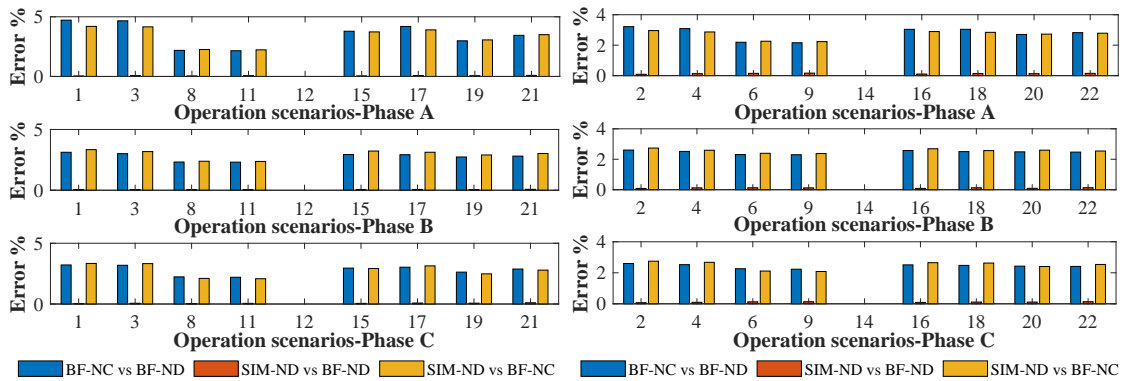
Figure 20. Current NRMSEs in the TP4-TALU4 branch for all operation scenarios

3.4. Factors of influence

The results of the waveform errors of the current signals allow analyzing the potential impact of operating the extractors (minimum and maximum use) and the luminaires (minimum and maximum use and high 10 Vdc dimmer level) in scenarios where the PV system operates at low solar irradiance (E2, E4, E6, E9, E14, E16, E18, E20, and E22). Fig. 21 presents the matrix representations of the impact on the waveform of the current signal of the TP4-PV and TP4-TALU4 branches of the network under study.

According to Figs. 21a and 21b, the number of luminaires or air extractors does not influence the waveform errors of the current signals of the branch feeding the TALU4 sub-lighting board. Similarly, NRMSEs close to 3,0 and 4,0 % indicate the impact of using the coupled Norton model to represent the

luminaires and air extractors, respectively.

Figs. **21**c and **21**d allow stating that the presence of the luminaires and air extractors does not affect the waveform of the current signal of the PV system, confirming that this estimation depends on the load model used. In this regard, the coupled Norton model more accurately estimates the current signal of the PV system when operating at low solar irradiance levels (**25**).
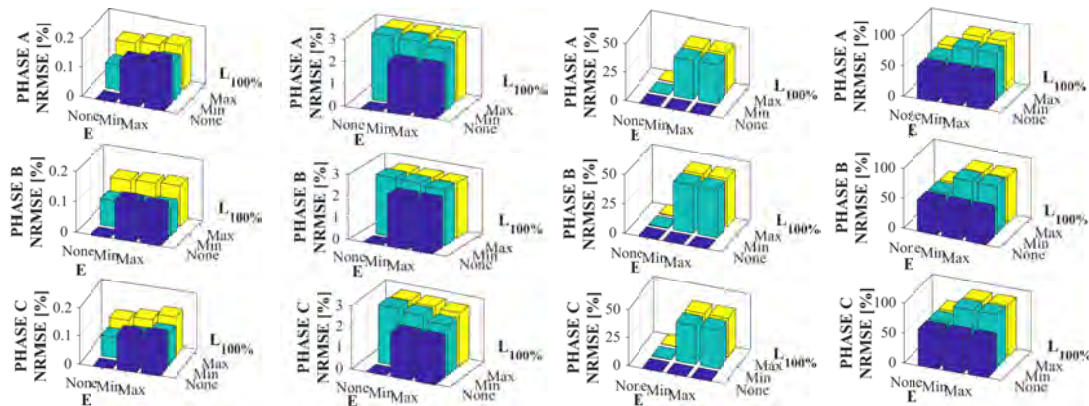

Figure 21. NRMSE load influence matrix for the TP4-TALU4 branch

3.5. Analysis of the power parameters

Considering the results obtained for the waveforms in Section **3.3**, an analysis of the power parameters (apparent power, active power, non-active power, and power factor) was performed for all the operation scenarios. Similarly, the errors in these parameters were calculated from the results of the BF-NC strategy.

Fig. **22** shows the power parameter values of the main network branches (SLACK-TP4, TP4-TALU4, and TP4-PV) for scenario 21. This figure reveals the imbalance between the phases of the PV system and the load circuits. In addition, the power factor has values below 0,97 due to the capacitive nature of the loads, which produces an increase in non-active power.

It should be noted that the differences in the apparent and active power values and, consequently, in the non-active power values are due to the coupled and decoupled Norton models' estimation capacity regarding the current signals.

As for the errors in the estimated power parameters when comparing the two BF strategies, Fig. **23** shows the relationship between these variables.

Fig. **23**a presents the apparent power errors for all the operation scenarios. The errors for the TP4-TALU4 branch are higher than 0,7 % in the scenarios where the dimmable luminaire works at its low dimmer level (0 Vdc), contrary to those where the luminaire works at maximum dimmer level (10 Vdc), where the errors are less than 0,8 %. Similarly, the errors in scenarios where the PV system
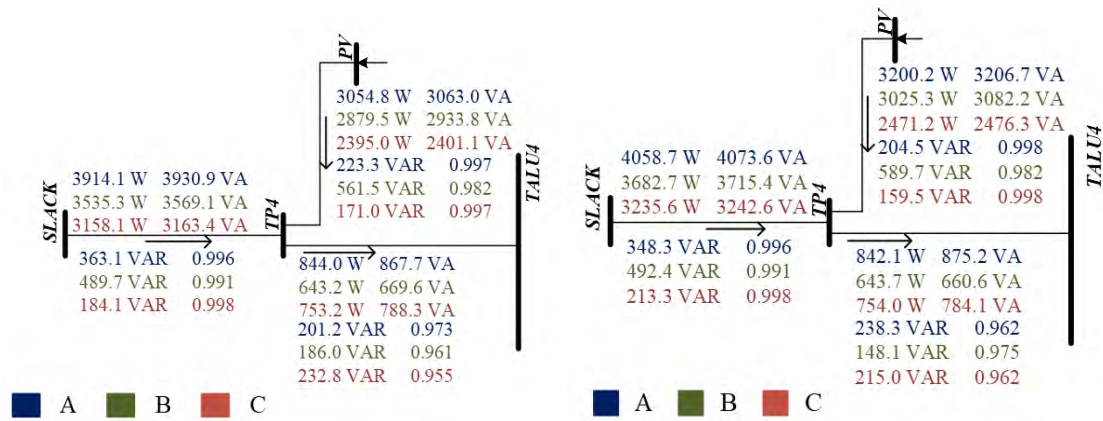
Figure 22. Estimated power parameters for scenario 21
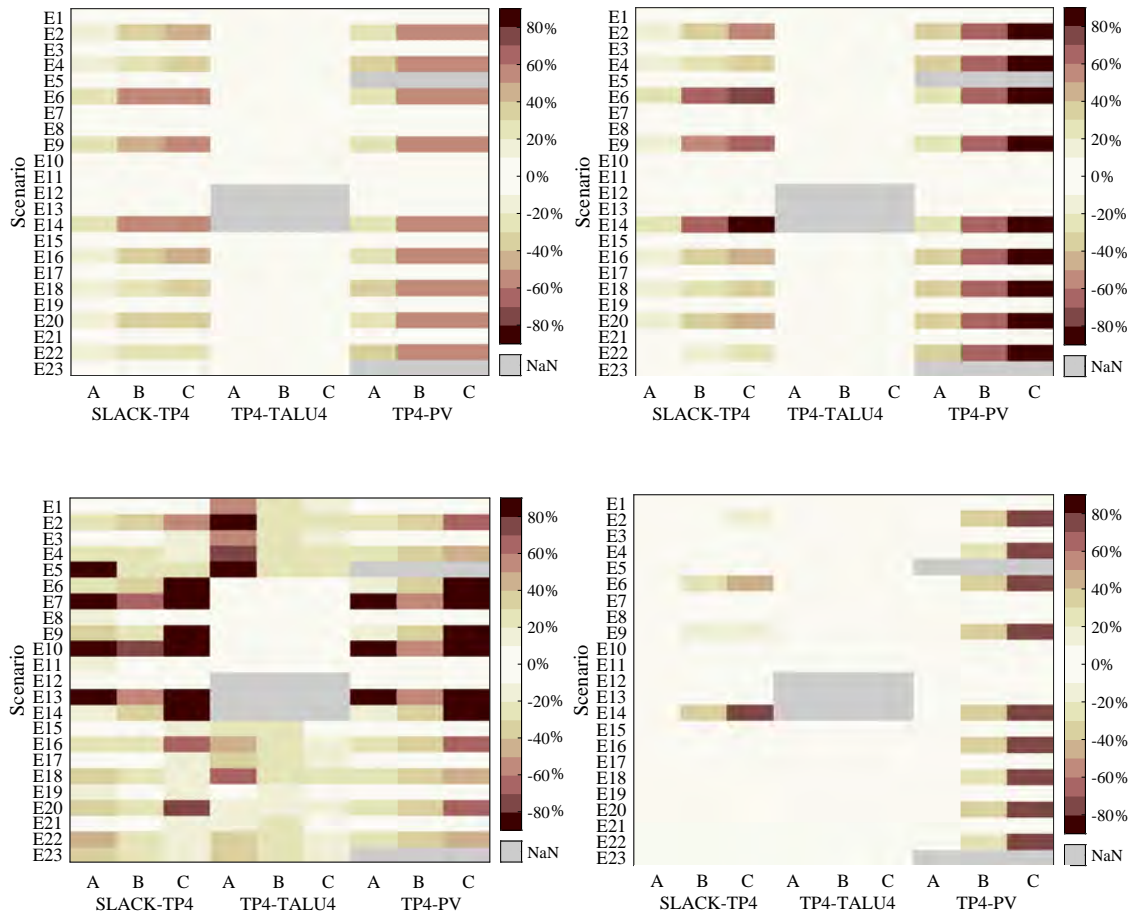

Figure 23. Percentage errors of power parameters (BF-NC vs BF-ND)

operates at low solar irradiance are above 20 %. In comparison, the errors do not exceed 5 % at high solar irradiance.

Fig. **23**b presents the errors regarding active power. For the TALU4 lighting sub-board, values between 0,1 and 0,4 % can be observed in all operation scenarios. However, the active power errors in the branch from the feeder to the general floor panel (SLACK-TP4) are influenced by the active power errors injected by the PV system. Low solar irradiance scenario errors are between 20 and 90 %, which is reflected in the SLACK-TP4 branch errors, mainly when the PV system works with air extractors.

For the non-active power errors in Fig. **23**c, the values are higher than 10 % in scenarios where the dimmable luminaires operate at a low dimmer level (0 Vdc). These errors are in the order of 60 and 80 %, respectively, when operating at a high dimmer level (10 Vdc). In addition, the PV system operating at low solar irradiance affects the non-active power errors of the feeder branch (SLACK-TP4).

Following the non-active power errors, the same behavior can be observed for the power factor errors of the TP4-PV branch. Therefore, the error values of the feeder branch to the main floor panel (TP4) are between 30 and 90 % for these drivers.

3.6. Performance analysis of the strategies

Tables **V** and **VI** present a summary of the performance analysis of the studied strategies in terms of the waveforms and RMS values of the voltage, current, and power parameters. The following symbol conventions is used in the Tables, ✓: poor (Error >10), ✓✓: ordinary (6 <Error <10), ✓✓✓: acceptable (1 <Error <5), ✓✓✓✓: good (0,1 <Error <0,9), and ✓✓✓✓✓: excellent (Error <0,1).

The BF-NC strategy was established as a reference for the performance analysis because, within the load models in the frequency domain studied in this research, the Norton model equivalent to the coupled admittance matrix presented in the literature accurately estimates the current of a nonlinear load (23, 25, 27–30).

According to the results in Table **V**, the three strategies used exhibit excellent performance (0,03-1,3 %) in estimating the waveforms and RMS values of the voltage signals of the nodes of the electrical network. In terms of current, Table **V** shows the excellent performance of the BF-NC strategy, as the harmonic interaction is considered in the modeling of the PV system and the loads. However, the BF-ND and SIM-ND strategies, when compared against BF-NC, showed an acceptable performance (5,0 %) in scenarios of high solar irradiance, as well as a poor performance (>10 %) in scenarios of low solar irradiance.

Similarly, Table **VI** shows the performance analysis of the apparent power (S), active power (P), non-active power (Q), and power factor (fp) parameters. The performance of the BF-ND and SIM-ND strategies regarding non-active power for high and low solar irradiance scenarios is poor (>10 %) because of the behavior of dimmable luminaires working together at the lowest dimmer level (0 Vdc) and the operation of the PV system at low solar irradiance levels.

Table V. Performance of the studied strategies in terms of waveforms and RMS voltage values

Strategy	Node	Voltage				Branch	Current			
		Waveform		RMS value			Waveform		RMS value	
		HGinc	LGinc	HGinc	LGinc		HGinc	LGinc	HGinc	LGinc
BF-NC	Performance	✓✓✓✓✓	✓✓✓✓✓	✓✓✓✓✓	✓✓✓✓✓	Performance	✓✓✓✓✓	✓✓✓✓✓	✓✓✓✓✓	✓✓✓✓✓
BF-ND	Performance	✓✓✓✓✓	✓✓✓✓✓	✓✓✓✓✓	✓✓✓✓✓	Performance	✓✓✓	✓	✓✓✓	✓
	Maximum error	0,03 %	0,09 %	0,03 %	0,09 %	Maximum error	5,0 %	45,0 %	5,0 %	60,0 %
	TP4	<0,01 %	<0,06 %	<0,01 %	<0,06 %	SLACK-TP4	2-2,5 %	20-45 %	2-5 %	12-60 %
	TALU4	<0,01 %	<0,06 %	<0,01 %	<0,06 %	TP4-TALU4	3-5 %	2,5-3 %	0,3-2,5 %	0,2-1 %
	PV	<0,01 %	<0,06 %	<0,01 %	<0,06 %	TP4-PV	2-2,5 %	30-40 %	2-5 %	20-60 %
	Lighting	<0,03 %	<0,09 %	<0,03 %	<0,09 %	Lighting	2,5-5 %	2,5-5 %	<3,0 %	<0,9 %
	Extractors	<0,02 %	<0,06 %	<0,02 %	<0,06 %	Extractors	<2,5 %	<2,5 %	<0,3 %	<0,4 %
SIM- ND	Performance	✓✓✓✓	✓✓✓✓	✓✓✓✓	✓✓✓	Performance	✓✓✓	✓	✓✓✓	✓
	Maximum error	0,3 %	0,8 %	0,7 %	1,3 %	Maximum error	5,0 %	90,0 %	5,0 %	300,0 %
	TP4	<0,04 %	<0,07 %	<0,02 %	<0,08 %	SLACK-TP4	2-2,5 %	12-60 %	2-5 %	15-150 %
	TALU4	<0,03 %	<0,08 %	<0,02 %	<0,08 %	TP4-TALU4	3-4,2 %	2-3 %	0,3-2,5 %	0,2-1 %
	PV	<0,03 %	<0,07 %	<0,02 %	<0,08 %	TP4-PV	2-2,5 %	50-90 %	2-5 %	2-300 %
	Lighting	<0,3 %	<0,8 %	<0,7 %	<2,0 %	Lighting	2,5-5 %	2,5-5 %	<3 %	<0,9 %
	Extractors	<0,23 %	<0,5 %	<0,7 %	<1,3 %	Extractors	<2,5 %	<2,5 %	<0,3 %	<0,3 %

Note: ✓ - Poor, ✓✓ - Ordinary, ✓✓✓ - Acceptable, ✓✓✓✓ - Good, ✓✓✓✓✓ - Excellent.

Table VI. Analysis of performance of strategies in terms of power parameters

Strategy	Branch	S		P		Q		fp	
		HGinc	LGinc	HGinc	LGinc	HGinc	LGinc	HGinc	LGinc
BF-NC	Performance	✓✓✓✓✓	✓✓✓✓✓	✓✓✓✓✓	✓✓✓✓✓	✓✓✓✓✓	✓✓✓✓✓	✓✓✓✓✓	✓✓✓✓✓
BF-ND	Performance	✓✓✓	✓	✓✓✓	✓	✓	✓	✓✓✓	✓
	Maximum error	5,0 %	60,0 %	5,0 %	90,0 %	60,0 %	290,0 %	3,0 %	76,0 %
	SLACK-TP4	0,1-5 %	13-60 %	3-4,5 %	10-90 %	0,5-18 %	13-290 %	<0,2 %	0,5-75 %
	TP4-TALU4	0,2-3 %	0,2-0,8 %	<0,4 %	<0,4 %	1,4-55 %	1,4-80 %	0,2-3 %	0,2-1 %
	TP4-PV	3-5 %	20-60 %	3-5 %	27-90 %	5-8 %	20-260 %	<0,1 %	8-76 %
	Lighting	0,5-2,8 %	0,6-0,8 %	<0,4 %	<0,3 %	15-60 %	24-80 %	0,9-3,1 %	0,8-1,1 %
	Extractors	0,2-0,3 %	0,1-0,4 %	<0,1 %	<0,4 %	1,.3-2,2 %	1,3-2,5 %	<0,3 %	<0,3 %
SIM-ND	Performance	✓✓✓	✓	✓✓✓	✓	✓	✓	✓✓✓	✓
	Maximum error	5,0 %	75,0 %	5,0 %	90,0 %	60,0 %	290,0 %	3,0 %	76,0 %
	SLACK-TP4	2,5-5 %	14-60 %	2,5-5 %	10-90 %	1-17 %	9-290 %	<0,1 %	0.4 %–75 %
	TP4-TALU4	0.5 %–2,5 %	0.1 %–0,8 %	<0,4 %	<0,4 %	1 %–55 %	1 %–80 %	0,2-3 %	0,2-1 %
	TP4-PV	3-5 %	20-75 %	3-5 %	27-90 %	4-9 %	20-260 %	<0,1 %	8-76 %
	Lighting	0,8-3,3 %	0,1-2,5 %	0,1-2,4 %	0,2-2,4 %	15-60 %	24-80 %	0,9-3 %	0,8-1 %
	Extractors	<0,9 %	<0,9 %	<0,9 %	<0,7 %	1,2-2,4 %	0,6-3,2 %	<0,3 %	<0,3 %

Note: ✓ - Poor, ✓✓ - Ordinary, ✓✓✓ - Acceptable, ✓✓✓✓ - Good, ✓✓✓✓✓ - Excellent.

4. Conclusions

In this study, the performance of three power flow solution strategies based on the BF sweep iterative method was evaluated while considering nonlinearity and load imbalance, harmonic

distortion in the feed signal, and the power injection of the PV system. A detailed analysis of the model's impact on the voltage and current signals and power parameters was conducted, as the selection of the load model influenced the results of the estimation of these variables.

The NRMSEs were less than 0,8 % in terms of voltage when comparing the SIM-ND and BF-ND approaches to BF-NC. Additionally, the maximum error obtained in the estimation of the RMS voltage values was 1,3 %. Therefore, all three approaches exhibit a satisfactory performance in estimating the voltage signal of the network.

Considering the current results, the NRMSEs and RMS values were less than 5,0 % in the operation scenarios where the PV system operated at high solar irradiance levels. In contrast, maximum NRMSEs of 45 % (BF-ND) and 90 % (SIM-ND) and maximum RMS current errors of 60 % (BF-ND) and 300 % (SIM-ND) were obtained when the PV system operated at low solar irradiance levels. Therefore, the BF-ND and SIM-ND strategies exhibit an acceptable performance during high solar irradiance operation, in contrast to the values reported for low solar irradiance operation, where the performance was regarded as ordinary.

Meanwhile, regarding the analysis of power parameters, the maximum errors for the apparent power, active power, and power factor were less than 5 % in the scenarios of high solar irradiance. The maximum errors were greater than 60 % when scenarios of low solar irradiance were analyzed. However, for the non-active power reported by the BF-ND, SIM-ND, and BF-NC approaches, there are errors of 60 % for high solar irradiance scenarios and 290 % for low solar irradiance scenarios. Therefore, the overall performance obtained by the three approaches in the analysis of power parameters is ordinary.

Finally, the BF algorithm, adjusted to the conditions of the studied distribution network, can easily be applied to other electrical networks with similar nonlinear elements and characteristics. There is also the possibility of integrating other DER types into the network analysis, such as electric vehicles or storage systems.

5. CRediT author statement

All authors contributed equally to the research.

6. Acknowledgments

References

[1] S. Ouali and A. Cherkaoui, "An improved backward/forward sweep power flow method based on a new network information organization for radial distribution systems," *J. Elect. Comp. Eng.*, vol. 2020, art. 5643410, 2020. https://doi.org/10.1155/2020/5643410 ↑3

[2] M. Milovanović, J. Radosavljević, and B. Perović, "A backward/forward sweep power flow method for harmonic polluted radial distribution systems with distributed generation units," *Int. Trans. Elect. Energy Syst.*, vol. 30, no. 5, pp. 1-17, 2020. https://doi.org/10.1002/2050-7038.12310 ↑3, 4

[3] A. Garcés-Ruiz, "Flujo de potencia en redes de distribución eléctrica trifásicas no equilibradas utilizando Matlab: Teoría, análisis y simulación cuasi-dinámica," *Ingeniería*, vol. 27, no. 3, art. e19252, 2022. https://doi.org/10.14483/23448393.19252 ↑3

[4] A. Suchite-Remolino, H. F. Ruiz-Paredes, and V. Torres-Garcia, "A new approach for PV nodes using an efficient backward/forward sweep power flow technique," *IEEE Latin America Trans.*, vol. 18, no. 6, pp. 992-999, 2020. https://doi.org/10.1109/TLA.2020.9099675 ↑3

[5] R. Taheri, A. Khajezadeh, M. H. Rezaeian Koochi, and A. Sharifi Nasab Anari, "Line independency-based network modelling for backward/forward load flow analysis of electrical power distribution systems," *Turkish J. Elect. Eng. Comp. Sci.*, vol. 27, no. 6, pp. 4551-4566, 2019. https://doi.org/10.3906/elk-1812-137 ↑3

[6] X. Wang, M. Shahidehpour, C. Jiang, W. Tian, Z. Li, and Y. Yao, "Three-phase distribution power flow calculation for loop-based microgrids," *IEEE Trans. Power Syst.*, vol. 33, no. 4, pp. 3955-3967, 2018. https://doi.org/10.1109/TPWRS.2017.2788055 ↑3

[7] A. Al-sakkaf and M. AlMuhaini, "Power flow analysis of weakly meshed distribution network including DG," *Eng. Technol. App. Sci. Res.*, vol. 8, no. 5, pp. 3398-3404, 2018. https://doi.org/10.48084/etasr.2277 ↑3

[8] M. Milovanović, J. Radosavljević, B. Perović, and M. Dragičević, "Power flow in radial distribution systems in the presence of harmonics," *Int. J. Elect. Eng. Comp.*, vol. 2, no. 1, pp. 10-19, 2019. https://doi.org/10.7251/IJEEC1801011M ↑3, 4

[9] D. Buła and M. Lewandowski, "Steady state simulation of a distributed power supplying system using a simple hybrid time-frequency model," *App. Math. Comp.*, vol. 319, pp. 195-202, 2018. https://doi.org/10.1016/j.amc.2017.02.028 ↑3

[10] M. A. Amini, A. Jalilian, and M. R. Pour Behbahani, "Fast network reconfiguration in harmonic polluted distribution network based on developed backward/forward sweep harmonic load flow," *Elect. Power Syst. Res.*, vol. 168, pp. 295-304, 2019. https://doi.org/10.1016/j.epsr.2018.12.006 ↑3, 4

[11] J. C. Hernandez, F. J. Ruiz-Rodriguez, F. Jurado, and F. Sanchez-Sutil, "Tracing harmonic distortion and voltage unbalance in secondary radial distribution networks with photovoltaic uncertainties by an iterative multiphase harmonic load flow," *Elect. Power Syst. Res.*, vol. 185, art. 106342, 2020. https://doi.org/10.1016/j.epsr.2020.106342 ↑3

[12] F. J. Ruiz-Rodriguez, J. C. Hernandez, and F. Jurado, "Iterative harmonic load flow by using the point-estimate method and complex affine arithmetic for radial distribution systems with

photovoltaic uncertainties," *Int. J. Elect. Power Energy Syst.*, vol. 118, art. 105765, 2020. https://doi.org/10.1016/j.ijepes.2019.105765 ↑3

[13] A. M. Kettner, L. Reyes-Chamorro, J. K. Maria Becker, Z. Zou, M. Liserre, and M. Paolone, "Harmonic power-flow study of polyphase grids with converter-interfaced distributed energy resources-Part I: Modeling framework and algorithm," *IEEE Trans. Smart Grid*, vol. 13, no. 1, pp. 458-469, 2022. https://doi.org/10.1109/TSG.2021.3120108 ↑3, 4

[14] W. Sun and G. P. Harrison, "Distribution network hosting capacity assessment: Incorporating probabilistic harmonic distortion limits using chance constrained optimal power flow," *IET Smart Grid*, vol. 5, no. 2, pp. 63-75, 2022. https://doi.org/10.1049/stg2.12052 ↑3, 4

[15] R. Satish, K. Vaisakh, A. Y. Abdelaziz, and A. El-Shahat, "A novel three-phase harmonic power flow algorithm for unbalanced radial distribution networks with the presence of D-STATCOM devices," *Electronics (Switzerland)*, vol. 10, no. 21, art. 2663, 2021. https://doi.org/10.3390/electronics10212663 ↑3, 4

[16] R. Satish, P. Kantarao, and K. Vaisakh, "A new algorithm for harmonic impacts with renewable DG and non-linear loads in smart distribution networks," *Technol. Econ. Smart Grids Sust. Energy*, vol. 7, no. 1, art. 8, 2022. https://doi.org/10.1007/s40866-022-00134-1 ↑3, 4

[17] D. Chathurangi, U. Jayatunga, M. Rathnayake, A. Wickramasinghe, A. Agalgaonkar, and S. Perera, "Potential power quality impacts on LV distribution networks with high penetration levels of solar PV," presented at *Int. Conf. Harmon. Qual. Power, ICHQP*, Ljubljana, Slovenia, 2018. https://doi.org/10.1109/ICHQP.2018.8378890 ↑4

[18] Z. Deng, G. Todeschini, K. L. Koo, and M. Mulimakwenda, "Modelling renewable energy sources for harmonic assessments in DIgSILENT PowerFactory: Comparison of different approaches," in *11th Int. Conf. Simul. Mod. Method. Technol. App., SIMULTECH 2021*, 2021, pp. 130-140. https://doi.org/10.5220/0010580101300140 ↑4

[19] W. Yuan, X. Yuan, L. Xu, C. Zhang, and X. Ma, "Harmonic loss analysis of low-voltage distribution network integrated with distributed photovoltaic," *Sustainability (Switzerland)*, vol. 15, no. 5, art. 4334, 2023. https://doi.org/10.3390/su15054334 ↑4

[20] S. M. Ahsan, H. A. Khan, A. Hussain, S. Tariq, and N. A. Zaffar, "Harmonic analysis of grid-connected solar PV systems with nonlinear household loads in low-voltage distribution networks," *Sustainability (Switzerland)*, vol. 13, no. 7, art. 3709, 2021. https://doi.org/10.3390/su13073709 ↑4

[21] G. Osma-Pinto and G. Ordóñez-Plata, "Measuring factors influencing performance of rooftop PV panels in warm tropical climates," *Solar Energy*, vol. 185, pp. 112-123, 2019. https://doi.org/10.1016/j.solener.2019.04.053 ↑5

[22] G. Osma-Pinto and G. Ordóñez-Plata, "Measuring the effect of forced irrigation on the front surface of PV panels for warm tropical conditions," *Energy Rep.*, vol. 5, pp. 501-514, 2019. https://doi.org/10.1016/j.egyr.2019.04.010 ↑5

[23] A. Martinez-Penaloza, L. Carrillo-Sandoval, and G. Osma-Pinto, "Determination and performance analysis of the Norton equivalent models for fluorescents and LED recessed lightings," presented at *2019 IEEE W. Power Elect. Power Qual. App., PEPQA 2019*, Manizales, Colombia, 2019. https://doi.org/10.1109/PEPQA.2019.8851554 ↑8, 16, 17, 24

[24] A. Martínez-Peñaloza, L. Carrillo-Sandoval, G. Malagón-Carvajal, C. Duarte-Gualdrón, and G. Osma-Pinto, "Determination of parameters and performance analysis of load models for fluorescent recessed lightings before power supply signal," *DYNA (Colombia)*, vol. 87, no. 215, pp. 163-173, 2020. https://doi.org/10.15446/dyna.v87n215.85239 ↑8, 16, 17, 21

[25] A. Martínez-Peñaloza and G. Osma-Pinto, "Analysis of the performance of the Norton equivalent model of a photovoltaic system under different operating scenarios," *Int. Review Elect. Eng. – IREE*, vol. 16, no. 4, pp. 328-343, 2021. https://doi.org/10.15866/iree.v16i4.20278 ↑ 8, 15, 16, 18, 22, 24

[26] A. Martínez Peñaloza, G. Osma-Pinto, and G. Ordóñez-Plata, "Parameter determination of coupled and decoupled admittance matrix methods of the Norton equivalent model for an air extractor," *Tecnura*, vol. 26, no. 74, pp. 17-34, 2022. https://doi.org/10.14483/22487638.18806 ↑8, 16

[27] Z. Guo *et al.*, "Aggregate harmonic load models of residential customers. Part 2: Frequency-domain models," in *2019 IEEE PES Innov. Smart Grid Technol. Europe, ISGT-Europe*, 2019, pp. 1-5. https://doi.org/10.1109/ISGTEurope.2019.8905746 ↑24

[28] X. Xu *et al.*, "Aggregate harmonic fingerprint models of PV inverters. Part 1: Operation at different powers," in *Int. Conf. Harmon. Qual. Power, ICHQP*, 2018 pp. 1-6. https://doi.org/10.1109/ICHQP.2018.8378824 ↑24

[29] S. Muller *et al.*, "Aggregate harmonic fingerprint models of PV inverters. Part 2: Operation of parallel-connected units," in *Int. Conf. Harmon. Qual. Power, ICHQP*, 2018, pp. 1-6. https://doi.org/10.1109/ICHQP.2018.8378835 ↑24

[30] E. Tavukcu, S. Müller, and J. Meyer, "Assessment of the performance of frequency domain models based on different reference points for linearization," *Renewable Energy Power Qual. J.*, vol. 17, no. 17, pp. 435-440, 2019. https://doi.org/10.24084/repqj17.337 ↑24

Alejandra Martínez Peñaloza

She received the BSc degree in Electric Engineering in 2018 and the MSc degree in Electric Engineering in 2022 from Universidad Industrial de Santander, Colombia. She is currently a PhD student at Universidad Industrial de Santander, Colombia. Her areas of interest include modeling and simulations of electrical networks, renewable distributed resources, and power quality, among others.
Email: alejandra2198146@correo.uis.edu.co

Gabriel Ordóñez Plata

Gabriel Ordóñez-Plata received the BE (*cum laude*) degree from the Universidad Industrial de Santander (UIS), Bucaramanga, Colombia, in 1985. He received the PhD degree in Electrical Engineering from Universidad Pontificia Comillas, Madrid, España, in 1993. Since 1985, he has been with the Electrical, Electronic and Telecommunications Engineering School (E3T) of UIS, Bucaramanga, Colombia, where he is currently a full professor. His research interests are related to the energy transition and sustainable development, which include green buildings, smart grids, smart metering, electrical power quality, and the rational and efficient use of energy.
Email: gaby@uis.edu.co

German Alfonso Osma Pinto

He received the BE (Electrical Engineering and Industrial Engineering), MS (Electrical Engineering), and PhD (Engineering) degrees from the Universidad Industrial de Santander (UIS), Bucaramanga, Colombia, in 2007, 2011, and 2016 respectively. He mainly conducts research on photovoltaics, green buildings, automation, distributed energy resources, resilience, and power quality. He has been with the Electrical, Electronic and Telecommunications Engineering School (E3T) of UIS, Bucaramanga, Colombia, since 2017, where he is currently an assistant professor.

Email: gealosma@uis.edu.co

Research

Application of Regular Grammar in the Syntactic Analysis of Email Addresses

Aplicación de gramática regular en el análisis sintáctico de direcciones de correo electrónico

Cristian Alejandro Fandiño-Mesa[1], Marco Javier Suárez-Barón[2]✉*, and César Augusto Jaramillo-Acevedo[3]

[1]Universidad Pedagógica y Tecnológica de Colombia (Sogamoso, Colombia)
[2]Universidad Pedagógica y Tecnológica de Colombia (Sogamoso, Colombia)
[3]Universidad Tecnológica de Pereira (Pereira, Colombia)

Abstract

Context: This article proposes the use of regular grammar as a strategy to validate the textual structures of emails. It focuses on the RFC 5321 standard and its syntax, formalizing regular grammars to apply production rules with the aim of validating the syntactic context of each structure of an email address.

Method: This article presents a literature review and the development of an email validation model. Related texts focus on the Internet Protocol, along with building automata that apply IPV4 protocol. There are three phases: the development of the model from syntax and regular grammar rules and its construction and application.

Results: The result is a functional application that validates email addresses based on regular grammars and existing regulations. When running efficiency tests, our application obtained a higher email validation margin in comparison with JFLAP. The library can work as a great analyzer of grammatical or lexical structures.

Conclusions: The email validation tool based on GR regular grammars contributes to the practical use of specialized algorithms in the field of computer science, since it is possible to apply it to the recognition of search patterns such as the analysis of lexical structures (e.g., NITs, alphanumeric codes, and valid URLs).

Keywords: email validation, formal grammar, regular expressions

*✉ **Correspondence:** marco.suarez@uptc.edu.co

Resumen

Contexto: En este artículo se propone el uso de la gramática regular como estrategia para validar las estructuras textuales de los correos electrónicos. El estudio se enfoca en el estándar RFC 5321 y su sintaxis, formalizando gramáticas regulares para aplicar reglas de producción en aras de validar el contexto sintáctico de cada estructura de una dirección de correo electrónico.

Método: Este artículo presenta una revisión de la literatura y el desarrollo de un modelo para la validación de correos electrónicos. Los textos relacionados se enfocan en el Protocolo de Internet junto con la construcción de autómatas que utilizan direccionamiento IPV4. El estudio tiene tres fases: el desarrollo del modelo a partir de la sintaxis y reglas gramaticales regulares y la construcción y aplicación del mismo.

Resultados: El resultado es una aplicación funcional que válida direcciones de correo electrónico con base en gramáticas regulares y la reglamentación existente. Al ejecutar pruebas de eficiencia, nuestra aplicación obtuvo un margen de validación de correos mayor en comparación con JFLAP. La librería puede funcionar como un gran analizador de estructuras gramaticales o léxicas.

Conclusiones: La herramienta de validación de correos electrónicos basada en gramáticas regulares GR contribuye al uso práctico de algoritmos especializados en la rama de la computación, dado que es posible aplicarla en el reconocimiento de patrones de búsqueda como el análisis de estructuras léxicas (*e.g.*, NITs, códigos alfanuméricos, y URL válidas).

Palabras clave: validación de correos electrónicos, gramática formal, expresiones regulares

Table of contents

1.   Introduction

The Finite State Machine (FSM), the stack automaton, and Regular Grammar (RG) have undergone extensive study in the context of computation theory and application in formal verification, formal analysis, software design, and natural language processing (1). The group of theory-based computing methods for the automatic analysis and representation of human languages is known as Natural Language Processing (NLP). However, in order for text to be automatically analyzed at the same pace as humans, there is still a long way to go, especially knowledge of natural language process PLN (2).

In the 1950s, Noam Chomsky began his study of natural languages, whose objective was to formally define their syntax (3). To this effect, Chomsky introduced generative grammar. Later, it was discovered that the syntax of programming languages can be described Chomsky's grammatical models (context-free grammars). Formal grammar is defined as the set of rules by which the chains of a language are constructed, that is, a grammar is a set of rules that describe a language. These rules are called *production rules* (3), and they describe how to form valid strings from the alphabet of the language.

Language recognition and the establishment of the rules for regular grammar enabled the advent of the stack automaton, oriented towards applications in the validation of emails. This automaton analyzes both basic address structures and those containing special characters. It works in line with the RFC 5321 and 5322 norms (4), as per the recommendations of the Internet Engineering Task Force (IETF). As some issues are currently solved thanks to the validation and detection of spam fraud, a list of valid and invalid addresses ensures functionalities for companies that handle mailing.

Most of the texts related to FSM focus on Internet Protocol (IP) resources to deal with identity theft and network operators. In (5) is proposed a finite automaton scheme that accepts the IPV4 class of addresses, providing the descriptions of the languages together with the IPs and their proper construction for the automaton. The states and transitions that comprise it are shown in said work, which discusses the design of an automaton that accepts the class of IP addresses so that they accept the class in IPV4. In (6), inconsistencies are shown which can allow attackers to bypass email authentication to impersonate arbitrary senders and forge emails signed by Domain Keys Identified Mail (DKIM) with the signature of a legitimate site.

The process includes verifying the structure of an email address based on currently valid regulations, identifying the indicated syntax and explaining the operation of DKIM. By performing various tests with bad addresses that are used for spamming and injection attacks, including cross-site scripting (XSS), SQL injection, and Remote Code Execution (RCE) or spoofing, the possible security flaws of organization when acquiring IT services are evidenced.

The problem with analyzing the structures of emails has to do with syntactic validation, which includes an analysis of the syntax that ensures the validity of an email, while semantic validation could allow only analyzing the addresses of specific domains.

This work is carried out through a review of specialized scientific literature and the construction of RG focused on the syntactic rules of email addresses. With the help of the JFLAP tool, the response of the automaton is validated. After several tests, both valid and invalid addresses are entered, verifying that each of these chains is fulfilled. Then, the algorithm is built, which consists of two parts: the logic of the class to perform validations and the Graphical User Interface (GUI). This algorithm is once again verified with several email addresses. Finally, the distribution of the library is prepared in a repository for third-party applications (Pypi) for later use. Using this library and platforms such as JFLAP, the response time when entering a number of emails from certain addresses or their validity can be checked and compared with accuracy, covariance and precision.

This work is organized as follows. It begins with a description of the materials, methods and methodology used in the design and validation of the proposed algorithm. This is followed by a review of the specialized literature on regular grammar along with its formal definition. Tables of RG rules are shown, along with the result obtained with JFLAP, ending with the tests conducted on the algorithm in specific scenarios, together with the application and subsequent installation of the designed library. Finally, the conclusions and proposals for future work are presented.

2. Subject development

2.1. Methodology

For email validation from RG, stack automata and Python programming were used. The theory involved is based on (1,2,7). In addition, the RFC 5321 and 5322 norms were reviewed, which propose a structure of mail forms. These regulations are the basis of the validation of the rules regarding regular grammar, and their objective is to ensure not only that the most common emails work but also those that possess the characteristics outlined in the regulations. During this process, the JFLAP platform and the PyCharm Community IDE were used to display a sketch of the automaton to be programmed.

The methodology applied in this work is depicted in Fig. **1**. It is observed that formal grammar reads the input string one symbol at a time (7), verifying that the chain complies with RFC standards, thus allowing to identify the entry of the mail in its two divisions (i.e., the local part and the domain part) since the grammar rules of each one have already been defined.

2.1.1. Formal definition of stack automata

A *stack automaton* is a finite automaton equipped with stack-based memory. Each transition is based on the current input symbol and on top of the stack (3). It optionally removes the top of the stack and optionally inserts new symbols in it. Initially, the stack contains a special symbol $Z0$ that indicates the bottom of the stack.

It is defined as $M = (Q, \Sigma, \Gamma, \delta, q_0, Z, F)$, where:

- Q is a set of states

- Σ is the alphabet of input symbols

- Γ is an alphabet of stack symbols

- δ is a transition function used to move from the current state to the next one

The transition function is described in Eq. (1), understanding that the element $(p, a, A, q, \alpha) \in \delta$ is a transition from M. This means that M in the state $p \in Q$ at the entrance a $\in \Sigma \cup \{\varepsilon\}$ and with $A \in \Gamma$. As a top battery symbol, it can be read a, change the state q, delete A, replacing it with the thrust a $\in \Gamma^*$. The component of the transitional relationship is given by $\Sigma \cup \{\varepsilon\}$. The stack automaton allows access and operations in deeper elements. Stack automata can recognize a strictly larger set of languages than insert automata (1). A stack automaton allows full access and makes it easy for stacked values to be
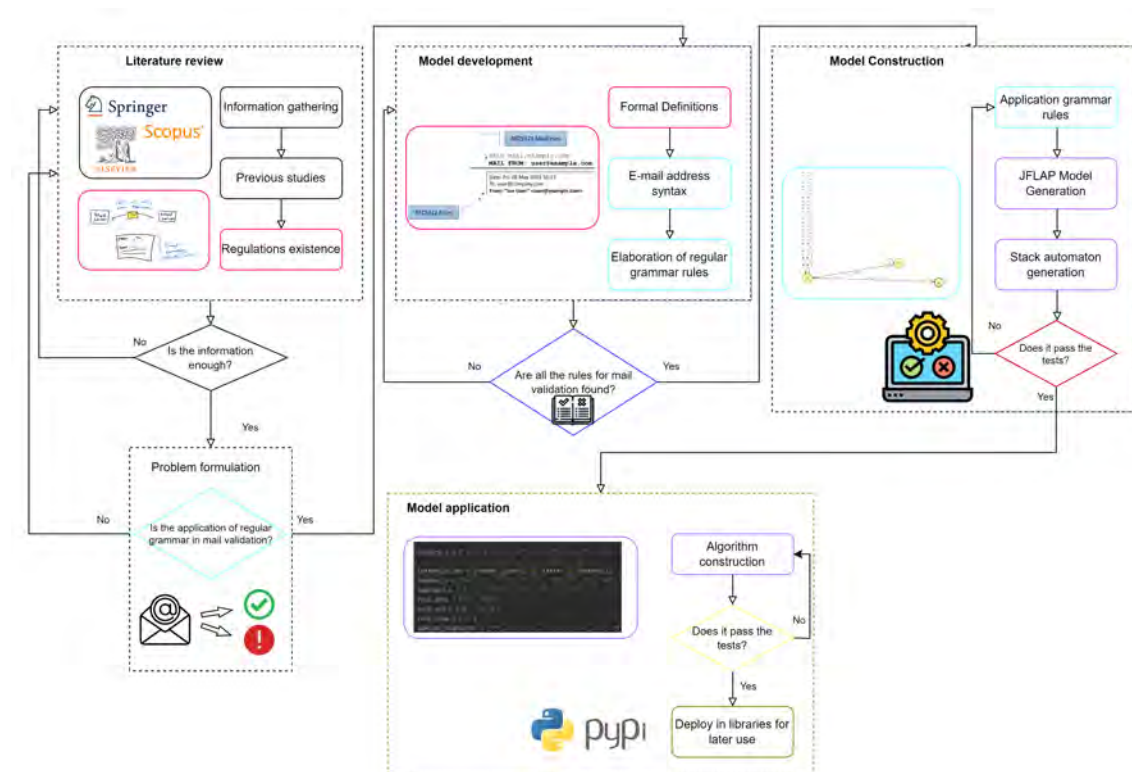
Figure 1. Diagram of the grammar analysis process

complete sub-stacks rather than a set of unique finite symbols. These automata (related to pushdown automata) can step left or right in the input string (surrounded by special end symbols to prevent them from escaping) and move up or down the string in read-only mode (2). A stack automaton is said not to be erased if it never leaves the stack.

The turnstile notation is represented by the symbol $\vdash$, which represents a movement. For example, $(p, b, T) \vdash (q, w, a)$. This implies that, while a transition is made from state p to state q, the input symbol b is consumed, and the top of the stack T is replaced by a new string a.

The sign $\vdash^*$ represents a sequence of movements.

The language accepted by a stack automaton can be defined in two different and equivalent ways (2):

- *Acceptance by final state.* The AP is said to accept the input by the final state if it enters any final state at zero or more moves after reading the entire input.

- *Acceptance by empty stack*. When reading the input string of the initial configuration for some APs, the AP stack is emptied (7).

2.1.2. Formal definition of RGs

Regular grammar generates regular language. RGs have a single nonterminal on the left side and a right side consisting of a single terminal or a single terminal followed by a nonterminal. Formally, a grammar consists of a set of nonterminal (or variables) V, a set of terminals Σ (the language alphabet), a beginning symbol S, which is a nonterminal, and a set of rewriting rules (productions) P (7).

A right-hand regular grammar (also called a *right-hand linear grammar*) is a formal grammar (N, σ, P, S) in which all production rules in P have one of the following forms:

$$A \to aB \tag{1}$$

$$A \to a \tag{2}$$

$$A \to \varepsilon \tag{3}$$

where A, B, and $S \in N$ are nonterminal symbols, $a \in \Sigma$ is a terminal symbol, and ε denotes the empty string, *i.e.*, the string of length 0. S is called the *start symbol* (8).

In a regular left grammar (also called a *left linear grammar*), all rules obey the following forms:

$$A \to Ba \tag{4}$$

The language described by a given grammar is the set of all strings that contain only terminal symbols and can be derived from the start symbol via the repeated application of production rules. These two types of grammars have the same generative power, *i.e.*, given a linear grammar on the left, there is always a linear grammar on the right that is equivalent to it, and *vice versa*. In addition, given a regular language, there is always (at least) a linear grammar on the left and a linear grammar on the right that generate it. There is no profound difference between left and right linear grammar.

A regular grammar is a quadruple (V, Σ, R, S), where:

- V is an alphabet of variables
- Σ is an alphabet of constants
- R, the set of rules, is a finite subset of $V \times (\Sigma V \cup \Sigma)$
- S, the initial symbol, is an element of V

This grammar, together with the set of rules, is determined under the elements of $V - \Sigma$, which are called *nonterminals* and are analogous to parts of speech. In the example, $G = (V, \Sigma, R, S)$ where $V = \{S, a, b\}, \Sigma = \{a, b\}$, and R has the rules $S \to aSb$ and $S \to \varepsilon$.

Nonterminals are generally represented by capital letters and terminals by lowercase letters. Therefore, a context-free grammar can be given simply by providing the rules and the starting symbol without a tuple of 4. The above-mentioned grammar can be represented as:

$$S \to aSb \tag{5}$$

$$S \to \varepsilon \tag{6}$$

Here is a derivation of this grammar.

$$S \implies aSb \implies aaSbb \implies aabb$$

Such a derivation has to eliminate the nonterminal. It is also possible to write this derivation as

$$S \implies {}^{*}aabb \tag{7}$$

Given a context-free grammar G, the language generated by G, $L(G)$, is the set of terminal strings that can be derived from the initial symbol for G.

2.1.3. Syntax

- Email syntax
  Each email address consists of three elements: the local part, the @ symbol (pronounced as "at"), and the domain name. The local part is placed before the @ symbol, and the domain name is placed after it (9). An example of this is the email johndoe@company.com, where " johndoe " is the local part and " company.com " is the domain. Emails are not valid without these items.

  parte_local@dominio

- Local part
  The local part is the username that indicates a unique name for the mailbox. It can contain

  - Uppercase and lowercase Latin letters (AZ, az)
  - Numerical values (from 0 to 9)
  - Special characters, such as #! % $ '& + * -/=? ^_'. {| }

  It should be noted that the period character (.) Is valid for the local part unless it is placed at the beginning or the end of an email address (9). Moreover, there cannot be two or more periods in a row in the email address (*e.g.*, John.. Doe @ company.com is not allowed).

  The local postmaster part is treated in a special way: it is not case-sensitive and should be forwarded to the email manager of the domain (10). Technically, all other local parts are case-sensitive. Therefore, jsmith@example.com specifies different mailboxes, but many organizations treat uppercase and lowercase letters as equivalent. In fact, RFC 5321 warns that "a host waiting to receive mail should avoid defining mailboxes where the local part is case sensitive"[p. 405] (11).

- @ symbol
  The @ symbol connects the domain and the person who owns the email address.

- Domain name
  A domain name consists of one or more parts separated by a period, such as example.com (9). Each part must not be longer than 63 characters and can contain the following:

- Uppercase and lowercase Latin letters (AZ, az)
- Numerical values (from 0 to 9), with the condition that the entirety if the domain cannot be numerical
- A dash (-), as long as it is not placed at the beginning or end of the domain name

The domain name indicates the name of the organization. It is an address that leads to the organization's website. When an email is sent, the sending mail server looks for another mail server that matches the domain name of the recipient's address (11). If someone sends a message to a user at company.com, the mail server first checks to see if there is a replying mail server at company.com. If so, it will contact the mail server to see if the username is valid. If the user is real, the email will be delivered.

- Standardization of local parts
  The interpretation of the local part of an email address depends on the conventions and policies implemented in the mail server. For example, case sensitivity can distinguish mailboxes that differ only in the uppercase of the characters in the local part, although this is not very common (11). Gmail ignores all dots in the local part of an @ gmail.com address to determine the identity of the account.

- Particularity
  There is a particularity that is added to the RG: the words dot and at are accepted *verbatim*, making reference to the signs used in the English language. These must be found within the square brackets to be accepted as valid email addresses. In the case of parentheses, they are allowed at either end of the email address in the local part, and they will be identified as comments. With the above, the emails (comment)test@mail.com and test(comment)@mail.com are valid. Table **I** shows some examples of valid and invalid emails.

Table I. Valid and invalid emails

Valid emails	Invalid emails
simple@example.com	Abc.example.com
very.common@example.com	A @ b @ c @ example.com
disposable.style.email.with+symbol@example.com	a "b (c) d, e: f; g<h>i [j \k] l@example.com
other.email-with-hyphen@example.com	just "notright@example.com
fully qualified-domain@example.com	this is "not \allowed@example.com
user.name+tag+sorting@example.com	this \still \"not \\allowed@example.com
x@example.com	i_like_underscore@but_its_not_allowed_in_this_part.example.com
example-indeed@strange-example.com	QA [icon] CHOCOLATE [icon] @ test.com
test/test@test.com	Testing.fail [at] failed@mail.com
mailhost!username@example.org	@ example.com
user %example.com@example.org	@ example.com
marc [at] mail [dot] is	Joe smith<email@example.com>
karmany [at] email [dot] net	.email @ example.com
test [at] email [dot] net [dot] co	email. @ example.com

2.2. Results and discussion

To verify that the application complied with the RFC 5321 and 5322 standards, it was subjected to a series of tests in different scenarios, where the operation of the main classes was evaluated along with their functions, as well as the results obtained, either in the console or within the application itself. In these tests, the entry of different email addresses and their operation was carried out together with the explanation of the class that performs the ratification. Finally, the algorithm was described and constructed, with all the grammatical rules applied in the validation of emails with the implemented library.

2.2.1. Construction of regular grammar

The RG for email addresses is as follows:

Chains W, where $W \in L(M)$ and $L(G)$. It is stated that $L(M)$ or $L(G)$ defines the language of grammar for $W \subseteq$ "All valid (not just common) email address structures".

RG is formally represented as:

$$(\{S, B, T, U, A, V, X, Z, T, E\}, \{a, b \ldots y, z - 0, 1 \ldots 8, 9\}, \{(S, aU), (A, .S), (U, @V), \ldots (R, a)\}, S)$$

The rules established for the construction of the RG were elaborated based on the syntax of the RFC 5321 and 5322 regulations. Tables **II** and III present the rules described for the local part, the @ sign, and the domain name.

Table **II** presents all possible characters (already explained) that can be generated, indicating that, when a period is detected, there must be continuity with at least one character, and, when the local part is finished, it must be followed by the @ sign. This is described in the states S, U, and A. For state X, this works in the same way as in the previous states, except for special characters. In this rule, a period may be needed, followed by other characters that accompany the domain, together with the opening of the square bracket (if that option is to be selected). After the period or without it, it is possible to have another combination of characters that includes the hyphen (valid by regulation). The rule can allow to continue writing after the script, moving on to the next one, which will no longer contain hyphens.

Table **III** corresponds to the period and the @ sign. The rule for accepting the expression dot (period) is added. It was also possible to determine the special case for accepting the word *at* (at).

After writing the characters comes a final character, since it is not possible for the domain part to contain a hyphen. The domain part ends with any character that is contained in the above-presented Tables, with the exception of the hyphen, as well as without continuing to any variable. The stack is made based on the construction of the RG, where, for each alphabet of the input symbols, the stack is filled or emptied depending on the states to which the automata goes. It can be seen, in Fig. **2**, that there are more stack automata rules, which can be interpreted with the already explained grammar, considering that the stack will be eliminated as the conditions are met.

Table II. Characters valid for the local part and domain of the email

State S	Transition	State X	Transition	State S	Transition	State X	Transition
S →	aU aA aS	X →	aY aX	S →	0U 0A 0S	X →	0Y 0X
S →	bU bA bS	X →	bY bX	S →	1U 1A 1S	X →	1Y 1X
S →	cU cA cS	X →	cY cX	S →	2U 2A 2S	X →	2Y 2X
S →	dU dA dS	X →	dY dX	S →	3U 3A 3S	X →	3Y 3X
S →	eU eA eS	X →	eY eX	S →	4U 4A 4S	X →	4Y 4X
S →	fU fA fS	X →	fY fX	S →	5U 5A 5S	X →	5Y 5X
S →	gU gA gS	X →	gY gX	S →	6U 6A 6S	X →	6Y 6X
S →	hU hA hS	X →	hY hX	S →	7U 7A 7S	X →	7Y 7X
S →	iU iA iS	X →	iY iX	S →	8U 8A 8S	X →	8Y 8X
S →	jU jA jS	X →	jY jX	S →	9U 9A 9S	X →	9Y 9X
S →	kU kA kS	X →	kY kX	S →	!U !A !S	X →	-Y -X
S →	lU lA lS	X →	lY lX	S →	#U #A #S		
S →	mU mA mS	X →	mY mX	S →	$U $A $S		
S →	nU nA nS	X →	nY nX	S →	%U %A %S		
S →	oU oA oS	X →	oY oX	S →	&U &A &S		
S →	pU pA pS	X →	pY pX	S →	'U 'A 'S		
S →	qU qA qS	X →	qY qX	S →	*U *A *S		
S →	rU rA rS	X →	rY rX	S →	+U +A +S		
S →	sU sA sS	X →	sY sX	S →	/U /A /S		
S →	tU tA tS	X →	tY tX	S →	=U =A =S		
S →	uU uA uS	X →	uY uX	S →	?U ?A ?S		
S →	vU vA vS	X →	vY vX	S →	^U ^A ^S		
S →	xU xA xS	X →	xY xX	S →	_U _A _S		
S →	yU yA yS	X →	yY yX	S →	'U 'A 'S		
S →	zU zA zS	X →	zY zX	S →	{U {A {S		
S →	[U			S →	|U |A |S		
				S →	}U }A }S		
				S →	-U -A -S		

The construction of the algorithm is carried out in two files, which contain the graphical user interface and the logical part of the email validation.

2.2.2. Application

This GUI was developed with the Tkinter package, which is a binding of the Tcl/Tk graphic library. The above is not a single library but consists of a few different modules, each with a separate functionality and its own official documentation for easy interface construction. This was done under the

Table III. Special mail rules

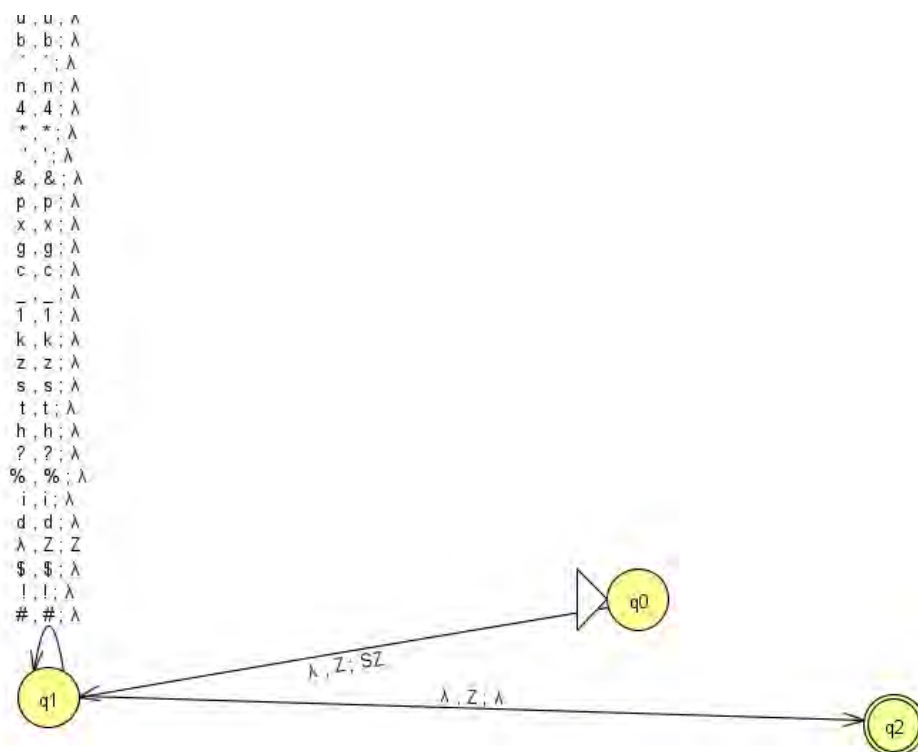| States	Transition
A	→ .S
U	→ @V
U	→ atC
B	→ .T
B	→ .V
B	→ dotD

Figure 2. Generated stack automaton

Model-View-Controller design pattern, in which the program is initialized along with its corresponding screen. In the model, the validateMail class is called to validate an email. If everything is correct, it will return the value with the email; otherwise, it will show an error message with the email.
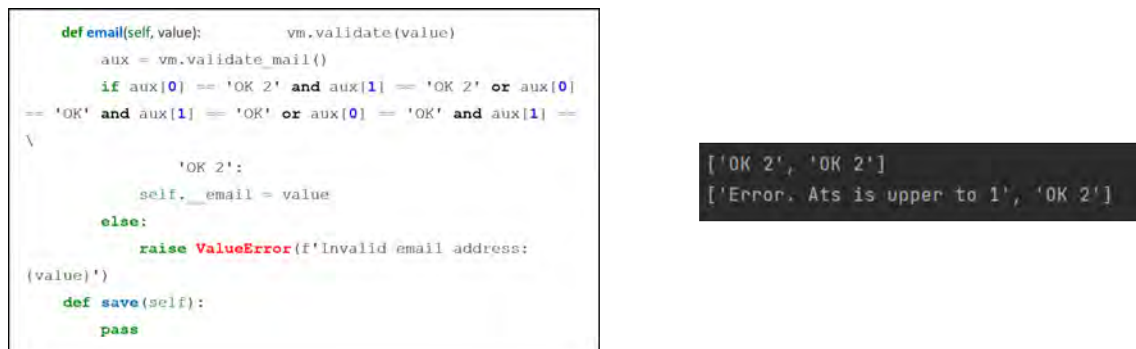
a. *Algorithm implementation*

In the logical part, the definition of global variables is proposed, describing the grammatical rules that must be fulfilled. These include lowercase and uppercase letters (using the upper function), numbers, special characters, the acceptance of symbols such as @ and the period, and adding square brackets.

When entering the validate function, a series of validations begins, such as the number of @ in the email and whether it contains atoms. Then, the mail is divided into two parts for verification, both the local part and the domain part, performing the corresponding iterations character by character. All the messages that are obtained in the results are stored in a list, from which it will be verified if the last two messages indicate that the email complies with the regulations. Next, test scenarios aimed at validating the application are presented, with the help of some of the classes that contain the main algorithm. This is done in different scenarios and under the input of several email addresses.

- *Scenario 1*

  When the program starts, it executes and creates the model instances with an example mail, together with the window with its size and the controller. The model carries out the instance by calling the main class, in which the email is verified. In this instance, the validation of the messages in the main class is performed by the stack. For an email to be valid, the last two messages are stored in an auxiliary variable, which will contain the last two positions, which would indicate the last two messages, as shown in Fig. 3a. For an email to be valid, it must have the message .ºK.ºr .ºK 2"; otherwise, it can indicate a message, such as the repetition of the @ character, two periods in a row, that the @ sign exists, or that it does not comply with any of the rules. This can be seen in Fig. 3b, for which the result will be shown in the console with both a valid email (first line) and an invalid email (second line).

Figure 3. Instance of the *validateMail* class with results in the console

- *Scenario 2*

  The algorithm contains the *validateMail* class, for which the *validate* function is entered and the string of characters from the mail is received. In the first case, the validation of the number of @ or *[at]* expressions is carried out. Assigning the message to the end of the queue indicates that the rule of @ is not being fulfilled. It will be given by finishing the execution of the class; otherwise, it will go to another function in which validations are performed for the local part and the domain. The validation of the @ sign can be seen in Fig. 4a along with the result obtained when executing it (Fig. 4b).

For the case where the number of characters is verified, which cannot exceed 64, the message is added to the final part of the already created queue. At this point, two messages are returned: the first would indicate the error, and the second the entry to a cycle. For the mail to be valid, it must have two messages with validation at the end of the queue.

Figure 4. Validation of the number of @ and of characters (a) with their corresponding results for each case (b)

If the number of @ in the email is met, then it will move on to the validation function, which receives the string of characters for the email. In this case, two things can occur: if it contains @, another series of validations are performed, and another function of the algorithm changes on; otherwise, it is indicated that the @ symbol is not present, since it was not detected in the path of characters. Unlike the previous function, by regulation, this one checks the location of the symbol at the beginning or at the end of the chain. If the email does not contain an @ sign, the message indicating the error is added to the bottom of the list. If everything is correct in the previous validation, an *enumerate* loop is entered, which iterates the chain, given that, in Python, the chain is an array and, therefore, it can be traversed. If a string goes to *enumerate*, the output will show the index and value of each character in the string.

It should be noted that the algorithm only uses a library, which complements the function in which it receives double quote or parenthesis characters, indicating whether all its elements are the same in a list and working in the case that comments are contained between parentheses and one desires to validate that only letters have been written in the string.

- *Scenario 3*
  If the local part of the email has less than 64 characters, the *validate_character_local* function will be called, which will verify the local part of the string and evaluate its characters one by one. With

this function, several results can be returned: if the characters are letters, numbers, and special characters, the returned value will be *True*, whereas, for periods and @, 3 or 4 will be returned. This can be seen in Fig. 5a. The above is done with lists that contain all the valid letters, numbers, symbols, and characters that comply with the grammar rules. In some cases, validation is carried out with the *zip* function, which can go through several lists in the same iteration, working for the lists of uppercase and lowercase letters, along with the *dot-at-sign* list. The characters are entered one by one, validating whether they are in any of the lists and returning the corresponding value; otherwise, *False* will be returned, *i.e.,* the result shown in Fig. 5b.

```
if validate_character_local(v) == 3:
                if word[i - 1] == word[i]:

last_message.append("repeat character dot")
                        break
                if word[i - 1] == '.' and
word[i] == '@':
                    last_message.append("repeat
character continue -at")
                        break
```

Figure 5. Validation of rules according to regulations and their results

If 3 is returned in the previous function, *validation* ensures that there are no repeated periods regarding their specific position with a loop, which allows the chain to be within a collection. Thus, if the route of the chain is found with two periods in a row, it will add the corresponding message to the list, iterating both in the previous position and in the current one. The validation also works for a period followed by an @ sign; the error is added to the last message, and the execution of the class ends. In this case, the validation of the local part is carried out, and the iteration is carried out with @.

Now, if the function returns 4, the message that an @ sign was detected is added to the list. If the email ends with @, an error will be displayed. After adding the message, the *validate_domain* function is entered, which receives the mail along with a number, which will indicate the cycle it must enter, be it 1, identifying the @ character, or 2, identifying the string "[at]. The above will depend on the result given in the *validate_character_domain* function. Then, in the same way, it is verified whether the periods are repeated or there are consecutive periods and @. If the rules are met, the message " OK 2" is added to the list, indicating that the domain part was successfully validated.

If 2 is returned in the *validate_domain* function, the string has been found to contain "[at", which is a special handling rule. From the above, the chain enters the functions 3 and 4, where the first function, which separates the local part of the domain with *split*, divides each time it finds a square bracket – if it contains more than one ([dot]), several separations of the string have to be performed. The first one contains the domain part, together with "at]", and is stored in *separate_-one*, resulting in "at] domain.com". Now, a new division is carried out, but the separating character

is the square bracket "]", in order to obtain only the part of the domain. This is stored in a variable to be able to return it.

Upon receiving the character 1, the string is separated with the identifier of the @ sign using the *split* function, which receives the character in which a string is going to be separated, storing it in a list, and, if it only contains one @, then the separation is saved in two positions in the list. The first is for the local part, and the second is for the domain part, given that the variable will apply the second position to perform the domain validation. Again, as the local part is in a variable, it is verified whether it has no more than 64 characters; if it does not contain them, the function *validates_character_domain* receives the part of the domain and performs the same validations of letters, numbers, and periods with @, adding the possibility that the domain may have an underscore. Finally, the last two positions of the list are returned to indicate their result in the corresponding iterations and validations of each function, so that, in the *App* class, it can be verified whether the valid characters are contained in the last two validations.

According to the aforementioned validation, the GUI can show the result for the typed email (correct or incorrect). Here, there are two functions for each of these two messages, which are identified with colors so that the user can easily see if the result was satisfactory (text in green) or not (text in red), obtaining in a variable the email entered from the function knows from the controller. Note that *self* represents instances of the classes and is used to obtain what is stored in each of the variables. In this way, it is possible to carry out the validation of an, as shown in Fig. **6**b.

Figure 6. Functions to show the result in the graphical interface

The grammar rules were established in global lists at the beginning of the code, so that they could be used in all the functions, allowing them to be used throughout the code without having to redefine them, as well as to work with the established values. The rules for the types of letters, numbers, special characters, @ and period rules, and lines were applied to each list (Fig. 7).
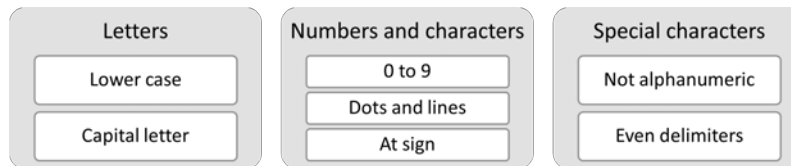

Figure 7. Grammar rules implemented for the algorithm

b Installing the generated library

To install the library, some characteristics are necessary, including the creation of the virtual environment with the corresponding command, within the folder for which the library will be used.

- *Scenario 1*

  The package is installed via a terminal command through the *Pypi* repository, which searches its repositories for the indicated package and downloads it. After this operation, it is possible to use the package (Fig. 8a). If the package was installed correctly, no error will be found in IDE (Fig. 8b). The terminal will display the information corresponding to the package from which the query is being made.

Figure 8. Library installation and package validation

- *Scenario 2*

  In this scenario, the utility of the library is accessed from the GUI. In it, the instance of the App class must be defined together with the call for the *mainloop ()* function. After the above, the window is displayed, in which it is possible to write email addresses for validation (Fig. 9).

- *Scenario 3*

  In this scenario, the library is used via the *validateMail* class, which uses its corresponding functions to enter the email address and show the result in the console: if the entry was valid, the result is *Mail is correct*; if not, it is *Mail is wrong*. This can be seen in Fig. 10.

  As seen in the previous scenarios, it was possible to use the library on another computer, either with the GUI or with the corresponding class, to be able to validate email addresses. In either case, the library complies with the RFC 5321 standard for the construction of an algorithm with regular grammars.
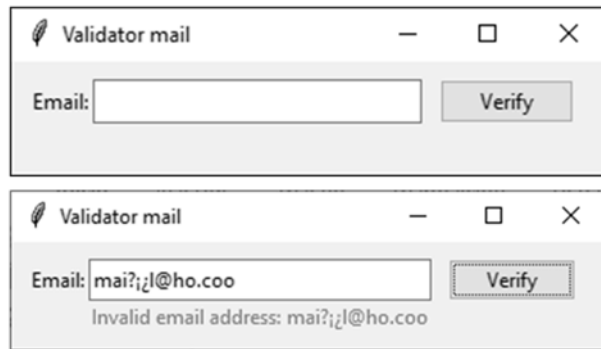
Figure 9. Using the library from the GUI

Figure 10. Valid and invalid emails

c. Algorithm effectiveness

When performing the validation of the library in real cases, its performance against the JFLAP program was verified. For this comparison of the number of executions *vs.* the effectiveness of results, tests were executed in both scenarios with the indicated number of 100 valid and 100 invalid addresses, with a certain increasing number of executions for them the results are presented in Table **IV**. This Table contains the information related to the valid and invalid emails applied in both parts. Note that the results should be the same.

These results corroborate the performance of the algorithm. According to the standard deviation found for both the algorithm and JFLAP, when executing valid emails, the former has a lower dispersion than the latter. Fig. **11** depicts the results with their corresponding linear regression, showing that the algorithm is more effective; on average, it reaches 99 emails evaluated in up to 150 executions, unlike the 97 obtained with JFLAP. In addition, when evaluating the 100 valid emails between 30, 50, 70, 90, and 110 executions, the algorithm has the highest accuracy, unlike the program with its grammar rules, although the former does not reach the full number of emails.

For the case with only 100 valid emails, it can be stated that the algorithm tends to be more efficient JFLAP; as the number of executions increases, it shows some differences with respect to the latter, whose trend line is not so steep. By comparing the equations generated by both cases, for every 20 executions, it can be expected that, on average, the truly valid emails tend to decrease, albeit not so periodically. This is because, for the algorithm, their number is greater. The variability percentage

Table IV. Execution results (library *vs.* JFLAP)

Executions	Email addresses		Result			
	Valid	Invalid	JFLAP		Library - Algorithm	
			Valid	Invalid	Valid	Invalid
5	100	100	100	100	100	100
10	100	100	100	100	100	100
30	100	100	99	100	100	97
50	100	100	95	97	99	96
70	100	100	95	97	99	97
90	100	100	97	97	99	98
110	100	100	96	95	98	97
130	100	100	96	95	98	96
150	100	100	99	92	96	95
Average			97	97	98,77	97,33
Precision			2,12	2,74	1,30	1,73
Accuracy			-3	-3	-1,22	-2,66
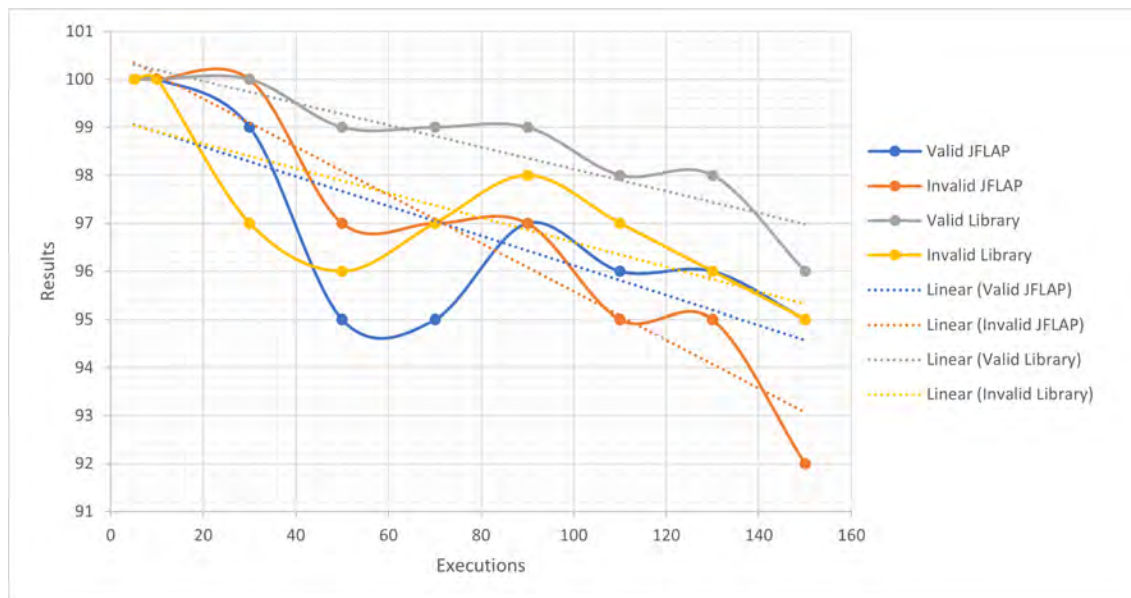
Figure 11. Results of (number of executions *vs.* validated emails)

is 85 % for the algorithm and 58 % for JFLAP. These results could have been generated by the resources of the test device or with the load that represents the multiple executions. The behavior of JFLAP shows a slight increase towards the end, unlike the library. Fig. **12** depicts the results and the equations. The opposite occurs with invalid emails: both had a different behavior because the algorithm tends to improve its results, as seen from the linear trend line. The accuracy of the
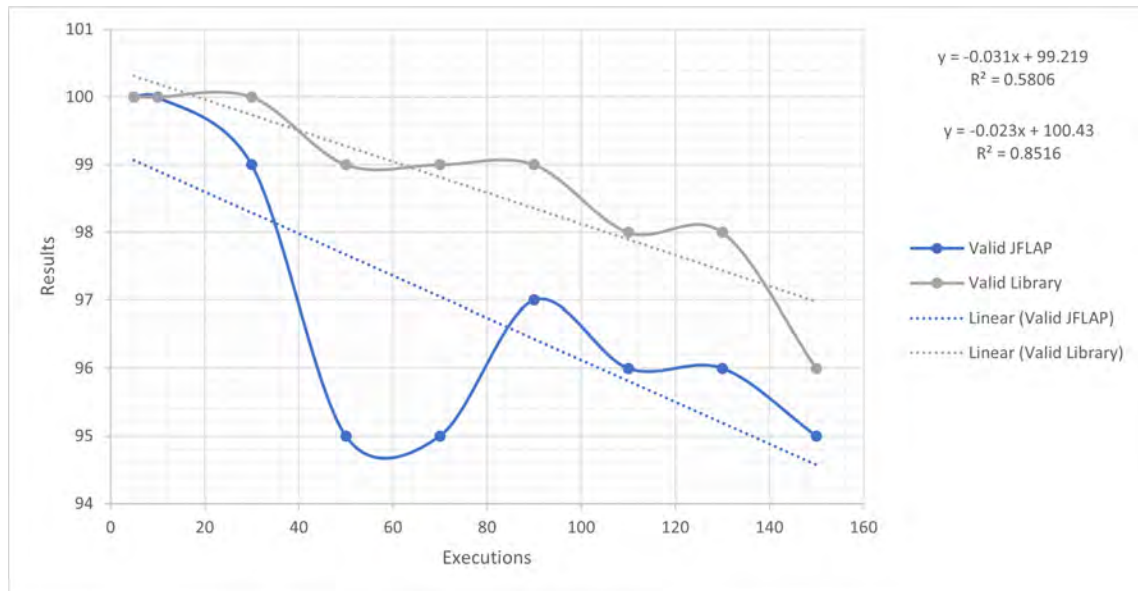
Figure 12. Valid emails for JFLAP and the library

algorithm is closer to zero, unlike JFLAP. The percentage of variability is 91 % for JFLAP and 59 % for the algorithm, since the data are less dispersed in the former than in the latter, which shows changes in the results between 50 and 90 executions. In this case, the library has better detection capabilities than JFLAP (Fig. 13).
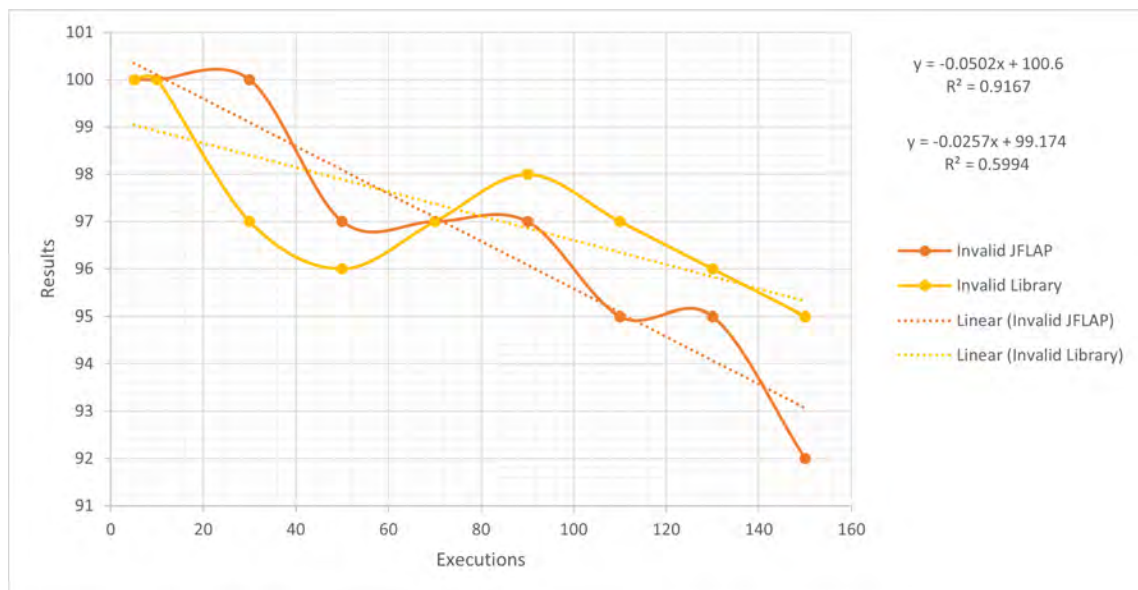

Figure 13. Invalid emails for JFLAP and the library

3.   Conclusions

This study constructed an email validation algorithm based on regular grammars and provides notions for its practical use in the study of the branch of computing. Due to its characteristics, the Python language is an excellent tool for working with verification algorithms, to the point that its effectiveness works for corporations that require email validation. Likewise, the effectiveness of the library could be verified when comparing the results obtained by the RG algorithm and JFLAP, obtaining a greater margin for the validation of emails.

Email validation was performed by means of regular grammars, providing a unique pattern that works for all email formats, along with the definition of rules according to RFC regulations, which follows the format and accordingly builds a pattern. Each new rule reduces the degree of freedom in the accepted addresses. The algorithm is improved in terms of the limitation of cycles, the construction of several lists so as not to have to go through a single one and improve effectiveness, and validation procedures, which makes it work optimally with the released library.

Currently, semantic and syntactic analysis for emails can be performed using APIs such as SendGrid Validation API, Abstract API, or Mailgun Email Validation, which accept formats such as JSON and CSV. Regex, which matches text strings, *e.g.*, characters, words or character patterns through regular expressions, is one of the most widely tested to perform mail validation. Unlike the APIs, the library created is for free use, and it is possible to adapt it according to specific needs. The difference with regex is that it parses the string from the regular expression, not from the regular grammar, since a regular expression is much less readable than the original grammar – it lacks the nonterminal names that document the meaning of each subexpression.

Due to its precise matching of search patterns and its compact nature, regular grammar can be applied to validate the email addresses entered by the user in most day-to-day scenarios, paving the way for future APIs based on the shared library. Likewise, there is potential for future work in this area, with a focus on enhancing the algorithm's capability to analyze various lexical structures. These include NITs, alphanumeric codes, valid URLs (to combat *Web Spoofing and phishing*), and the validation of both urban and rural addresses. The library can serve as a great analyzer of grammatical or lexical structures, which are needed in the information technology industries, and it can even be complemented with machine learning for higher precision.

4.   CRediT author statement

Marco-Javier Suárez-Barón: conceptualization, formal analysis, research, methodology, software, validation, writing-original draft.
Cristian Alejandro Fandiño: conceptualization, formal analysis, research, programming.
Cesar Jaramillo: software validation, writing, methodology.

References

[1] K. Dokter, F. Gadducci, B. Lion, and F. Santini, "Soft constraint automata with memory," *J. Logical Alg. Meth. Programm.*, vol. 118, art. 100615, 2021. https://doi.org/10.1016/j.jlamp.2020.100615 ↑2, 4

[2] T. Yamakami, "Between SC and LOGDCFL: Families of languages accepted by polynomial-time logarithmic-space deterministic auxiliary depth-k storage automata," in *Computing and Combinatorics*, C. Y. Chen, W. K. Hon, L. J. Hung, and C. W. Lee, Eds., Berlin, Germany: Springer, 2021, pp. 164-175. https://doi.org/10.1007/978-3-030-89543-3_14 ↑2, 4, 5

[3] K. Shuang, Y. Tan, Z. Cai, and Y. Sun, "Natural language modeling with syntactic structure dependency," *IJ Math. Sci. Comp.*, vol. 523, pp. 220-233, 2020. https://doi.org/10.1016/j.ins.2020.03.022 ↑3, 4

[4] J. Schwenk, *Guide to internet Cryptography*, Cham, Germany: Springer, 2022. https://doi.org/10.1007/978-3-031-19439-9 ↑3

[5] P. R. Chandra, K. Sravan, and M. S. Chakravarthy, "A new approach to the design of a finite automaton that accepts class of IPV4 addresses," *IJ Math. Sci. Comp.*, vol. 5, no. 1, pp. 65-79, 2019. https://doi.org/10.5815/ijmsc.2019.01.06 ↑3

[6] J. Chen, V. Paxson, and J. Jiang, "Composition kills: A case study of email sender authentication," in *29th USENIX Security Symposium*, 2020, pp. 2183-2199. ↑3

[7] E. G. Vázquez and T. G. Saiz, *Introduction to the theory of automata, grammars and languages*, Madrid, Spain: Editorial Universitaria Ramón Areces, 2022. ↑4, 5, 6

[8] A. Sharma and R. Kumar, "Imbalanced learning of regular grammar for DFA extraction from LSTM architecture," in *Soft Computing for Problem Solving*, M. Thakur, S. Agnihotri, B. S. Rajpurohit, M. Pant, K. Deep, and A. K. Nagar, Eds., Berlin, Germany: Springer, 2023, pp. 85-95. https://doi.org/10.1007/978-981-19-6525-8_8 ↑6

[9] M. Novo-Lourés,. D. Ruano-Ordás, R. Pavón, R. Laza, S. Gómez-Meire, and J. R. Méndez, "Enhancing representation in the context of multiple-channel spam filtering," *Inf. Processing Management*, vol. 59, no. 2, art. 6, 2022. https://doi.org/10.1016/j.ipm.2021.102812 ↑7

[10] G. Howser, *Computer networks and the Internet. A hands-on approach*, Berlin, Germany: Springer, 2020. https://doi.org/10.1007/978-3-030-34496-2 ↑7

[11] H. Tschabitscher, "LifeWire," 2021. [Online]. Available: https://www.lifewire.com/are-email-addresses-case-sensitive-1171111 ↑7, 8

Cristian Alejandro Fandiño Mesa

Systems and computing engineer, UPTC, Sogamoso, Colombia. Research assistant for the GALASH-UPTC group.

Email: cristian.fandino02@uptc.edu.co

Marco Javier Suárez Barón

Systems engineer, PhD in Strategic Planning and Technology Management, UPAEP, Mexico, Master of Information Management, Escuela Colombiana de Ingeniería. Associate professor at UPTC. Director of the GALASH research group.
Email: marco.suarez@uptc.edu.co

César Augusto Jaramillo Acevedo

Systems and computing engineer, MSc in Systems and Computing Engineering from Universidad Tecnológica de Pereira. Director and researcher in projects related to the Industry 4.0, precision agriculture, education, and business development. He has been a professor-researcher of Universidad Tecnológica de Pereira for more than 12 years. He has been active in research groups whose areas of interest and teaching are related to software engineering, compilers, AI, IoT systems, the cloud, distributed systems, and the Industry 4.0.
Email: swokosky@utp.edu.co

Research

Preliminary Approach for UAV-Based Multi-Sensor Platforms for Reconnaissance and Surveillance applications

Enfoque preliminar de una plataforma multi-sensor basada en UAV para aplicaciones de reconocimiento y vigilancia

Nicolas Amezquita[1,2] , Sergio Gonzalez[1,2] *, Marco Teran[1,2] , Camilo Salazar[1,2]
John Corredor[3,4] , and Germán Corzo[3,4]

[1]Electronic Engineering Program, Sergio Arboleda University, Bogotá, Colombia.
[2]SIKU Research Group, Sergio Arboleda University, Bogotá, Colombia.
[3]Colombian National Army, Colombia.
[4]CIGA Research Group, Colombian National Army, Bogotá, Colombia.

Abstract

Context: Unmanned Aerial Vehicles (UAVs) equipped with remote sensing platforms have become increasingly popular due to their applications in aerial surveillance, environmental control, and disaster response. However, the limited flight range and on-board energy resources of UAVs pose significant challenges to their practical deployment and operating efficiency, which has led to the exploration of energy-efficient platforms for remote sensing.

Method: This paper proposes a preliminary approach for UAV multi-sensor reconnaissance and surveillance platforms (MRSS) that target low energy consumption. The approach implemented four sensor modules controlled by one multi-functional integrated edge computer for control and data collection, which can be interchanged according to battery lifetime requirements.

Results: The main contribution of this work was an analysis of the energy consumption behavior of sensor modules managed by an embedded system with edge computing capabilities as the central control unit.

Conclusions: The high energy consumption associated with modules such as GEOINT leads to deep discharge in excess of 20 % DOD, resulting in a maximum battery degradation of 2,4 years.

Keywords: Unmanned Aerial Vehicles (UAVs), multi-sensor reconnaissance and surveillance system (MRSS), geospatial intelligence (GEOINT), signals intelligence (SIGINT), measurement and signature intelligence (MASINT)

*✉ **Correspondence:** sergio.gonzalez@usa.edu.co

Resumen

Contexto: Los vehículos aéreos no tripulados (UAV) equipados con plataformas de sensores remotos se han hecho cada vez más populares debido a sus aplicaciones en vigilancia aérea, control medioambiental y respuesta ante catástrofes. Sin embargo, la limitada autonomía de vuelo y los limitados recursos energéticos a bordo de los UAV plantean importantes retos para su despliegue práctico y su eficiencia operativa, lo que ha llevado a explorar plataformas energéticamente eficientes para la teledetección.

Métodos: En este artículo se propone un enfoque preliminar para plataformas de reconocimiento y vigilancia multisensor (MRSS) dirigidas a un bajo consumo energético. El enfoque implementa cuatro módulos de sensores controlados por un ordenador multifuncional de borde integrado para la recopilación de datos, que pueden intercambiarse en función de los requisitos de duración de la batería.

Resultados: La principal contribución de este trabajo fue un análisis del comportamiento del consumo de energía de los módulos de sensores gestionados por un sistema integrado con capacidad de computación frontera como unidad de control central.

Conclusiones: El elevado consumo de energía asociado a módulos como el GEOINT conduce a una descarga profunda superior a un DOD de 20 % que provoca una degradación máxima de 2,4 años de la bateria.

Palabras clave: vehículos aéreos no tripulados (UAV), sistema de reconocimiento y vigilancia multisensor (MRSS), inteligencia geoespacial (GEOINT), inteligencia de señales (SIGINT), inteligencia de firmas (MASINT)

Table of contents

1.   Introduction

Recent advances in remote sensing (RS) for data collection processes during rescues, monitoring, and the search for solutions to reduce the impact of natural disasters on human societies have sparked the intrest of the research community. RS is the science of data collection from a distance while using sensors (Fig. 1). Remote sensors offer a comprehensive outlook and a plethora of information concerning various systems. They facilitate data-driven decision-making grounded in the current and anticipated conditions of specific variables. Typically, the technologies employed in RS are limited to detecting and measuring electromagnetic energy, spanning both visible and non-visible radiation, which interacts with surface materials and the atmosphere. According to these characteristics, RS is seen as an essential tool for risk assessment, surveillance, reconnaissance, and rescue operations (1).
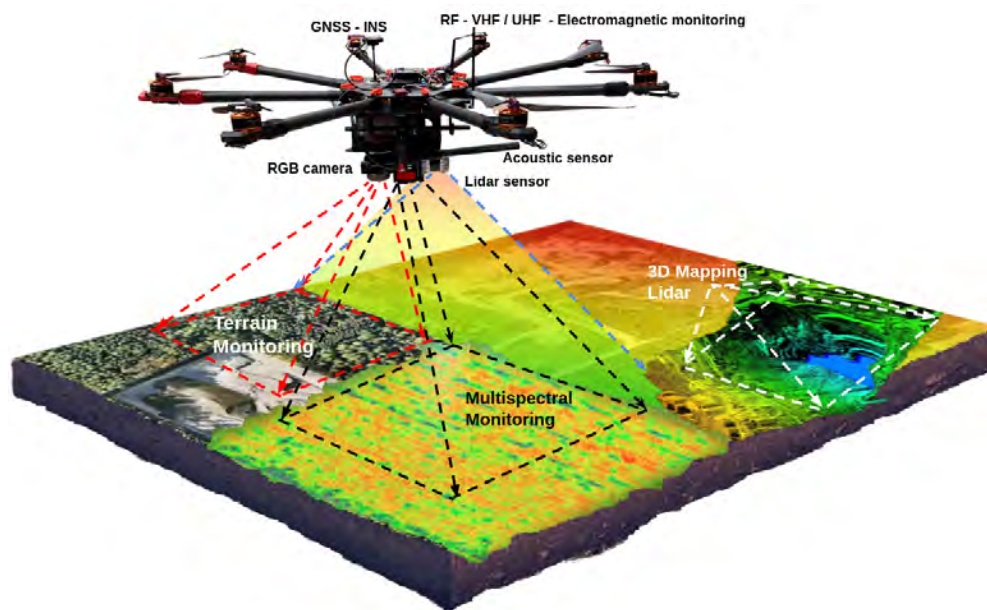

Figure 1. Multi-modal sensor data platform based on UAVs for monitoring, reconnaissance, and surveillance tasks such as multi-spectral image analysis. The picture shows the different sensor modules, *i.e.*, 3D LiDAR imaging and photogrammetry for mapping and recognition, acoustic localization, and electromagnetic spectrum analysis in real-time applications (1)

Unmanned Aerial Vehicles (UAVs) are a category of aircraft that is suited for remote operation and control by a designated pilot, commonly referred to as the *UAV control operator*. While UAVs have been predominantly deployed in military contexts, there has been a notable surge in their deployment for civil applications, as is the case of agriculture. UAVs equipped with RS platforms have emerged as powerful tools for reconnaissance and surveillance applications (Fig. 1). These advanced systems provide real-time situational awareness, target identification, and data collection capabilities in various operating scenarios. Fig. 2 shows typical strategies to gather, process, and analyze temporal and spatial (terrain monitoring) data, as well as to combine it with other information (*e.g.*, remote sensors)

to support management decisions. With the increasing demand for extended mission endurance and optimized operational efficiency, energy-efficient methods have become crucial for UAV remote sensors in reconnaissance and surveillance missions. This introduction provides an overview of energy efficiency in UAV RS platforms for reconnaissance and surveillance, highlighting the significance of energy optimization and its impact on mission effectiveness (1).

Fig. 3 shows different sensor categories that can be installed in different positions of UAVs, so that the vehicle has the capability to effectively sense and comprehend its environment from all perspectives. Low-cost UAVs are now indispensable for on-site fast data collection using Multi-Sensor Reconnaissance Surveillance System (MRSS) technologies to aid disaster management, such as mapping, monitoring, and the autonomous deployment of flying robots (2). In addition, UAVs employ smart interfaces to accomplish various objectives, including detecting radiation on the terrain and monitoring a wide range of attributes from physical features to thermal emissions in a given region. For instance, the use of UAVs for RS has proven to be the most effective approach for monitoring terrain via imagery. In contrast to RS utilizing satellite imagery or that performed from manned aircraft, UAVs provide the opportunity to obtain images with exceptional spatial and temporal resolution because of their capacity to maneuver and fly at low altitudes. One such application is accurate and evidence-based forecasting of farm produce using spatial data collected via UAVs (3). With the gathered information, farmers can find fast and efficient solutions to any issues detected, make better management decisions, improve farm productivity, and ultimately generate higher profits (3). Collecting real-time data helps farmers to immediately evaluate and react to environmental events. The final results include reduced operating costs, improved crop quality, and increased yield rates (4). Therefore, the selection of sensors is one of the fundamental building blocks of real-time RS (5). In conclusion, UAV RS is becoming an important means for reconnaissance and surveillance thanks to the flexibility, efficiency, and low cost of UAVs, while still yielding systematic data with high spatial and temporal resolutions (6).

Surveillance, reconnaissance, and targeting are critical factors for providing users with real-time situational awareness. The ability to instantly process and disseminate data collected from the field is vital in achieving terrain dominance. The MRSS is a sophisticated and smart multi-sensor surveillance and reconnaissance system that requires considering the multifariousness of devices (sensors) as well as the user's requirements. In particular, a UAV-MRSS system integrates several sensors that capture different types of information with specific integration and processing needs (8). Fig. 3 shows different sensor categories that can be installed at different positions in UAV-MRSS platforms, so that the UAV can perceive its surroundings well from every angle.

(9) categorized the MRSS technologies of satellites, UAVs, or manned aircraft based on their detection of non-contact energy reflection from the Earth. However, the feasibility of using satellite MRSS technologies has some shortcomings. First, satellites have a specific time cycle for acquiring information, including image capture. Second, the cost of satellite technology is considerably high (10). Third, the image resolution is low, making it difficult to obtain detailed features. Fourth, the temporal and spatial resolution of satellites is restricted, and environmental conditions such as cloud cover can impede a reliable operation (4). Fifth, the use of manned aircraft is often not feasible due to high costs,
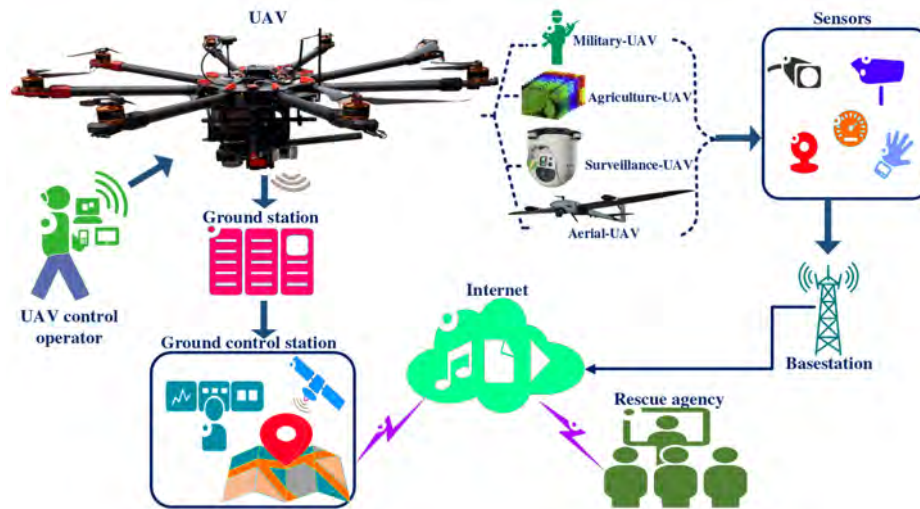
Figure 2. Block diagram depicting the integration of UAV surveillance and recognition systems in scenarios involving rural and urban security. A UAV-based multi sensor platform generates multi-modal data used at the different stages in the workflow of a civil or military system for alert, surveillance, and search and rescue operations (7)
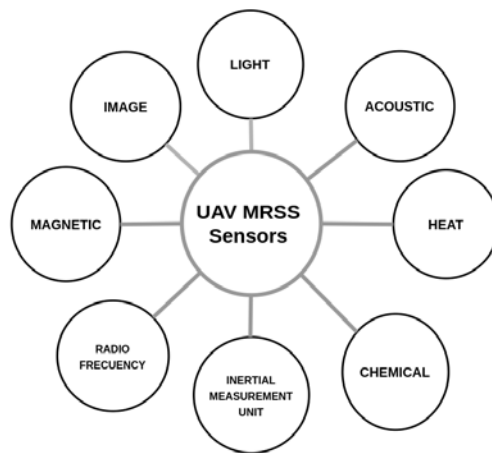

Figure 3. UAV-MRSS sensor options according to the data generated by the different types of sensors and their manufacturing technology

and it is not always possible to conduct multiple flights to acquire multiple crop images. The primary drawback of satellite technology is its high cost, making it inaccessible to many small and medium-scale commercial and subsistence farmers. This has led to the emergence of alternative delivery platforms (*e.g.*, UAVs) (11, 12). UAVs are capable of rapidly covering vast and remote areas, reducing labor costs and requiring minimal operator space.

UAV-MRSS systems are noteworthy for their integration of several sensors, each with distinct information capture requirements and processing specifications (8). The three primary means of merging multiple sensors on platforms are as follows: *redundant sensors*, in which all sensors provide the same information; *complementary sensors*, *i.e.*, the sensors provide independent (disjoint) types of information; and *coordinated sensors*, where the sensors sequentially gather information (13).

(13) implemented three fundamental MRSS management strategies for synchronization. These strategies are part of a centralized scheme (Fig. 4) where all sensors provide measurements to a central node. Additionally, the distributed scheme, illustrated in Fig. 5 is employed, wherein nodes exchange information at a specified communication rate, *e.g.*, every five scans (a one-fifth communication rate). The centralized scheme may be regarded as a particular instance of the distributed scheme, where the sensors communicate with each other in every scan.Finally, the decentralized scheme (Fig. 6) is employed where there is no synchronization between the sensor nodes (13).
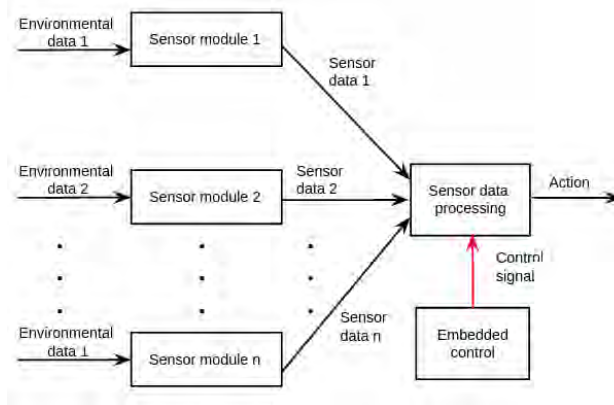

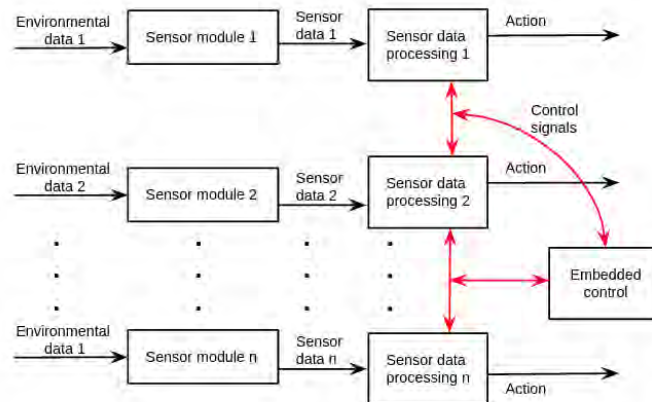**Figure 4.** Block diagram of the components in a centralized control system

Figure 5. Block diagram of the components in a distributed control system
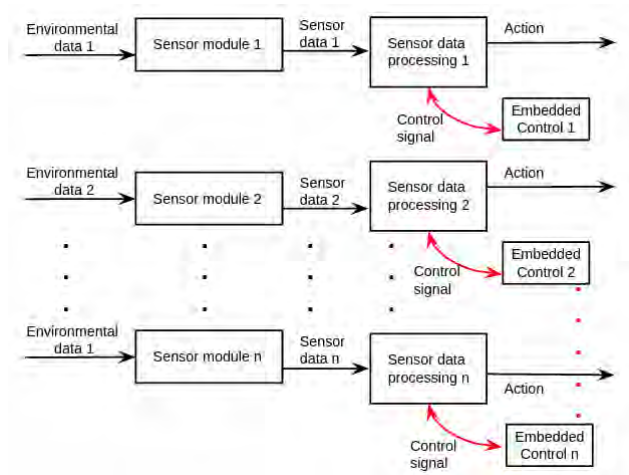
Figure 6. Block diagram of the components in a decentralized control system

Given their considerable potential and the progress made in the field, UAVs will inevitably overcome some of the limitations of traditional MRSS. Specifically, UAVs possess proper Global Positioning Systems (GPS) in their software, which allows them to be programmed and guided with precision to specific locations. In comparison with manned aircraft, they are suitable for both regular and emergency scenarios. Furthermore, UAVs support a wide range of altitudes, are highly flexible, and have no strong demand for take-off and landing sites. Their high work efficiency is derived from being less affected by the external environment and capable of making secondary measurements at any given time. UAVs can be adapted easily to different types of reconnaissance and surveillance tasks, as well as to different growth stages. With their onboard autopilot system, UAVs can be controlled automatically and require less human intervention during data collection. The advantages of these platforms for MRSS applications include their high spatial resolution and the possibility of highly flexible and timely control due to reduced planning time. Consequently, most developed countries have adopted the latest precision agriculture technologies using UAVs to enhance their productivity (14).

New technologies and advancements in UAVs pose new challenges. For instance, smaller and medium-sized UAV platforms are only capable of carrying a limited number of multi-sensors, and the sensor-UAV configuration is exclusive, which means that data can only be collected from a single type of sensor. Furthermore, UAVs have payload limitations when compared to ground vehicles, which can result in equipment weight constraints. Additionally, environmental factors can impact the quality of the data collected by UAVs due to the lack of environmental controls. Aerial data collected by UAVs generally have a spatial resolution lower than those collected by ground systems. Moreover, precise geopositioning systems, which are required for military applications, precision agriculture, and land survey applications in civil engineering, mining, or disaster prevention and management, are not typically integrated into most platforms of this size. Moreover, there is scant literature on fully autonomous, cost-effective, multi-sensor UAV systems with standardized information extraction procedures for use in reduced-input precision agriculture applications.

Based on the above, the objective of this research is to develop a preliminary approach for the efficient use of energy consumption in UAV-based multi-sensor platforms for reconnaissance and surveillance (MRSS), which allows configuring multi-sensor modules for simultaneous or individual operation. In this vein, the aim of this paper is to propose a new UAV-based MRSS platform equipped with a set of modules (*e.g.*, SIGINT, MASINT, GEOINT, navigation module) in order to monitor the environment and collect data in real time, making efficient of battery power.

The focal point of is research was the amalgamation of sensor modules through parallel computing. This integration allowed acquiring data, specifically georeferenced data including point measurements, reflectance spectra, and optical images. This facilitated the post-processing of subsequent data and the analysis of features.

To develop the preliminary approach, the following considerations were made. (i) The objective of this study is to develop a UAV-based multi-sensor platform for surveillance and reconnaissance applications, which entails the creation of both mechanical components and software programming for simultaneous multi-sensor data collection. (ii) The lifetime of the battery is assessed by using several sensor modules. This proposed system can cover vast areas and high altitudes while maintaining an energy-efficient approach, unlike the aircraft-based alternatives.

The research question is the following: *What are the technologies adopted by multi-sensor UAV platforms for efficient energy consumption in surveillance and reconnaissance tasks?* To answer this question, a multi-sensor UAV architecture based on MRSS technologies is proposed, and the energy consumption and battery voltage required for efficient use are established.

This document is organized as follows. In Section 2, the state of the art pertaining to UAV-based multi-sensor technologies is presented. Section 3 provides a comprehensive description of the proposed multi-sensor platform, along with a meticulous analysis of its major components. The results are presented in Section 4, offering a detailed insight into the energy consumption and battery life of a multi-sensor UAV platform. Section 5 is primarily focused on interpreting the data gathered while evaluating the approach. Finally, Section 6 provides some concluding remarks and highlights the paper's valuable contributions.

2. Related works

This section classifies some publications on surveillance and reconnaissance technologies that are relevant to the topic and analyzes several typical problems, including UAV multi-sensor platforms and embedded technologies for different applications,the limitations of using a single sensor to estimate certain characteristic features compared to the combining information from multiple sensor types that have the potential to reflect more complex information and provides a better opportunity for accurate yield estimation (15). Many interesting works have been carried out in this regard. For example, (16) described the implementation of a multisensor UAV system capable of flying with three sensors and different monitoring options. The feasibility of implementing a UAV platform utilizing RGB,

multispectral, and thermal sensors was evaluated for particular objectives in precision viticulture. This platform proved to be a valuable asset for swift multifaceted monitoring in a vineyard (16).

(17) presented an integrated monitoring approach able to provide a spatially detailed assessment of thermal stress in vineyards, combining high-resolution UAV RS and WSN proximal sensing.

The authors of (18) developed an autonomous multi-sensor UAV imaging system designed to provide spectral information related to water management for a pomegranate orchard. The system is composed of a primary UAV platform, a multispectral camera, a thermal camera, an external GPS receiver, a stabilization gimbal mechanism, and a Raspberry Pi microprocessor. All of these components are seamlessly integrated into a unified platform.

(19) presented a combination of CCD cameras and a small (and low-cost) laser scanner with inexpensive IMU and GPS for a UAV-borne 3D mapping system. Direct georeferencing is accomplished via automatization using all of the available sensors, thereby eliminating the need for any ground control points.

(20) presented a real-time, multi-sensor-based landing area recognition system for UAVs, which aims to enable these platforms to land safely on open and flat terrain and is suitable for comprehensive unmanned autonomous operations. This approach is built upon the combination of a camera and a 3D LiDAR.

(15) evaluated the performance of a UAV-based RS system in cotton yield estimation. This system was equipped with an RGB, multispectral, and infrared thermal cameras to capture images of a cotton field at two distinct growth stages, namely flowering and the one prior to harvesting. The resulting sequential images were processed to produce orthomosaic images and a Digital Surface Model (DSM). Said images were then aligned with the georeferenced yield data obtained by a yield monitor installed on a harvester.

(21) and (22) combined a UAV-based RGB camera, a multispectral camera, and a thermal camera to estimate the leaf chlorophyll content of soybean. The results indicated that multiple types of information could measure chlorophyll content with higher accuracy.

(23) developed a ground-based platform that included an ultrasonic distance sensor, an infrared thermal radiometer, an normalized difference vegetation index (NDVI) sensor, a portable spectrometer, and an RGB web camera to efficiently monitor multiple soybean and wheat plant traits.

(24) proposed a semi-automatic sensing system for phenotyping wheat cultivars in field conditions. They employed a hyperspectral radiometer and two RGB cameras as the basis of the system, enabling the calculation of two distinct vegetation indices that are highly correlated to leaf chlorophyll content, as well as the fraction of green area per unit of ground area.

(25) developed a field phenotyping system that incorporated three sensing modules to measure plant canopy height, temperature, and the NDVI. Three distinct data loggers were employed to capture sensor data. Said data were post-processed and subsequently combined into separate plots, which were then subjected to further analysis.

(28) reported a high throughput phenotyping system for cotton. This system included sensors that automatically measured plant height, the ground cover fraction, the NDVI, and canopy temperature.

(29) presented the open-source design of a multi-sensor UAV system with ROS that can be used for plant phenotyping and precision crop management. Data processing was introduced to extract plot-level phenotypic traits from calibrated images, and its performance was comparable to that of analogous studies.

UAV-based multi-sensor platforms are able to collect large amounts of high-dimensional data in short periods of time, which poses a challenge for modeling methods (30). In this regard, (31) evaluated UAV-based multi-sensor data fusion for wheat yield prediction at the grain filling stage and developed an ensemble learning framework to improve the yield prediction accuracy of machine learning (ML) models. This study employed ML techniques for amalgamating multi-sensor data acquired through UAVs, which were found to enhance the precision of crop yield predictions. The results convincingly demonstrated that multi-sensor data captured by low-altitude UAVs can be effectively exploited for early grain yield prediction via a data fusion approach and an ensemble learning framework with remarkable accuracy.

(32) a multi-sensor payload for UAVs. This payload allowed generating multispectral point clouds with remarkable sub-centimeter precision. The authors integrated high-frequency navigation results from a Global Navigation Satellite System, photogrammetric bundle adjustment, and a specialized point cloud registration algorithm, improving the quality of the reconstructed point cloud by reducing the occurrence of ghosting effects and minimizing the amount of noise.

Most of the aforementioned works focus on particular UAV RS platforms capable of amassing substantial volumes of high-dimensional data and/or efficiently executing data processing in short timeframes, as opposed to addressing the energy consumption issues associated with sensor modules (payload). In the foreseeable future, more and more UAVs will take to the skies and deeply integrate real-time surveillance technology, affecting all aspects of our daily lives (33,34). UAVs allow taking high spatial resolution images due to their maneuverability at low altitudes.

3. Multi-sensor platform based on MRSS technologies

This section proposes a UAV-based multi-sensor platform for the integration of several sensor modules based on MRSS. This platform employs a new real-time modular architecture (*i.e.*, a software and hardware architecture) for use in any type of UAV reconnaissance and surveillance applications. According to previous works, the design and functionality of UAV multi-sensor platforms have several

characteristics, such as spectral, spatial, radiometric, and temporal resolutions. These characteristics are often a response to the limitations imposed by the laws of physics and the current state of technological development. Spatial and temporal resolution requirements vary significantly with regard to monitoring terrestrial, oceanic, and atmospheric features and processes. Each RS application has its own unique resolution requirements, resulting in trade-offs between spatial resolution and coverage, electromagnetic signal bandwidth, number of spectral bands, and signal-to-noise ratios. A multi-sensor platform is a sensor system that is precisely stabilized and can be used day and night to detect, observe, and identify objects, as well as for target tracking and rescue operations. It is specifically designed for day- and night-time operations and can function in adverse weather conditions. Thus, said platforms are compact and lightweight, making it easy to integrate into existing systems. When dealing with multiple module sensors, an efficient MRSS management strategy plays an important role in achieving a high overall performance (Fig. 7).
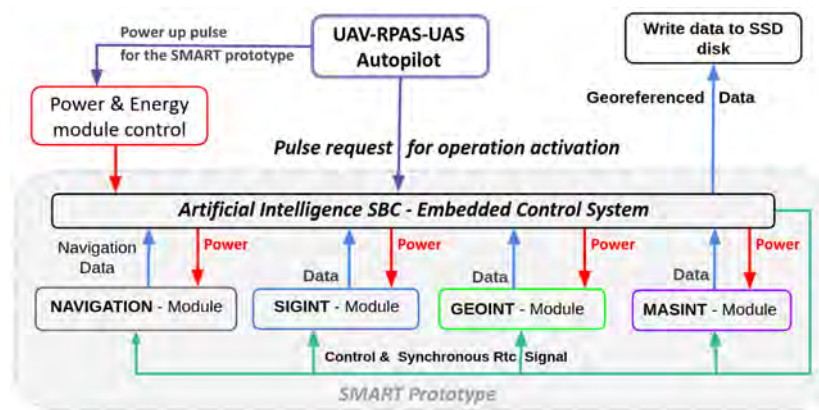

Figure 7. Interconnection between power and energy control, computing, data storage, navigation, and sensor modules and the flight control system for MRSS management, based on (35)

An MRSS management strategy can be regarded as a general strategy that controls sensing actions, including sensor prioritization, sensor selection and sensor interaction. Sensor management has mainly one operation mode: sensor module assignment. This mode decides which sensor module combination will be assigned to which target over an area. The sensor module assignment problem involves determining the minimum additional energy consumption that would allow for a specific diagnostic. Fig. 8 illustrates an MRSS management strategy, which is executed via parallel computing control throughout three distinct stages. The process input involves four image-independent information sources in the form of RGB, multi-spectral, thermal, and LiDAR images. Given that the sensor modules generate data with varying features, independent processing is carried out. In the first pre-processing stage, the datasets are subjected to outlier detection and removal. Aftwerwards, the data are synchronized with respect to the system initialization moment, with the designated sampling period. In the final stage, the synchronized data undergo fusion. The detections recorded by the sensor modules are independently merged using an averaging operation and are subsequently fused with a complementary filter. The UAV's onboard controller can then perform data processing in real time, which facilitates field decisions and coordination.
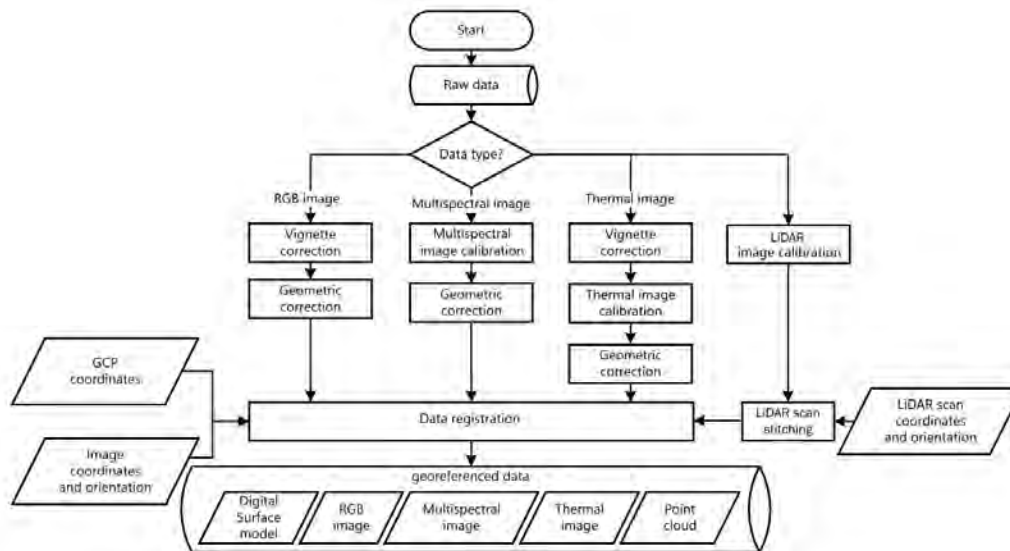
Figure 8. Flow diagram for the processing and georeferencing of different data types generated for the GEOINT module

The following subsections present a detailed description of the hardware and software used for our proposal. First, the hardware architecture is described, followed by the software architecture of the system.

3.1. Hardware architecture

Hardware architecture is a depiction of the physical arrangement of hardware components in a UAV, including the sensor modules and their interconnectivity (Fig. 9). The UAV's hardware, which serves as a malleable mission controller, is tailored to deliver peak performance for vital missions.

The UAV platform used in this study (Fig. 9a) is a multi-rotor Tarot X8 II that boasts an impressive payload capacity of 8 kg and a flight time of 15 min. Its lightweight construction allows for a take-off weight of 10 kg with a 6S 22.000 mAh battery supply. The platform is equipped with eight power arms; it is an 8-axis multi-copter that features electric a retractable landing gear and a 5-degree umbrella-type folding arm. The autonomous flight of the UAV is governed by an autopilot (CubePilot), which operates on a dual CPU control system based on a GPS board, 3-axis accelerometers, yaw-rate gyros, and a 3-axis magnetometer, in order to follow a predetermined waypoint route. Flight parameters are communicated to the ground via a radio link operating at 2,4 GHz, whereas another channel at 5,8 GHz is employed for the transmission of RS data. In order to ensure optimal functionality and safeguard the UAV against electrical mishaps associated with the sensors, the aviation control and multi-sensor platform are powered by two separate power supplies. The sensors employed this work are depicted in Figs. 9a, 9b, 9c, and 9d, and correspond to: 1) UAV telemetry, 2) Vectornav VN200 antenna (GNSS-INS), 3) UAV GPS antenna, 4) UAV autopilot, 5) RF receiver autopilot, 6) GNSS-INS sensor (Vectornav
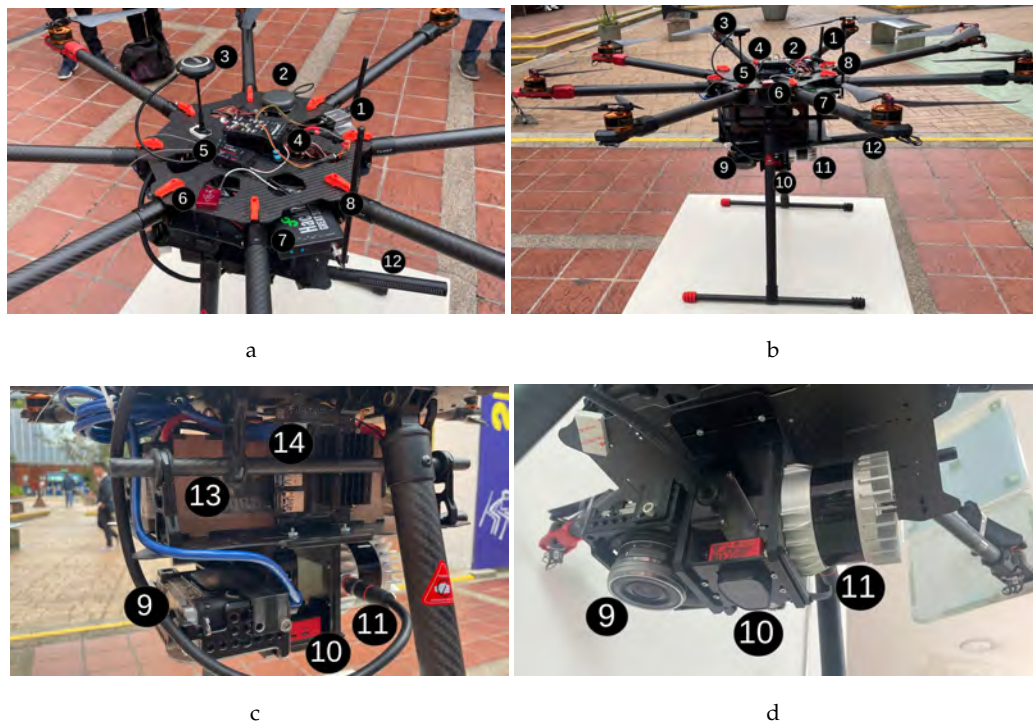
Figure 9. UAV hardware for the proposed multi-sensor platform: a) top view of the assembly of the UAV, RF receivers, antennas, GPS, GNSS-INS, and autopilot modules; b) fully-assembled UAV including batteries, sensors, controller, and propeller; c) embedded control systems and onboard sensor types used for UAV applications; d) onboard multi-imaging sensors

VN200), 7) HackRF-One transceiver, 8) HackRF-One antenna, 9) DSLR Camera, 10) Parrot Sequioa multi-spectral camera, 11) LiDAR camera (ouster OS1-32U, OSO-32U), 12) XLRS outdoor microphone.

The aforementioned sensors have different and, to some extent, complementary selectivity regarding the morphological and spectral properties of the collected information, thus allowing multi-sensor data to determine complex features, increase the robustness of the system, and enable multi-feature determination. The payload weight is 1,8 kg, and the total weight of the UAV is 8,2 kg. The hardware sensor module (Fig. 9) is managed via parallel computing control (Fig. 9c). The control, which is responsible for reading the sensor module data and preparing it for transfer, is a fundamental unit for calculation within a sensor module. It serves to regulate task scheduling, energy consumption, communication protocols, coordination, data manipulation, and data transfer. The power consumption of the processor is predominantly determined by the duration of its support for sleep mode, and it is directly linked to the operation mode. The power consumption of these components is influenced by the operating voltage, the duty-cycle internal logic, and, most significantly, by an efficient manufacturing technology.

The Jetson-nano is used as a parallel computer controller that manages the onboard image sensors, Sony RGB, multispectral and 3D lidar, which transmit the images through the USB and Ethernet

ports respectively.The weight of the hardware sensor module is 2,3 kg, and the dimensions are $180 \times 180 \times 110mm$ in length, width, and height. The hardware sensor module was developed as a purpose-built device.

The hardware sensor module requires two batteries to operate, which are shown as number 13 in Fig. **9**. The hardware sensor module is powered by two 600W-hr lithium ion battery packs that also provide power to payloads through a dedicated enable circuit. Each battery pack has four 8,4 V Li-ion cells NP-F750-5600 mAh in series, which are also known as *3S* and generate a nominal value of 22,2 V. The hardware sensor module is equipped with a current limiting circuit that serves to deactivate the power supply for the payload in the event of an unintentional current surge. The mean power for every payload connector must not surpass 50 W. In the case of an over-current incident that disables the module's power, the current limiting circuit can be reinstated via power cycling using the power button.

3.2.   Software architecture

Software architecture involves making decisions about how software modules will interact with each other to meet the desired functionality and quality in the integrated system. As shown in Fig. **10**, the proposed software architecture embodies a strategic approach. Its design was meticulously crafted to efficiently regulate and synchronize measurements from all sensor modules while simultaneously storing data sensors in the parallel computing control.

The software architecture satisfies a number of functional and non-functional requirements, including dynamic discovery, remote execution, and data retrieval and modification. Firstly, in the case of dynamic discovery, new sensor modules can be connected while the system is operational, and existing modules will be notified of their presence. Secondly, for remote execution, the customer sends function parameters and waits for the provider sensor module to return results. Lastly, for data retrieval and modification, the modules can report the internal state through variables, which can be synchronously queried or modified by other modules.

Additionally, the software architecture facilitates an intuitive protocol design and execution, allowing users to select the appropriate module for each mission, configure the necessary parameters, and execute the protocol with ease. Consequently, the functionality and purpose of each sensor module in the hardware sensor module have been meticulously defined during the module development process. The software, hardware, and operating systems have all been carefully analyzed to achieve optimal performance in embedded hardware, which will manage and integrate all inputs generated by the different modules that make up the system.

The software architecture management strategy used real time parallel computing control based on embedded edge computing. Fig. **11** shows the MRSS management system, which uses real time parallel computing for task assignment through a symmetric multi-processor (MPCore CPUs) from the embedded control system. MRSS parallel computing has two significant benefits: first, it controls the processes independently and increases the real-time data processing performance of each module: second, it makes efficient use of energy consumption, increasing its cost-effectiveness and reliability.
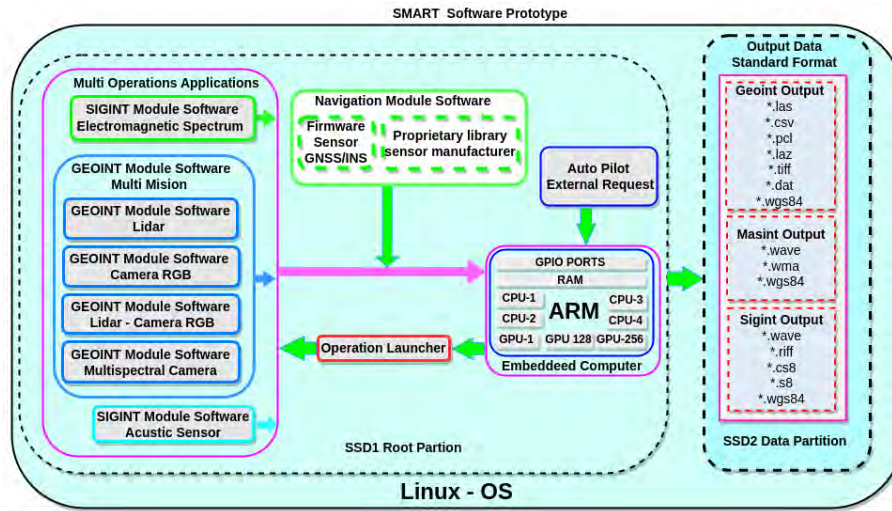
Figure 10. Interaction between software module components, including the multi-operations applications block, the navigation software module, the operation launcher, data storage, and the operating system. The multi-operations applications block manages multi-sensor hardware software modules, while the operation launcher executes autopilot requirements. The navigation software module handles geo-reference data and navigation, and data storage stores information in standard formats. These modules make up the MRSS management software architecture.
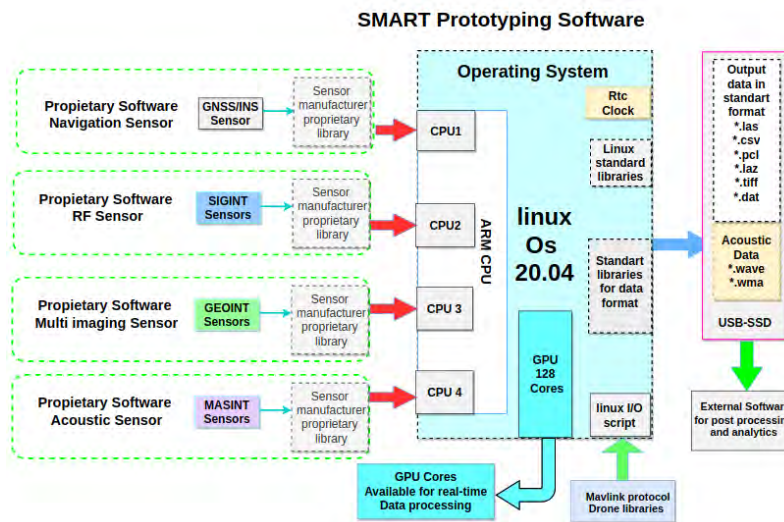

Figure 11. Interaction of software modules and their allocation to a particular core of the main processor for MRSS control utilizing real-time parallel computing

The software architecture employs an embedded Linux board as the main onboard control module to extract data from the sensor modules. The embedded onboard controller runs a custom Ubuntu 20.04 ARM, which is used to control the sensors and acquire data. Our software architecture was

implemented using the C++ and OpenCL languages. Using C++ is highly appropriate in the modeling of multi-sensor engagements in UAVs. Conversely, OpenCL, an open and non-proprietary standard for the parallel programming of various accelerators utilized in heterogeneous computing, is well-suited for cross-platform applications and can be found in supercomputers and embedded platforms.

Fig. **12** corresponds to an interaction diagram showcasing the mutual engagement between sensor modules and parallel computing control during a UAV mission, as well as the way in which said modules function synchronously and their sequence. The interaction diagram serves as a means to illustrate the dynamic behavior of modules. The procedures that bring about real-time interaction take place when the request is made, and they are subsequently dismantled after the process has culminated. The transfer of sensor data from one module to the embedded control is illustrated by the labeled arrows.

Each individual occurrence of an event module is comprehensively paired with a distinct instance of a sensor module. These modules support a multitude of ideal sensor data sets, as well as a set of impairment parameters, ultimately producing a meticulously curated collection of sensor data. This particular collection of data is inclusive of sensor errors that are determined and classified based on the
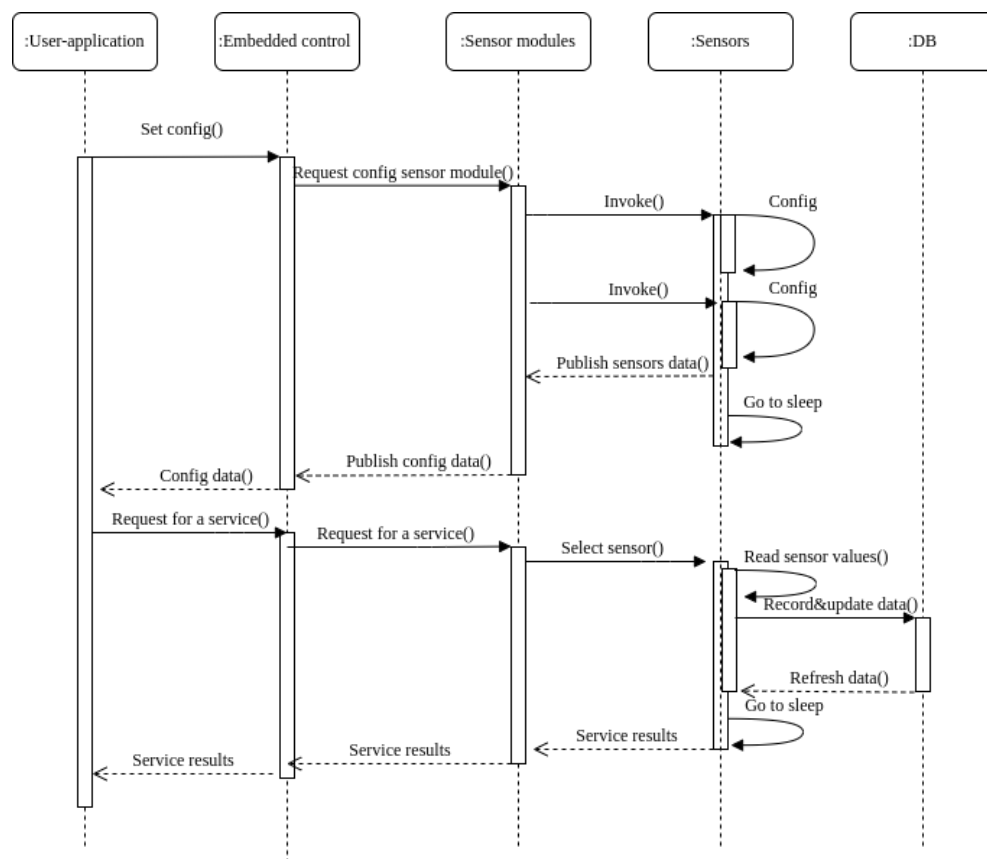

Figure 12. UML sequence diagram for the MRSS platform

impairment parameters and the ideal input data. In current times, the processing of remote sensing that pertains to UAVs is primarily conducted in the ground system after the acquisition of images. As UAVs are equipped with an extensive array of sensors (payload), the data obtained by these sensors are inherently diverse, and the aims and objectives they serve are equally varied.

The software architecture includes four modules (GEOINT, SIGINT, MASINT, and navigation), which represent all sensors and the corresponding electronic devices for data collection. The following sections provide a detailed description of the above-mentioned modules.

3.2.1.   Geospatial intelligence (GEOINT) module

GEOINT is an interdisciplinary field that incorporates the techniques of geography, cartography, and aerial photography, as well as computer science, mathematics, and computer-based modeling, to support national security, public safety, disaster prevention, and relief. GEOINT analysis uses data from multiple sources to create a comprehensive visual representation of an area of interest. Fig. **13** shows the GEOINT module components. The precise task of the GEOINT module is to effectively identify and concisely consolidate information within designated plot boundaries.
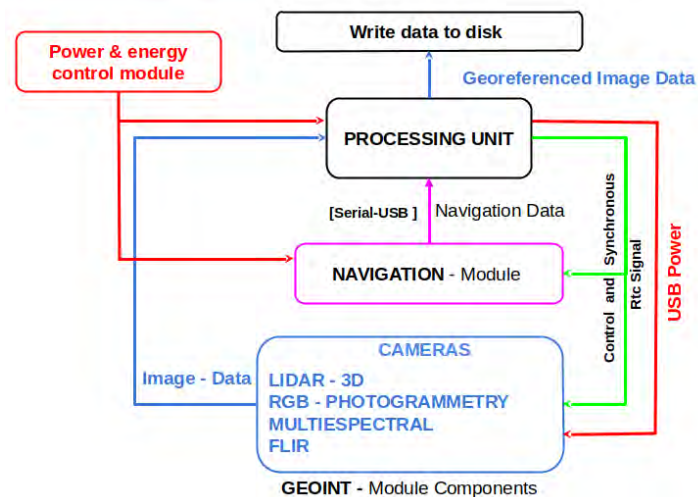

Figure 13. GEOINT block diagram composed of three major components. To produce multi-imaging data and their geo-localization, the processing unit employs the GEOINT module and navigation module components.

GEOINT analysts must be able to effectively communicate their findings to decision-makers and other users of GEOINT products. They must also be able to work effectively as part of a team and use a variety of GEOINT-related software applications.

3.2.2.   Signals intelligence (SIGINT) module

The main objective of SIGINT is to monitor the radio spectrum to obtain basic information about a signal, such as its power and frequency, in order to identify possible threats in the area where a survey

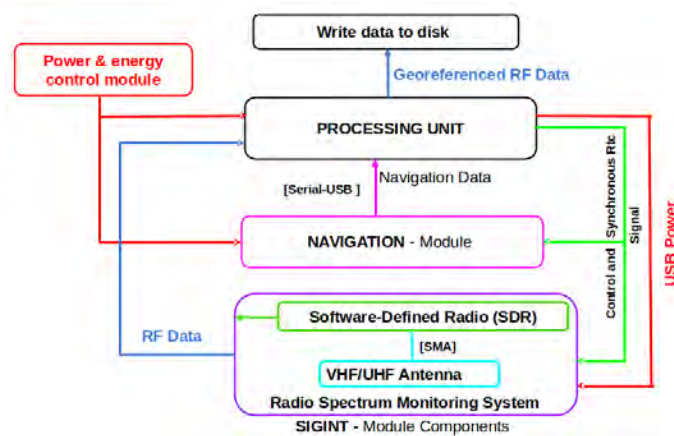is conducted. Its general block diagram is shown in Fig. **14**.

Figure 14. SIGINT block diagram, which consists of three main parts. The processing unit uses SIGINT and navigation module components to generate radio frecuency data and their geo-localization.

The SIGINT diagram is shown in Fig. **15**. Here, the SIGINT module is controlled by a processing unit responsible for executing the following tasks: detecting, capturing, recording, and storing data in the form of radio frequency signals in the bands parameterized by means of SDR hardware. This is based on software requirements.

Figure 15. Fundamental constituent components of the SIGINT module, such as the VHF/UHF antenna, SDR (26), and the process unit.

A block design implementation of our proposed SIGINT methodology was presented in a preliminary work (27). The SDR design breaks with the paradigm of prefabricated communication devices, since it contains an RF block that can be reprogrammed and/or reconfigured using a System-on-Chip (SoC) or an embedded system such as an FPGA through a program or custom software solution.

3.2.3.　Measurement and signature intelligence (MASINT) module

Spectrum monitoring is an automated and intelligent infrastructure that operates in real-time, utilizing machine-machine technology to obtain and accumulate monitoring data. This data is then made readily available to regulators in an intuitive manner for the purpose of dynamic, intelligent, and efficient spectrum management. To this effect, this subsection proposes a MASINT module for acoustic monitoring via acoustic sensors. The proposed architecture of the MASINT module is presented in Fig. **16**. It consists of a processing data unit, a navigation unit, a sensor module, and a data storage unit. The

MASINT module includes acoustic sensors designed to capture sounds from different sources, which can be analyzed for different purposes. Acoustic sensors are commonly employed as cost-effective and straightforward devices to cater to band-specific monitoring prerequisites, complemented by their signal processing capabilities.
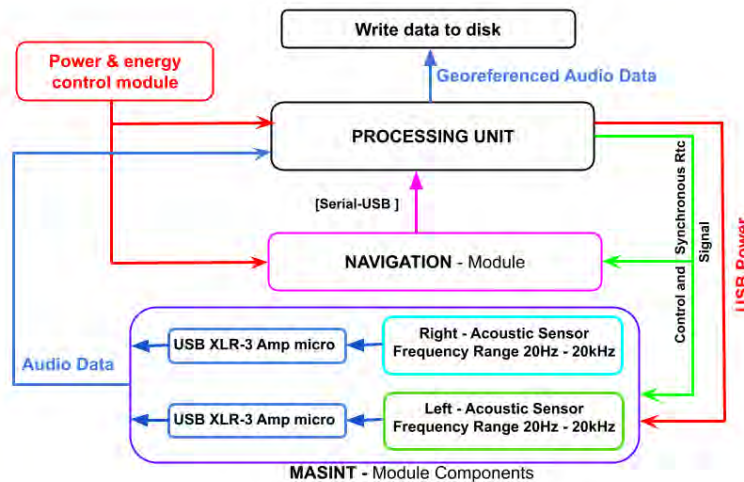

Figure 16. MASINT block diagram consisting of three main parts. The processing unit uses MASINT and navigation module components to generate acoustic data and their geo-localization.

Fig. **16** shows a diagram of the components used for the MASINT module. For acoustic data generation in recognition tasks, it has a single sensor per platform and it is used whenever the system is moving with geo-referencing. In the case of surveillance applications, several acoustic sensors arranged to estimate direction and distance can be selected. However, this is not part of the initial objective, and only a possible implementation will be studied in the future. The main features of this module include three measurement data for radio monitoring and signal analysis and processing.

3.2.4. Navigation module

The navigation module works at the same time or in synchrony with the data collection of each one of the different sensors in the SIGINT, GEOINT, and MASINT modules to correctly geo-reference the data sensed. The real-time clock (RTC) is used as a basis from an embedded system. Fig. **17** shows the navigation module diagram and its respective components. Among the UAV navigation techniques, the Global Navigation Satellite System (GNSS) and the Inertial Navigation System (INS) modules are extensively employed given their global reach and ease of use in relative navigation. Nevertheless, GNSS observations are susceptible to various types of faults that stem from transmission degradation, ionospheric scintillations, multipath, spoofing, and numerous other factors. On the other hand, the Inertial Navigation System module is used to determine the data in space, angular velocities, and accelerations. It is constructed upon the basis of at least one 3-axis gyro and a 3-axis accelerometer.
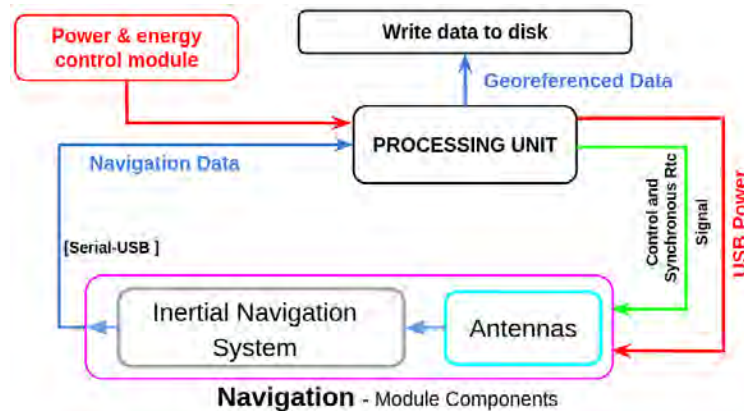
Figure 17. Navigation module consisting of two main parts: the processing unit and the navigation module components. The processing unit utilizes data from the UAV navigation module components for geo-localization purposes.

4.   Experiments and results

This section presents the research results regarding energy utilization and the lifetime of batteries in a multi-sensor UAV system. Under normal conditions, all devices on the platform are connected to a single battery, and each module is non-simultaneously activated. For experimental evaluations, each module is connected separately to the battery, and data are collected for 15 min. Experimental evaluations were conducted to understand the impact of energy consumption on performance and battery life, which is crucial for the efficient and sustainable design of these platforms. Energy consumption was analyzed in different operating modes of the sensor modules, both static and dynamic, and the energy components of each module were examined in detail. Additionally, battery lifetime was analyzed while considering factors such as capacity, state of charge, and degradation over time. The obtained results provide valuable insights for decision-making regarding sensor selection, energy management, and UAV mission planning.

4.1.   Energy consumption model for MRSS platform

This subsection section provides an experimental assessment in order to showcase the plausibility of the suggested UAV-based RS platform. In the base case, all sensor modules have two modes of operation (static and dynamic), in which they consume a certain amount of power depending on the configuration used. For a connected device, the voltage and current vary depending on its operating state; if it is transmitting or receiving over a period of time, power consumption increases.

1. Static mode is the fixed amount of energy consumed consistently for a particular module (*e.g.*, the MASINT module). Static mode, which is also defined as *sleep mode* is the energy consumed E_{sleep} in the absence of any activity. Table **I** shows the energy consumption of different sensor modules. When a sensor module is operating in this particular state, the energy utilization of each module can be approximated, taking into account the time and power consumption. An illustration of this

is the calculation of the energy consumption E_{sleep} in inactive operation, as demonstrated in Eq. (1):

$$E_{Sleep} = P_{Sleep} \times t_{Sleep} \tag{1}$$

where P_{Sleep} and t_{Sleep} are the power consumption and time duration in static mode, respectively.

2. Dynamic mode is the energy required for states in which each device consumes an amount of energy E_{device} during active operation, *e.g.*, a camera capturing and processing a frame Eq. (2). To calculate the dynamic mode, the energy dissipated in any particular configuration over 15 minutes of operation is measured, obtaining an average energy measurement. The energy is determined in the same way as that in static mode, *i.e.*, by multiplying the power consumption and the time duration, as shown in (2):

$$E_{device} = I_{active} \times V \times t_{active} \tag{2}$$

Table I. Energy consumed by the sensor modules

Sensor module	Operation mode	Energy consumption (Wh)	Estimated discharge voltage (V)	DoD (%)
Embedded controller ARM-AARCH64	Static	0,16	8,07	1,5
	Dynamic	1,17	7,89	11
GEOINT	Static	1,05	7,91	10
	Dynamic	9,77	6,66	72
SIGINT	Static	0,34	8,04	3
	Dynamic	3,29	7,51	30
MASINT	Static	0,30	8,05	2,5
	Dynamic	2,23	7,70	20
Navigation	Static	0,18	8,07	1,5
	Dynamic	1,43	7,84	13

Table **I** shows the energy consumption data, estimated discharge voltage data, and deep of discharge data in dynamic and static modes obtained from each sensor modules, this modules were explained previously in Section 3.2. The energy consumption in dynamic mode for the each sensor module was calculate using Eq. (3) by each of the devices (*i.e.*, embedded controller, microphones, *etc.*).

$$E_{dynamic} = E_{WU} + E_{vecnav} + E_{proc} + E_{pyle} + E_{shure} \tag{3}$$

where E_{WU} is the energy consumed by the embedded controller; E_{vecnav} is the energy consumed by the Vectornav; E_{pyle} is the energy consumed by the Pyle amplifier microphone, and E_{shure} is the energy consumed by the Shure amplifier microphone typical devices used in the case of the MASINT module.

Table **I** shows the estimated discharge voltage for each sensor module in dynamic and static modes. Eq. (4), which relates the consumed energy E to the discharged voltage V of the battery, is given by

$$E = V \times Q \tag{4}$$

where E is the consumed energy, V is the discharged voltage of the battery, and Q is the battery capacity. The aforementioned equation posits that the energy consumed is equivalent to the multiplication of the voltage discharged and the capacity of the battery.

Finally, to estimate the battery lifetime of a MRSS platform, it is necessary to take a close look at the energy consumption of each device in the sensor modules. After establishing an average energy consumption as a baseline, designers can calculate the battery lifetime using the method proposed in Section 4.2. This paper does not deal with battery lifetime prediction methods.

4.2.   Battery lifetime

The battery in dynamic mode constitutes a pivotal consideration in the selection of a secondary energy source. Rechargeable batteries have a limited lifespan and progressively deteriorate regarding their capacity to retain charges over time, which is an irreversible phenomenon. The reduction in battery capacity concomitantly diminishes the duration for which the product can be powered, commonly referred to as *runtime*. The battery's lifetime is primarily influenced by the cycle life. The cycle life of a battery is defined as the total number of charge and discharge cycles that the battery can complete before experiencing a decline in performance. The depth of discharge (DoD) significantly affects the cycle life of Li-ion batteries. The DoD represents the amount of battery storage capacity utilized. Li-ion batteries are deep-cycle batteries, possessing DoDs of approximately 95 %. The typical estimated life of a Li-ion battery is roughly seven years or 2.000 to 2.500 full charge/discharge cycles before the capacity falls below 80 %, whichever occurs first. Conversely, the State of Charge (SOC) constitutes a significant parameter of li-ion batteries, indicating the level of charge within a battery cell. According to (37) and (38), the SOC indicates the instantaneous charge of a battery as a percentage of its maximum capacity (39), which is given by Eq. (5).

$$SOC(t) = \frac{Q(t)}{Q_{max}} 100\,\% \tag{5}$$

where the instantaneous maximum capacity is represented as Q_{max}, while the Coulomb counting method is employed to obtain the instantaneous stored charge $Q(t)$, wherein Q_0 is indicative of the initial battery charge.

$$Q(t) = Q_0 - \int_0^t I_{batt}(t)dt \tag{6}$$

Similarly, the depth of discharge (DoD) serves as an indicator of the proportion of the overall capacity that has been discharged Eq. (7).

$$DoD(t) = \frac{Q_{max} - Q(t)}{Q_{max}} 100\,\%. \tag{7}$$

According to the literature (37), the maximum capacity of a battery typically fades to 80 % of its original value before it is considered to have reached the end of its life. Hence, it is imperative to engage in regular maintenance and appropriate handling of batteries in order to extend useful life. An accurate forecast of the long-term effectiveness and wellness of batteries requires modeling battery degradation. The service capabilities of Li-ion batteries as storage systems are impacted by the deterioration of their capacity. The prognosis of battery health is facilitated by the estimation of lifetime and capacity. An estimation of battery lifetime can be made by considering the transaction period and consumption of

the selected configuration. To determine the battery lifetime LT, one must divide the battery capacity C_{Bat} by the average device current consumption I_L over time Eq. (8).

$$LT = \frac{C_{bat}}{I_L}.$$
(8)

Raw data collection in this regard is based on taking measurements and then cleaning and processing them to analyze the energy consumption behavior of each device, *i.e.*, the embedded control with each sensor module. The average is the sum of the amount of current consumed when collecting data, scaled by the ratio of time that the sensor module is collecting data. Fig. **18** allows graphing and tabulating the collected power consumption data collected, as well as a real-time visualization of each sensor module.
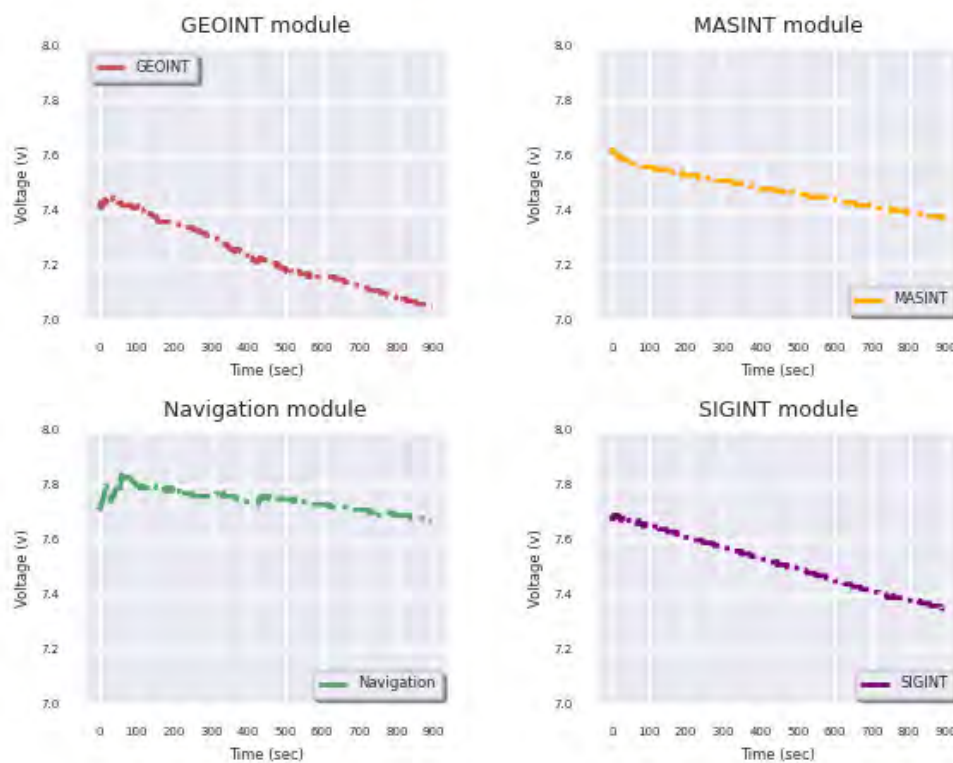

Figure 18. Dynamic-mode behavior of the battery voltage with respect to each sensor module: a) GEOINT, b) MASINT, c) navigation, d) SIGINT

The time presented in Figs. **18** and **19** is around 15 min (*i.e.*, 900 seconds), during which the battery's discharge voltage is produced from each one of the sensor modules. The battery's discharge voltage is the amount of electrical potential (voltage) loss caused by the sensor module in dynamic mode. The cut-off Voltage (Vco) is the voltage at which the battery is specified to be fully discharged. In this sense, Vco is equal to 6,1 V. While there is usually charge remaining, operation at voltages lower than Vco can damage the battery.

Fig. **18** shows the discharge voltage caused by the sensor module, which determines the fraction of power withdrawn from the battery according to the sensor module used (*e.g.*, SIGINT). For example, if the DoD of the NP-F750 battery is 20 % (as given by the manufacturer), then only 20 % of the battery capacity can be used by the sensor modules. In addition, according to the manufacturer, the lifetime of a NP-F750 battery is in the range of 2.000-2.500 cycles. A daily cycle of charge and discharge for approximately seven years is ensured. After this period, the battery retains 80 % of its initial capacity, allowingit to operate for 2.000 cycles. It is only when the battery's aging process has progressed to the point where voltage drops render the battery unusable that the capacity fades to 60 %.
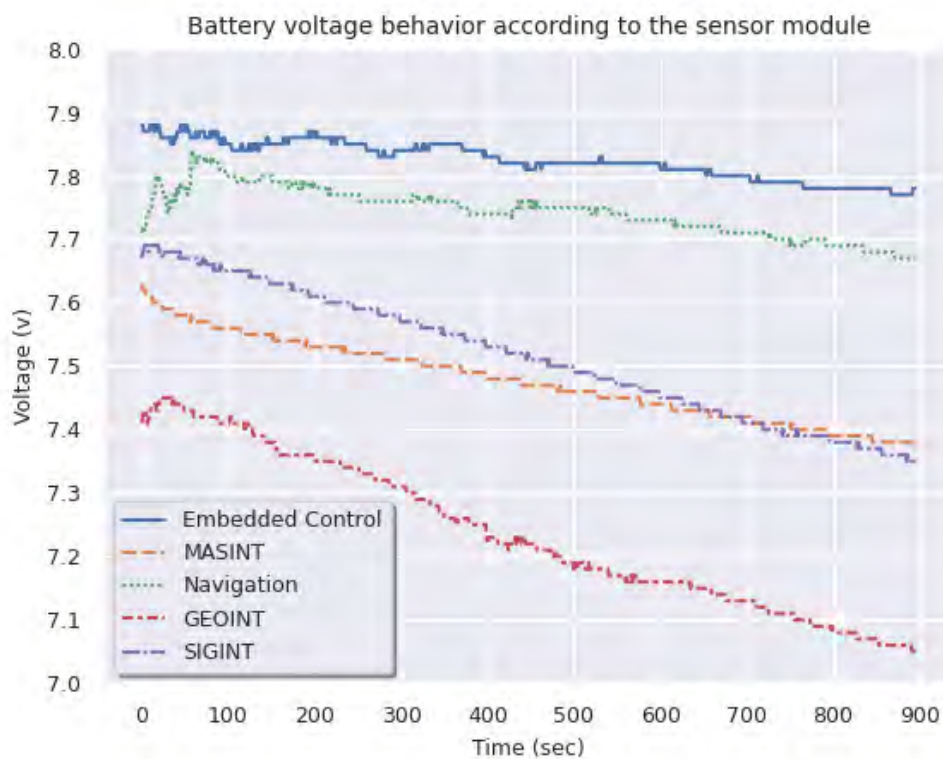

Figure 19. Correspondence between the discharge voltage of the battery and each individual sensor module. Blue represents the embedded control, orange represents MASINT, green represents navigation, red represents GEOINT, and purple represents SIGINT.

For the embedded control, an expected discharge voltage of 8,07 V and a 1,5 % DoD were taken as a theoretical reference for the static mode, in addition to an expected theoretical value of 7,89 V and a DoD of 11 % for the dynamic mode **I**. Fig. **19** shows that a discharge voltage of 7,78 V is reached, with a depth of discharge of 16 % for the dynamic mode. According to these results, the life cycles for the continuous use of this module are approximately 2,625. This entails a battery lifetime of 7,35 years.

As for the GEOINT module, an expected discharge voltage of 7,91 volts and a 10 % DoD were taken as reference for the static mode, as well as an expected theoretical value of 6,66 V and a DoD of 72 % for the dynamic mode **I**. In Fig. **19**, a DoD of 47 % is observed, reaching a discharge voltage 7,16 V (deep cycling), which entails a battery lifetime of 4,6 years.

Regarding the MASINT module, an expected discharge voltage of 8,05 V and a 2,5 % DoD were taken as reference for the static mode. For the dynamic mode, an expected theoretical value of 7,70 V and a DoD of 20 % were used. Fig. **19** shows that a discharge voltage of 7,5 V is reached, with a depth of discharge of 30 % in dynamic mode. According to these results, the life cycles for continuous use of this module are approximately 1.937. This entails a battery lifetime of 5,4 years.

The theoretical reference for the navigation module included an expected discharge voltage of 8,07 V and a 1,5 % DoD for the static mode and 7,84 V and 13 % for the dynamic mode **I**. Fig. **19** shows that a discharge voltage of 7,67 V is reached, with a depth of discharge of 21,5 % in dynamic mode, *i.e.*, the life cycles for continuous use of this module are approximately 2.453, which entails a battery lifetime of 6,86 years.

Finally, for the SIGINT module, an expected discharge voltage of 8,04 V and a 3 % DoD were taken as a theoretical reference for the static mode, as well as 7,51 V and 30 % for the dynamic mode **I**. Fig. **19** shows that a discharge voltage of 7,34 V was reached, with a depth of discharge of 38 % in dynamic mode, entailing 1.937 life cycles and a battery lifetime of 5,425 years.

5. Discussion

This manuscript proposes an integrated multi-sensor platform with the objective of achieving high throughput data collection. The platform comprises eight sensing modules: a Vectornav vn200(GNSS-INS), a HackRF One, a DSLR Camera (Sony Alpha-A6000), two XLRS outdoor microphones, a LiDAR Camera (ouster OS1-32U, OSO-32U), and a Parrot Sequoia multi-spectral camera. The use of UAVs in lieu of terrestrial means of data collection has rapidly garnered widespread acceptance due to their significantly improved efficiency. Despite being more difficult to implement than conventional methods, the integration of an all-encompassing approach has the potential to ensure uniform and precise outcomes.

The development of a multi-sensor platform may be an important breakthrough for the maturity of emerging UAV applications, especially when architectures are created to support the development of such platforms. Nevertheless, the development of architectures should also be combined with energy consumption analyses regarding implementation, deployment, and performance, bringing these architectures to a more realistic setting. This analysis allows studying the real and theoretical behavior of a battery regarding the discharge voltage, DoD, and the energy consumed. This approach highlights the importance of battery characterization in order to have a real time reference that ensures successful multi-data collection missions with UAV platforms. It is anticipated that, with each charge and discharge cycle, the actual values will diminish considerably as a result of battery degradation.

The efficient scheduling and budgeting of battery power in multi-sensor applications has become a critical design issue. In this sense, our work studies how energy consumption, battery lifetime, and multi-sensor capabilities affect battery lifetime. The high energy consumption associated with modules such as GEOINT leads to deep discharge in excess of a 20 % DoD, resulting in a maximum battery degradation of 2,4 years. These findings allow designers of multi-sensor platforms to determine the necessary battery capacities to enhance sensor energy consumption, thereby minimizing the total costs of UAV-based RS platforms.

Although considerable efforts have been devoted to the development of multi-sensor platforms for UAVs, there are several formidable challenges in this field. A crucial task is to accurately estimate the energy consumption requirements of each component. By selecting an appropriate multi-sensor approach during the design phase, the hardware underpinning the platform can be optimized for energy efficiency, thereby facilitating the effective power management of the system. However, certain multi-sensor modules lack comprehensive insights into the battery aging process. Consequently, it is desirable to devise a means of integrating the identification of aging mechanisms with online battery health assessment.

Battery lifetime may be influenced by deep cycling, as is the case of the GEOINT module. In contrast to other deep-cycle batteries, fractional charges extend the lifespan of a lithium battery.

Finally, the effect of parallel computing control on energy consumption is considered. It is observed that, when two processors are used, the management strategy dynamically increases the frequency of the processors, resulting in increased energy consumption. On the contrary, when using four processors, the management decreases the processors' frequency of operation, resulting in reduced energy consumption.

6. Conclusions

This study formulated, constructed, and evaluated a preliminary approach for a multi-sensor system based on MRSS technologies for a Tarot x8 UAV. This platform involved the parallel integration of specialized and flexible sensor modules in real-time parallel computing control for UAV environmental data collection.

An exhaustive analysis of the energy consumption behavior was conducted for each sensor module, in order to find efficient energy usage and thus estimate the battery lifetime. The idea is to make efficient use of the batteries via the parallel scheduling of the processors. This scheduling implies that each module works independently in relation to the data capture programmed at a given time.

Additionally, this research focused on how to integrate the multiple sensor modules into the UAV platform. The benefits of this approach could facilitate the adoption of UAVs in the ever-developing field of multipurpose UAV applications such as precision agriculture, search and rescue missions based on acoustic location and detection, fast 3d mapping in real time, and emergency response in natural

disasters. Multipurpose UAVs provide powerful multi-modal sensing data information that reduces response times and increases safety, but many of them lack fast mapping capability due to their lack of parallelism in real-time data processing. In real-life teams on the ground, be it in the public safety or humanitarian aid sectors, there is a need for quick and reliable aerial insights to plan and deliver successful operations in remote, complex, and often unsafe environments.

The results of this study serve to enhance the pre-existing advantages of UAVs for decision-making. Furthermore, our work presents a distinctive and innovative input for future development to establish uniformity in data collection. This is accomplished by emphasizing the potential of complete automation in the collection of multi-range data with UAVs.

A management control for a multi-sensor platform which uses parallel computing was proposed. The goal of parallel management is to monitor and control multiple sensor modules to increase their efficiency and reliability and reduce energy consumption in real-time applications. Improved efficiency and reliability has to do with reducing data errors, minimizing outage times, and maintaining acceptable data synchronization with other sensor modules.

Energy consumption is a major concern for UAV technologies. A significant waste of energy occurs due to active sensing, which is typically avoided by turning off the sensor (sleep mode), while no sensing is underway. As future work, an exact energy consumption algorithm for evaluating UAV multi-sensor platforms is required. To assess the lifetime of the power supply (battery) in real time, the energy attributes of the sensor modules must be estimated. Research in this regard has been actively increasing given the wide scope of applications that can profit from such an innovation.

Our approach can greatly enhance the development process of multi-sensor platforms and guarantee mission success by offering a methodical and effortless approach to validate these platforms based on energy consumption. Future research may broaden the scope of this approach to encompass the modeling of multi-sensor platforms and the creation of energy management software. This will be a natural progression of this project. Another future work can involve a multi-sensor data processing (MSDP) software that will be developed as a core module of the data processing system (DPS) for several applications. MSDP and DPS methods will be adopted in order to process data from multiple sensors for any software architecture to support multiple flight missions.

UAV-based multi-sensor platform designers must analyze the energy consumption profile of their application to fully understand the demand and the factors that influence it. Thus, in order to mitigate the impact of frequent battery changes, manufacturers of UAV-based multi-sensor platforms need to understand how the sensor modules consume power while running, which help them estimate battery life.

7. Funding

8. Acknowledgments

9. CRediT author statement

Conceptualization, S.G., N.A., and J.C.; software, N.A., S.G., M.T., and C.S.; validation, S.G, and N.A.; research, N.A., S.G., M.T., C.S., J.C., and G.C.; resources, S.G., N.A., and J.C.; Data curation, S.G., N.A., and J.C.; writing – original draft, S.G. and N.A.; supervision, S.G., N.A., and J.C. All authors have read and agreed to the published version of the manuscript.

References

[1] G. Keaton, "LiDAR surveying technology advantages," 2021. [Online]. Available:`https://ecko360industrial.com/2021/06/28/lidar-surveying-technology-advantages/`↑3, 4

[2] H. Yao, R. Qin, and X. Chen, "Unmanned aerial vehicle for remote sensing applications — A review," *Remote Sens.*, vol. 11, no. 12, art. 1443, 2019. `https://www.mdpi.com/2072-4292/11/12/1443`↑4

[3] C. Yinka-Banjo and O. Ajayi, "Sky-farmers: Applications of unmanned aerial vehicles (UAV) in agriculture," in *Autonomous Vehicles*, G. Dekoulis, Ed., London, UK: IntechOpen, 2019, ch. 6. `https://doi.org/10.5772/intechopen.89488`↑4

[4] J. Cuaran and J. Leon, "Crop monitoring using unmanned aerial vehicles: A review,". *Agricultural Reviews*, vol. 42, no. 2, pp. 121-132, 2021. `https://doi.org/10.18805/ag.R-180`↑4

[5] M. Pashine and P. Mundhada, "Implementation of real time monitoring in the field of agriculture," *Int. Res. J. Eng. Technol.*, vol. 8, no. 12, pp. 665-669, 2021. `https://www.irjet.net/archives/V8/i12/IRJET-V8I12114.pdf`↑4

[6] Z. Yang *et al.*, "UAV remote sensing applications in marine monitoring: Knowledge visualization and review," *Sci. Total Environ.*, vol. 838, part 1, art. 155939, 2022. https://doi.org/10.1016/j.scitotenv.2022.155939 ↑4

[7] P. Maddikunta, S. Hakak, M. Alazab, S. Bhattacharya, T. Gadekallu, W. Khan, and Q. Pham, "Unmanned aerial vehicles in smart agriculture: Applications, requirements, and challenges," *IEEE Sens. J.*,vol. 21, no. 16, pp. 17608-17619, 2021. https://doi.org/10.1109/JSEN.2021.3049471 ↑5

[8] J. Pavón, J. Gómez-Sanz, A. Fernández-Caballero, and J. Valencia-Jiménez, "Development of intelligent multisensor surveillance systems with agents," *Robotics Auton. Syst.*, vol. 55, no. 12, pp. 892-903, 2007. https://doi.org/10.1016/j.robot.2007.07.009 ↑4, 6

[9] H.Abdullahi, F. Mahieddine, and R. Sheriff, "Technology impact on agricultural productivity: A review of precision agriculture using unmanned aerial vehicles," in *Int. Conf. Wireless Sat. Syst.*, 2015, pp. 388-400. https://doi.org/10.1007/978-3-319-25479-1_29 ↑4

[10] S. Liaghat and S. Balasundram, "A review: The role of remote sensing in precision agriculture," *American J. Agricul. Biolog. Sci.*, vol. 5, no. 1, pp. 50-55, 2010. https://thescipub.com/pdf/ajabssp.2010.50.55.pdf ↑4

[11] N. Yin, R. Liu, B. Zeng, and N. Liu, "A review: UAV-based remote sensing," *IOP Conf. Ser. Mater. Sci. Eng.*, vol. 490, art. 062014, 2019. https://iopscience.iop.org/article/10.1088/1757-899X/490/6/062014/pdf ↑5

[12] A. Opeyemi and N. David, "An RGB sensor-based aerial robotic platform for sustainable precision agriculture," 2020. [Online]. Available: https://ic-sd.org/wp-content/uploads/2020/11/Abioye-Ayodeji.pdf ↑5

[13] S. Tzafestas, *Introduction To mobile robot control*, Amsterdam, The Netherlands: Elsevier, 2014. https://doi.org/10.1016/B978-0-12-417049-0.00012-2 ↑6

[14] P. Velusamy, S. Rajendran, R. Mahendran, S. Naseer, M. Shafiq, and J. Choi, "Unmanned aerial vehicles (UAV) in precision agriculture: Applications and challenges," *Energies*,vol. 15, no. 1, art. 217, 2022. https://doi.org/10.3390/en15010217 ↑7

[15] A. Feng, J. Zhou, E. Vories, K. Sudduth, and M. Zhang, "Yield estimation in cotton using UAV-based multi-sensor imagery", *Biosyst. Eng.*, vol. 193, pp. 101-114, 2020. https://doi.org/10.1016/j.biosystemseng.2020.02.014 ↑8, 9

[16] A. Matese and S. Di Gennaro, "Practical applications of a multisensor UAV platform based on multispectral, thermal, and RGB high-resolution images in precision viticulture," *Agriculture*, vol. 8, no. 7, art. 116, 2018. https://doi.org/10.3390/agriculture8070116 ↑8, 9

[17] S. Di Gennaro *et al.*, "Multisensor approach to assess vineyard thermal dynamics combining high-resolution unmanned aerial vehicle (UAV) remote sensing and wireless sensor network (WSN) proximal sensing," *Scientia Horticulturae*, vol. 221, pp. 83-87, 2017. https://doi.org/10.1016/j.scienta.2017.04.024 ↑9

[18] P. Katsigiannis, L. Misopolinos, V. Liakopoulos, T. Alexandridis, and G. Zalidis, "An autonomous multi-sensor UAV system for reduced-input precision agriculture applications," in *2016 24th Med. Conf. Control Automation (MED)*, 2016, pp. 60-64. https://doi.org/10.1109/MED.2016.7535938 ↑9

[19] M. Nagai, T. Chen, A. Ahmed, and R. Shibasaki, "UAV borne mapping by multi sensor integration," 2008. [Online]. Available: https://www.isprs.org/proceedings/xxxvii/congress/1_pdf/207.pdf ↑9

[20] F. Liu, J. Shan, B. Xiong, and F. Zheng, "A real-time and multi-sensor-based landing area recognition system for UAVs," *Drones*, vol. 6, no. 5, art. 118, 2022. https://doi.org/10.3390/drones6050118 ↑9

[21] M. Stein, S. Bargoti, and J. Underwood, "Image based mango fruit detection, localisation and yield estimation using multiple view geometry," Sensors, vol. 16, no. 11, art. 1915, 2016. https://doi.org/10.3390/s16111915 ↑9

[22] M. Maimaitijiang *et al.*, "Unmanned aerial system (UAS)-based phenotyping of soybean using multi-sensor data fusion and extreme learning machine," *ISPRS J. Photogramm. Remote Sens.*, vol. 134, pp. 43-58, 2017. https://doi.org/10.1016/j.isprsjprs.2017.10.011 ↑9

[23] G. Bai, Y. Ge, W. Hussain, P. Baenziger, and G. Graef, "A multi-sensor system for high throughput field phenotyping in soybean and wheat breeding," *Comp. Electronics Agricul.*, vol. 128, pp. 181-192, 2016. https://doi.org/10.1016/j.compag.2016.08.021 ↑9

[24] A. Comar, P. Burger, B. Solan, B. Frederic, F. Daumard, and H. Jean-François, "A semi-automatic system for high throughput phenotyping wheat cultivars in-field conditions: Description and first results," *Funct. Plant Biol.*, vol. 39, no. 11, pp. 914-924, 2012. https://doi.org/10.1071/fp12065 ↑9

[25] P. Andrade-Sánchez *et al.*, "Development and evaluation of a field-based high-throughput phenotyping platform," *Funct. Plant Biol.*, vol. 41, no. 1, pp. 68-79, 2014. https://doi.org/10.1071/fp13126 ↑10

[26] E. Torres-Garzón, J. Guevara, and Y. Mendoza-Prieto, "Estudio sobre el desarrollo de un prototipo para monitoreo del espectro radioeléctrico utilizando SDR," *Revista Perspectivas En Inteligencia*, vol. 14, no. 23, pp. 303-323, 2022. https://doi.org/10.47961/2145194X.344. ↑18

[27] M. Terán, J. Aranda, J. Marín, E. Uchamocha, and G. Corzo-Ussa, "A methodology for signals intelligence using non-conventional techniques and software-defined radio," presented at the *2021 IEEE Col. Conf. Comm. Comp. (COLCOM)*, Cali, Colombia, May 26-28, 2021. https://doi.org/10.1109/COLCOM52710.2021.9486297 ↑18

[28] B. Sharma and G. Ritchie, "High-throughput phenotyping of cotton in multiple irrigation environments," *Crop Sci.*, vol. 55, no. 2, pp. 958-969, 2015. https://doi.org/10.2135/cropsci2014.04.0310 ↑10

[29] R. Xu, C. Li, and S. Bernardes, "Development and testing of a UAV-based multi-sensor system for plant phenotyping and precision agriculture," *Remote Sens.*, vol. 13, no. 17, art. 3517, 2021. https://www.mdpi.com/2072-4292/13/17/3517 ↑10

[30] O. Montesinos-López *et al.*, "Predicting grain yield using canopy hyperspectral reflectance in wheat breeding data," *Plant Meth.*, vol. 13, art. 4, 2017. https://doi.org/10.1186/s13007-016-0154-2 ↑10

[31] S. Fei *et al.*, "UAV-based multi-sensor data fusion and machine learning algorithm for yield prediction in wheat," *Prec. Agricul.*, vol. 24, pp. 187-212, 2022. `https://doi.org/10.1007/s11119-022-09938-8` ↑10

[32] M. Vlaminck, L. Diels, W. Philips, W. Maes, R. Heim, B. Wit, and H. Luong, "A multisensor UAV payload and processing pipeline for generating multispectral point clouds," *Remote Sens.*, vol. 15, no. 6, art. 1524, 2023. `https://doi.org/10.3390/rs15061524` ↑10

[33] X. Li and A. Savkin, "Networked unmanned aerial vehicles for surveillance and monitoring: A survey," *Future Internet*, vol. 13, no. 7, art. 174, 2017. `https://doi.org/10.3390/fi13070174` ↑10

[34] A. Gupta, H. Gupta, P. Kumari, R. Mishra, S. Saraswat, and T. Dutta, "A real-time precision agriculture monitoring system using mobile sink in WSNs", in *2018 IEEE Int. Conf. Adv. Net. Telecom. Syst. (ANTS)*, Indore, India, December 16-19, 2018. `https://doi.org/10.1109/ANTS.2018.8710048` 10

[35] Y. Mendoza-Prieto, S. Sopo, and E. Torres-Garzón, "Evaluación de captadores fotovoltaicos para suministro complementario de energía en aeronaves remotamente tripuladas," *Revista Perspectivas en Inteligencia*, vol. 12, no. 21, pp. 261-274, 2021. `https://doi.org/10.47961/2145194X.226` ↑11

[36] J. Machado, "Software defined radio: Basic principles and applications," *Revista Facultad de Ingeniería*, vol. 24, no. 38, pp. 79-96. `http://www.scielo.org.co/pdf/rfing/v24n38/v24n38a07.pdf` ↑

[37] K. Mallon, F. Assadian, and B. Fu, "Analysis of on-board photovoltaics for a battery electric bus and their impact on battery lifespan," *Energies*, vol. 10, no. 7, art. 943, 2017. `https://doi.org/10.3390/en10070943` ↑22

[38] I. Acero *et al.*, "Method for validating CubeSat satellite EPS through power budget analysis aligned With mission requirements," *IEEE Access*, vol. 11, pp. 43316-43332, 2023. `https://doi.org/10.1109/ACCESS.2023.3271596` ↑22

[39] C. Wu, J. Fu, X. Huang, X. Xu, and J. Meng, "Lithium-ion battery health state prediction based on VMD and DBO-SVR," *Energies*, vol. 16, no. 10, art. 3993, 2023. `https://doi.org/10.3390/en16103993`https://www.mdpi.com/1996-1073/16/10/3993 ↑22

Nicolás Amézquita Gómez

He received a *cum laude* degree in Electronic Engineering in 2004 from Universidad Pedagógica y Tecnológica de Colombia. From 2004 to 2019, he worked as a researcher at different universities and technology companies in Spain and the United States as follows. From 2004 to 2008: researcher at the PhD(c) in Artificial Intelligence at Universitat Politècnica de Catalunya and researcher in Mobile Robotics and Intelligent Systems at the Institute of Robotics and Industrial Informatics (IRI) (CSIC-UPC). In 2009, he received a Master's degree in Computer Security and Intelligent Systems in Sensory Systems Applied to Industry (SSAI). In 2009, he received an excellent *cum laude* PhD degree in Computer Science and Engineering. Both of these degrees were granted by Universitat Rovira i Virgili in Spain. From 2013 to 2019, he patented the following inventions: Producing video bits for space time video summary, Patent class: to facilitate tuning or selection of video signal (725/38), Patent

number application: 20130081082, USA Vilynx Inc. Palo Alto, CA, USA; Patent class: target tracking or detecting (382/103), Patent number application: 10410679, US; Patent class: operator interface (725/37), Patent number application: 8869198, USA, purchased by Apple on October 27th, 2020, Palo Alto, CA, USA. His research interests are computer vision, artificial intelligence, parallel computing for embedded systems, autonomous and robotic systems, and digital signal processing. He is currently researching at the project titled *Modular Multi-mission Monitoring System for Remotely Piloted Aircraft Systems* (MMMS-RPAS) at the Electronic Engineering Department of Universidad Sergio Arboleda (Bogotá, Colombia).
Email: nicolas.amezquita@usa.edu.co

Sergio Ramiro González Bautista

He is a PhD and a Master in Electronic Engineering from Pontificia Universidad Javeriana. Bachelor in Electronic Engineering from Universidad Pedagógica y Tecnológica de Colombia (UPTC). His research interests are focused on automatic maintenance management systems, cyber-physical architectures for Industry 4.0, and Automated Guided Vehicles (AGVs). He is currently researching at the project titled Modular Multi-mission Monitoring System for Remotely Piloted Aircraft Systems (MMMS-RPAS) at the Electronic Engineering Department of Universidad Sergio Arboleda (Bogotá, Colombia).
Email:sergio.gonzalez@usa.edu.co

Marco Teran

He received a BS degree in Electronic Engineering and a MSc degree in Electronics from the Bauman Moscow State Technical University (Russia). He has experience in research at the "Progress"Scientific Research Institute in the area of communications and satellite navigation. He served as an ATSEP engineer at Aeronáutica Civil (Colombia). Since 2014, he has been an associate professor of the School of Exact Sciences and Engineering of Universidad Sergio Arboleda (Bogotá, Colombia). His current research interests include indoor positioning, RADAR, and GNSS technologies, as well as Internet of Things (IoT) applications. He is currently pursuing a PhD at Pontificia Universidad Javeriana. He is currently researching at the project titled Modular Multi-mission Monitoring System for Remotely Piloted Aircraft Systems (MMMS-RPAS) at the Electronic Engineering Department of Universidad Sergio Arboleda (Bogotá, Colombia).
Email: marco.teran@usa.edu.co

Camilo Salazar

He received a BS degree in Electronic Engineering from Escuela Colombiana de Ingenieria Julio Garavito, a specialization in Telecommunications from Universidad Piloto de Colombia, and a Master's degree in Telecommunications and ICT Regulation from Universidad Santo Tomás. Extensive knowledge in SDR (Software-Defined Radio) development and mobile communications. He is currently researching at the project titled Modular Multi-mission Monitoring System for Remotely Piloted Aircraft Systems (MMMS-RPAS) at the Electronic Engineering Department of Universidad Sergio Arboleda (Bogotá, Colombia).
Email: camilo.salazar@usa.edu.co

John Corredor

He is a PhD from Universidad Autónoma de Barcelona (Spain) with a *cum laude* degree. He has participated in projects and training courses in the field of Artificial Intelligence and Data Science, particularly in design and development with applications involving Machine Learning, Data Mining, Computer Vision, Performance Prediction in High Performance Computing (HPC), multi-core computer architectures, operating systems, hybrid systems for AI, communication theory, optimization, parallel architectures, robotics, teaching methodologies for engineering, programming paradigms, and high availability computing (HTC), among other topics. Extensive experience in research project management and social impact. He is currently a research professor at the School of Intelligence and Strategic Counterintelligence of the Ministry of Defense of Colombia, as well as at the Faculty of Engineering of Pontificia Universidad Javeriana (Bogotá, Colombia).
Email: john.corredor@esici.edu.co

Germán Darío Corzo

He es a major of the Colombian Army and received his Electronic Engineering degree in 2004 from Universidad Distrital of Bogotá, as well as a Master's degree from Pontificia Universidad Javeriana in 2014. He worked for 15 years in the areas of signals intelligence (SIGINT), Geospatial Intelligence (GEOINT), and Measurement and Signature Intelligence (MASINT). He has spent 3 years working in the Army's Science, Technology, and Innovation area. His research interest are telecommunications, artificial intelligence, Industry 4.0, and technological strategies.
Email: german.corzo@buzonejercito.mil.co

Research

Comparative Analysis of the Use of Nanosilica and Fly Ash in Hydraulic Concrete

Análisis comparativo del uso de nanosílice y ceniza volante en el concreto hidráulico

Sara Cristina Solache de la Torre[1] [ID], David Joaquín Delgado-Hernández[2] [ID], and Juan Carlos Arteaga-Arcos[3] [ID][✉]*

[1]Facultad de Arquitectura y Diseño, Universidad Autónoma del Estado de México Cerro de Coatepec s/n, Toluca, Estado de México, C.P. 50130
[2]Facultad de Ingeniería, Universidad Autónoma del Estado de México Cerro de Coatepec s/n, Toluca, Estado de México, C.P. 50130
[3]Facultad de Ciencias, Universidad Autónoma del Estado de México Campus el Cerrillo, Carretera Toluca-Ixtlahuaca km 15.5, Estado de México, C.P. 50200

Abstract

Context: Nowadays, nanomaterials constitute an innovative alternative for the construction sector. This study evaluates the benefits of adding nanosilica and fly ash to Portland cement concrete in terms of its mechanical strength properties.

Method: 45 specimens were used to compare the compressive strength and durability of concrete mixtures with nanosilica and fly ash. The specimens were studied after 7, 14, and 21 days to determine their maximum resistance.

Results: The addition of small amounts of nanosilica (up to 1 %) significantly improved the compressive strength of the concrete. In contrast, a large amount of fly ash (up to 8 %) was required for a noticeable effect.

Conclusions: Concrete with nanosilica yielded the best results in terms of mechanical strength. The key to improving concrete through nanosilica and fly ash is to reduce the water-to-cement ratio using chemical agents that reduce porosity and increase resistance.

Keywords: concrete, nanosilica, fly ash, strength

*[✉] **Correspondence:** scsolache@gmail.com, jcarteaga_mx@yahoo.com.mx

Resumen

Contexto: Hoy en día, los nanomateriales representan una alternativa innovadora para el sector de la construcción. Este estudio evalúa los beneficios de añadir nanosílice y ceniza volante al concreto de cemento Portland en función de sus propiedades de su resistencia mecánica.

Método: Se utilizaron 45 especímenes para comparar la resistencia a la compresión y la durabilidad de mezclas de concreto con nanosílice y ceniza volante. Los especímenes fueron estudiados a los 7, 14 y 21 días para determinar su máxima resistencia.

Resultados: La adición de cantidades pequeñas de nanosílice (hasta 1 %) mejoraron significativamente la resistencia a la compresión del concreto. En contrate, se necesitó una gran cantidad de ceniza volante (hasta 8 %) para lograr un efecto notable.

Conclusiones: El concreto con nanosílice dio los mejores resultados en cuanto a resistencia mecánica. La clave para mejorar el concreto con nanosílice y ceniza volante es reducir la relación cemento-agua utilizando agentes químicos que reduzcan la porosidad y aumenten la resistencia.

Palabras clave: concreto, nanosílice, cenizas volantes, resistencia

Table of contents

1.   Introduction

Concrete is currently the most widely used material in the construction industry. Therefore, research is being conducted with the aim of improving its physical properties and reducing its environmental impact. In recent years, studies and applications involving concrete have intensified in order to increase its strength and prevent cracking or micro-fissures occurring throughout the curing process via innovative materials such as nanotechnology and the utilization of supplementary cementitious materials (*e.g.*, fly ash), which have played an important role in this regard (1).

Improving the performance of concrete is important for two reasons. Firstly, the demand for construction products and services is increasing as the world population grows. Portland cement, the essential concrete binder, accounts for nearly 80 % of concrete-related CO_2, emissions, as well as 5-7 % of the global CO_2, emissions (2). Secondly, the construction sector is one of the most polluting industries (3). However, it also produces the greatest economic wealth, progress, and social welfare around the world (4). Therefore, a balance is required to continue building without significant negative effects on the environment. (5) reported that as much as 50 % of reinforced steel use could be reduced

by increasing concrete's compressive strength. Durable and high strength concrete is the main concern in future production as far material and eco-efficiencies are concerned.

Nanotechnology has begun to gain importance in this research area. Nanoparticles and nanosilica are commonly used to reinforce polymers and increase their hardness, modulus of elasticity, weatherability, flammability, *etc*. (6). In architecture and construction, the applications of nanotechnology range from improving the traditional mechanical properties of concrete to improved products such as paints, sealants, and glasses (to make them repellent against bacteria and other harmful biological agents). Nanotechnology has also shown its usefulness in improving the thermal and strength properties of materials, among other benefits (7).

Nanotechnology is the study, design, creation, synthesis, manipulation, and application of materials, devices, and functional systems through the control of matter at the nanoscale, as well as the utilization of phenomena and properties related to it (8). The application of nanoparticles to enhance the durability and mechanical properties of cementitious composites was explored in the report issued by the RILEM Technical Committee (197, *Nanotechnology in Construction Materials*, TC 197-NCM) (9).

This type of technology faces various challenges in the construction sector. The fact that it handles submicrometric dimensions, which are imperceptible to the human eye, makes it intangible for industry professionals. However, its impact on the physical properties of a wide variety of everyday objects has been found to be so significant that it can modify the human experience in the construction industry. Since concrete is composed of various materials, it is crucial to know the chemical and physical properties of its materials before mixing them. The hardened properties of concrete are governed by many factors, such as chemical properties, physical properties, the water-to-cement ratio, cement contents, cement type, and quality control during production, among others (10).

The technical literature highlights the benefits of combining ordinary Portland cement (OPC) with nanomaterials such as nanosilica. (11) demonstrated that the compressive strength developed by OPC mortars containing nanosilica particles was considerably better than that obtained with fly ash. In Mexico, it is not common to use OPC; the commercially available cements are the so-called *Composite Portland Cement* (CPC). These CPCs contain supplementary cementitious materials added in different proportions, as per NMX-C-414-0NNCCE-2017 (12). The objective of this research was to verify whether the previously reported benefits of utilizing nanomaterials on OPC are valid for concrete elaborated with CPC.

Thus, in the following paragraphs, we will first describe what nanosilica is and its properties, highlighting the way it contributes to improving the concrete mix. Then, we will do the same with fly ash. Once both nanomaterials have been presented, we will describe the methodology used to carry out some laboratory tests. Then, we will outline the experimental results, discuss the main findings, and, finally, present some recommendations and conclusions derived from this research.

2.　Nanosilica

Silica is a compound composed of silicon and oxygen, which is present in some materials such as quartz or opal (13). Its chemical formula is SiO_2. On a smaller scale, nanosilica consists of nanoparticles with a uniform size ranging from 250 to 450 nm in diameter. Nanosilica has two surfaces: external and internal (pores). A large external surface area allows it to adequately fill the voids that exist in a concrete mix (14). Fig. **1** shows the structure of nanosilica, with the outer surface of the sphere surrounding the nanosilica particle and the internal pores visible, demonstrating that it is not a compact material.
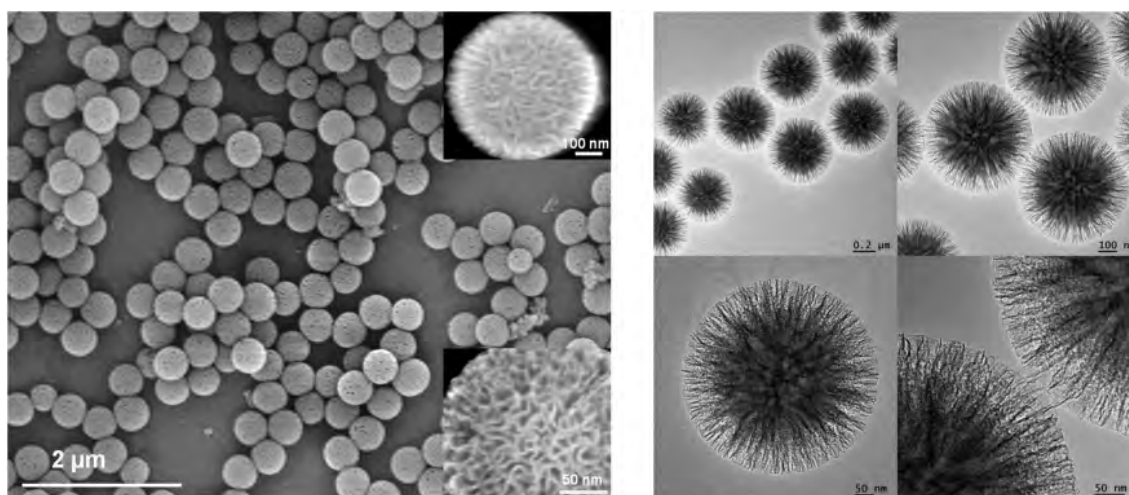

Figure 1. Structure of nanosilica particles (14)

Nanosilica has a fibrous morphology. Therefore, it has good thermal and hydrothermal resistance, as well as a high mechanical stability. This is due to the fact that its particles have dendrimeric fibers (in the form of angles arranged in three dimensions to form spheres), thus allowing easy access to the surface. It has been found that, by adding nanosilica, concrete acquires the following properties (15):

- Greater plasticizing and water reducing power

- Increased mechanical strength at initial and final ages

- Reduced permeability and increased durability

- The ability to prevent segregation and excessive exudation

- Improved finish and surface texture

One of the most important mechanical properties of cement paste is its tensile strength, which directly affects cracking due to shrinkage. If the cement paste has a low tensile strength, the cracking may be greater, and it can affect the durability of the structure. Nanosilica can help to reduce the harmful pores and permeability, as well as to increase the strength of the calcium-silicate-hydrate (C-S-H), thus optimizing the durability and mechanical properties of concrete (16). The use of nanosilica is beneficial to reducing the presence of cracks.

To better understand the existence of cracks, it is essential to note that there are two types of pores within the microstructure of cement paste. Firstly, there are gel pores with diameters <10 nm, which are considered part of the C-S-H triad, where C refers to CaO (calcium oxide), S corresponds to SiO_2 (silicon dioxide), and H refers to H_2O (water). Secondly, there are capillary pores ranging from 10 nm to 10 μm (17). The water that is not consumed in the hydration process is generally stored in these pores, which weakens the concrete, as there are no bonds with the hydrated calcium silicate (18). Air inclusions and void spaces may also occur where the paste does not consolidate correctly. To achieve quality concrete, the addition of nanosilica and ash admixtures, as well as the spaces between them, must be covered with paste. Therefore, the production process should have the appropriate conditions and undergo quality controls. The water-to-cement ratio is a fundamental factor to increase or decrease compressive strength, permeability, and resistance to weathering (19).

The main purpose of improving materials using nanomaterials is to reduce structures' costs of construction and maintenance, to speed up construction times, and to ensure the desired performance. It also aims to improve the physical and chemical characteristics of materials for various purposes.

To illustrate the practical use of the presented concepts, we could name an example. In Mexico, the Luminaket Polyamide Concrete company, founded by architect Jesús Cervantes Herrera, incorporates nanobots (metallic semiconductors) into hydraulic concrete. When in contact with sunlight, a chemical reaction takes place which reduces pollution, global warming, and acid rain in large metropolises (20).

Before proceeding with the description of fly ash, some general points should be summarized. From an engineering point of view, the complex cement-based structure at the nanoscale is evolving, aiming for stronger and more durable concrete. These new materials have better properties, such as electrical conductivity and less moisture absorption. Therefore, nanosilica concrete constitutes an innovation in the development of new construction materials.

3. Fly ash

The thermoelectric industry, like the construction sector, has recently experienced significant growth. However, this growth has resulted in the overexploitation of resources, particularly coal, which is one of the primary fuels used. The burning of coal generates millions of tons of waste containing toxic levels of heavy metals and minerals, most of which end up in landfills, posing a threat to health and the environment (21). Large amounts of fly ash and slag are discarded every minute due to the high consumption of coal in combustion processes, with between 80 and 250 kg of waste obtained from one ton of coal (22).

The use of fly ash in concrete, much like nanosilica, improves its mechanical properties due to the granulometry, size, distribution, shape, and texture of the particles. These effects reduce water consumption in fly ash concrete mixes (23). Fly ash is used in concrete worldwide to modify the properties of fresh and hardened concrete, and it is an environmentally friendly solution, as it is an industrial byproduct from thermoelectric plants. The physical properties and chemical composition of

fly ash vary depending on the coal and the power plant. Fly ash is classified by its CaO (calcium oxide) content, with those having less than 10 % being classified as *low calcium oxide fly ash* and those with more than 10 % *as high calcium oxide fly ash* (24).

Fly ash is primarily pozzolanic. This makes it highly binding and is derived from its ability to react with calcium hydroxide, forming hydraulic compounds similar to those generated during the clinker hydration of cement (after calcining limestone and clay, *i.e.*, a hydraulic binder). The pozzolanic reaction produces less porosity in the cement paste, making it more durable and stronger. It also increases impermeability and steel strength against corrosion (25). These benefits make fly ash an ideal component in concrete to enhance firmness and durability while recycling and reusing industrial waste. Cement with a pozzolanic aggregate such as fly ash offers several advantages. For example, the aluminosilicates present in the pozzolan react with the calcium hydroxide released in the hydration of Portland cement, which is a slow reaction (thus reducing heat); consumes calcium hydroxide, improving resistance to acid environments; and fills the spaces resulting from the hydration reaction of the cement, increasing impermeability and mechanical strength (26).

The addition of fly ash to concrete provides several benefits, including reducing the water demand in the mix and decreasing the energy consumption and CO_2 emissions associated with cement production (27). The key to improving concrete lies in its cementitious base, which combines with other materials such as coarse aggregates and continuous reinforcements, such as reinforcing steel rods or dispersed reinforcements (*e.g.*, short fibers of different materials). Therefore, the cementitious base or bond matrix is of the utmost importance in improving concrete properties (*i.e.*, mechanical properties) (28).

The potential applications of nanomaterials and the economic impacts they generate open up different possibilities, such as a new generation of concrete and the development of materials that comply with current regulations with a lower environmental impact. In short, the use of fly ash and nanosilica helps reduce the energy consumption and CO_2 emissions associated with cement production. However, currently, fly ash is only used in Mexico for landfill purposes, but it has great potential to improve materials in the construction industry.

It is important to note that the use of concrete with these admixtures may not immediately solve the environmental problem, but it demonstrates the potential to create functional materials that may help improve spaces both visually and functionally.

4.   Methodology

It has been reported in the literature that the addition of nanosilica to concrete can accelerate the hydration process and reduce the use of cement, resulting in more resistant nanocomposites with better mechanical properties. Laboratory strength tests have confirmed that the resulting materials have superior properties when compared to the existing ones. The use of nanomaterials aims to ensure free links at the nano level, which can generate strong bonds between the cement matrix and other

materials, resulting in increased strength and improved curing properties.

CPC, as specified by the NMX-C-414-0NNCCE-2017 Mexican standard (12), is a combination of Portland cement clinker, calcium sulfate, and a mix of pozzolanic materials, which are, in essence, reactive silicon dioxide (SiO_2) and aluminum oxide (Al_2O_3), blast furnace slag, and/or limestone. This type of cement is comparable with European Portland-composite cement CEM II/B-M, according to the EN 197-1 standard (29).

In this research, laboratory tests were conducted to validate the effectiveness of using nanosilica in concrete. Two types of variables were considered, dependent and independent, with the former referring to compressive strength and durability and the latter to proportional design for the hydraulic concrete mix, the water ratio, the granulometry of the coarse aggregate, and durability, as evaluated with the ACI-522R (30). Sampling methods and materials testing were conducted according to N-CMT2-02-005 (31).

The laboratory tests aimed to compare the compressive strength and durability of the cement mixture with nanosilica and fly ash. The results help to determine which of the two aggregates reacts better with cement, ultimately resulting in the production of an innovative material. The tests performed are outlined below.

4.1.   Laboratory tests (procedure)

Taking the aforementioned standards as a reference, different experiments were carried out in the laboratory of Universidad Autónoma del Estado de México's Faculty of Engineering. The steps considered in the process were the following:

1. The molds were made of stainless steel, as a non-absorbent material was required which did not react with the cement. Before using the molds, they were covered with mineral oil. The size of each cylinder was 15 cm in diameter by 30 cm in height (Fig. 2).

2. The mixture was made with each ingredient previously weighed. Fig. 3 shows how the mixtures were generated, as well as their physical appearance before being poured into their corresponding molds. The cement used was commercially available CPC.

    River or mine sand was also used. The 200 mesh fines were removed, and nanosilica and fly ash were added. This was done to understand their function and real application in the construction industry.

3. The mixtures were added to the containers and vibrated with a rod to remove the air from the mixture. Subsequently, they were poured into the corresponding molds to generate standard size cylinders for strength and durability testing (Fig. 4).

4. Finally, several cylinders were made, which were used to perform the experiments. They are shown in Fig. 5.

Figure 2. Molds used to make the specimens

Figure 3. Concrete with fly ash (left) and nanosilica in concrete (right)

Once the cylinders were generated, they were allowed to dry in pairs. For the first pair, the process took seven days; for the second, 14 days; and the last one was left to dry for 28 days. The tests performed on the samples are described later in this document.

Before presenting the laboratory tests, the process followed for the preparation of the mixtures is described. Table I summarizes the proportions used to produce the cylinders that would later be subjected to compression tests. The amount of nanosilica and water used in the compositions was varied.

Table I. Proportion of the concrete mix with nanosilica

Cement (g)	% Nanosilica	Fine aggregate (g)	Coarse aggregate (g)	Water (ml)
472.8	0.8 %	472.8	750.5	260
472.8	1.0 %	472.8	750.5	210.27

Figure 4. Pouring the concrete mixture into the molds

Figure 5. Molds in the drying process

For the mixture of hydraulic concrete and nanosilica, the ratio of cement and sand was 1:1. Regarding the amount of nanosilica, 0,8 and 1 % were used in order to determine the amount that yielded the best resistance results. These quantities of nanosilica were taken from (32), a recent research work that recommends a dosage between 0,6 and 1 % of nanosilica admixture in concrete. The compressive strength tests of the specimens were carried out for materials of 7, 14, and 28 days of age.

For the desired comparison, the same was done with the other material of interest; for the case of concrete with fly ash aggregate, the mix design is presented in Table **II**. Here, only the proportion of fly ash was varied, leaving the other variables constant, including the amount of water.

The amount of fly ash used was determined from (26), whose authors recommend the use of fly ash as a substitute for cement in a range from 2,5 to 10 %, taking into account that, from 10 % onward, the strength value of concrete decreases (33).

Table II. Proportion of the concrete mix with fly ash

Cement (g)	% Fly ash	Fine aggregate (g)	Coarse aggregate (g)	Water (ml)
447.8	5	472,8	750,5	212,7
447.8	8	472,8	750,5	212,7

For this work, proportions of 5 and 8 % were used to obtain an adequate strength.

To carry out the laboratory tests in an orderly and systematic manner, in order for them to be replicated by interested readers, the sampling and material testing methods established in the N-CMT2-02-005 were used. The steps described below were followed.

1. 24 hours after casting, the samples were demolded and water-stored until test time. The curing of the samples was carried out at room temperature (25 °C).

2. The specimens were labeled with their characteristics. Immediately afterwards, a sulfur cap was placed on them so that the face was completely smooth and showed no anomalies at the time of carrying out the strength test. Figs. **6-9** show the steps of this first stage in the preparation process.

Figure 6. Demolded and labeled specimens

3. The samples were then tested in the compression machine (PILOT, Controls) to collect data allowing to understand the behavior of the materials. Figs. **10** and **11** present both the testing machine and the way in which the results were generated. Fig. **12** shows the fractured specimen after being subjected to the compression test.

The next section summarizes the results obtained.

Figure 7. Arrangement of specimens prior to placement of sulfur

Figure 8. Placement of sulfur

Figure 9. Specimen ready for resistance tests

Figure 10. Compressive strength testing machine

Figure 11. Graphic results provided by the compressive strength testing machine

5. Results and discussion

Adding nanosilica significantly improves concrete's compressive strength properties. Its use is economical since it requires small amounts, and a good performance is very feasible. In the admixture, it favors the durability of concrete. Fig. **13** shows the strengths obtained at 7, 14, and 28 days for the two types of mix used. As can be seen, the values range between 230 and 280 kg/cm^2.

It was found that a nanosilica-based admixture can reduce the use of water by up to 24 % (Table **I**). This confirms that, by adding nanomaterials to concrete, the mixture is integrated by filling the spaces that are generated during the hydration process.

Thus, it can be stated that the use of nanosilica greatly influences the strength of concrete. The difference in the amounts of nanosilica used in the mixtures is minimal (just 0,2 %). Therefore, it is necessary to carry out more tests in the future, using larger amounts of this material and aiming to obtain greater resistance. It is important to point out that, during the curing process of the concrete

Figure 12. Fractured specimen after being subjected to the strength test

mixture, the specimen was compacted, accelerating the hydration process. The setting time decreased because the nanoparticles' hydration reaction is faster than that of the concrete (34).

As for fly ash, a similar behavior was observed Fig. **13** shows the resistances of the tested specimens over time. The observed range now varies from 215 to 255 kg/cm^2. In the case of nanosilica, the increase in resistance is constant; fly ash tends to have less increase.

Thus, it is verified that the use of fly ash in the concrete mixture produces a slower increase in resistance. However, the resistances are suitable for use in light traffic pavements.

Fig. **13** shows the strengths obtained for both aggregates.

It is important to note that there is no big difference in the results, although the concrete with nanosilica shows higher strengths from the start. In contrast, in the concrete with fly ash, the strength only increased after the 28th day of setting.

The amount of nanosilica used was minimal compared to that of fly ash. This brings us to the question whether stronger concretes can be produced with a higher amount of nanosilica.

The results found so far indicate that there is an improvement when using nanomaterials in the concrete mix. These findings agree with those reported in previous studies. It has been documented
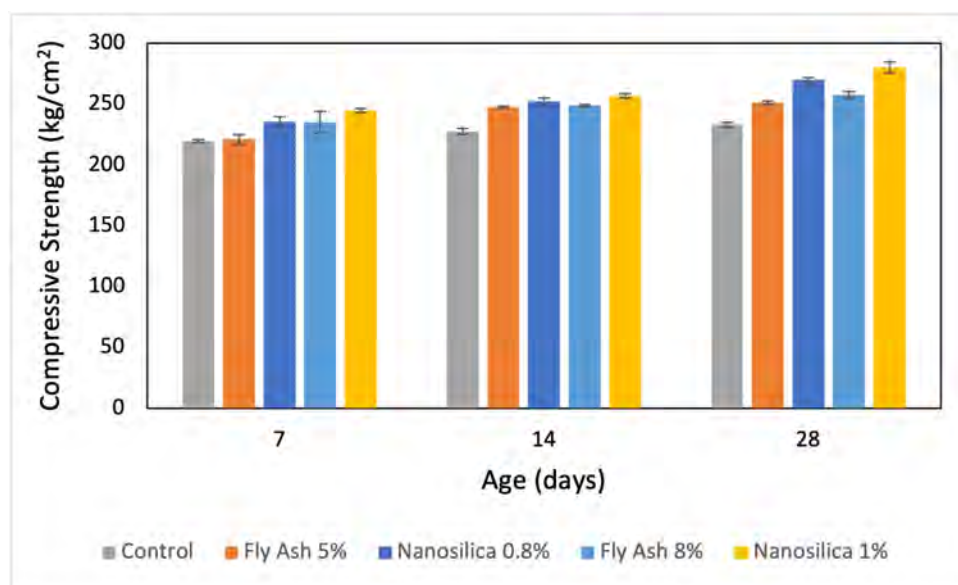
Figure 13. Compressive strength

that compressive strength increases significantly with the addition of nanosilica due to the pozzolanic reaction, as it quickly produces a C-S-H gel. This reduces the porosity of structures, given the nanometric size of nanosilica particles (35).

This also provides benefits such as pollution reduction, lower construction costs due to lower material requirements, high strength, good workability, high impermeability, and no need for using superplating agents (36). It must be acknowledged that, due to the limitations of human and material resources to carry out this research, the studied sample is limited. The results show that the addition of these aggregates to concrete improves their performance. More research is necessary to confirm our results.

6. Conclusions

This study analyzed the benefits of incorporating nanosilica and fly ash into hydraulic concrete mixtures, concluding that the compressive strength substantially improves with nanosilica.

Based on the results obtained, the material that yielded the best results was concrete with nanosilica. This aggregate had a greater impact on improving the properties of concrete. It should be noted that the results of this research will be the input for a new project.

The purpose of this research was to verify whether common concrete elaborated with CPC shows improved properties when adding nanosilica and fly ash.

Considering the above, it is concluded that the key to improving concrete through nanosilica and fly ash is the composition of the mixture. It is key to reduce the amount of cement paste (*i.e.*, cement base) so that the new aggregate occupies the free space. With the voids filled, there is no more poor, porous concrete. In the same way, the mechanical properties of the binder, which is the cement paste, could be improved.

Finally, it can be stated that concrete technology is an area that has drawn the attention of the academic and professional community. As it is a centennial material, any improvements that contribute to improving the performance of concrete are always welcome. Thus, this research is an attempt to improve the compressive strength of this important material, which has a prominent future in the construction industry.

7.   CRediT author statement

Sara Cristina Solache de la Torre: Formal analysis, methodology, resources, writing (original draft).
David Joaquín Delgado Hernández: Supervision, validation, writing (review and editing).
Juan Carlos Arteaga Arcos: Data curation, validation, supervision, writing (review and editing).

References

[1] S.W.M. Supit and F.U.A. Shaikh, "Durability properties of high volume fly ash concrete containing nano-silica", *Mater. Struct.*, vol. 48, 2015. https://doi.org/10.1617/s11527-014-0329-0. ↑2

[2] J. Saloma *et al.*, "Improvement of Concrete Durability by Nanomaterials", *Procedia Eng.*, vol. 125, pp. 608-612, 2015. https://doi.org/10.1016/j.proeng.2015.11.078. ↑2

[3] A. Suzuki and G. Sundararajan, "Deposition of Titania Nanoparticles on the Surface of Acid Treated Multiwalled Carbon Nanotubes Advanced Materials for Sustainable Development", *Mater. Sci. Eng.*, Jun. 2010. https://doi.org/10.4028/www.scientific.net/AMR.117.27. ↑2

[4] S. Hernández, Vida útil en el diseño sustentable de edificios, teoría y práctica, México DF: Ed. Trillas, 2015. ↑2

[5] P. Pacheco-Torgal *et al.*, "Nanoparticles for high performance concrete (HPC1)", 2013. https://doi.org/10.1533/9780857098832.1.38 ↑2

[6] J.-Y. Shih, T.-P. Chang, and T.-C. Hsiao, "Effect of nanosilica on characterization of Portland cement composite", *Mater. Sci. Eng.*, vol. 424, no. 1-2, pp. 266-274, 2006. https://doi.org/10.1016/j.msea.2006.03.010 ↑3

[7] S. Hernández, Nanomateriales con aplicación en arquitectura y construcción, México DF: McGraw-Hill, 2021. ↑3

[8] "¿Qué es la nanotecnología?" Vida Inteligente. [Online]. Available: https://www.euroresidentes.com/futuro/nanotecnologia/nanotecnologia_que_es.htm. ↑3

[9] H. Biricik and N. Sarier, "Comparative study of the characteristic of Nano Silica, Silica Fume and Fly ash, incorporated cement Morters", *Mater. Res.*, vol. 3, pp. 579, Dec. 2013. [Online]. Available: http://doi.org/10.1590/S1516-14392014005000054 ↑3

[10] M. T., M. Moonis Z., and A. B., "Effect of nano-silica on mechanical, microstructural and durability properties of cement-based materials", *J. Build. Eng.*, vol. 65, 2023. https://doi.org/10.1016/j.jobe.2022.105676 ↑3

[11] M. J., "Nanomaterials - the driving force", *Mater. Today*, vol. 7, no. 12, pp. 20-29, 2004. https://doi.org/10.1016/S1369-7021(04)00627-3 ↑3

[12] *Mexican-Standard-NMX-C-414-ONNCCE-2017. Building industry, hydraulic cement, specifications and test methods*. Washington (DC): National Organization for Normalization and Certification of Building and Edification. ↑3, 7

[13] C. Díaz, "Real Academia Española (RAE)-Asociación de Academias de la Lengua Española (ASALE): Ortografía de la lengua española," Onom, n.o 24, pp. 403–309, dic. 2011. https://doi.org/10.7764/onomazein.24.18 ↑4

[14] "Atomic Layer Deposited (ALD) TiO2 on Fibrous Nano-Silica (KCC-1) for Photocatalysis: Nanoparticle Formation and Size Quantization Effect", Laboratory of Material Surface Engineereing and Nanofabrications, 2017. [Online]. Available: https://doi.org/10.1021/acscatal.6b00418.s001 ↑4

[15] "Nanotecnología en el concreto", 2010. [Online]. Available: http://nanosilice.blogspot.com ↑4

[16] F. Althoey *et al.*, "Impact of Nano-silica on the hydration, strength, durability, and microstructural properties of concrete: A state-of-the-art review", *Case Studies Const. Mat.*, vol. 18, 2023. https://doi.org/10.1016/j.cscm.2023.e01997 ↑4

[17] M. Garrido, "Modificación estructural del Gel C-S-H irradiado con láser continúo de CO_2", doctoral thesis de la Facultad de Ciencias Químicas Universidad Complutense de Madrid, Madrid, 2018. [Online]. Available: https://dialnet.unirioja.es/servlet/tesis?codigo=230002 ↑5

[18] R. Guzmán, "El uso de Nanotubos de Carbono en el Concreto para mejorar su desempeño y durabilidad," 2012. [Online]. Available: https://es.studenta.com/content/110942884/el-uso-de-nanotubos-de-carbono-en-el-concreto-para-mejorar-su-desempeno-y\-durabi ↑5

[19] Chuzón Villacorta *et al.*, "Diseño de concreto f´c= 210 kg/cm^2 adicionado con Nanosílice para mejorar su resistencia a la compresión, Tarapoto 2020", [Online]. Available: https://hdl.handle.net/20.500.12692/59055 ↑5

[20] "Luminakret nanotecnología. Mejores materiales sustentables para la construcción", 2017. [Online]. Available: https://luminakret-nanotecnologia.ueniweb.com/#about_us ↑5

[21] "Las trampas del carbón; Informe sobre las Centrales térmicas de Cárbon en España", Greenpeace.es, septiembre 2015. [Online]. Available: http://archivo-es.greenpeace.org/espana/Global/espana/2015/Report/cambio-climatico/las-trampas-del-carbon.pdf ↑5

[22] M. Espinosa *et al.*, "Análisis del comportamiento de los lixiviados generados en un vertedero de residuos sólidos municipales en la ciudad de la Habana", *Rev. Int. Contaminación Ambientas*, vol. 26, no. 4, 2010. `https://www.scielo.org.mx/scielo.php?script=sci_arttext&pid=S0188-49992010000400006` ↑5

[23] C. Aire and L. Aguilar, "Ensayos de control del concreto lanzado con fibras en el túnel de la línea 12 del metro de la CDMX", 2019. [Online]. Available: `https://doi.org/10.21041/conpat2019/v1cc353` ↑5

[24] B. J. Jaigua Romero and S. E. Vázquez Urgilés, "Estudio de Hormigones de altas prestaciones utilizando áridos y cemento local, cenizas volcánicas naturales y súper-plastificante", 2010. `http://dspace.ucuenca.edu.ec/handle/123456789/727` ↑6

[25] L. Espinoza and I. Escalante, "Comparación de las propiedades del concreto utilizando escoria de alto horno como reemplazo parcial y total del cemento Pórtland ordinario", *Nexo Rev. Cient*, vol. 21, no. 01, pp. 11-18, 2008. `https://doi.org/10.5377/nexo.v21i01.405` ↑6

[26] P. Caballero et al., "Optimización del concreto mediante la adición de nanosílice, empleando agregados de la cantera añashuayco de arequipa", *Rev. Ing. Constr.*, vol. 36, no. 1, Perú, Apr. 2021. `http://dx.doi.org/10.4067/S0718-50732021000100071` ↑6, 9

[27] S. Huaquiato and G. Belizario, "Utilización de la ceniza volante en la dosificación del concreto como sustituto del cemento", Revista de Investigación Altoandina – *Rev. Investig. Altoandin*, vol. 20, no. 2, 2018. `https://doi.org/10.18271/ria.2018.366` ↑6

[28] K. Sobolev, "Effect of complex admixtures on cement properties and the development of a test procedure for the evaluation of high-strength cements", *Advances in Cement Research*, 2003. ↑6

[29] J.C. Arteaga-Arcos et al., "The usage of ultra-fine cement as an admixture to increase the compressive strength of Portland cement mortars", *Constr Build Mater.*, vol. 42, pp. 153, 2013. `https://doi.org/10.1016/j.conbuildmat.2013.01.017` ↑7

[30] American Concrete Institute, "ACI PRC-121-08 Guide for concrete Construction Quality System in Conformance with ISO9001", 2008. ↑7

[31] "Calidad del concreto hidráulico", N-CMT-2-02-005/04. [Online]. Available: `https://normas.imt.mx/normativa/n-cmt-2-02-005-04.pdf`. ↑7

[32] P. Abhilash *et al.*, "Effect of nano-silica in concrete; a review", *Constr Build Mater.*, vol. 278, 2021. `https://doi.org/10.1016/j.conbuildmat.2021.122347` ↑9

[33] S. Huaquiato and G. Belizario, "Utilización de la ceniza volante en la dosificación del concreto como sustituto del cemento", Rev. de Investigacíñon Altoandinas - *Rev. Investig. Altoandin*, vol. 20, no. 2, 2018. `https://doi.org/10.18271/ria.2018.366` ↑9

[34] H. Anda, "Instituto Tecnológico y de Estudios Superiores de Occidente, Sonora, Mex", Laboratorio experimental del departamento de Ingeniería civil y minas, 2024. `https://www.studocu.com/es-mx/document/instituto-tecnologico-y-de-estudios-superiores-de-occidente/mecanica-de-solidos/cabeceo-con-mortero-de-azufre/7564337` ↑13

[35] P. Zhang *et al.*, "Nanoparticle-reinforced building materials with applications in Civil engineering", *Adv. Mech. Eng.*, vol. 12, 2014. `https://doi.org/10.1177/1687814020965438` ↑14

[36] M.R. Arefi and S. Rezaei-Zarchi, "Synthesis of Zinc Oxide Nanoparticles and Their Effect on the Compressive Strength and Setting Time of Self-Compacted Concrete Paste as Cementitious Composites", *International Journal of Molecular Sciences*, vol. 13, no. 4, 2012. https://doi.org/10.3390/ijms13044340 ↑14

Sara Cristina Solache de la Torre

is an architect who graduated from Instituto Tecnológico y de Estudios Superiores de Monterrey. She holds a Master's Degree in Design from Universidad Autónoma del Estado de México. Her research interests are focused on the area of construction technology, with a current dedication to the research of composite materials technology for the construction industry.

Email: scsolache@gmail.com

David Joaquín Delgado Hernández

holds a PhD in engineering from the University of Birmingham, England. He is the author of four books and more than 100 technical articles, and he has led ten scientific research projects on engineering. He has given more than 25 international conferences in countries such as Germany, Argentina, Bolivia, Colombia, Chile, China, South Korea, Costa Rica, the United States, Holland, England, Ireland, Malaysia, Mexico, Peru, Singapore, and Turkey. David has worked for the Federal Electricity Commission, a Mexican company that generates electricity. He is currently an associate professor at the Faculty of Engineering of Universidad Autónoma del Estado de México.

Email: delgadoh01@yahoo.com

Juan Carlos Arteaga Arcos

has been an associate professor at the Faculty of Sciences of Universidad Autónoma del Estado de México since 2011. His area of specialty is materials sciences and structural analysis. He is currently focused on the development of sustainable building materials, biomaterials, and technological innovation.

Email: jcarteaga_mx@yahoo.com.mx

UNIVERSIDAD DISTRITAL
FRANCISCO JOSÉ DE CALDAS

Research

Comparative Analysis between Singular Spectral Analysis and Empirical Mode Decomposition for Structural Damage Detection

Análisis comparativo entre el análisis singular espectral y la descomposición modal empírica para detección de daño estructural

Elisa C. González[1] [ID][✉]*, Gladys E. Salcedo[2] [ID], and Leonardo Cano[3] [ID]

[1]Facultad de Ingeniería, Universidad del Quindío, Grupo de Investigación y Asesoría en Estadística (Armenia, Colombia)
[2]Programa de Matemáticas, Universidad del Quindío, Grupo de Investigación y Asesoría en Estadística (Armenia, Colombia)
[3]Facultad de Ingeniería, Universidad del Quindío, Grupo de Investigación Quimbaya

Abstract

Context: In recent years, thanks to technological advances in instrumentation and digital signal processing, noninvasive methods to detect structural damage have become increasingly important. Vibration-based structural health monitoring (SHM) techniques allow detecting the presence and location of damage from permanent changes in the fundamental frequencies of signals. A successfully employed method for damage detection is empirical mode decomposition (EMD). Another method, less used in this field of study, is singular spectral analysis (SSA). This paper describes both methods and presents a simulation study aimed at comparing them and identifying which one is more effective in detecting structural damage.

Method: The methods of a reference study known as *benchmark SHM* were applied to facilitate the comparison. To evaluate the effectiveness of both methods, Monte Carlo simulation was employed. To control the random noise and other factors inherent to the simulation, the procedure was repeated 1.000 times for each type of damage.

Results: In the case of severe damage, both methods showed a good performance. However, when the damage was slight, the changes in the fundamental frequency were not apparent. However, a significant change in the amplitude level was observed. In this case, SSA obtained the best results.

Conclusions: The EMD and SSA methods, together with high-pass filtering, detected severe damage when the acceleration records had low or no noise. When the acceleration records were contaminated with noise, the likelihood of EMD detecting the damage decreased dramatically. One of the advantages of SSA over EMD is that, for moderate or mild damage patterns, the former does not require filters or the use of the Hilbert-Huang transform to detect damage. In general, it was found that SSA was more effective in detecting damage.

Keywords: Hilbert-Huang transform, signal analysis, structural health monitoring, time-frequency analysis

*✉ **Correspondence:** ecgonzalez@uniquindio.edu.co

Resumen

Contexto: En los últimos años, gracias a los avances tecnológicos en instrumentación y procesamiento digital de señales, los métodos no invasivos para la detección de daños estructurales se han vuelto cada vez más importantes. Las técnicas de monitoreo de salud estructural (SHM) basadas en vibraciones permiten identificar la presencia y ubicación del daño a partir de cambios permanentes en las frecuencias fundamentales de las señales. Un método empleado con éxito para la detección de daño es la descomposición modal empírica (EMD). Otro método menos utilizado en este campo de estudio es el análisis singular espectral (SSA). En este artículo se describen ambos métodos y se realiza un estudio de simulación para compararlos e identificar cuál es más efectivo en la detección del daño estructural.

Métodos: Se aplicaron los métodos de un estudio de referencia conocido como *benchmark SHM problem* para facilitar la comparación. Para evaluar la efectividad de ambos métodos, se empleó la simulación Monte Carlo. Para controlar el ruido aleatorio y otros factores inherentes a la simulación, se repitió el procedimiento 1.000 veces para cada tipo de daño.

Resultados: En el caso de daño severo, ambos métodos mostraron un buen desempeño. Sin embargo, cuando el daño fue leve, los cambios en la frecuencia fundamental no fueron aparentes. Sin embargo, se observó un cambio significativo en el nivel de amplitud. En este caso, el método SSA obtuvo los mejores resultados.

Conclusiones: Los métodos EMD y SSA, junto con el filtro de paso alto, detectaron daños severos cuando los registros de aceleración tenían poco o ningún ruido. Cuando los registros de aceleración estaban contaminados con ruido, la probabilidad de que el EMD detectara el daño disminuyó drásticamente. Una de las ventajas del SSA sobre el EMD es que, para patrones de daño moderado o leve, el primero no requiere filtros ni el uso de la transformada Hilbert-Huang para detectar el daño. En general, se encontró que el SSA es más efectivo para la detección de daño.

Palabras clave: transformada Hilbert-Huang, análisis de señales, monitoreo de salud estructural, análisis tiempo-frecuencia

Table of contents

1.   Introduction

1.1.   General aspects

In recent decades, many researchers have paid special attention to avoiding the sudden failure of structural components through early damage detection. There are several techniques for damage analysis, including vibration-based methods. However, it is necessary to implement a time series-based algorithm to process the large amount of information provided by sensors and simplify the measurement of structural conditions.

A method that provides good results for damage detection is the Hilbert-Huang transform (HHT), which combines empirical mode decomposition (EMD) with Hilbert spectral analysis. Additionally, there is a new approach called *singular spectral analysis* (SSA), which has been widely employed in recent years. For example, according to (1) and (2), singularities can be associated with cracks, damage, or environmental changes. Specifically, SSA is a time-series analysis technique that decomposes the signal into specific principal components that describe its trend, fundamental frequencies, and singularity effects.

EMD and SSA allow decomposing a signal into mono-component signals (*i.e.*, signals with a single fundamental frequency). Once the decomposition is performed, it is possible to use Hilbert spectral analysis to study the decomposed signals in the time-frequency domain and observe whether there is a change in the natural frequencies (*i.e.*, structural damage). This is valid in a broad field of applications, such as the detection of brain damage (3).

This article compares the effectiveness of SSA and EMD in detecting structural damage based on a simulation study that applied these methods to the dynamic acceleration response of a four-story steel structure with different damage patterns. This acceleration response was generated through a computer program called *Datagen*, which simulates a reference known as the *benchmark SHM problem* developed by the IASC-ASCE structural health research group (4).

1.2.   Background

Different tools have been developed to study damage from changes in natural frequencies, with the purpose of monitoring structural health. This is associated with the mass and stiffness matrix of the structure. Generally, the mass tends to remain constant, so, if there are frequency changes, they will be caused by changes in stiffness. When this variation is longstanding, it indicates damage to the structure. For example, (5) performed modal identification and detection of damage in beam-type structures by analyzing methods based on natural frequency changes.

(6) used instantaneous phase data obtained from single-component decomposition for damage detection in a three-story building. (7) proposed a damage index called the *EMD energy damage index* for structural damage detection, corroborating its applicability through numerical and experimental studies. (8) described the beginnings, current state of the art, and potential advances in diagnostic

and damage detection analysis. They developed a new method for system identification and damage detection using actual output data from vibration records, based on the direct application of time and frequency averaging representation (MTFR) and frequency domain decomposition (FDD).

(9) performed a comparative review on different damage detection methods, including ARMA models, parameter identification tools, NexT/ERA identification systems, damage indices, EMD, EMD+HHT (Hilbert-Huang transform), AR models, and others. These methods, when applied to a benchmark problem, allowed analyzing the advantages and disadvantages of each of these methods and their detection capabilities with regard to different damage patterns.

Recent research has implemented different methods for vibration-based damage detection. For example, (10) used the recursive spectral singular analysis algorithm to identify structural damage, using a single channel in real time as input, and produced a lagged Hankel time matrix of the series. This method allowed obtaining information about the current state of the structure – in this case, a cantilever beam subjected to seismic excitation. (11) proposed the use of multivariate empirical modal decomposition to locate damage in structures via measurements. (12) used EMD with adaptive noise to identify the presence, location, and severity of damage in a steel truss bridge model. They built the object of study under laboratory conditions and they experimentally subjected the bridge to white noise excitations.

(9) confirmed that EMD, together with the Hilbert-Huang transform, can detect specific damage patterns. They further verified this result and implemented SSA, which is still an innovative algorithm for structural damage detection in the field of civil engineering.

2. Materials and methods

This section briefly explains some concepts regarding damage, as well as some mathematical concepts associated with time-frequency analysis.

2.1. Levels of structural damage

In civil engineering, the concept of damage has different meanings and interpretations. In this study, *structural damage* is defined as the changes (almost always permanent) in structural properties such as stiffness, strength, and dynamics, in addition to losses of acceptable structural performance according to pre-established behavior criteria (8).

The effects of damage in a structure can be classified into four levels, as follows (13):

- Level 1 indicates the presence of damage in the structure
- Level 2. Level 1+ determines the geometric location of the damage
- Level 3. Level 2+ quantifies the severity of the damage
- Level 4. Level 3+ predicts the remaining service life of the structure

Generally, vibration-based damage identification methods that do not use a structural model mainly provide level 1 and 2 damage identification.

2.2. Empirical mode decomposition (EMD)

EMD is a method for decomposing a given signal into a set of elementary signals called *intrinsic mode functions* (IMFs), which are defined by the following conditions (14):

1. The number of extremes (max and min) and zero crossings must not differ by more than one.

2. At any given instant, the average between the envelope of maximum points and that of minimum points must be close to zero.

The iterative procedure proposed by Huang to obtain IMFs is as follows:

1. Identifying the extreme points of the function $x(t)$ (max. and min.).

2. Interpolating between the maximum points using a cubic spline to obtain an envelope $e_{\text{máx}}(t)$. The same is done with the minimum points to obtain $e_{\text{mín}}(t)$. The envelopes should cover the entire signal.

3. Calculating the average of the envelopes $m(t) = \frac{(e_{\text{máx}}(t) + e_{\text{mín}}(t))}{2}$.

4. Calculating $h(t) = x(t) - m(t)$, where $h(t)$ is the IMF candidate. Steps 1-4 should be iterated with $h(t)$ as the new function until the two aforementioned conditions for IMFs are met.

5. Once the conditions have been met, $h(t)$ becomes the first IMF.

6. Calculating the residue $r(t) = x(t) - \sum \text{IMF}$, $r(t)$ becomes the new function, and the steps are repeated to find the next $\sum \text{IMF}$.

7. The procedure is repeated until the residual can be considered negligible or is a monotonic function (no max. or min.).

In summary, this process is based on generating envelopes defined by the max. and min. of a series and subtracting the average of these envelopes from the initial series.

2.3. Singular spectral analysis (SSA)

This method incorporates classical time series analysis elements such as spectral analysis (15), digital signal processing, dynamic systems, and multivariate statistics. SSA consists of decomposing an original signal into a set of uncorrelated components from which three characteristics can be extracted: trend, oscillation, and noise (16, 17). This decomposition is based on the Karhunen-Löeve covariance matrix. The procedure is has four steps:

Step 1: Decomposition of the time series

Let $Y = \{y_1, y_2, \ldots, y_N\}$ be the observed time series with a size N. Consider the matrix $\mathbf{X}$ of dimension $L \times K$ given by

$$\mathbf{X} = \begin{bmatrix} \mathbf{X}_1 \\ \vdots \\ \mathbf{X}_K \end{bmatrix} = \begin{pmatrix} y_1 & y_2 & y_3 & \cdots & y_K \\ y_2 & y_3 & y_4 & \cdots & y_{K+1} \\ y_3 & y_4 & y_5 & \cdots & y_{K+2} \\ \vdots & \vdots & \vdots & \ddots & \vdots \\ y_L & y_{L+1} & y_{L+2} & \cdots & y_N \end{pmatrix}. \tag{1}$$

L is the length of the window, such that $2 \leq L \leq N$, $K = N - L + 1$ is the number of columns in the matrix $\mathbf{X}$ and each $\mathbf{X}_i = (y_i, \ldots, y_{i+L-1})^T$, $1 \leq i \leq K$. Choosing the length L is one of the greatest challenges when working with SSA, mainly for non-stationary series, since a large window may require higher computational efforts, and a small window may separate the noise from the trend components.

Note that $\mathbf{X}$ is a matrix of trajectories known as the Hankel matrix, where the component $y_{i,j}$ of row i and column j satisfies $y_{i,j} = y_{i-1,j+1} = y_{i+1,j-1}$, leading to $\mathbf{X}$ having equal elements over the anti-diagonals.

Step 2: Decomposition of X into singular values (SVD)

Let $\mathbf{W} = \mathbf{X}\mathbf{X}^T$ be a square matrix $L \times L$. Then, the positive eigenvalues $(\lambda_1 > \lambda_2 > \ldots > \lambda_d)$ of $\mathbf{W}$ and their corresponding eigenvectors $\mathbf{U}_1, \mathbf{U}_2, \ldots, \mathbf{U}_d$ are found. The square root of the eigenvalues $\sqrt{\lambda_i}$ of $\mathbf{W}$ are the singular values of the matrix $\mathbf{X}$, and the corresponding eigenvectors $\mathbf{U}_i$ are the left singular vectors of the matrix $\mathbf{X}$.

Other singular vectors computed by Eq. (2) correspond to the right singular vectors of the matrix $\mathbf{X}$.

$$\mathbf{V}_i = \frac{\mathbf{X}^T \mathbf{U}_i}{\sqrt{\lambda_i}}, \quad i = 1, \ldots, d. \tag{2}$$

Each eigentriplet $(\sqrt{\lambda_i}, \mathbf{U}_i, \mathbf{V}_i)$ of the matrix $\mathbf{X}$ determines the corresponding components, and all eigentriplets determine a d-dimensional subspace in $\mathbb{R}^L$. Then,

$$\tilde{\mathbf{X}}_i = \sqrt{\lambda_i} \mathbf{U}_i \mathbf{V}_i^T, \quad i = 1, \ldots, d, \tag{3}$$

and the matrix $\mathbf{X}$ can be expressed as

$$\mathbf{X} = \tilde{\mathbf{X}}_1 + \tilde{\mathbf{X}}_2 + \ldots + \tilde{\mathbf{X}}_d. \tag{4}$$

Step 3: Grouping the eigentriplets

This step selects the desired components from all those obtained in step 2. Usually, the selection criterion is determined *a priori*, which can be a problem since SSA projects the original data into different orthogonal components, but it is not easy to find all the components with the required information, given that this depends on the window length selected in step 1.

Once the expression (4) has been obtained, in this step, the set of indices is partitioned $\{1, \ldots, d\}$ into m disjoint subsets $\mathbf{I}_1, \ldots, \mathbf{I}_m$. Let $\mathbf{I} = \{i_1, \ldots, i_p\}$. Then, the resulting matrix $\mathbf{X_I}$ corresponding to group

I is defined as $\mathbf{X_I} = \mathbf{X}_{i_1} + \ldots + \mathbf{X}_{i_p}$. A matrix is calculated for each group $\mathbf{I}_1, \ldots, \mathbf{I}_m$, and the expansion of (4) leads to the decomposition

$$\mathbf{X} = \tilde{\mathbf{X}}_{\mathbf{I}_1} + \ldots + \tilde{\mathbf{X}}_{\mathbf{I}_m}. \tag{5}$$

The procedure for selecting the sets $\mathbf{I}_1, \ldots, \mathbf{I}_m$ is called *eigentriplet clustering*. Furthermore, a relation given by (6) can be defined, which quantifies the degree of approximation of the original signal's windows.

$$R = \frac{\displaystyle\sum_{i \in \mathbf{I}} \lambda_i}{\displaystyle\sum_{i=1}^{d} \lambda_i}. \tag{6}$$

Step 4: Averaging the diagonals

In reconstructing the required signal from the selected components, each matrix $\mathbf{X}_{\mathbf{I}_j}$ of the decomposition given in Eq. (5) is transformed into a new series of length N, using the procedure for averaging over the diagonals, which defines the value of the time series as an average of the diagonals corresponding to each matrix in $\mathbf{X}_{\mathbf{I}_j}$.

This procedure is based on the following: let $\mathbf{Q} = (q_{i,j})$ be any $L \times K-$size matrix, where each element $q_{i,j}, (i + j = l)$ becomes an element of Hankel's matrix. Thus,

$$\tilde{q}_{i,j} = \begin{cases} \frac{1}{l-1} \displaystyle\sum_{m=1}^{l-1} q_{m,l-m} & 2 \leq l \leq L - 1 \\ \frac{1}{L} \displaystyle\sum_{m=1}^{L} q_{m,l-m} & L \leq l \leq K + 1 \\ \frac{1}{K+L-l+1} \displaystyle\sum_{m=l-K}^{L} q_{m,l-m} & K + 2 \leq l \leq K + L. \end{cases} \tag{7}$$

This is known as the *Hankelization procedure*, and applying it to all components of the $\mathbf{X}_{\mathbf{I}_j}$ matrices yields a reconstructed series $\tilde{\mathbf{X}}^{(k)} = (\tilde{x}_1^{(k)}, \ldots, \tilde{x}_N^{(k)})$. Therefore, the initial series $y_1, y_2, \ldots, y_N$ is decomposed into the sum of m reconstructed series, as follows:

$$\tilde{Y}_t = \sum_{k=1}^{m} \tilde{x}_t^{(k)}, \quad t = 1, \ldots, N. \tag{8}$$

Each component provides part of the retained energy obtained from the original series. Clearly, the larger the number of components is, the greater the information collected from the initial series. Therefore, another challenge in working with SSA is identifying the number of components to be used in the reconstruction procedure. In order to solve this problem, specific experimental tests are performed together with eigenvalue analysis in order to have better accuracy in selecting the number of components needed for the reconstruction process.

The residual r_t can be calculated by considering the difference between the original and the reconstructed series, as follows:

$$r_t = Y_t - \tilde{Y}_t. \tag{9}$$

2.4. Structural health monitoring benchmark problem

Applying different methods to different structures can generate specific difficulties when making comparisons. In this sense, the structural health monitoring research group (IASC-ASCE) developed a series of reference problems known as *benchmark SHM problems*, which are divided into two phases. This section details the first phase of this study, based on the simulated response of a test structure to which the two methods for damage detection were applied.

2.4.1. Benchmark structure

The benchmark structure is a four-story steel structure with three portal frames in each direction, 2,50 m spans, and 3,60 m floor height. The elements are made of 300 W hot-rolled steel with a nominal yield strength of 300 MPa. The sections are unusually designed for a scale model. All columns are oriented so that their strong axis is in the x-direction and their weak axis is in the y-direction, while the strong axis of the inter-story beams is in the z-direction. There are two diagonal suspenders on each floor of each exterior face, which can be removed to simulate damage. There is one floor slab per compartment: four 800 kg slabs on the first level and four 600 kg slabs each on the second and third levels. On the fourth level, there are four 400 kg slabs or three 400 kg slabs and one 550 kg slab to create some mass asymmetry.

Through the benchmark problems, and using the finite element method, it is possible to generate a dynamic analysis in time with 12 or 120 degrees of freedom (DOF). 12 DOF restrict all motions except two horizontal translations and one rotation per floor, while the 120 DOF case has only one constraint. The nodes at the base have the exact horizontal translation and rotation in the plane. On the other hand, the columns and floor beams are modeled as Euler-Bernoulli beams, and the braces are bars with no bending stiffness (4).

The damage patterns introduced in the structure are shown in Table **I** and shown in Fig. **1**. According to (9), the removal of braces in the story, which leads to stiffness reduction, is considered as major damage scenario and the weakening of beam column joint by loosening of bolts or reduction of stiffness for braces is considered as minor damage scenario of the structure". Therefore, severe damage patterns correspond to 1 and 2, moderate damage patterns are denoted a 3, 4, and 5, and the slight damage pattern is 6. The modeled damage patterns are predefined, and the analysis is carried out accordingly.

3. Results

3.1. Identifying damage time instants and locations

To study the sensitivity of the studied methods in detecting these damages, Table **II** indicates some parameters for the simulation study of the benchmark problem. The force is calculated using the FAST

Table I. Benchmark problem damage cases (9)

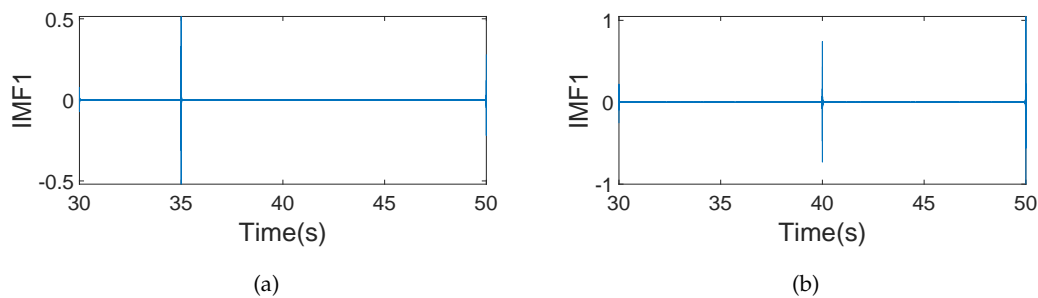| Damage patterns	Nature of the damage
Damage patterns 1	No stiffness in 1st floor braces
Damage patterns 2	Damage pattern 1 + no stiffness in 3rd floor braces
Damage patterns 3	No stiffness in one 1st floor brace
Damage patterns 4	Damage pattern 3 + no stiffness in one 3rd floor brace
Damage patterns 5	Damage pattern 4 + weakened beam-column connection
Damage patterns 6	2/3 stiffness in one 1st floor brace

(a) No stiffness in 1st floor braces

(b) No stiffness in 1st floor braces and no stiffness in 3st floor braces

(c) No stiffness in one 1st floor brace

(d) No stiffness in one 1st floor brace and no stiffness in one 3st floor brace

(e) No stiffness in one 1st floor braces and no stiffness in one 3st floor brace. Beam-Column

(f) 2/3 stiffness in one 1st floor brace
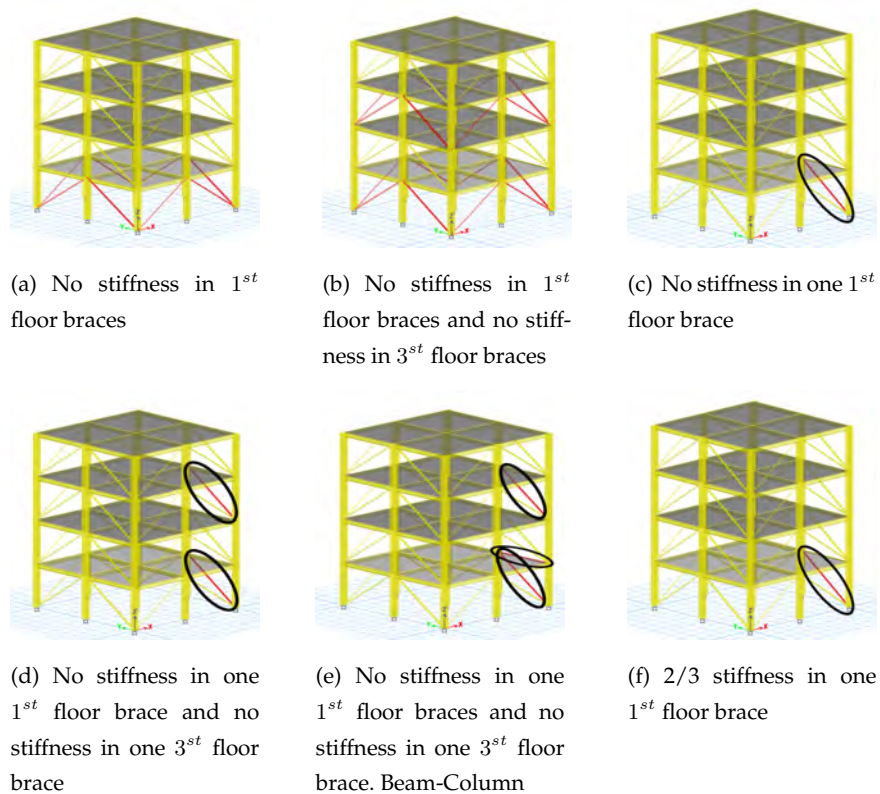
Figure 1. Damage scenarios for the benchmark structure (9)

Nigam-Jennings method, $e = 1\%$ damping is fixed to the critical, the time step size is $dt = 0,001$, and, in this case, the force intensity is $F = 150$. This is a constant coefficient that the program uses to calculate excitations. It also uses a filter index called $Findx$, a Boolean value (0 or 1) indicating whether or not the excitations should pass through a Butterworth filter (for more details, see (4)). Similarly, all acceleration records were simulated up to $t = 80s$. For the sake of clarity in the graphs, only $30s$ and $50s$ are shown in the figures, both for EMD and SSA.

Table II. Fixed model parameters in the simulation study

Parameter	Value
e	1%
dt	$0,001$
t	$80s$
F	150
$Findx$	1

Fig. **2** shows the acceleration records of the first and second floors for damage patterns 1 and 2, respectively (without noise). To these signals, a high pass filter = 250 Hz was applied. Figs. **3**aand **3**b show that, on the first floor, the damage occurs at 35 s, while, on the second floor, it occurs at 40 s. It is clear from the results that, if the noise pollution is either zero or very small, the EMD method is capable of detecting the damaging time instants and locations. The same happens when applying the reconstructed components (RCs) version of SSA. Fig. **4** shows that, on the first floor, the peak occurs at 35 s and, on the second floor, at 40 s.

(a)   (b)
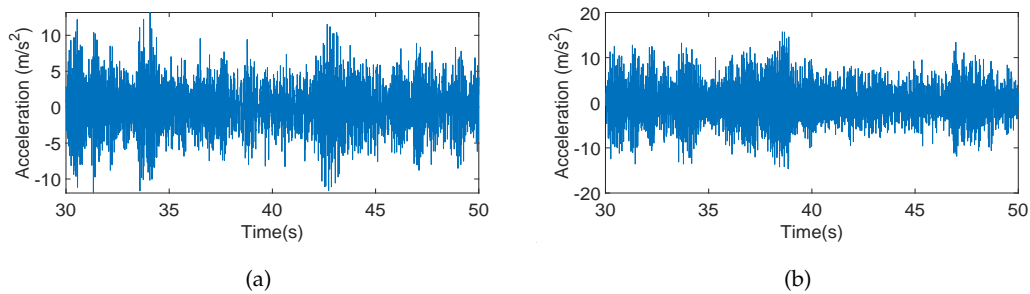
Figure 2. Acceleration records: (a) first floor, (b) second floor. All graphs correspond to damage pattern 2.

(a)   (b)

Figure 3. IMF1: (a) first floor, (b) second floor. All graphs correspond to damage pattern 2.

<div align="center">(a)　　　　　　　　　　　　　　　　　　　　　(b)</div>
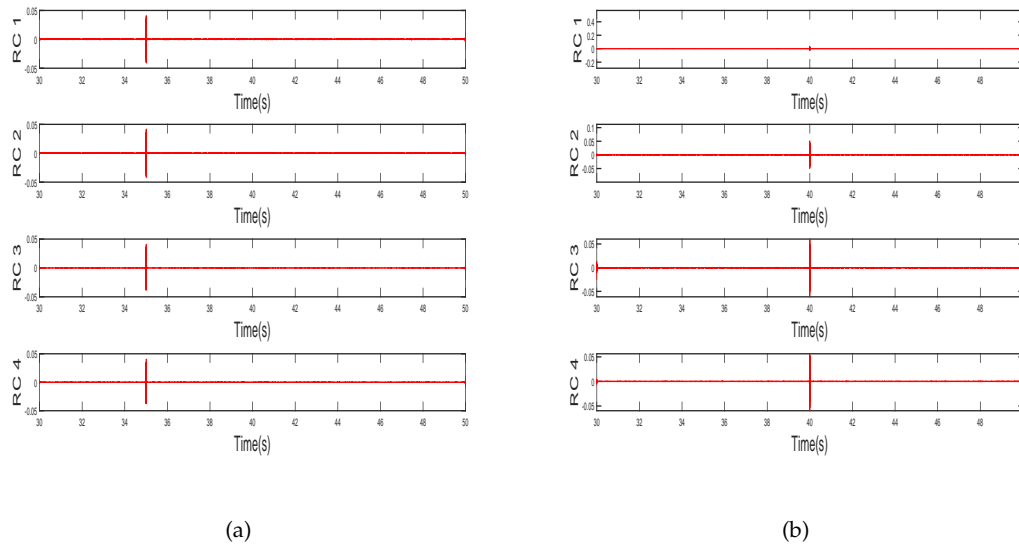
Figure 4. RCs for damage patterns 1 and 2: a) first floor, b) second floor

When the acceleration records are polluted by noise and the resulting magnitude of the damage spike is smaller than the noise levels, then the damage spike merges with the noise. For example, in Fig. **5**, a signal with a noise level of $10\,\%$ and damage pattern 2 was generated. This corresponds to the acceleration records of the first floor.

It is worth mentioning that the model considers two sensors on each floor (one on the left side and the other on the right side). Therefore, there are two acceleration records for each floor. Fig. **2** only shows one acceleration record per floor, since both are identical when the structure is symmetrical and the signal is not contaminated. However, when the signal is contaminated with noise, the acceleration records of each sensor per floor are different. However, this paper only shows the sensor on the right side of the first floor, as shown in Fig. **5**.

By processing the signals via EMD, the first IMF was obtained (Fig. **6**) using a high pass filter = 250 Hz for the sensor signal on the right side. However, it was not possible to identify the discontinuity peak, which was confused with noise. According to (**18**), EMD's ability to detect signal damage at a noise level of $10\,\%$ is about $30\,\%$ in the benchmark problem.

To overcome this difficulty, we first identified if there was a change in frequencies (*i.e.*, if there was damage) using the Fourier transform, and then we used the Hilbert-Huang transform to identify the instant at which this change occurred. As shown in Fig. **7**, the Fourier transform was applied to the acceleration records. Each of the four natural frequencies was divided into two. This division may indicate the occurrence of damage, and it is quite evident in the first and second natural frequencies.
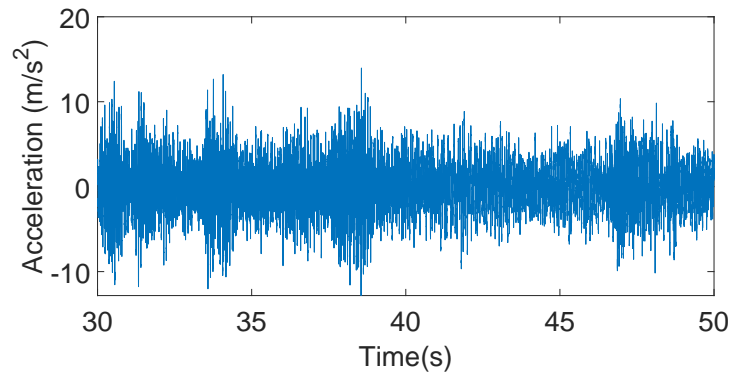
Figure 5. First floor acceleration records for damage pattern 2: sensor on the right side
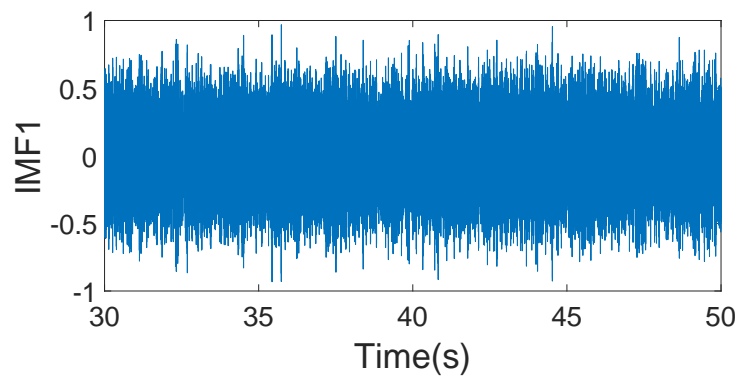

Figure 6. First IMFs for damage pattern 2 with a highpass filter: sensor on the right side of the first floor
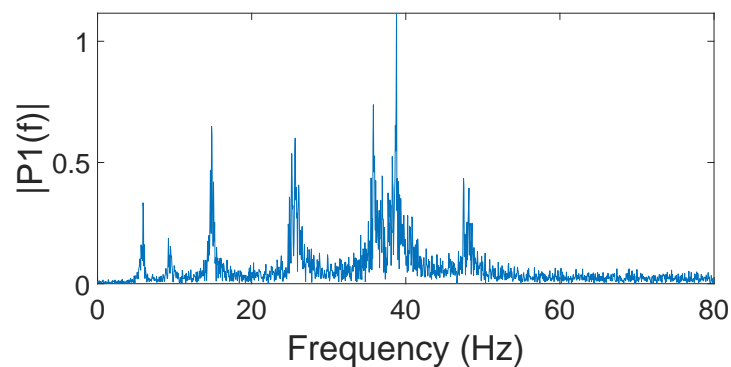

Figure 7. Fourier transform for damage pattern 2: sensor on the right side of the first floor

To identify the instant at which the damage occurred, we decided to use a bandpass filter and perform the frequency-time decomposition using the Hilbert-Huang transform. Fig. 7 shows that the first natural frequency could be between 5 and 10,5 Hz. Therefore, a bandpass filter (bandpass (X,[5 10,5], Fs)) was used, and applied EMD was applied as shown in Fig. 8. The first plot corresponds to the

filtered signal, and the others are the IMFs corresponding to the decomposition of the measured signal in the first modal response. By applying the Hilbert-Huang transform to all the IMFs, the frequency-time decomposition of the first modal response was obtained.
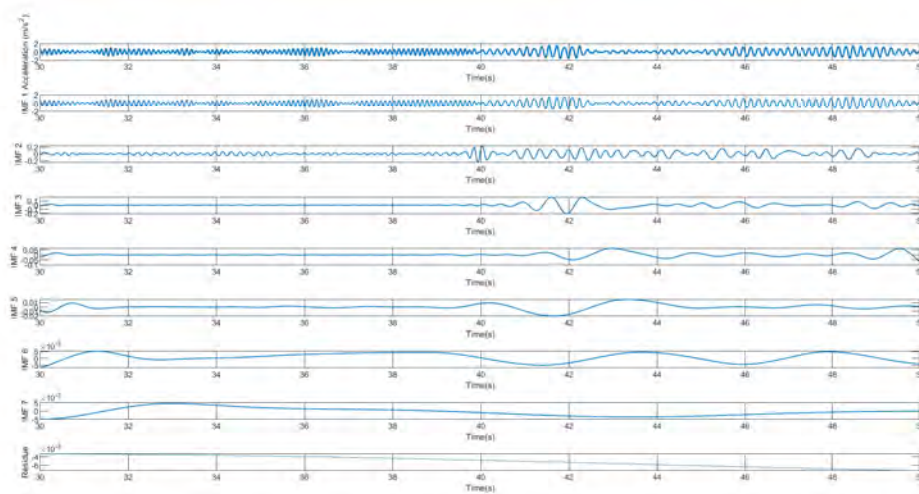
Figure 8. EMD for damage pattern 2 with a bandpass filter: sensor on the right side of the first floor

Fig. **9** shows a frequency *vs.* time plot. The average frequency of the first mode changed from 9,6 to 5,6 Hz at time instant t = 40 s. Therefore, the time instant at which the damage occurred was accurately detected. However, in the other modal responses, the splitting of the natural frequencies was not so prominent. When the Hilbert-Huang transform was applied, the frequency *vs.* time plots also showed that the change occurred at 40 s.
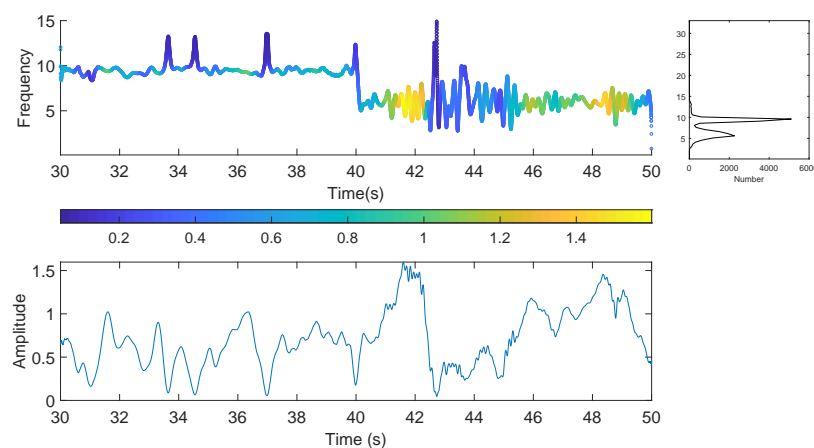
Figure 9. Hilbert-Huang transform for the first modal response (damage pattern 2): sensor on the right side of the first floor

Then, SSA was applied. Fig. **10** presents the RCs of this method. A bandpass filter (bandpass (X,[5 10,5], Fs)) was applied to the signal. Although, in the RC1 and RC2, a change in the signal behavior had already been observed at 40 s, the Hilbert-Huang transform was applied to each RC. Fig. **11** shows the Hilbert-Huang transforms of RC1 for the sensor. The average frequency of the first mode changed from 9,6 to 5,6 Hz at t = 40 s. Therefore, we accurately detected when the damage occurred by using SSA, and the results agreed with those of EMD.
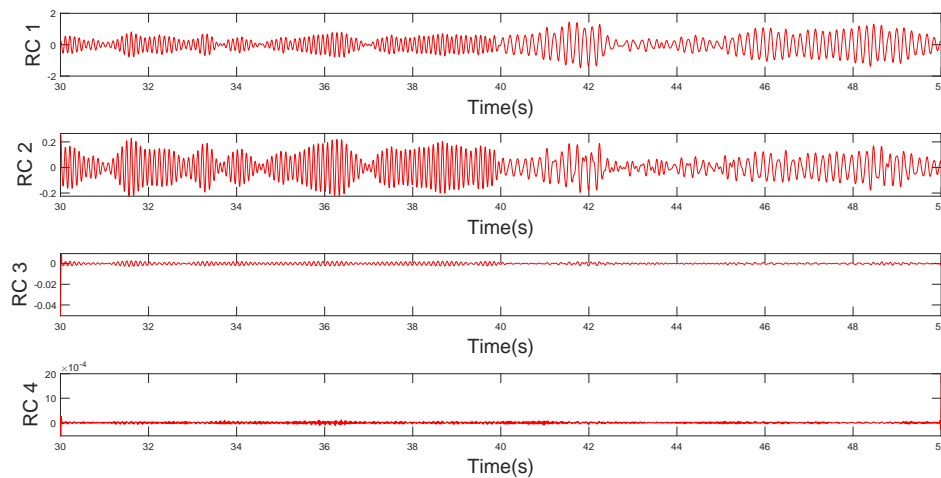
Figure 10. RC for damage pattern 2: sensor on the right side of the first floor
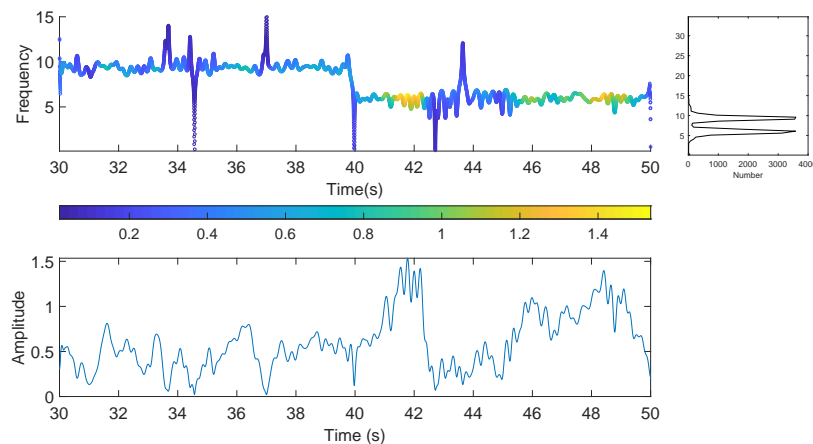
Figure 11. Hilbert-Huang transform for RC1 (damage pattern 2): sensor on the right side of the first floor

Fig. **12** shows the acceleration records of the first and second floors for damage pattern 4. To these signals, a bandpass filter (bandpass(X,[37,5 48], Fs)) was applied, which was obtained from the Fourier transform. Then, the EMD method was used. The first IMFs for each of the floors in Fig. **13** were

applied. On all floors, there was a significant change in the behavior of the signal at 40 s. Additionally, the Hilbert-Huang transform was applied, as shown in Fig. **14**. Here, the frequency change was small since this damage pattern is considered to be moderate. However, there was a significant change in the amplitude level at 40 s. The accelerations of the other floors showed the same behavior.
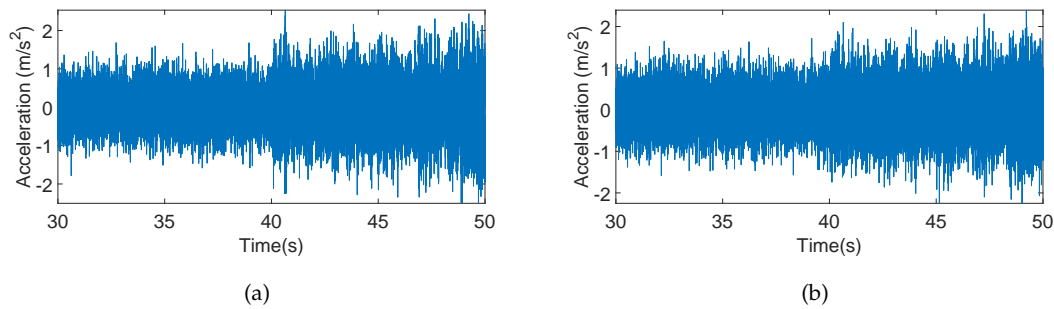

(a)   (b)

Figure 12. Acceleration records: a) first floor, b) second floor. All plots correspond to damage pattern 4 as obtained from the sensor on the right side in the x-direction.

(a)   (b)
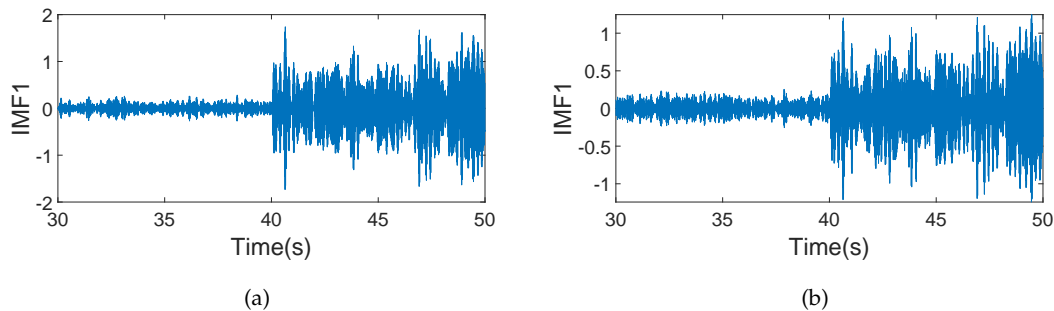
Figure 13. IMF 1: a) first floor, b) second floor. All plots correspond to damage pattern 4, obtained from the sensor on the right side in the x-direction.

Then, SSA was applied. Fig. **15** presents the RCs, where, unlike EMD, it is not necessary to apply any filter. Although, in RC1 and RC2, a change in the signal behavior was observed at 40 s, the Hilbert-Huang transform was applied to each RC. Fig. **16** depicts the Hilbert-Huang transforms of RC1 for both sensors. Like EMD, the frequency change was small, but there was a clearly significant change in the amplitude level at 40 s.

Fig. **17** illustrates the acceleration records of the first and second floors for damage pattern 6. To these signals, a bandpass filter (bandpass (X,[37,5 48], Fs)) was applied, which was obtained from the Fourier transform. Subsequently, the EMD method was used. The first IMF for each of the floors is presented in Fig. **18**. Note that the signal changed at 40 s on floors 1 and 4. This was further verified when the Hilbert-Huang transform was applied (Fig. **19**), where the frequency change was not so evident on any of the floors. However, on floors 1 and 4, a change in the signal amplitude was
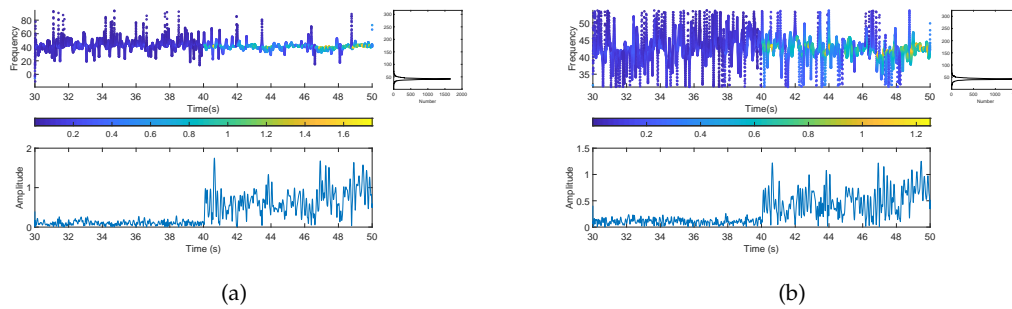
Figure 14. Hilbert-Huang transform for the first modal response: a) first floor, b) second floor. All plots correspond to damage pattern 4.
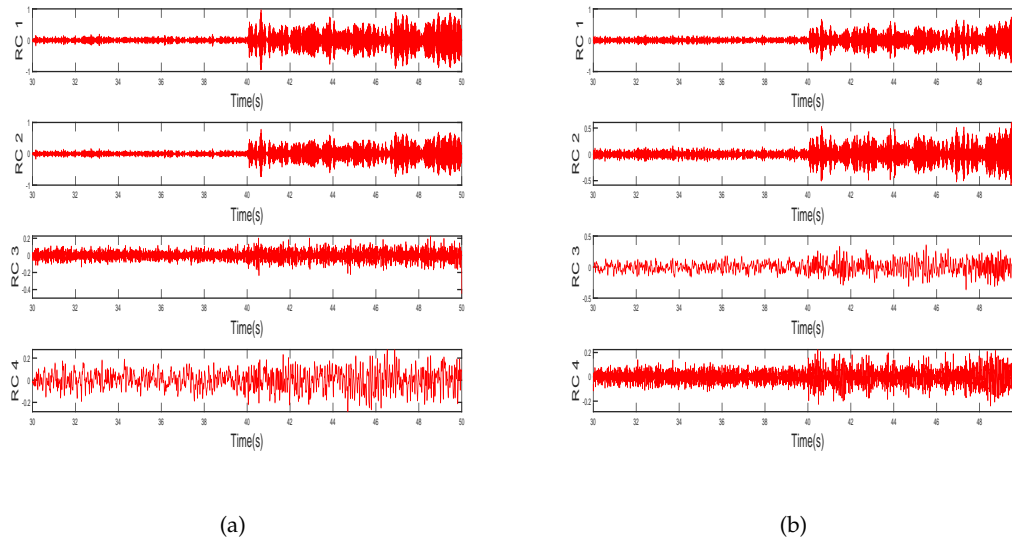

Figure 15. RC for damage pattern 4: (a) first floor, (b) second floor

observed at 40 s. In contrast, on floors 2 and 3, there was no significant change, which is why it is not necessary to include the graphs. This could indicate that the damage only occurred on floors 1 and 4.

Then, SSA was applied. Fig. **20** presents the RCs. Unlike EMD, it was not necessary to apply any filter. On floors 1 and 4, there was a change in the amplitude of the signal at 40 s, while, on floors 2 and 3, there was no significant change. This could indicate that the damage only occurred on floors 1 and 4, or that the damage on floors 2 and 3 was too slight for the method to detect it. This result can be verified from the amplitude levels shown in the Hilbert-Huang transform (Fig. **21**).
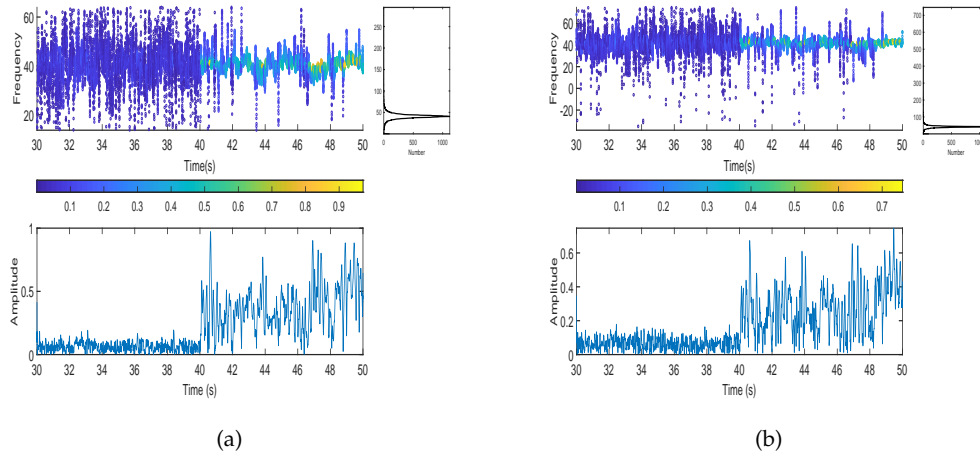
Figure 16. Hilbert-Huang transform for RC1 (damage pattern 4): a) first floor, b) second floor, c) third floor, d) fourth floor
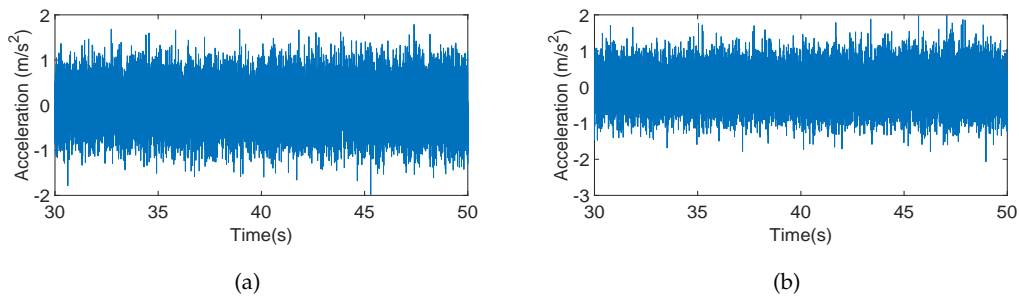

Figure 17. Acceleration records: a) first floor, b) fourth floor. All graphs correspond to damage pattern 6.
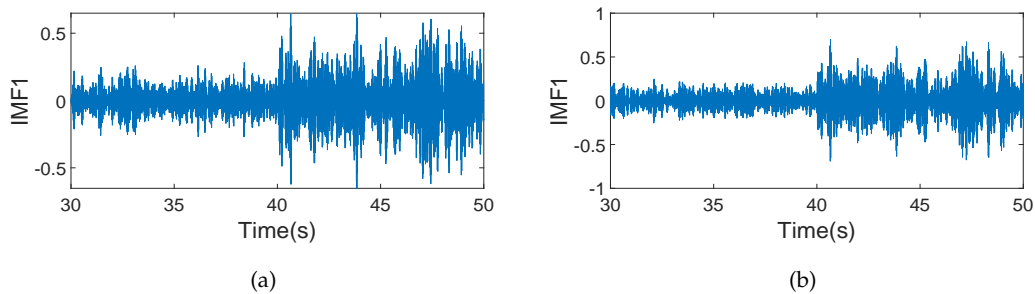

Figure 18. IMF 1: a) first floor, b) fourth floor. All graphs correspond to damage pattern 6.

3.2. Comparative analysis between EMD and SSA

Based on the above, it can be stated that, when the damage is severe, the characteristic frequency of the signal changes over time, so the empirical distribution of the frequencies is bimodal, which indicates
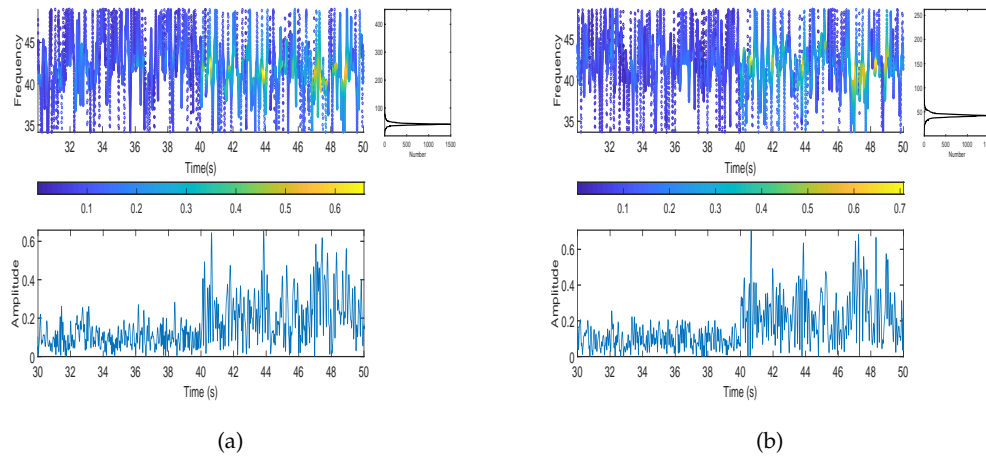
(a)   (b)

Figure 19. Hilbert-Huang transform for the first modal response: a) first floor, b) fourth floor. All plots correspond to damage pattern 6.

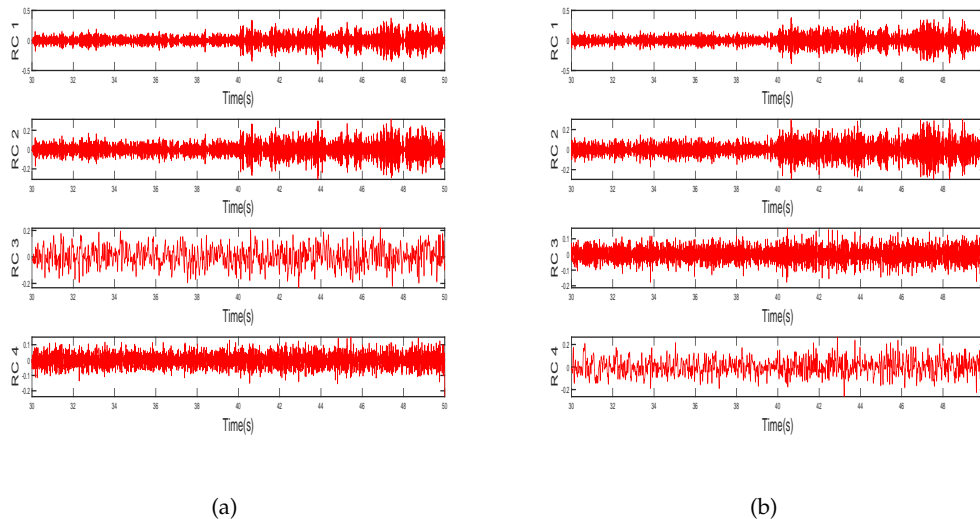(a)   (b)

Figure 20. RCs for damage pattern 6: a) first floor, b) fourth floor

the presence of two characteristic frequencies of the signal, one before and the other after the damage. On the other hand, when there is no damage, the signal retains its fundamental frequency over time.

In order to evaluate the effectiveness of both methods, a Monte Carlo simulation study was conducted, wherein a vibration signal for each type of damage was initially generated. They were like those performed in the previous section, where the noise is normal with a zero mean and one variance. The null hypothesis was that the distribution of frequencies was unimodal, in which case there should
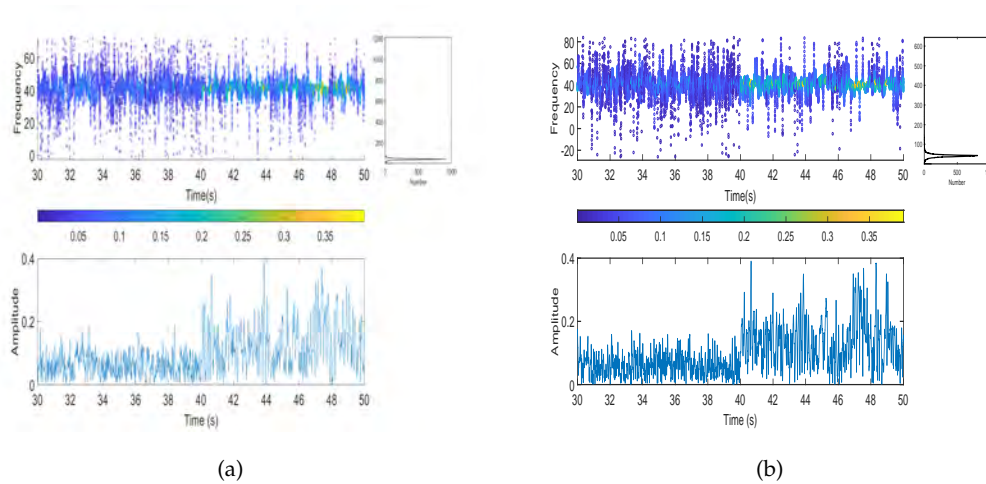
(a)   (b)

Figure 21. Hilbert-Huang transform for RC1 (damage pattern 6): a) first floor, b) fourth floor

be no change in the fundamental frequency of the signal. The alternative hypothesis involved the presence of more than one mode, indicating structural damage. Note that, if the p-value of the statistical test is less than 0,05 (the significance level), the null hypothesis is rejected, and the test detects damage. To control the included random noise and other factors inherent to the simulation, the procedure was repeated 1.000 times. The result of these simulations is the percentage of detection in each damage scenario.

Fig. **22** shows the results of this simulation study, namely the detection percentage for each of the methods. We concluded that, for severe damage, both methods ideally identified the damage However, for damage patterns 3, 4, and 6, the detection capacity of both methods decreased substantially (note that it was evaluated through the identification of frequency changes). This is due to the fact that, for these damage patterns, the frequency variation is 1 Hz or less, as presented in (**18**). Generally, SSA exhibits better statistics than EMD. It is worth mentioning that the script to apply the hypothesis test was developed in the Python language.

4. Conclusions

The EMD method, along with a high pass filter, detected severe damage when the acceleration records had low or no noise.

When the acceleration records were contaminated with noise, the likelihood of EMD detecting the damage decreased dramatically. To reduce the noise phenomenon, the Hilbert-Huang transform was applied. EMD, along with a bandpass filter and the Hilbert-Huang transform allowed detecting severe, moderate, and slight damage with a noise level of 10 %.
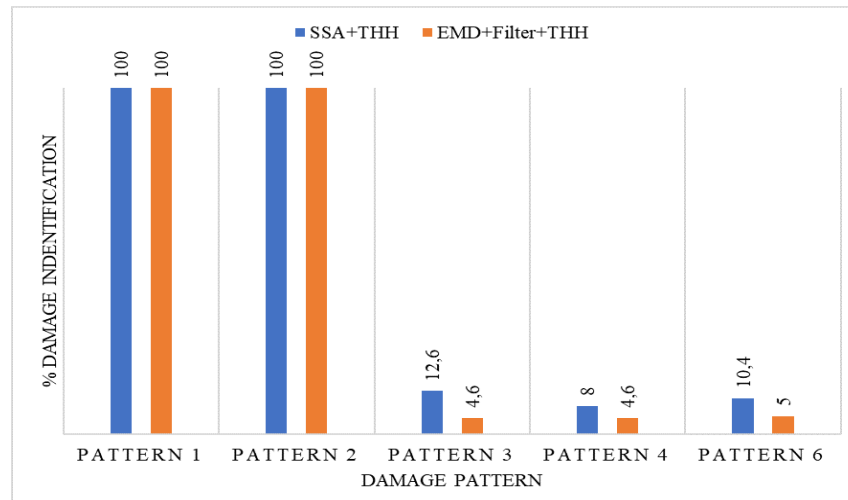
Figure 22. Percentage of damage identification for each method

The SSA method with high-pass filters detected severe damage when the acceleration records had low or no noise.

When the acceleration records were contaminated with noise and the damage patterns were severe (patterns 1 and 2), SSA, bandpass filters, and the Hilbert-Huang transform could effectively detect the damage.

When the damage was moderate or mild (patterns 3, 4, and 6), SSA detected the damage without any filter, and it was not necessary to apply the Hilbert-Huang transform in any of its components (RCs).

One of the advantages of SSA over EMD is that, for moderate or mild damage patterns, it does not require filters or the use of the Hilbert-Huang transform to detect the damage.

When the damage was severe, both methods showed a noticeable change in the fundamental frequency. However, when the damage was slight, the change in fundamental frequency was not apparent. However, a significant change in the amplitude level was observed. In general, we found that SSA is more effective in detecting damage.

5. CRediT author statement

All authors contributed equally to the research.

References

[1] C.-H. Loh, C.-H. Chen, and T.-Y. Hsu, "Application of advanced statistical methods for extracting long-term trends in static monitoring data from an arch dam,"*Struct. Health Mon.*, vol. 10, pp. 587-601,

Nov. 2011. https://doi.org/10.1177/1475921710395807 ↑

[2] L. Chin-Hsiung, C. Chia-Hui, and M. Chien-Hong, "Detecting seismic response signals using singular spectrum analysis,"*Sensors Smart Struct. Tech. Civil Mech. Aerospace Sys.*, vol. 7647, pp. 535-546, 2010. https://doi.org/10.1117/12.846427 ↑

[3] B. Medina and L. Duque, "Fuzzy entropy relevance analysis in DWT and EMD for BCI motor imagery applications, *Ingeniería*, "vol. 20, no. 1, pp. 9-19, 2015. https://doi.org/10.14483/udistrital.jour.reving.2015.1.a01 ↑

[4] E. Johnson, H. Lam, L. Katafygiotis, and J. Beck, "Phase I IASC-ASCE structural health monitoring benchmark problem using simulated data,"*J. Eng. Mech.*, vol. 130, no. 1, pp. 3-15, 2004. https://doi.org/10.1061/(asce)0733-9399(2004)130:1(3) ↑

[5] G. Gilbert-Rainer and P. Zeno-Iosif, "Modal identification and damage detection in beam-like structures using the power spectrum and time–frequency analysis,"*Signal Proc.*, vol. 96, part A, pp. 29-44, 2014. https://doi.org/10.1016/j.sigpro.2013.04.027 ↑

[6] D. Pines and L. Salvino, "Structural health monitoring using empirical mode decomposition and the Hilbert phase,"*J. Sound Vibr.*, vol. 294, no. 1, pp. 97-124, 2006. https://doi.org/10.1016/j.jsv.2005.10.024 ↑

[7] N. Cheraghi and F. Taheri, .ᴬ damage index for structural health monitoring based on the empirical mode decomposition,"*J. Mech. Mater. Struct.*, vol. 2, pp. 43-61, March 2007. https://doi.org/10.2140/jomms.2007.2.43 ↑

[8] L. Cano, .ᵒn time-frequency analysis for structural damage detection,"PhD thesis, Univ. Puerto Rico, Puerto Rico, 2008. [Online]. Available: https://www.researchgate.net/publication/257138876_On_Time-Frequency_Analysis_for_Structural_Damage_Detection ↑

[9] D. Swagato and S. Purnachandra, "Structural health monitoring techniques implemented on IASC-ASCE benchmark problem: A review,"*J. Civil Struct, Health Monitor.*, vol. 8, pp. 689-718, 2018. https://doi.org/10.1007/s13349-018-0292-5 ↑

[10] B. Basuraj , H. Budhaditya, and P. Vikram, Real time structural damage detection using recursive singular spectrum analysis,ïn *13th Int. Conf. App. Stat. Prob. Civil Eng.*, 2019, pp. 1-8. https://s-space.snu.ac.kr/bitstream/10371/153487/1/358.pdf ↑

[11] S. Sony and A. Sadhu, "Multivariate empirical mode decomposition-based structural damage localization using limited sensors,"*J. Vibr. Control*, vol. 28, no. 15-16, pp. 1863-2167, 2021. https://doi.org/10.1177/10775463211006965 ↑

[12] D. Yansong, S. Zongzhen, and G. Kongzheng, "Structural damage identification under variable environmental/operational conditions based on singular spectrum analysis and statistical control chart,"*Struct. Control Health Monitor.*, vol. 28, no. 6, pp. 1-19, March 2021. https://doi.org/10.1002/stc.2721 ↑

[13] J. I. Campos Hernández, Ïnnovador método para detectar daño estructural, funciones de la bifurcación frecuencial modal (modal frequency splitting functions),"Master thesis, Inst. Polit. Nac., Mexico, 2018. [Online]. Available: http://tesis.ipn.mx/handle/123456789/27096 ↑

[14] R. Zhang, M. Asce, S. Ma, E. Safak, and S. Hartzell, "Hilbert-Huang transform analysis of dynamic and earthquake motion recordings,"*J. Eng. Mech. ASCE*, vol. 129, no. 8, pp. 861-875, 2003. `https://doi.org/10.1061/(asce)0733-9399(2003)129:8(861)` ↑

[15] L. Plazas, M. A. Avila, and A. Torres, "Spectral estimation of UV-Vis absorbance time series for water quality monitoring,"*Ingeniería*, vol. 22, no. 2, pp. 211-225, 2017. `https://doi.org/10.14483/udistrital.jour.reving.2017.1.a01` ↑

[16] K. Liu, S. Law, Y. Xia, and X. Zhu, "Singular spectrum analysis for enhancing the sensitivity in structural damage detection,"*J. Sound Vibr.*, vol. 333, no. 2, pp. 392-417, 2014. `https://doi.org/10.1016/j.jsv.2013.09.027` ↑

[17] M. A. de Oliveira, J. V. Filho, V. Lopes, and D. J. Inman, .ᴬ new approach for structural damage detection exploring the singular spectrum analysis,"*J. Intel. Mater. Syst. Struct.*, vol. 28, no. 9, pp. 1160-1174, 2017. `https://doi.org/10.1177/1045389x16667549` ↑

[18] J. Yang, Y. Lei, S. Lin, and N. Huang, "Hilbert-Huang based approach for structural damage detection,"*J. Eng. Mech.*, vol. 130, no. 1, pp. 85-95, 2004. `https://doi.org/10.1061/(asce)0733-9399(2004)130:1(85)` ↑

Elisa C. González

Born in Pasto, Colombia. She received a BS degree in Mathematics at Universidad de Nariño, a Master in Biomathematics at Universidad del Quindío, and a degree in Civil Engineering at Universidad del Quindío (Colombia). She is currently a PhD student in Statistics at USP, Brasil. She is a member of Grupo de Investigación y Asesoría en Estadística. Her research work is focused on stochastic processes, time series analysis, mathematical modeling, and structural analysis.
E-mail: ecgonzalez@uniquindio.edu.co

Gladys E. Salcedo

Born in Pijao, Colombia. She received a BS degree in Mathematics at Universidad del Quindío, a Master in Statistics at the University of São Paulo (Brazil), and a PhD in Statistics at the University of São Paulo (Brazil). She is a member of Grupo de Investigación y Asesoría en Estadística. Her research work is focused on stochastic processes, statistical modeling, and time series analysis.
E-mail: gsalcedo@uniquindio.edu.co

Leonardo Cano

Born in Armenia, Colombia. He received a BS degree in Civil Engineering at Universidad del Quindío, a MSc in Civil Engineering (Earthquake Engineering) at Universidad de los Andes, and a PhD in Civil Engineering (Structural Engineering) at the University of Puerto Rico, Mayaguez Campus. He is a member of the Colombian Earthquake Engineering Association (AIS), the Earthquake Engineering Institute (EERI), the Seismological Society of America (SSA), and the Quimbaya research group of Universidad del Quindío. His research work is focused on earthquake and structural engineering and structural forensic engineering.
E-mail: lcano@uniquindio.edu.co